UNIVERSIDAD COMPLUTENSE DE MADRID
FACULTAD DE FARMACIA
Departamento de Química en Ciencias Farmacéuticas

TESIS DOCTORAL

Sensores basados en nanopartículas de conversión ascedente para la detección de oligonucleótidos de ARN/ADN

Sensors based on upconverting nanoparticles for the detection of RNA/DNA oligonucleotides

MEMORIA PARA OPTAR AL GRADO DE DOCTOR

PRESENTADA POR

Diego Méndez González

Directores

Jorge Rubio Retama
Marco Laurenti
Enrique López Cabarcos

Madrid
Ed. electrónica 2019

UNIVERSIDAD
COMPLUTENSE
MADRID

Sensores basados en nanopartículas de conversión ascendente para la detección de oligonucleótidos de ARN / ADN

Sensors based on upconverting nanoparticles for the detection of RNA/DNA oligonucleotides

Diego Méndez González

Facultad de Farmacia
Dpto. de química en ciencias farmacéuticas

Tesis Doctoral

Mención doctorado internacional

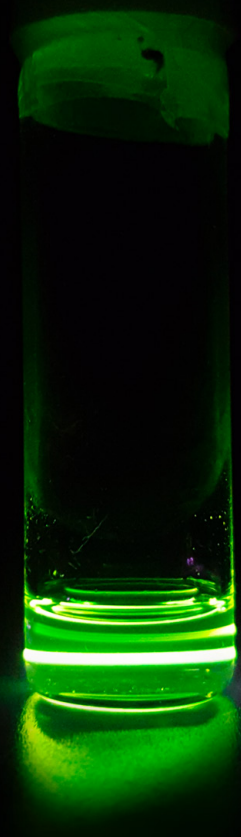

Directores

Prof. Dr. Jorge Rubio Retama

Prof. Dr. Marco Laurenti

Prof. Dr. Enrique López Cabarcos

UNIVERSIDAD COMPLUTENSE DE MADRID

FACULTAD DE FARMACIA

Departamento de química en ciencias farmacéuticas

Sensores basados en nanopartículas de conversión ascendente para la detección de oligonucleótidos de ARN / ADN

MEMORIA PRESENTADA PARA OPTAR AL GRADO DE DOCTOR CON MENCIÓN INTERNACIONAL

Diego Méndez González

Directores

Prof. Dr. Jorge Rubio Retama

Prof. Dr. Marco Laurenti

Prof. Dr. Enrique López Cabarcos

Madrid 2019

COMPLUTENSE UNIVERSITY OF MADRID

FACULTY OF PHARMACY

Department of chemistry in pharmaceutical sciences

Sensors based on upconverting nanoparticles for the detection of RNA /DNA oligonucleotides

MEMORANDUM TO REQUEST THE PHD DEGREE WITH INTERNACIONAL MENTION

Diego Méndez González

Supervisors

Prof. Dr. Jorge Rubio Retama

Prof. Dr. Marco Laurenti

Prof. Dr. Enrique López Cabarcos

Madrid 2019

UNIVERSIDAD COMPLUTENSE MADRID

DECLARACIÓN DE AUTORÍA Y ORIGINALIDAD DE LA TESIS PRESENTADA PARA LA OBTENCIÓN DEL TÍTULO DE DOCTOR

D./Dña. Diego Méndez González

con número de DNI/NIE/Pasaporte _____, estudiante en el Programa de Doctorado D9BI - DOCTORADO EN FARMACIA, de la Facultad de Farmacia de la Universidad Complutense de Madrid, como autor/a de la tesis presentada para la obtención del título de Doctor y titulada:

SENSORES BASADOS EN NANOPARTÍCULAS DE CONVERSIÓN ASCENDENTE PARA LA DETECCIÓN DE OLIGONUCLEÓTIDOS DE RNA/DNA // SENSORS BASED ON UPCONVERTING NANOPARTICLES FOR THE DETECTION OF RNA/DNA OLIGONUCLEOTIDES

y dirigida por: Enrique López Cabarcos, Jorge Rubio Retama y Marco Laurenti.

DECLARO QUE:

La tesis es una obra original que no infringe los derechos de propiedad intelectual ni los derechos de propiedad industrial u otros, de acuerdo con el ordenamiento jurídico vigente, en particular, la Ley de Propiedad Intelectual (R.D. legislativo 1/1996, de 12 de abril, por el que se aprueba el texto refundido de la Ley de Propiedad Intelectual, modificado por la Ley 2/2019, de 1 de marzo, regularizando, aclarando y armonizando las disposiciones legales vigentes sobre la materia), en particular, las disposiciones referidas al derecho de cita.

Del mismo modo, asumo frente a la Universidad cualquier responsabilidad que pudiera derivarse de la autoría o falta de originalidad del contenido de la tesis presentada de conformidad con el ordenamiento jurídico vigente.

En Madrid, a 25 de abril de 2019

Fdo.: 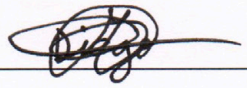

Esta DECLARACIÓN DE AUTORÍA Y ORIGINALIDAD debe ser insertada en la primera página de la tesis presentada para la obtención del título de Doctor.

Agradecimientos

"Lo urgente no deja tiempo para lo importante". Y lo importante, sin duda, son las personas. Cualquier trabajador apasionado e involucrado en un proyecto de carácter personal, con seguridad puede comprender la sensación de "deber tiempo" a las personas que ocupan un lugar especial en sus vidas: tanto por la ausencia física inherente a las horas consumidas en él, como a la ausencia involuntaria, aún estando de cuerpo presente, fruto de estar continuamente inmerso en pensar nuevas ideas.
Investigar es probablemente una de las profesiones más estimulantes y apasionantes que pueda haber, aunque el sacrificio que exige es alto: tiempo, laborable y con frecuencia también personal, así como una continua demanda física y mental. Sin embargo en investigación, como en la vida, el "tick-tack" dicta.
Por eso, esta sección de mi tesis es tan importante para mí como el trabajo presentado en las próximas páginas. A continuación me gustaría agradecer a todas las personas que de una manera u otra han tenido un impacto, directo o indirecto, en el desarrollo de esta tesis:

Jorge, te debo el haber podido experimentar la vida de investigador durante varios años ya, algo con lo que solía soñar de estudiante pero que creía quimera. Gracias por engancharme a este mundillo y darme la oportunidad de investigar. Quién me iba a decir que una beca de colaboración acabaría llevándome a un doctorado. Has favorecido que piense por mí mismo y que pueda investigar campos en los que creo y que me apasionan. Esa oportunidad no es tan común en ciencia y te lo agradezco muchísimo. Junto con Marco hemos vivido años duros, pero gracias al esfuerzo de todos hemos logrado que esto despegue, ¡Y ahora la familia crece!. Estoy muy contento con lo que hemos ido logrando todos juntos.
Marco, eres un compañero de lab genial, ojalá me encuentre muchos como tú en el futuro. Tienes cualidades que no se encuentran fácilmente: responsabilidad, profesionalidad, compañerismo, saber escuchar. Gracias por las risas y el buen rollo, has sido mamá pato en muchos aspectos y espero que podamos seguir trabajando juntos muchos años más. Te deseo la mejor de las suertes y que sigas creciendo como docente e investigador, creo que puedes llegar a hacer muy bien ambas funciones.
Enrique, hay pocas cosas que me impresionen más que la jovialidad y la forma de ser que demuestras en el día a día, sobre todo después de tanto tiempo en docencia e investigación. Haces que acertadamente parezca que nada tenga la importancia exagerada que le solemos dar, sobre todo si lo relativizamos al conjunto de la vida en sí misma. Espero acabar logrando aplicar plenamente dicha filosofía. Al mismo tiempo gracias por hacerme reparar en cuánto condiciona nuestra visión del mundo la rama académica que conforma la base de nuestra formación: el dejar de enfocar un problema desde un punto de vista tan químico, y ver cómo éste toma otra dimensión al enfocarlo desde uno más físico.

Sonia y Óscar, Óscar y Sonia, no podría hablar del uno sin el otro. Si hubiera podido tener más directores de tesis, sin duda también lo serían ustedes. Son unas personas encantadoras y a las que les debo mucho. No sólo son unos profesores magníficos, sino unos investigadores excelentes. Son la prueba viviente de que el conocimiento y el saber hacer no son incompatibles con la humildad, la paciencia, el respeto a quien sabe menos, y al trabajar codo con codo enseñando con sus amables y dedicadas explicaciones. He aprendido muchísimo con ustedes. Ojalá siga conociendo personas con la calidad humana que derrochan, y que pueda trabajar con ustedes muchos años más.

Paulino, no podría contar la cantidad de veces que me has hecho reír durante el doctorado. Te doy las gracias por esos buenos momentos tanto en el lab como fuera (e.g. esa cara de perro porque nos pille lloviendo, tengamos que aparcar bajo el agua, y nos intenten timar en Jerusalén jajaja). Has sido un poco como mi hermano mayor en los inicios de la tesis, y te agradezco muchísimo tanto los consejos como las largas conversaciones. Muchas de éstas acabaron haciéndome meditar muchas cosas, lo que considero la prueba de ser conversaciones valiosas. Mucha suerte con el camino que has tomado, ¡Aunque sé que no la necesitas!

Al grupo de investigación, en especial a las nuevas y prometedoras investigadoras Vivian e Irene, y a las incorporaciones temporales como Pedro y Alicia. Gracias por estos meses, en los que habéis creado un ambiente tan genial y habéis llenado de vida no sólo nuestra sala y el laboratorio, sino el departamento entero. Para mi ha sido un placer enseñarles y ayudarles en todo lo que ha estado en mi mano, ejerciendo esta vez yo el papel de mamá pato. Muchísima suerte con sus respectivas tesis, son personas muy competentes y estoy convencido de que lo harán genial. Y no se desesperen si algo no les sale de primeras, que cada fallo conduce un paso más cerca del acierto.

A la unidad docente de química física y física aplicada del departamento de química en ciencias farmacéuticas. Estoy muy agradecido por la ayuda diaria y por la cálida acogida por parte de todos. En especial a Visi, Juani y a Piedad, por cuidarnos y ayudarnos tanto. A Marian y a Begoña por la ayuda y la gran amabilidad a la hora de prestarme parte de su instrumental de laboratorio. A Paz, Monte y Cristina por ser siempre tan cariñosas y atentas conmigo. A Concepción Civera y a Ignacio por la ayuda desinteresada y estar siempre al pie del cañón. A Miguel Ángel, Pepe y Concepción Arias por los consejos y la ayuda prestada. A Niuris e Inma, por las agradables charlas entre prácticas y celebraciones de departamento. A Marco Filice por las conversaciones y las risas, y a su grupo, lleno de personas encantadoras y siempre dispuestas a ayudar: Mario, Karina y Marzia.

A Tero Soukka por acogerme con tanta amabilidad en su laboratorio, por toda la ayuda durante la preparación de mi estancia, por creer en mi proyecto, y por estar abierto en todo momento a la discusión científica. A todo su grupo, por el buen trato, su paciencia, explicaciones y buen hacer durante mi estancia.

A Edu y Elena, por las explicaciones, la paciencia y su fructífera colaboración investigadora.

A mi familia, a la cual dedico especialmente esta tesis y todos los trabajos no incluidos en esta disertación. A mi hermano Juan Luis, porque es el principal responsable de plantar la semilla de la curiosidad desde mi infancia, con nuestras competiciones de construcción de barcos o trampas, y demás proyectos lúdico-científicos. Espero poder lograr devolverte la ayuda que me has prestado siempre y el fuerte apoyo que me has brindado en todo momento: incluso haciendo realidad alguna de las ideas que tenía en mente, como la construcción del prototipo LED presentado en la publicación 5. A mi hermana, porque siempre has sido una de las personas más adorables y cariñosas que conozco, y cuya presencia siempre me ha dado tranquilidad y seguridad. Haces que me sienta en casa a pesar de estar a 2000 km. Siempre me he divertido mucho contigo, y ahora ya podemos hasta irnos de cañas y filosofar un poco sobre el mundo, ¡Qué rápido pasa el tiempo!. Gracias por todo tu apoyo durante la tesis. A mis queridos Padres, Juan Antonio y María del Carmen, por haber logrado todo: Ser unos profesionales, unas personas y unos padres increíbles, proveernos de una buena educación (no sólo académica, también humana), hacernos percibir el valor de las cosas y luchar por aquello en lo que creemos. Sin duda son actores responsables de que hoy pueda estar cerca de terminar un doctorado. También fueron mi fundación MCGL&JAMA durante los complicados inicios, tal como recoge el trabajo de investigación con doi "10.1016/j.eurpolymj.2016.01.013". A mi tía Montse y a mi abuela Micaela. Siempre me dan la mejor bienvenida que se pueda tener. Gracias por el inmenso apoyo incondicional que me muestran siempre. Abuela, eres una de las mujeres más lúcidas y aventureras que conozco. A todos mis tíos y primos por el cariño, el apoyo y el interés en esta aventura: a Felipe, Loles, Everto, Isora, Lito, Petra Magdalena, Carmen Rosa, Yared y toda la familia.
A mi buena y querida abuela Serafina, a mi tía "Lala", y a mi inquieto y curioso abuelo Eduardo, aunque ya no estén con nosotros. También a mi tío Eduardo, cuya curiosidad innata siempre llegó a mis oídos y despertó admiración.

A mis amigos, sin los que la vida no sería tan divertida. A David y Dani, a los que tengo un profundo cariño, con los que siempre he podido contar, y los que tiran de mi para exprimir la vida siempre un poquito más. A Miriam, cuyo carácter singular, interesantes conversaciones, y coñas continuas, la hacen una amiga única.
A Carlos Vilas, cuya vitalidad inagotable, afectuoso carácter, y amistad incondicional, lo hacen un amigo imprescindible. A Jonás, que después de tantos años de amistad, y aún desde el otro lado del globo, no deja de demostrarme el poder de la voluntad. A Carlos y a Patricio, por el apoyo y por esos divertidos años compartiendo piso, así como últimamente nuestras más frecuentes conversaciones sobre ciencia y el futuro en general. Mucha suerte con vuestros respectivos doctorados. A Yago, por su saber escuchar, por tantas conversaciones, reflexiones,

y buenas vivencias compartidas. La mejor de las suertes en el nuevo camino que inicias. A Erik, Emma, Pino, Pablo, María y Alejandro, por tantas conversaciones y vivencias, por hacerme sentir en casa cada vez que nos encontramos de nuevo.
A la increíble Aida, con su enorme corazón y su fortaleza admirable. Gracias por un año tan genial en el piso. Espero que tengas muchísima suerte en todo aquello que te propongas, ya que sé que fuerza no te falta. A Lucía, por esas conversaciones tan interesantes en las que siempre acabo aprendiendo alguna cosa nueva. A Bea, por todo su cariño, tantísimas conversaciones, sus buenos consejos y su inestimable amistad. Eres una persona muy valiosa. Gracias por acompañarme durante este viaje y por animarme a que me lanzara a investigar. Siempre tendrás "familia" tanto en Madrid como en Canarias.
Con especial cariño a Sara, con quien he tenido la increíble fortuna de poder compartir tantas vivencias bonitas. Sin ti esta tesis no habría sido la misma. Gracias por tu ayuda, apoyo y curiosidad, por tu humor magnífico e imaginación, por tu enorme cariño e infinita paciencia. Ah, y por el inve'nadero y cosas afines.

Apoyo técnico y financiero

Quería agradecer a la Bill & Melinda Gates Foundation (grant OPP1128411), al Ministerio de educación y competitividad (proyectos FIS2013-41709, SAF2014-56763-R, MAT2014-55065-R y MAT2017-83111-R), a la UCM-Santander (proyecto PR26/16-12B-3), y a la comunidad autónoma de Madrid (proyecto B2017/BMD-3867 RENIM-CM) por el apoyo financiero durante el desarrollo de esta tesis, así como a UCM-Santander por el contrato predoctoral (CT17/17-CT18/17), y a la COST Action CM1403 "the european upconversion network from the design of photon-upconverting nanomaterials to (biomedical) applications".
Quería agradecer también al centro de microscopía nacional (UCM, Madrid) y a sus técnicos por los consejos y los servicios prestados.
Finalmente agradecer a Juan Luis Méndez González por la construcción del prototipo LED presentado en la publicación 5, y a Sara López París por la ayuda en el diseño de la portada y algunas de las figuras presentadas en esta tesis.

"*Magic is matching an effect with a misleading cause.*
Science is a kind of magic, until it is not"

"*Magia es relacionar un efecto con una causa errónea.*
La ciencia es una clase de magia, hasta que deja de serlo"

Index / Índice

Abstract / Resumen

Abstract

Since the discovery of miRNAs in the early 90's, their study during the last two decades have put the bases for the understanding of the biosynthesis, mechanism of action, and importance of these short sequences on gene regulation. Highly conserved among animals, plants, and even viruses, their role in gene translation repression as well as the regulation of other miRNA sequences has revealed as an upstream way to control and correct the cell's gene expression. Thus regarded as a possible new generation of drugs for the treatment of diseases due to their biological activity, they are also potential diagnostic biomarkers: while the presence of foreign miRNA sequences in the human organism can be used for the early diagnosis of infections, the alteration of the normal endogenous miRNA expression profiles is revealing as a promising tool for the diagnosis and prognosis of important conditions like cancer or Alzheimer disease.

Latest advances in chemistry and nanotechnology are starting to offer tools for the direct detection of miRNAs, whose low detectability is mainly due to their low serum concentration and their low melting temperatures upon hybridization with the probes designed for their detection. On the one hand, new chemistries are starting to appear on the biosensing field, such as "copper-free" click chemistries or photo-activated chemical reactions, offering new possibilities for detection and quantification. On the other hand, traditional organic dyes are starting to be replaced by new reporters that overcome, by far, the optical properties exhibited by them. Some examples are the widely known quantum dots, or the new and promising upconverting nanoparticles (UCNPs), which are permitting to build very sensitive sensors and assays.

UCNPs exhibit anti-Stokes emissions that are far away from their excitation wavelength, located at the near infrared region (NIR). They perform this process very efficiently by using continuous wave lasers and other simple instrumentation, whereas common dyes and other materials usually require expensive femtosecond pulsed lasers to produce anti-Stokes emissions by two-photon-absorption processes that are orders of magnitude less efficient.

The photon upconversion anti-Stokes process produced by UCNPs, together with the physical-chemical properties of these nanoparticles, permits to avoid some of the most important limitations that arise when using common luminescent reporters such as autofluorescence, photobleaching, or fluorescence intermittency. For these reasons, the synthetic control of UCNPs, their surface functionalization, and conjugation with suitable biomolecules to apply them as reporters may permit to design a whole new generation of very sensitive detection systems based on the direct sensing (i.e. without signal amplification methods) of targeted analytes, which will be most likely accompanied of time and cost-effective assays and reduction of bias, as well as easier point of care diagnostics.

This thesis work is focused on the synthesis of UCNPs, their functionalization, fundamental study, and bioconjugation for the development of highly sensitive RNA/DNA oligonucleotide detection systems, using UCNPs as labels. Firstly, an introduction is presented, explaining the miRNA biosynthesis, mechanism and clinical potential ("section I.1"). Next, the mechanism, optical features, and advantages of UCNPs are compared with reporters currently used in bioimaging and detection or still under intense research, like organic dyes and quantum dots ("section I.2"). A wide review on the state of the art of UCNPs in biodetection, both in homogeneous and heterogeneous assays, is presented as the end of the introduction ("section I.3"). In this section the properties of UCNPs, their application to different platforms, the discussion of sensing strategies using these labels, their impact in the performance of the detection systems, and future prospects are discussed.

The experimental chapters of this thesis are divided in two different sections: The first one focus on fundamental studies on resonance energy transfer processes using UCNPs as donors and CdTe quantum dots (Q-dots), or gold nanoparticles (AuNPs), as acceptors ("section III.1"). The coating of UCNPs with silica shells of different thicknesses permitted to study the influence of the Q-dots proximity on the upconversion luminescence. After estimating the Förster radius for this system, and taking into account the multi-emitter nature of UCNPs, we were able to explain the total Förster resonance energy transfer (FRET) efficiencies obtained experimentally and to estimate the FRET efficiency for the different individual Erbium ions (Er^{3+} ions) within the UCNP as a function of their distance to the Q-

dots. As result, we established some general guidelines when aiming to improve total FRET efficiencies and to apply UCNPs/CdTe Q-dots pairs to the construction of FRET sensors. In a second work, the effect of the AuNPs size on the upconversion luminescence was studied. Smaller AuNPs proved to favor luminescence quenching of the UCNPs, while the bigger AuNPs exerted an increasing effect on raising the radiative decay rate of Er^{3+} ions due to the Purcell effect, translating in a progressive luminescence enhancement as AuNP size increased. This study permitted to find an optimum AuNP size for the quenching of UCNPs' luminescence (i.e. ~14 nm), while establishing an AuNP size limit from which an effective luminescence enhancement could be achieved (i.e. 66 nm) and improved with larger sizes. These results should be considered when designing sensors based on upconversion luminescence quenching or enhancement.

The second experimental section is mainly focused on the application of new approaches to the direct detection of DNA/miRNA in heterogeneous assays using UCNPs as labels ("section III.2"). In the first work presented in this section, silica-coated UCNPs were bioconjugated with amino-modified single-stranded DNA (ssDNA) to give upconversion probes with specific biological response towards the targeted oligonucleotide in the assay. The grafted ssDNA also had an azide modification, which permitted to form a covalent bond by Cu-free click chemistry with a DBCO modification contained in a second ssDNA probe. This reaction occurred with high specificity, when both azide and DBCO modifications were in close proximity upon hybridization of the probes with the targeted sequence. This strategy allowed the use of repeated or/and harsh washes to reduce the non-specific binding of UCNPs during the assay, while the specific signal formed due to the presence of the target was conserved due to its covalent nature. As result, the assay showed a very good sensitivity (limit of detection, LOD = 100 fM).

The second work was based on a photochemical ligation between two ssDNA probes, one attached to the UCNPs and the other one being free in solution and containing a photoactivatable nucleotide. This photochemical covalent ligation proceeded only in the presence of the targeted oligonucleotide sequence and under UV irradiation (365 nm). This reaction proved to be very specific and also allowed the use of repeated or/and harsh washes during the assay developed with this strategy, which translated in an astonishing sensitivity (LOD = 21 fM).

The photochemical ligation was achieved also using NIR light at 980 nm as external excitation, and the upconversion emission at 365 nm of Ytterbium / Thulium-doped UCNPs as local source of UV photons. The requirement of UV light for the ligation to proceed allowed the control of the place where the reaction took place in a solid support, as well as the exact time when the reaction started and stopped, which could be used to form patterns specifically in the presence of the targeted sequence.

Keywords: Upconverting nanoparticles, silica, quantum dots, gold nanoparticles, FRET, quenching, enhancement, Purcell effect, sensor, heterogeneous assay, click chemistry, photoligation, miRNA, oligonucleotide, luminescence, microwell, pattern, probe.

Resumen

Desde el descubrimiento de los miARNs, a principios de los 90s, su estudio durante las últimas dos décadas ha sentado las bases para la comprensión de la biosíntesis, mecanismo de acción, e importancia de estas pequeñas secuencias en la regulación de los genes. Conservados ampliamente entre animales, plantas, e incluso virus, su rol en la represión de la traducción genética, al mismo tiempo que en la regulación de otras secuencias de miARN, se presenta como una forma de controlar y corregir la expresión génica situada al inicio de la cadena de procesos celulares. Así, considerados como una posible nueva generación de fármacos para el tratamiento de enfermedades, debido a su actividad biológica, son también potenciales biomarcadores para diagnóstico: Mientras la presencia de secuencias de miARN extraño en el organismo humano puede ser usada para el diagnóstico precoz de infecciones, la alteración de los perfiles de expresión normales de miARN endógeno se está presentando como una herramienta prometedora para el diagnóstico y el pronóstico de importantes enfermedades como el cáncer o la enfermedad de Alzheimer.

Los últimos avances en química y nanotecnología, están empezando a ofrecer herramientas para la detección directa de miARNs, cuya baja detectabilidad se debe principalmente a su baja concentración en suero y su baja temperatura de fusión (o melting) durante la hibridación con las sondas usadas para su detección. Por un lado, nuevas estrategias químicas están empezando a aparecer en el campo de la biodetección, tales como químicas click sin cobre o reacciones químicas foto-activables, ofreciendo nuevas posibilidades para la detección y la cuantificación. Por otro lado, los fluoróforos convencionales están empezando a ser reemplazados por nuevas etiquetas que superan sustancialmente las propiedades ópticas exhibidas por éstos. Algunos ejemplos son los conocidos puntos cuánticos, o las nuevas y prometedoras nanopartículas de conversión ascendente (UCNPs), las cuales están permitiendo construir sensores y ensayos muy sensibles.

Las UCNPs exhiben emisiones de tipo anti-Stokes que están lejos de la longitud de onda de excitación, la cual se localiza en la región infrarroja (NIR). Son capaces de llevar a cabo este proceso de manera muy eficiente usando láseres de onda continua y otra instrumentación sencilla, mientras que los fluoróforos comunes y otros materiales normalmente requieren costosos láseres pulsados de femtosegundo para producir emisiones anti-Stokes por medio de procesos de absorción de dos fotones, que son órdenes de magnitud menos eficientes.

El proceso anti-Stokes de conversión ascendente de fotones producido por las UCNPs, junto con las propiedades físico-químicas de estas nanopartículas, permiten evitar algunas de las limitaciones más importantes que surgen cuando se usan las etiquetas luminiscentes más comunes, como son la autofluorescencia, el foto-blanqueado y la intermitencia de fluorescencia.

Por estas razones, el control sintético de las UCNPs, su funcionalización superficial, y conjugación con biomoléculas adecuadas para aplicar las UCNPs como etiquetas podrían permitir el diseño de una nueva generación de sistemas de detección de alta sensibilidad basados en la detección directa (i.e. sin métodos de amplificación de señal) de analitos de interés, lo cual probablemente estaría acompañado de ensayos con una mejor relación tiempo y coste / beneficio y una reducción de los sesgos y la irreproducibilidad, así como un diagnóstico más fácil en zonas alejadas de laboratorios especializados.

Este trabajo de tesis se centra en la síntesis de UCNPs, su funcionalización superficial, su estudio fundamental, y su bioconjugación para el desarrollo de sistemas de detección con alta sensibilidad de oligonucleótidos de RNA/DNA, usando las UCNPs como etiquetas. En primer lugar se presenta una introducción explicando la biosíntesis, el mecanismo, y el potencial clínico del miRNA ("sección I.1"). A continuación se compara el mecanismo, las propiedades ópticas y las ventajas de las UCNPs con etiquetas usadas en bioimagen y detección, o que aún están bajo intensa investigación, como fluoróforos orgánicos y puntos cuánticos ("sección I.2"). Al final de la introducción se presenta una amplia revisión del estado del arte de las UCNPs en biodetección, tanto en ensayos homogéneos como heterogéneos ("sección I.3"). En esta sección se discuten las propiedades de las UCNPs, su aplicación a diferentes plataformas, las estrategias de detección usando

estas etiquetas, su impacto en el rendimiento de los sistemas de detección y las perspectivas futuras del campo.

Los capítulos experimentales de esta tesis se dividen en dos secciones diferentes: La primera se centra en estudios fundamentales sobre procesos de transferencia de energía por resonancia usando UCNPs como donadores y puntos cuánticos (Q-dots) de CdTe, o nanopartículas de oro (AuNPs), como aceptores ("sección III.1"). El revestimiento de las UCNPs con recubrimientos de sílice de distintos grosores permitió estudiar la influencia de la proximidad de los Q-dots en la luminiscencia conversión ascendente. Después de estimar el radio de Förster para este sistema, y tener el cuenta la naturaleza multi-emisora de las UCNPs, fuimos capaces de explicar las eficiencias totales de transferencia energética por resonancia de Förster (FRET) halladas experimentalmente y de estimar la eficiencia de FRET para los distintos iones individuales de Erbio (iones de Er^{3+}) dentro de la UCNP en función de su distancia a los Q-dots. Como resultado, establecimos algunas recomendaciones para mejorar las eficiencias de FRET totales y aplicar el par UCNPs/Q-dots de CdTe a la construcción de sensores FRET. En un segundo trabajo, se estudió el efecto del tamaño de las AuNPs en la luminiscencia de conversión ascendente. Las AuNPs más pequeñas probaron favorecer la desactivación de la luminiscencia de las UCNPs, mientras que las más grandes ejercieron un efecto incremental sobre el aumento de la tasa de decaimiento radiativo de los iones de Er^{3+} debido al efecto Purcell, lo que se tradujo en un aumento progresivo de la luminiscencia a medida que el tamaño de las AuNPs crecía. Este estudio permitió encontrar un tamaño óptimo de AuNP para la desactivación de la luminiscencia de las UCNPs (i.e. 14-21 nm), al mismo tiempo que establecer un tamaño límite de AuNP a partir del cual se pudo obtener un aumento efectivo de la luminiscencia y mejorado con tamaños mayores. Estos resultados deberían considerarse a la hora de diseñar sensores basados en desactivación o aumento de la luminiscencia de conversión ascendente.

La segunda sección experimental se centra en la aplicación de nuevas estrategias para la detección directa de ADN/miARN en ensayos heterogéneos usando UCNPs como etiquetas ("sección III.2"). En el primer trabajo presentado en esta sección, se bioconjugaron UCNPs recubiertas con sílice con cadenas sencillas de ADN (ssDNA) modificadas con grupos amino para dar sondas de conversión ascendente

con una respuesta biológica específica en el ensayo hacia el oligonucleótido diana. Las ssDNA fijadas también tenían una modificación con grupo azida, la cual permitió formar un enlace covalente mediante química click "sin cobre" con una modificación con DBCO contenida en una segunda sonda de ssDNA. Esta reacción ocurrió con alta especificidad, cuando la azida y el DBCO estaban en cercana proximidad debido a la hibridación de las sondas con la secuencia diana. Esta estrategia permitió el uso de lavados repetidos o/y fuertes para reducir la unión no específica de las UCNPs durante el ensayo, mientras que la señal específica formada debido a la presencia de la diana se conservó debido a su naturaleza covalente. Como resultado, el ensayo mostró una sensibilidad muy buena (límite de detección, LOD = 100 fM).

El segundo trabajo se basó en una ligación fotoquímica entre dos sondas de ssDNA, una unida a las UCNPs y la otra estando libre en solución y conteniendo un nucleótido foto-activable. Esta ligación fotoquímica covalente progresó sólo en presencia de la secuencia del oligonucleótido diana y bajo irradiación con luz UV (365 nm). Esta reacción probó ser muy específica y también permitió el uso de lavados repetidos o/y fuertes durante el ensayo desarrollado con esta estrategia, lo cual se tradujo en una sensibilidad asombrosa (LOD = 21 fM). La ligación fotoquímica se logró también usando luz NIR a 980 nm como excitación externa, y la emisión de conversión ascendente a 365 nm de las UCNPs dopadas con Ytterbio/Tulio como fuente local de fotones de UV. El requisito de luz UV para que la ligación progrese permitió controlar el lugar en el que la reacción tenía lugar en un soporte sólido, así como el momento exacto en el que la reacción empezaba y terminaba, lo que pudo ser usado para formar patrones específicamente en presencia de la secuencia diana.

Palabras clave: Nanopartículas de conversión ascendente, sílice, puntos cuánticos, nanopartículas de oro, FRET, desactivación, aumento, efecto Purcell, sensor, ensayo heterogéneo, química click, fotoligación, miARN, oligonucleótido, luminiscencia, micropocillo, patrón, sonda.

I. Introduction

I) Introduction

Since the very development of basic tools by our early ancestors, technology has turned into an essential matter for the continuity of our existence and our adaptation as species.[1–3] The manipulation of matter, either by joining basic materials to get a new non-phenotypically provided skill or tool, by carrying out chemical reactions to reorganize atoms in search of new properties, or by studying and modifying biological molecules and processes to exert an effect in living organisms, are all part of technology, as is also the knowledge required to make all of this possible. Manipulation of matter can be extended to different scales, being technology itself the one allowing to push the field to new limits, such as the nanoscale. In this range, the properties of matter can experience sudden changes compared to their macroscopic or "bulk" counterparts, due to quantum mechanics related effects (e.g. quantum confinement in semiconductors), the high surface to volume ratios exhibited by these materials, and other size-related phenomena. Already envisioned by the physicist Nobel laureate Richard Feynman in his speech "There's plenty of room at the bottom",[4] but actually starting to materialize in the work of previous (R. A. Zsigmondy)[5] and later researchers like K. Eric Drexler,[6] R. Smalley, R. Curl and H. Kroto,[7] just to mention a few, the implications of manipulating matter at the atomic, molecular and supramolecular scales have led to the dawn of a new field: Nanotechnology. This includes disciplines as diverse as microfabrication, surface and colloids science, molecular biology, chemistry, physics, molecular engineering, or physical chemistry, as far as they deal with materials exhibiting, at least, one dimension sized from 1 to 100 nanometers. This implies that a widely multidisciplinary knowledge is often required in nanotechnological research, especially when it comprises from the synthesis to the application of the nanomaterial. Although not exempt of concerns, such as nanotoxicity or important environmental impacts derived from their massive production, the potential of these new materials offers the possible solutions to face some of our contemporary challenges: energy storage, increased efficiency of renewable energy production, or new strategies for diagnosis, drug delivery and the study and manipulation of biological systems (sometimes referred as

bionanotechnology), to mention a few. In this regard, the increasing availability of methods to synthesize and design colloidal nanoparticles with singular properties have allowed a step forward to the fulfillment of greatly desired features in biodetection, such as miniaturization, multiplexing, high sensitivity, and direct (non-amplified) detection. Thus, noble metal nanoparticles, quantum dots, or upconverting nanoparticles conform just some examples of promising reporters that are substituting traditional organic dyes as labels for biodetection, due to their enhanced optical and physicochemical properties. The minute amounts of analytes that can be potentially detected by these means open the possibility of directly detecting new biomarkers, such as miRNAs, bypassing some bias occurring in common tasks like retro-transcription and PCR amplification protocols.

This thesis focuses on the synthesis, surface functionalization, bioconjugation and application of upconverting nanoparticles in the development of systems for the direct detection of short DNA/RNA sequences, specially intending to exploit to the greatest extent the very unique optical properties of these labels in the biosensing field.

References

(1) Parker, S. T.; Gibson, K. R. A Developmental Model for the Evolution of Language and Intelligence in Early Hominids. *Behav. Brain Sci.* **1979**, *2*, 367.

(2) Kuhn, S. L. *Mousterian Lithic Technology: An Ecological Perspective*; Princeton University Press: Princeton, New Jersey, 2014.

(3) Toth, N. The First Technology. *Sci. Am.* **1987**, *256*, 112.

(4) Feynman, R. P. There's Plenty of Room at the Bottom. *Eng. Sci.* **1960**, *23*, 22.

(5) Zsigmondy, R. Ueber Wässrige Lösungen Metallischen Goldes. *Justus Liebig's Ann. der Chemie* **1898**, *301*, 29.

(6) Drexler, K. E. Molecular Engineering: An Approach to the Development of General Capabilities for Molecular Manipulation. *Proc. Natl. Acad. Sci.* **1981**, *78*, 5275.

(7) Curl, Robert F.; Kroto, Harold W.; Smalley, R. E. The Nobel Prize in Chemistry 1996 - The discovery of carbon atoms bound in the form of a ball is rewarded https://www.nobelprize.org/prizes/chemistry/1996/press-release/.

I.1 microRNA

Amongst the different kinds of non-coding RNA molecules that have been discovered over the last decades (e.g. microRNAs, siRNAs, piRNAs), the relative abundance and the influence of microRNAs (miRNAs) over essential cellular processes have put them under the spotlight of research. Although lin-4 represents the first historic example of miRNA discovered in *C. elegans* in 1993 ,[1] it was not until the discovery of a second miRNA sequence (let-7),[2] seven years later, that researchers started to wonder about the presence of these biomolecules among different species, including human beings. Ever since, thousands of miRNAs have been found in animals, plants, and even viruses, proving the essential role of these 21-24 nucleotide (nt) long RNA sequences for the well-functioning of these living systems.[3–5]

I.1.1 miRNA biosynthesis and mechanism

The transcribed miRNA genes are only biologically active after being processed by different steps, in which the required cellular machinery and pathways varies between different evolutionarily evolved animals and plants.
In the case of animal miRNAs, most sequences are codified in intergenic regions, and around half of all discovered miRNAs are clustered and expressed as poly-cistronic transcrips while, less commonly, a minority possess their own promoters. RNA polymerase II (Pol II) is normally in charge of miRNA gene transcription, whose products are known as "primary miRNAs" (pri-miRNAs) that are several kilobases long sequences containing local stem loop structures. Animal miRNAs are firstly processed in the cell nucleus, being cleaved at the 5' and 3' stem of the loop structure and releasing a 60-70 nt hairpin structure named "precursor miRNA" (pre-miRNA). This step is carried out by the enzyme "Drosha" in conjuction with the protein "DGCR8" in humans, which already define one end of the mature miRNA,[6,7] see Figure I.1.1.1. These pre-miRNAs are then transported to the cytoplasm by the nuclear transport receptor "exportin-5" (EXP5). Once in the cytoplasm, the ribonuclease "Dicer" (in association with other proteins like

Argonaute family proteins (Ago 1-4), "TRBP", and "PRKRA or PACT") measure 22 nt from the previously defined miRNA matured terminus by Drosha, and cleaves the miRNA strand. The Dicer associated proteins are not required for the processing of pre-miRNA, but for the formation of the RNA-induced silencing complex (RISC). Once the pre-miRNA has been proccessed, one strand of the double stranded miRNA product is degraded, while the other remains bounded to Ago as the mature miRNA. It seems that the selection of the strand which will remain in the complex to perform the silencing function is based on the thermodynamic stability of the two ends of the miRNA duplex. The one with the less stable end (miRNA*) will be unwinded by a RNA Helicase and degraded by the Ago protein. Once the single stranded mature miRNA is obtained, it can guide the RISC to its target mRNA for silencing it (see Figure I.1.1.1 for whole biosynthesis process).[8]

The maturation of miRNA in plants is different. On the one hand, Dicer like-1 (DCL-1) is the only protein responsible for plant miRNA processing, while HASTY (HST), an homologue of exportin-5, is in charge of transporting the miRNAs from the cell nucleus to the cytoplasm. Besides, the association of the miRNAs with the Ago proteins can take place either in the nucleus or in the cytoplasm.

Mature miRNAs can silence their mRNA targets by two main mechanisms: translation represion, or mRNA degradation, whose selection will depend on different factors. Most animal miRNA present bulges and multiple mismatches upon binding to their target sites within the messenger RNA (mRNA), usually located as multiple copies in their 3' untranslated region (3' UTR). On the other hand, plant miRNA binding sites are in the centre of their complementary regions, and posesses a high degree of complementarity with their target mRNA. The level of miRNA-mRNA complementarity, and the number, position and kind of mismatches determines if the target mRNA will suffer degradation or translational repression. In general, central mismatches promote translational repression, while high complementarity favors direct mRNA degradation. Although Ago slicer activity represents one of the main mechanisms by which target mRNA can be degraded, it has been shown that other mechanisms like deadenylation, decapping, and exonucleolytic digestion of mRNA can also occur.[9]

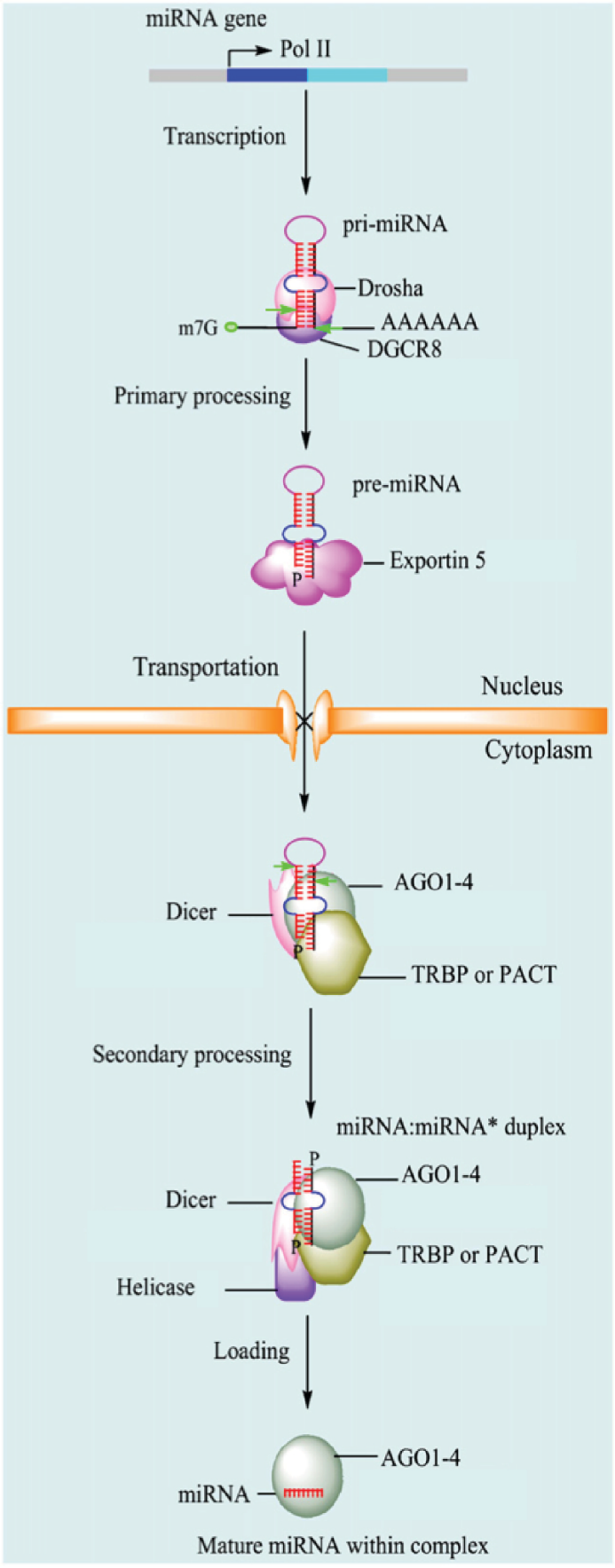

Figure I.1.1.1 animal miRNA biosynthesis process. Modified with permission of [8]

On the other hand, translational repression can proceed by blocking the 43S PIC (pre-initiation complex) recruitment or the ribosomal scanning, by deadenylation and displacement of poly(A) binding protein (PABP), and by recruiting protein translational repressors (DDX6 or 4E-T),[10] see Figure I.1.1.2 for further details.

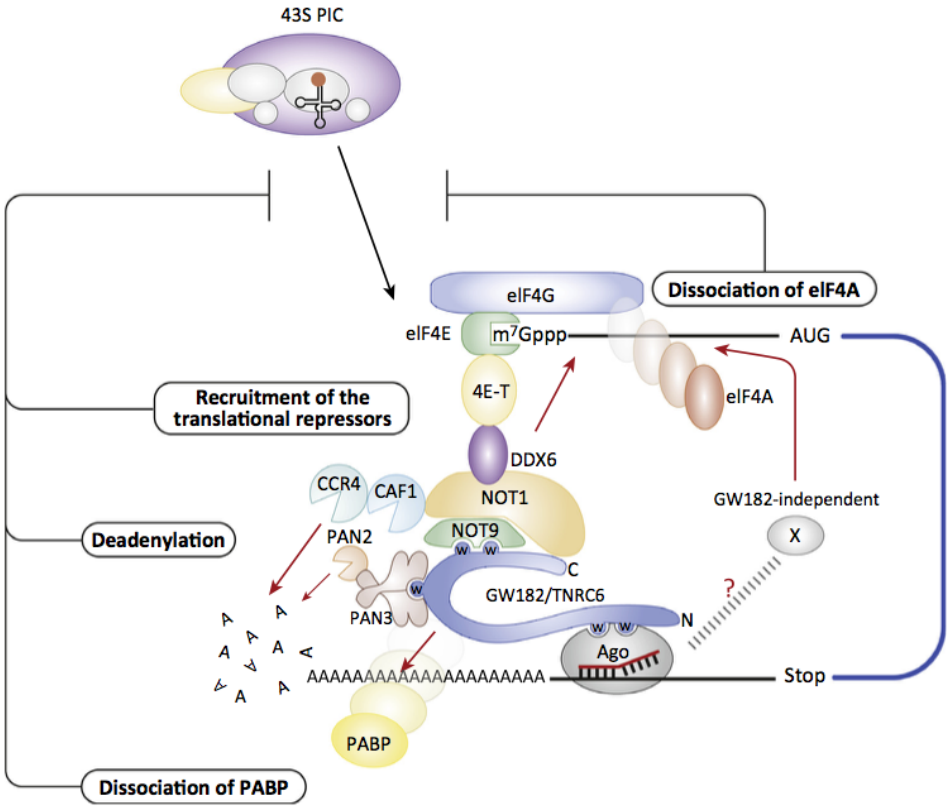

Figure I.1.1.2 Animal miRNA translation repression mechanisms. GW182 recruits translational repressors (DDX6 or 4E-T) onto the target mRNA, although the exact mechanism by which the repression occurs remains unclear. The miRNA-mediated displacement of ATP-dependent helicase eIF4A from the cap-binding complex eIF4F also repress the mRNA translation, by blocking the 43S PIC recruitment or ribosomal scanning. Deadenylation and displacement of poly(A)-binding protein (PABP) through GW182 and CCR4-NOT are also contributors to the overall mRNA translational repression. Reproduced with permission of reference [10]

I.1.2 Functions and biological importance

The presence of miRNAs and some of their cellular machinery goes back to animal phyla existing even before the emergence of Bilateria (animals with bilateral symetry), hundred million years ago. While sponges (*Amphimedon queenslandica*) and starlet sea anemone (*Nematostella vectensis*) are some species proving this fact, they are also a living record that demonstrates the high dynamic evolution of these regulatory biomolecules between species, as represented by the great differences in miRNA precursors sizes and sequences.[11]

In discovering and determining the function of miRNAs within the different species, three main approaches have been proved specially useful: Genomic experiments, forward genetics, and reverse genetics. The first approach initially makes use of miRNAs computational predictions, to further cloning the genes containing these sequences. This will permit studying if they are processed by the organisms to give the mature miRNA sequences while establishing their function. On the other hand, the use of forward genetics consists in isolating the mutant genes of individual organisms that shows phenotypic differences compared with the common organism. Finally, reverse genetics is based on either the overexpression or the "knock out" of specific genes as a mean to discover their function.[12]

The prediction by bioinformatics of miRNA sequences in plants, and thus their discovery, is considerable easier than in animals. This is because miRNA sequences in plants are highly complementary to their target mRNAs, allowing a quick and confident identification of the possible sequences involved in their regulation. miRNAs have an important role controlling developmental stages in plants, either by cleavage or translational repression of mRNA targets. In fact, this is their main function, as most discovered plant miRNAs target transcription factor gene families, specially those related to cell differentiation and developmental regulatory networks. Even among the few sequences whose targets are not transcription factors, some of them seem to exert a negative feedback on the expression of the above mentioned miRNAs.[13] In general, plant miRNA regulatory functions can be splitted into three categories (see Figure I.1.2): First, defining a specific spatial expression pattern of their targets, due to the expression of

miRNAs and their targets on contiguous, but nonoverlapping, plant domains. This mechanism can be responsible for creating assymetry in the plant, for example. Second, preventing variations in pattern and expression levels of targets, by sharing expression in overlapping plant domains. This has a "buffering" effect, diluting possible target expression differences in nearby plant domains. Third, exerting temporal regulation of target gene accumulation, thus regulating the developmental transitions.[14]

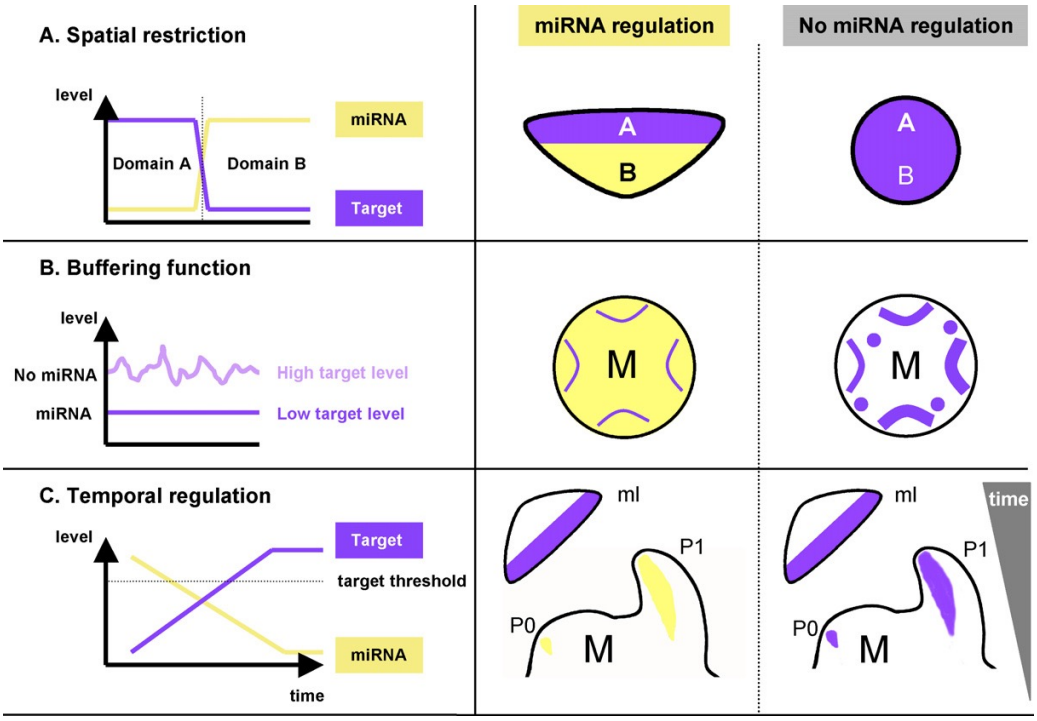

Figure I.1.2 Types of regulation by plant miRNAs. (A) Spatial restriction of target accumulation. The target of the miRNA tends to accumulate in domain A, where the miRNA is not present, while accumulation of the miRNA in domain B, depletes the target. Under miRNA regulation, target accumulation is restricted to the adaxial domain (domain A). (B) Buffering of target expression. Reduction and homogeneization of target expression levels under miRNA regulation in the meristem,"M". In the wild type miRNA accumulates in the meristem and boundary regions, where it overlaps with the target. When miRNA is not present, the expression of the target is increased in boundary regions. (C) Temporal regulation. A concentration gradient of miRNA expression over time is accompanied of an opposite gradient of target. The miRNA is expressed at early stages, avoiding the presence of target. The miRNA is absent in mature leaves "ml", leading to the accumulation of the target there. When lacking miRNA regulation, the expression of target occurs prematurely in "P0" and "P1" (leaf primordia 0 and 1, respectively). Adapted with permission from reference [14].

As highlighted previously, identification of miRNA sequences in animals is much more challenging than in plants. The reason is the reduced complementarity between the sequences and their target mRNAs. This makes the bioinformatic predictions noisier and more prone to false positives, while needing to use "evolutionary conservation" of the miRNA sequences between species as a criterion for their discovery, and not as a mean to validate the predicted targets. Another characteristic from animal miRNAs is that they are often clustered in the genome in the form of tandems.[12,15] When these clustered miRNAs are similar in sequence, the gene products may act additively to regulate a set of mRNAs. On the other hand, the presence of different sequences clustered together suggests their coordinated expression to regulate various targets simultaneously.
It is remarkable that, although specific miRNA sequences can be conserved through phylogenetically distant species (like vertebrates and insects), the targets of these shared miRNAs sequences highly differ (i.e. the genes in which the targeted binding sites reside).[12] This suggests the plasticity and evolutionary dynamics of the miRNA regulatory systems within the cells.
Similarly to plants, some animal miRNAs also share an evolutionarily conserved role in transcriptional regulation. However, only a minority of miRNA sequences are involved in these tasks while, in contrast, the vast majority regulates the expression of genes related to diverse biological processes. In fact, to which extent miRNAs are involved in these processes is evident when some reports predict that over one third of human genes may be regulated by these biomolecules.[16] The experimental validation of the diverse functions of animal miRNAs is wide: The influence of miR-196 in mouse limb development,[17] the muscle-specific miR-1 controlling the balance between differentiation and proliferation of cardiomyocytes during cardiogenesis,[18] the expresion of miR-375 in pancreatic islets that inhibits the glucose-induced insulin secretion by targeting Myotrophin gene (reducing exocitosis),[19] the participation of miR-32 in antiviral defense mechanisms,[20] or the role of miR-15a and miR-16-1 as tumor supressors[21], to mention a few.[8] Interestingly, the relatively recent discovery of miRNA sequences being exchanged between cells, using exosomes, has proved that they also can function as hormones or intercellular communication mediators.[22] This fact

evidence even more the important role of miRNAs in living organisms, as well as their increasing clinical relevance.

I.1.3 Clinical potential and challenges

The ubiquity of miRNAs, and the fact that they take part in the control of so many different and important cell processes, poses a reasonable question: Can their misregulation be responsible, at least in part, for the origin of certain diseases? Truth is that there is an increasing number of diseases that are starting to show a correlation with altered levels of different miRNAs. Thus, very important conditions such as neurodegenerative (e.g. Alzheimer disease)[23] or immune-related diseases (e.g. Multiple sclerosis),[24] virus infections (e.g. Hepatitis C virus),[25] or different kinds of cancer (e.g. Lung cancer),[26] to mention a few, are accompanied of aberrant miRNA expression patterns.[27] These findings are of high clinical importance: On the one hand, as miRNA function studies have shown, their expression tend to be tissue-specific and mirrors the cell physiological nature and state[28]. This implies that the deviation of cells from their normal states can be reflected in the form of specific aberrant miRNA profiles. Because of this, the potential of these profiles, in order to quickly identify the tissues where this aberrant miRNA expression is taking place, stands up as a powerfull tool in early diagnosis and prognosis of human diseases. In fact, The Cancer Program of the US National Cancer Institute sponsored in 2006 the workshop entitled "MicroRNA: Potential for Cancer detection, diagnosis and prognosis", bringing together leaders in the miRNA field to discuss the real potential of these biomolecules as cancer diagnosis biomarkers.[29] Ever since, a high amount of works characterizing and assessing the potential in diagnosis of miRNA profiles, specially those sequences present in serum or other body fluids that could be easily gathered, has been reported.[30–34] The authors often try to select the lowest possible amount of miRNAs, but with the highest significance, to simplify the diagnosis of specific cancers and diseases while pursuing high sensitivity and specificity.

On the other hand, the discovery that several diseases show this miRNA misregulation, together with the upstream position of miRNA in gene regulation, makes them both potential therapeutic targets and therapeutics themselves. The

former, because the correction of a miRNA overexpression, by targeting and inhibiting those specific miRNAs, can restore the normal levels of the repressed proteins, thus obtaining the therapeutic effect.[35] The latter, because the administration of synthetic miRNA or miRNA mimetics into diseased tissues as a "miRNA replacement therapy" may supress a harmful gene and recover normal cell functions such as proliferation, apoptosis, etc.[8]

The huge importance of all this fundamental research can be reflected by the increasing interest from pharmaceutical companies in the field. As an example, Rosetta genomics, together with Columbia University Medical Center, has developed a diagnostic test based on miRNA detection to distinguish between squamous and nonsquamous lung cancer patients.[36] The fact that miRNAs are naturally ocurring biomolecules has several advantages when used as therapeutics. For instance, they will have a higher probability to be safe for human use, giving more confidence and reducing the investment-associated economic risk during their development. In fact, several pharmaceutical companies are starting to focus on exploiting miRNAs as treatments for diseases: In 2008, Santaris was close to initiate clinical trials with SPC3649, a locked nucleic acid (LNA) against miR-122 for the treatment of hepatitis C virus (HCV), while GlaxoSmithKline and Regulus Therapeutics allied to develop novel miRNA-targeted drugs for inflammatory diseases.[37] Thus, miRNA based diagnostics and therapies have a promising future forward, although some challenges need to be adressed. The short length, existence of miRNA isoforms and high sequence similarities, are features that turn the reliable identification and quantification of miRNAs into a very difficult task. It is already known that the use of different commercialized miRNA detection platforms shows poor consistency between each other,[38] and that base composition, structure and isoforms (O-methyl modifications being especially important), are partially responsible of this impact. Other parameters such as sample preparation and the strategies used for the experimental analyses (e.g. enzymatic ligations, reverse transcriptions) have also notorious influence by introducing variability.[39] In this regard, the development of nanotechnology is playing a key role by offering new and direct detection methods that can bypass these bias,[39] as well as contribuiting to solve miRNA issues when used as therapeutics (such as tissue targeting and developing drug delivery platforms).[40]

References

(1) Lee, R. C.; Feinbaum, R. L.; Ambros, V. The C. Elegans Heterochronic Gene Lin-4 Encodes Small RNAs with Antisense Complementarity to Lin-14. *Cell* **1993**, *75*, 843.

(2) Reinhart, B. J.; Slack, F. J.; Basson, M.; Pasquinelli, E.; Bettinger, J. C.; Rougvie, E.; Horvitz, H. R.; Ruvkun, G. The 21-Nucleotide Let-7 RNA Regulates Developmental Timing in Caenorhabditis Elegans. *Nature* **2000**, *403*, 901.

(3) Muljo, S. A.; Kanellopoulou, C.; Aravind, L. MicroRNA Targeting in Mammalian Genomes: Genes and Mechanisms. *Wiley Interdiscip. Rev. Syst. Biol. Med.* **2010**, *2*, 148.

(4) Zhang, B.; Pan, X.; Cobb, G. P.; Anderson, T. A. Plant microRNA: A Small Regulatory Molecule with Big Impact. *Dev. Biol.* **2006**, *289*, 3.

(5) Grundhoff, A.; Sullivan, C. S. Virus-Encoded microRNAs. *Virology* **2011**, *411*, 325.

(6) Lee, Y.; Ahn, C.; Han, J.; Choi, H.; Kim, J.; Yim, J.; Lee, J.; Provost, P.; Rådmark, O.; Kim, S.; et al. The Nuclear RNase III Drosha Initiates microRNA Processing. *Nature* **2003**, *425*, 415.

(7) Han, J.; Lee, Y.; Yeom, K.-H.; Kim, Y.-K.; Jin, H.; Kim, V. N. The Drosha-DGCR8 Complex in Primary microRNA Processing. *Genes Dev.* **2004**, *18*, 3016.

(8) Wahid, F.; Shehzad, A.; Khan, T.; Kim, Y. Y. MicroRNAs: Synthesis, Mechanism, Function, and Recent Clinical Trials. *Biochim. Biophys. Acta - Mol. Cell Res.* **2010**, *1803*, 1231.

(9) Behm-Ansmant, I.; Rehwinkel, J.; Doerks, T.; Stark, A.; Bork, P.; Izaurralde, E. mRNA Degradation by miRNAs and GW182 Requires Both CCR4:NOT Deadenylase and DCP1:DCP2 Decapping Complexes. *Genes Dev.* **2006**, *20*, 1885.

(10) Iwakawa, H. oki; Tomari, Y. The Functions of MicroRNAs: mRNA Decay and Translational Repression. *Trends Cell Biol.* **2015**, *25*, 651.

(11) Grimson, A.; Srivastava, M.; Fahey, B.; Woodcroft, B. J.; Chiang, H. R.; King, N.; Degnan, B. M.; Rokhsar, D. S.; Bartel, D. P. Early Origins and Evolution of microRNAs and Piwi-Interacting RNAs in Animals. *Nature* **2008**, *455*, 1193.

(12) Ambros, V. The Functions of Animal microRNAs. *Nature* **2004**, *431*, 350.

(13) Bartel, D. P. MicroRNAs: Genomics, Biogenesis, Mechanism, and Function. *Cell* **2004**, *116*, 281.

(14) GARCIA, D. A miRacle in Plant Development: Role of microRNAs in Cell Differentiation and Patterning. *Semin. Cell Dev. Biol.* **2008**, *19*, 586.

(15) Lau, N. C.; Lim, L. P.; Weinstein, E. G.; Bartel, D. P. An Abundant Class of Tiny RNAs with Probable Regulatory Roles in Caenorhabditis Elegans. *Science.* **2001**, *294*, 858.

(16) Lewis, B. P.; Burge, C. B.; Bartel, D. P. Conserved Seed Pairing, Often Flanked by Adenosines, Indicates That Thousands of Human Genes Are microRNA Targets. *Cell* **2005**, *120*, 15.

(17) Hornstein, E.; Mansfield, J. H.; Yekta, S.; Hu, J. K.-H.; Harfe, B. D.; McManus, M. T.; Baskerville, S.; Bartel, D. P.; Tabin, C. J. The microRNA miR-196 Acts Upstream of Hoxb8 and Shh in Limb Development. *Nature* **2005**, *438*, 671.

(18) Zhao, Y.; Samal, E.; Srivastava, D. Serum Response Factor Regulates a Muscle-Specific microRNA That Targets Hand2 during Cardiogenesis. *Nature* **2005**, *436*, 214.

(19) Poy, M. N.; Eliasson, L.; Krutzfeldt, J.; Kuwajima, S.; Ma, X.; MacDonald, P. E.; Pfeffer, S.; Tuschl, T.; Rajewsky, N.; Rorsman, P.; et al. A Pancreatic Islet-Specific microRNA Regulates Insulin Secretion. *Nature* **2004**, *432*, 226.

(20) Lecellier, C.; Dunoyer, P.; Arar, K.; Lehmann-Che, J.; Eyquem, S.; Himber, C.; Saïb, A.; Voinnet, O. A Cellular MicroRNA Mediates Antiviral Defense in Human Cells. *Science.* **2005**, *308*, 557.

(21) Cimmino, A.; Calin, G. A.; Fabbri, M.; Iorio, M. V; Ferracin, M.; Shimizu, M.; Wojcik, S. E.; Aqeilan, R. I.; Zupo, S.; Dono, M.; et al. miR-15 and miR-16 Induce Apoptosis by Targeting BCL2. *Proc. Natl. Acad. Sci.* **2005**, *102*, 13944.

(22) Yoshioka, Y.; Katsuda, T.; Ochiya, T. *Circulating microRNAs in Disease Diagnostics and Their Potential Biological Relevance*; Igaz, P., Ed.; Experientia Supplementum; Springer Basel: Basel, 2015; Vol. 106.

(23) Hu, Y.-B.; Li, C.-B.; Song, N.; Zou, Y.; Chen, S.-D.; Ren, R.-J.; Wang, G. Diagnostic Value of microRNA for Alzheimer's Disease: A Systematic Review and Meta-Analysis. *Front. Aging Neurosci.* **2016**, *8*, 1.

(24) Keller, A.; Leidinger, P.; Lange, J.; Borries, A.; Schroers, H.; Scheffler, M.; Lenhof, H.-P.; Ruprecht, K.; Meese, E. Multiple Sclerosis: MicroRNA Expression Profiles Accurately

Differentiate Patients with Relapsing-Remitting Disease from Healthy Controls. *PLoS One* **2009**, *4*, e7440.
(25) Jopling, C. L.; Yi, M.; Lancaster, A. M.; Lemon, S. M.; Sarnow, P. Modulation of Hepatitis C Virus RNA Abundance by a Liver-Specific MicroRNA. *Science.* **2005**, *309*, 1577.
(26) Yanaihara, N.; Caplen, N.; Bowman, E.; Seike, M.; Kumamoto, K.; Yi, M.; Stephens, R. M.; Okamoto, A.; Yokota, J.; Tanaka, T.; et al. Unique microRNA Molecular Profiles in Lung Cancer Diagnosis and Prognosis. *Cancer Cell* **2006**, *9*, 189.
(27) Li, Y.; Kowdley, K. V. MicroRNAs in Common Human Diseases. *Genomics, Proteomics Bioinforma.* **2012**, *10*, 295.
(28) Lagos-Quintana, M.; Rauhut, R.; Yalcin, A.; Meyer, J.; Lendeckel, W.; Tuschl, T. Identification of Tissue-Specific MicroRNAs from Mouse. *Curr. Biol.* **2002**, *12*, 735.
(29) Tricoli, J. V.; Jacobson, J. W. MicroRNA: Potential for Cancer Detection, Diagnosis, and Prognosis. *Cancer Res.* **2007**, *67*, 4553.
(30) Roth, C.; Rack, B.; Müller, V.; Janni, W.; Pantel, K.; Schwarzenbach, H. Circulating microRNAs as Blood-Based Markers for Patients with Primary and Metastatic Breast Cancer. *Breast Cancer Res.* **2010**, *12*, R90.
(31) Bianchi, F.; Nicassio, F.; Marzi, M.; Belloni, E.; Dall'Olio, V.; Bernard, L.; Pelosi, G.; Maisonneuve, P.; Veronesi, G.; Di Fiore, P. P. A Serum Circulating miRNA Diagnostic Test to Identify Asymptomatic High-Risk Individuals with Early Stage Lung Cancer. *EMBO Mol. Med.* **2011**, *3*, 495.
(32) Hennessey, P. T.; Sanford, T.; Choudhary, A.; Mydlarz, W. W.; Brown, D.; Adai, A. T.; Ochs, M. F.; Ahrendt, S. A.; Mambo, E.; Califano, J. A. Serum Microrna Biomarkers for Detection of Non-Small Cell Lung Cancer. *PLoS One* **2012**, *7*, e32307.
(33) Chen, X.; Hu, Z.; Wang, W.; Ba, Y.; Ma, L.; Zhang, C.; Wang, C.; Ren, Z.; Zhao, Y.; Wu, S.; et al. Identification of Ten Serum microRNAs from a Genome-Wide Serum microRNA Expression Profile as Novel Noninvasive Biomarkers for Nonsmall Cell Lung Cancer Diagnosis. *Int. J. Cancer* **2012**, *130*, 1620.
(34) Manterola, L.; Guruceaga, E.; Pérez-Larraya, J. G.; González-Huarriz, M.; Jauregui, P.; Tejada, S.; Diez-Valle, R.; Segura, V.; Samprón, N.; Barrena, C.; et al. A Small Noncoding RNA Signature Found in Exosomes of GBM Patient Serum as a Diagnostic Tool. *Neuro. Oncol.* **2014**, *16*, 520.
(35) Mack, G. S. MicroRNA Gets down to Business. *Nat. Biotechnol.* **2011**, *29*, 459.
(36) H. Ohad, R. G. Mining genes from junk (Part II) https://seekingalpha.com/article/72184-rosetta-genomics-mining-genes-from-junk-part-ii.
(37) Regulus. GlaxoSmithKline and Regulus Therapeutics Form Strategic Alliance To Develop microRNA Targeted Therapeutics to Treat Inflammatory Diseases http://ir.regulusrx.com/releasedetail.cfm?releaseid=712395. Apr 17, 2008.
(38) Leshkowitz, D.; Horn-saban, S.; Parmet, Y.; Feldmesser, E. Differences in microRNA Detection Levels Are Technology and Sequence Dependent. *RNA* **2013**, *19*, 527.
(39) Chugh, P.; Dittmer, D. P. Potential Pitfalls in microRNA Profiling. *Wiley Interdiscip. Rev. RNA* **2012**, *3*, 601.
(40) Chen, Y.; Gao, D.-Y.; Huang, L. In Vivo Delivery of miRNAs for Cancer Therapy: Challenges and Strategies. *Adv. Drug Deliv. Rev.* **2015**, *81*, 128.

I.2 Reporters in bioassays

Collecting qualitative and quantitative information is fundamental to start comprehending the causal relationships taking place in the world surrounding us. Nevertheless, when studying microscopic systems, we need to use strategies that can transduce the information from events ocurring at this scale to measurable signals. Only after this, we will be able to verify and get evidences of what happens at this scale, based on the qualitative and quantitative information we can gather by these means. In general, a reporter is a (macro)molecular transductor that permits to turn the microscopic event into a detectable signal. Thus, the generation of measurable electrons by Glucose Oxidase in the presence of glucose,[1] the hybridization of a dye-marked DNA probe with a targeted DNA sequence as a mean to detect its presence if fluorescence is observed,[2] or detecting the specific emission of a photoluminescent nanoparticle coupled to an antibody as a way to reveal the existence in a sample of the targeted antigen,[3] are representative examples of how different reporters are used in bioassays.

In this section, the fundamentals of different reporters used in biodetection will be explained, their features compared, and the reasons for choosing upconverting nanoparticles for the development of the systems presented in this thesis exposed.

I.2.1 Fluorescence and organic dyes

The excellent sensitivity yielded by fluorescence-based detection techniques[4] has turned dye-labelling of molecular probes into a very useful reporter strategy in molecular biology and analytical chemistry. In fact, a pletora of systems based on this property have been developed to detect and quantify analytes of interest such as DNA, RNA and proteins. Some important and currently used techniques using fluorescence as transduction signal are the widely used quantitative polymerase chain reaction (q-PCR), gel electrophoresis and blotting techniques, microarrays or DNA chips, and HPLC (see Figure I.2.1.1).

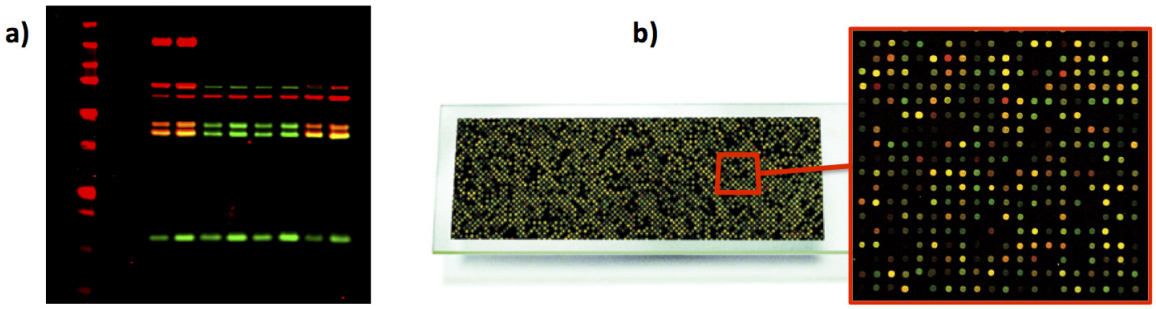

Figure I.2.1.1 a) The image depicts the electrophoretic bands from a western blot, revealed by fluorescence. b) In this picture a DNA chip is shown. The magnification depicts the DNA array, where the intensity of the spots belonging to different sequences is revealed by fluorescence.

Fluorescence is a phenomenon typically exhibited by aromatic organic molecules and some minerals, although it can also occur in some individual elements like those from the group of lanthanides (e.g. europium and terbium ions).[5] The process of fluorescence starts with the absorption of one photon of a certain wavelength by an orbital electron of a molecule or atom. The energy of this absorbed photon permits the electron to reach a singlet excited state that is paired to the electron in the ground state (i.e. they have opposite spin), see Figure I.2.1.2a. Because of this, the return of the electron to the ground state is spin-allowed, and happens quickly as follows: first the excited electron relaxes vibrationally through non-radiative processes, eventually decaying to the ground state by emitting a photon at a longer wavelength than the one from the absorbed one. The speed of this process implies that fluorescence lifetimes "τ" are normally in the scale of nanoseconds or even below.

In contrast to the singlet formed in fluorescence, a triplet excited state can be formed upon photon absorption as part of a phenomenon called intersystem crossing, which can be promoted by the presence of heavy atoms like Br or I due to spin-orbit coupling. In this case, the excited electron is no longer paired with the electron in the ground state, as they have the same spin (see Figure I.2.1.2b). Consequently, the transition to the ground state by means of emitting a photon will be slow, as it is forbidden by Pauli's exclusion principle, and it leads to what is known as phosphorescence. The relativelly slow emission rates of this process are

reflected in the phosphorescence lifetimes, which usually are in the order of milliseconds to seconds.[6]

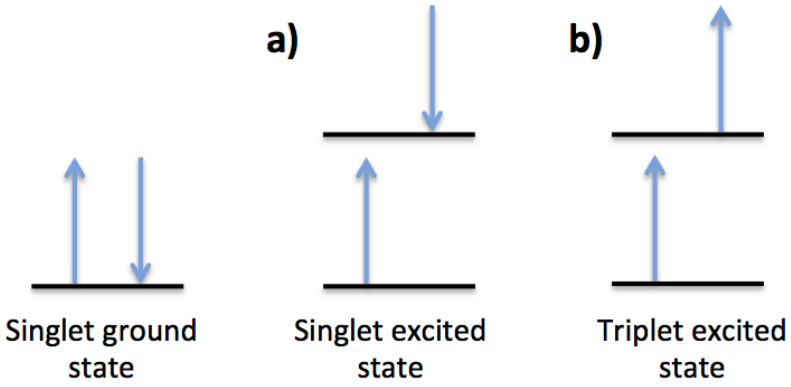

Figure I.2.1.2 a) Singlet excited state, typical from fluorescence processes. b) Triplet excited state, normally taking place in phosphorescence processes. The direction of the arrows represents the spin of the electron.

The different steps in the fluorescence and phosphorescence mechanisms can be otherwise clearly expressed using a Jablonski diagram (Figure I.2.1.3). Upon absorption of a photon (energy = $h \cdot \nu_{Exc}$) there is an electron transition from the singlet ground state (S_0) to a first singlet excited electronic state (S_1):

$$S_0 + h \cdot \nu_{Exc} \rightarrow S_1$$

where "h" is the Planck's constant and "ν_{Exc}" is the frequency of light .

At these states, the electrons can be in a number of different vibrational energy levels (depicted as 0, 1 and 2 in the Jablonski diagram). Thus, after absorption of the photon, the electron can internally suffer relaxation processes by "non-radiative transitions" within the S_1 state, in which part of the energy is dissipated as heat (changing its vibrational state within the electronic level, see Figure I.2.1.3).

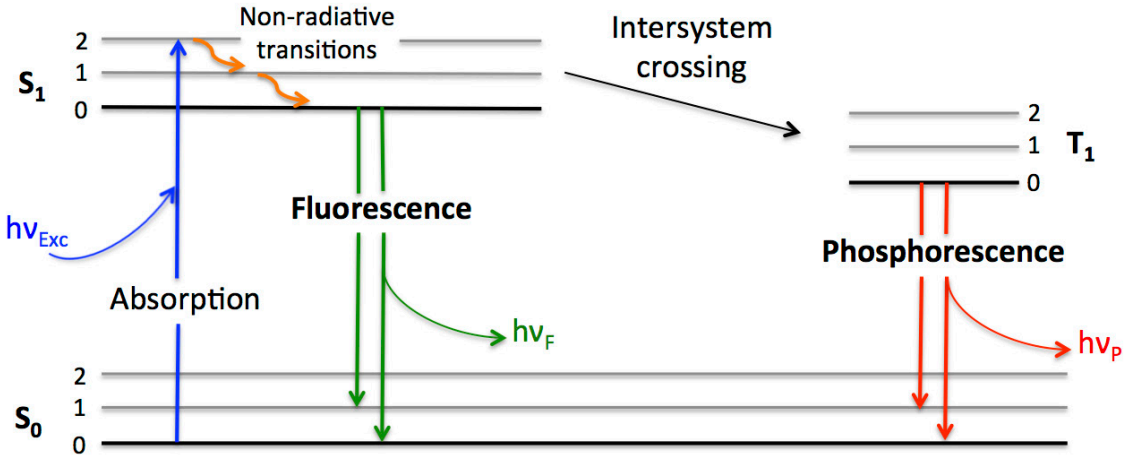

Figure I.2.1.3 Jablonski diagram. The ground state is depicted as S_0. S_1 refers to the first singlet excited state, while T_1 refers to the first triplet excited state. 0, 1 and 2 correspond to the different internal vibrational states within the electronic levels. The blue arrow symbolizes the excitation of the electron upon photon absorption. Orange arrows represent the non-radiative relaxations between the different vibrational states. The remaining arrows represent the return of the electron to the ground state by the emission of a photon through fluorescence mechanism (green) or phosphorescence mechanism (red).

There are a number of other different processes through which relaxation can occur, such as quenching, energy transfer, or solvent interactions. All these processes are actually responsible for the characteristic "Stokes shift" presented by fluorescence emissions (i.e. the emission of a less energetic photon, of longer wavelength, upon the transition to the ground state), see Figure I.2.1.4.

Electrons in the S_1 state can also suffer a spin conversion to the first triplet excited state (T_1), depicted in the figure as "intersystem crossing". In this T_1 state, the transition of the electron to the ground state conforms the process previously defined as phosphorescence, whose emitted photon upon relaxation is shifted to even longer wavelengths compared to fluorescence. Molecules that contain heavy atoms like iodine or bromine are usually phosphorescent, as they favor the intersystem crossing and increase the phosphorescence quantum yields.[6]

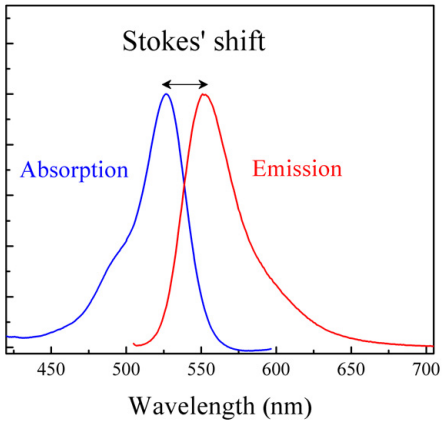

Figure I.2.1.4 Stokes shift. After different non-radiative relaxation mechanisms (e.g. heat dissipations), the fluorophores' excited electrons lose part of the energy taken from the absorbed photons. As consequence, the emitted photons during fluorescence are less energetic (i.e. of longer wavelengths) than the absorbed photons (shorter wavelengths).

Fluorescence lifetime and quantum yield are probably the most important features of photoluminescent materials: the former because it conditions the amount of time that the fluorophore spends in its excited state interacting with the environment. The latter because it reflects the efficiency of the fluorescence process of a particular fluorophore in certain defined conditions.

The fluorescence lifetime is defined as the average time the fluorophore spends in its excited state before returning to the ground state, and it can be expressed as:

$$\tau = \frac{1}{\Gamma + K_{nr}} \qquad \text{Ec. I.2.1.1}$$

where "Γ" is the emissive rate of the fluorophore, and "K_{nr}" is the non-radiative decay to the ground state S_0, see Figure I.2.1.5. All possible non-radiative relaxation mechanisms are included in K_{nr} for simplicity. Fluorescence lifetimes are usually close to 10 ns in organic dyes, but it is important to highlight that as fluorescence emission is a random process, and this feature is an average value, only a few molecules emit their photons precisely when $t = \tau$.

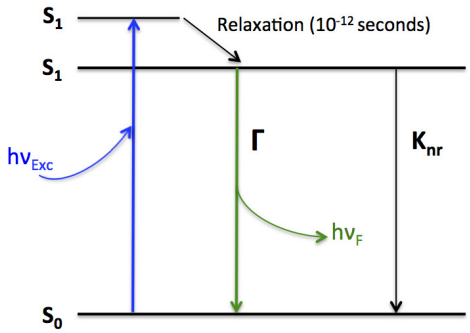

Figure I.2.1.5 Simplified Jablonski diagram in which emissive rate (Γ) and non-radiative decay (K_{nr}) are depicted. The relaxation step, which occurs quickly enough (10^{-12} s) to take place before the photon emission, is the responsible of the Stokes Shift showed by fluorescence emissions.

We have mentioned that another important feature of fluorophores is quantum yield. This property can be defined as the number of photons emitted by the fluorophore relative to the number of photons that it absorbed (Ec. I.2.2), and can be expressed using the mathematical terms defined previously (Ec. I.2.3):

$$Q = \frac{Photons_{(Em)}}{Photons_{(Abs)}} \quad \text{Ec. I.2.1.2} \qquad Q = \frac{\Gamma}{\Gamma + K_{nr}} \quad \text{Ec. I.2.1.3}$$

Thus, the closer the quantum yield approaches to unity ($K_{nr} << \Gamma$), the more efficient the fluorescence process will be. Some examples of organic dyes, together with their fluorescence quantum yields (Q), are shown in Table I.2.1.1.[7]

Dye	QS	C153	Fl	R6G	R101	OX1
Solvent	0.105 M HClO	Ethanol	0.1 M NaOH	Ethanol	Ethanol	Ethanol
Absorbance (nm)	270–400	350–500	400–550	425–575	475–620	500–710
Emission (nm)	385–700	465–750	490–690	505–750	540–750	615–950
Q	0.59	0.53	0.89	0.91	0.915	0.15

Table I.2.1.1 Quantum yield, absorbance and emission wavelength of different organic dyes: Quinine sulfate dihydrate (QS), Coumarin 153 (C153), Fluorescein (Fl), Rhodamine 6G (R6G), Rhodamine 101 (R101) and Oxazine 1 (OX1). In the first five fluorophores their relative quantum yields has been determined, using the absolute quantum yield from R101. Extracted from reference [7].

As shown in the table, there are very efficient dyes like Rhodamine 101, whose quantum yield approaches the unity and thus yield strong emissions. Due to this high performance, fluorophores have often been used for the detection and study of a wide variety of biomolecules, as they permit to obtain good sensitivities. However, there are three main limitations regarding the use of these molecules as reporters. First, organic dyes suffer from what is called "photobleaching", a degradation process of the fluorophore upon excitation by which it stops emitting light, due to the rupture of structural bonds or non-specific reactions with its environment. This implies a depletion of fluorophore over time and a fading of fluorescence upon excitation-emission cycles,[8] so long exposures and high power densities can especially affect the quality of the signal,[9] and thus the reliability and sensitivity of the detection and imaging systems based on these molecules, as shown in Figure I.2.1.6.[10]

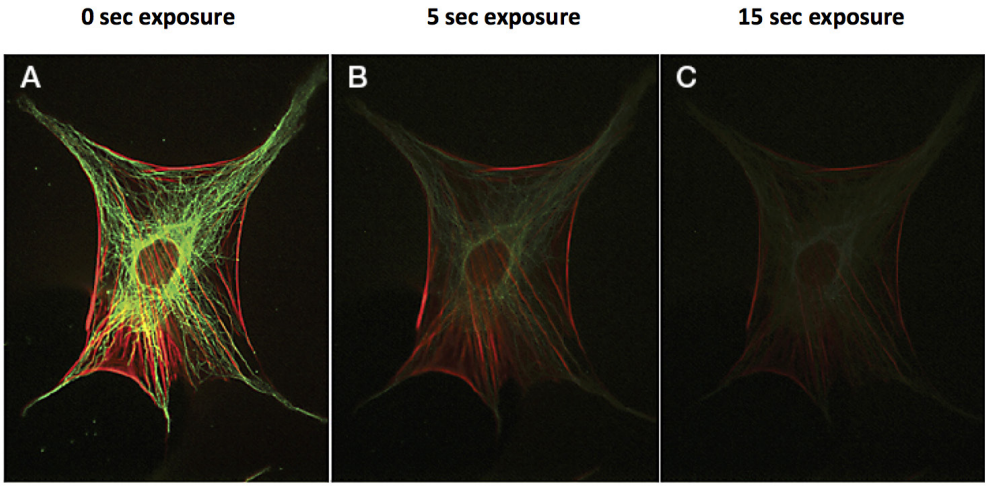

Figure I.2.1.6 Photobleaching of fluorescein and Texas red organic dyes, staining cytoskeleton in cells, after excitation with 488 nm or 594 nm lasers for 0 sec (A), 5 sec (B) and 15 sec (C). From ref. [10].

Second, a phenomenon known as "fluorescence intermittency" or "blinking", which consists in the random switching of dye's emission between "on" and "off" states due to the competition between radiative and non-radiative relaxation pathways. As this phenomenon occurs randomly, due in part to variations in the local media surrounding the molecule, the quantification of small amounts of dye-marked analytes becomes very difficult. It is important to remember that even just the

detection of the fluorophore in these conditions can be challenging due to photobleaching, considering that the excitation power densities required to detect the fluorescence signal in these cases are very high.

Last, but not least, "autofluorescence" also hampers the sensitivity of imaging and detection systems that require dyes. This is because fluorescence is not an uncommon process among organic molecules. In fact, there exist many biological molecules that show this phenomenon under illumination at proper wavelengths (see Table I.2.1.2 for some examples).

Biomolecule	Absorbance (nm)	Emission (nm)	Organism	Reference
Chlorophyll a	320-460 550-690	660-760	Plants	11
Cholecalciferol	200-320	380-460	Animals	12
Collagen	270-370	305-450	Animals	13
Folic acid	217-346	450	All	12
Melanin	340-400	360-560	Animals	14
NAD(P)H	340	450	All	13
Retinol	250-400	500	Animals and Bacteria	12
Riboflavin	300-490	500-700	All	15
Tryptophan	280	350	All	16
Tyrosine	270	305	All	17

Table I.2.1.2 Absorbance and emission wavelengths of different biomolecules that contribute to autofluorescence.

This causes cellular components and also organelles such as mitochondria and lysosomes to exhibit a basal level of fluorescence without staining them with synthetic organic dyes, see Figure I.2.1.7.[18] Consequently, this phenomenon makes difficult to distinguish the organic dye signal from the autofluorescence signal when the dye is present at relatively low concentrations.

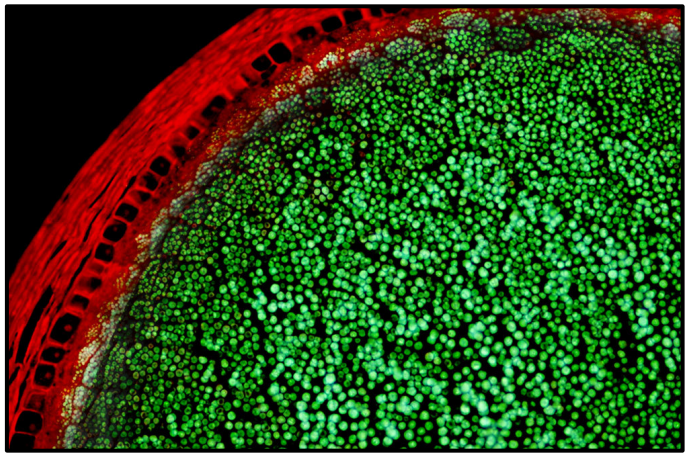

Figure I.2.1.7. Autofluorescence emission from a section of corn kernel (*Zea mays*), Ex=450-550 nm. This phenomenon arises in plant tissues from endogenous biomolecules such as lignins, chlorophyll, carotene and xantophyll. From ref. [18].
When comparing the absorbance and emission wavelengths between synthetic dyes and endogenous biomolecules (Table I.2.1.1 and Table I.2.1.2, respectively) one can realize that, while trying to excite and detect minute amounts of dye-marked molecules, biomolecules are also going to be excited and their fluorescence is going to interfere with the synthetic dye signal detection.

As fluorescence is a relatively simple, versatile, and sensitive technique, different approaches, like time-resolved fluorescence, have been explored to overcome some of their limitations. Nevertheless, continuous advances in nanotechnology and materials science have permitted to design and synthesize new and promising photoluminiscent materials that might substitute these organic reporters, due to their better performances and reliability. Two of these promising reporters are going to be discussed in the next sections, namely, quantum dots (Q-dots) and upconverting nanoparticles (UCNPs).

I.2.2 Quantum dots

A semiconductor is a material that shows an electrical conductivity falling between that of a conductor (e.g. gold) and an insulator (e.g. glass). The electrical resistance of semiconductors can decrease under certain circumstances, such as, temperature

or irradiation with light of certain wavelengths, showing then an electrical conductor-like behaviour.

The excitation with light of bulk semiconductors results in the formation of an excited electron and a hole, which is the place at which the electron was within the valence band before excitation and now presents a positive charge. Both electron and hole are known as exciton or charge carriers. These are separated a number of molecules or ions away within the material, a distance that is referred to as "Bohr exciton radius", while they are bound by weak coulombic attraction. The minimum energy required to form these charge carriers is known as the "band gap" of the semiconductor, and it is the energy difference between the top of the valence band and the bottom of the conduction band (Figure I.2.2.1). After the formation of this electron-hole pair, it is transported through the semiconductor until it is either relaxed by emitting a photon due to the radiative recombination of the electron and the hole, trapped, annihilated if it collides with another exciton (e.g. when high intensity laser excitation is used), or relaxed by matrix phonons.[19]

Interestingly, when the size of semiconductor particles is smaller than their Bohr exciton radius a spatial confinement of the charge carriers occurs, so the valence and conduction bands split into discrete, quantized, electronic levels.

The fewer number of atoms resulting from the nanometric size of semiconductors reduces the number of possible energy states compared to bulk materials, explaining the quantization of the energy levels.

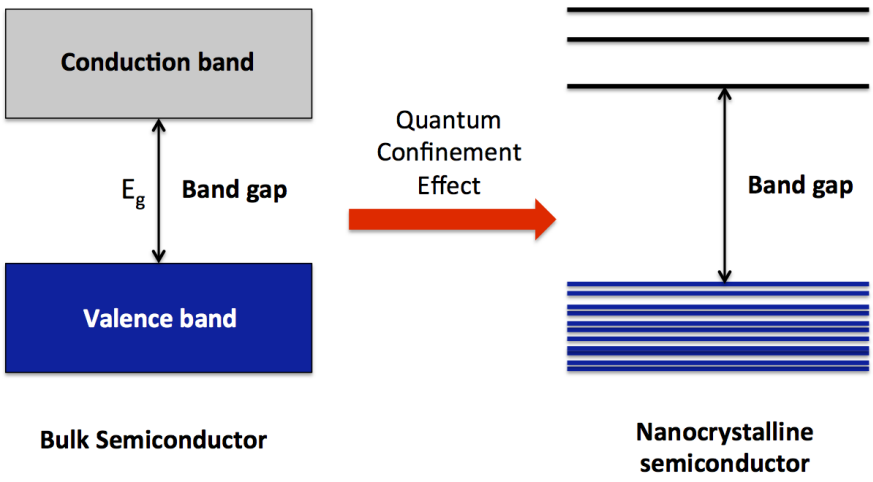

Figure I.2.2.1 Quantum confinement effect on quantization of valence and conduction band electronic transitions, and on band gap energy increment.

At the same time, the quantum confinement caused by the nanometric dimensions of the semiconductor reduces electron mobility, which increases the energy required to form the electron-hole pair and thus the energy band gap, see Figure I.2.2.1. The latter fact implies that the energy of the absorbed photon required to bridge this gap will be higher, and so it will be the energy of the photon emitted. As a consequence, it is possible to tune the optical absorption and emission properties of the nanometric semiconductor by simply varying its size and shape Figure I.2.2.2.[20]

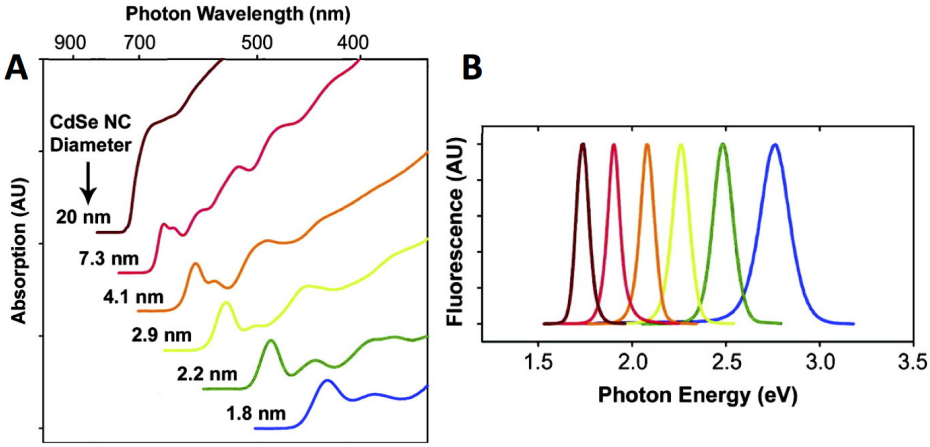

Figure I.2.2.2. CdSe nanocrystals. Size-dependent absorption (A) and emission (B). Adapted with permission of ref. [20].

Quantum dots (Q-dots) are semiconductor nanocrystals normally ranging 1-10 nm in diameter. They receive their name due to the number of spatial dimensions through which electrons and holes can move freely without experience quantum confinement (i.e. 2D structures: quantum wells; 1D structures: quantum wires; 0D structures: quantum dots).[21]

Their versatility mainly arise from the control of their optical properties, which can be achieved by varying their size, shape, semiconductor material and core/shell nanostructured architectures, see Figure I.2.2.3A and B.[22] This fact turns them very interesting materials for biosensing, especially for multiplexed analyses, as they can emit at different wavelengths while being simultaneously excited in the UV region (Figure I.2.2.2A and Figure I.2.2.3A).

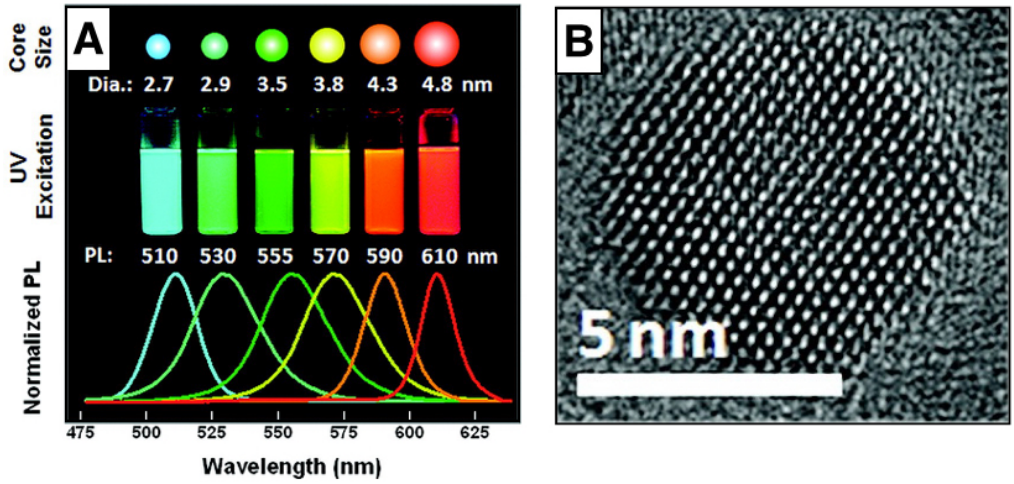

Figure I.2.2.3. A) Size-dependant photoluminescence of CdSe/ZnS quantum dots under UV excitation. B) Transmission electron microscopy (TEM) picture of a CdSe/ZnS (core/shell) quantum dot. Adapted with permission of ref. [22].

Besides this useful tunability, Q-dots also show a remarkable combination of large Stokes shifts (>100 nm), high quantum yields (Q = 0.1-0.9) and large molar extinction coefficients (10^5-10^7 $M^{-1}{\cdot}cm^{-1}$), being comparable, or even surpassing in certain cases, those shown by organic dyes. Another difference with traditional fluorophores are their longer lifetimes, normally in the 10-100 ns range. Q-dots also confers some advantages over traditional dyes, such as higher photostability. This reduces the possibilities of photobleaching when using these nanocrystals for imaging or detection purposes, allowing higher reliability and sensitivity.

Nevertheless, their small size is accompanied by several disadvantages. Their high surface-to-volume ratio (>10% of the atoms from the nanocrystal are on the surface) makes them very susceptible to the environment, which manifests by quenching effects, oxidation, and other phenomena. As a consequence, these exert changes in their photoluminescent properties, in reversible or irreversible ways, although some of them, like the high surface-to-volume ratio, can be used advantageously in sensing applications for the construction of efficient FRET systems.

Fluorescence intermittency (i.e. blinking) of Q-dots is also a limitation when using these reporters, although it can be partially addressed by using core-shell

nanoarchitectures, where the surface of the quantum dot is more isolated from the surrounding media (Figure I.2.2.3B).

As with organic dyes, autofluorescence remains an important bottleneck when trying to detect small concentrations of Q-dots, which still limits the potential sensitivity of the detection systems relying on this technology.

Further comparative studies between Q-dots and organic dyes can be found elsewhere.[23]

I.2.3 Photon upconversion and upconverting nanoparticles

Photon upconversion is a process by which two or more low energy photons are absorbed, while a high-energy photon is emitted in exchange. This will imply, for example, the absorption of several photons from the near infrared region (NIR), e.g. at 980 nm, and the emission of a fewer number of photons in the visible or UV regions (e.g. 665 nm or 365 nm). This upconversion phenomenon may seem confusing at first glance, especially after exposing the theory behind organic dyes and Q-dots, characterized by Stokes-shifted emissions. Nevertheless, this anti-Stokes process, although not very common, can ocurr in certain materials containing transition metals, actinides, and lanthanide ions due to their singular electronic features.[24] In fact, trivalent Lanthanide ions (Ln^{3+}) have very unique electronic properties: their upconversion emissions result from 4f-4f intraorbital transitions that are shielded from their environment by the more external, fully occupied, $5s^25p^6$ orbital shells (Figure I.2.3.1). This translates in remarkably stable photoluminescent emissions, substantially independent of particle size and environmental effects (e.g. lacking spectral shifts of their emission peaks as consequence of environmental changes).[25] These intra-4f electronic transitions of lanthanide ions form electric dipoles, forbidden by quantum mechanical selection rules, which are eventually relaxed due to local crystal field-induced intermixing of the f states with higher electronic configurations.[26] The forbidden nature of the 4f-4f transitions results in very long lifetimes (up to tens of milliseconds) for excited electrons in the energy levels of lanthanide ions. In fact, these long lifetimes are one of the key features allowing photon upconversion processes to occur.

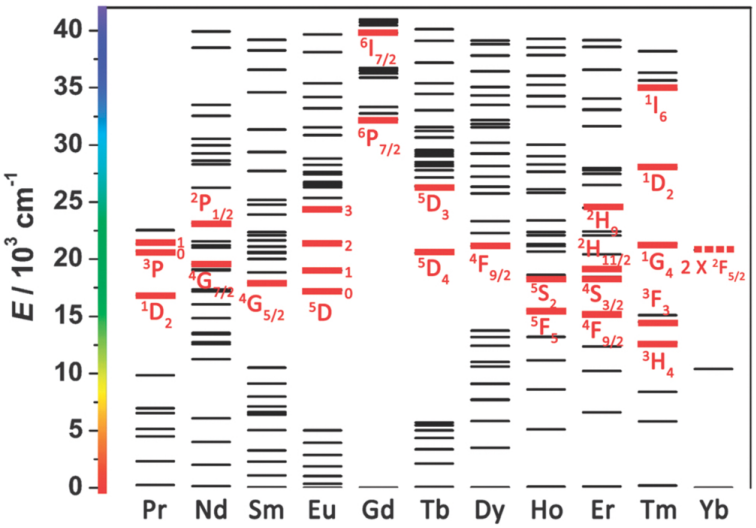

Figure I.2.3.1 Partial energy level diagrams of Ln^{3+}. Upconverting-emissive excited levels are marked in red. Reproduced from Ref. [25] with permission from The Royal Society of Chemistry.

To date, photon upconversion has been found to proceed in Ln^{3+}-doped materials by five different possible mechanisms, namely: Excited-state absorption (ESA), Energy transfer upconversion (ETU), cooperative sensitization upconversion (CSU), photon avalanche (PA) and cross relaxation (CR), although the last process is more a mean by which upconversion color output can be tuned, or efficient photon avalanche systems can be built, than an upconversion mechanism itself.[26]

Energy transfer upconversion (ETU) is by far the most explored and applied process, due to its superior quantum efficiency (*ca.* 10^{-3}) in comparison with others like ESA (*ca.* 10^{-5}) and CSU (*ca.* 10^{-6}).[25] In fact, most of the currently available and researched upconverting materials are based on this process, including the ones discussed in this thesis. Thus, we are going to focus on this mechanism, although more information about the remaining processes can be found elsewhere.[24–26]

ETU typically involves two different Ln^{3+}, a sensitizer and an activator (see Figure I.2.3.2), and its mechanism proceeds as follows: The sensitizer harvest low energy photons, going from its ground state to its metastable level (E_1). Then, it successively transfers the harvested energy to the ground state, or excited state E_1, of the second Ln^{3+} ion, the activator. While each energy transfer to the activator from the surrounding sensitizer ions excites it to upper emitting states (E_1, E_2, etc),

as a consequence the sensitizers return back to their ground state. Eventually, the successively excited activator ion releases all the transferred energy in the form of a high-energy photon (or upconverted photon).

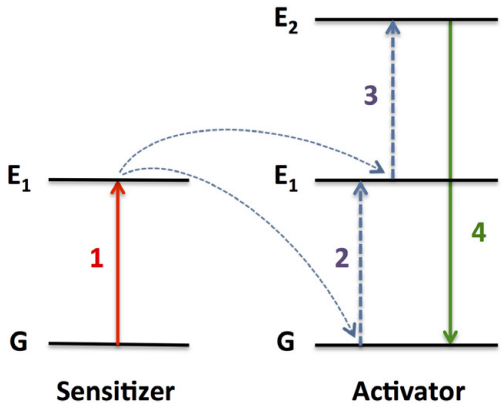

Figure I.2.3.2 Energy transfer upconversion (ETU) mechanism. The sensitizer excites to its "E_1" energy level by absorbing a photon (1). Then, it successively transfers its energy to the activator, which is excited to its E_1 (2) and E_2 (3) energy levels before relaxing to its ground state "G" by emitting a high-energy photon (4).

Two examples of commonly used Ln^{3+} pairs are Yb^{3+}/Er^{3+} and Yb^{3+}/Tm^{3+}, where Yb^{3+} acts as the sensitizer (absorbing 980 nm NIR light), and Er^{3+} and Tm^{3+} are the activators (giving green and blue anti-Stokes emissions, respectively).

The different energy transfer steps responsible for the upconverted emissions from both Ln^{3+} pairs are depicted in Figure I.2.3.3.

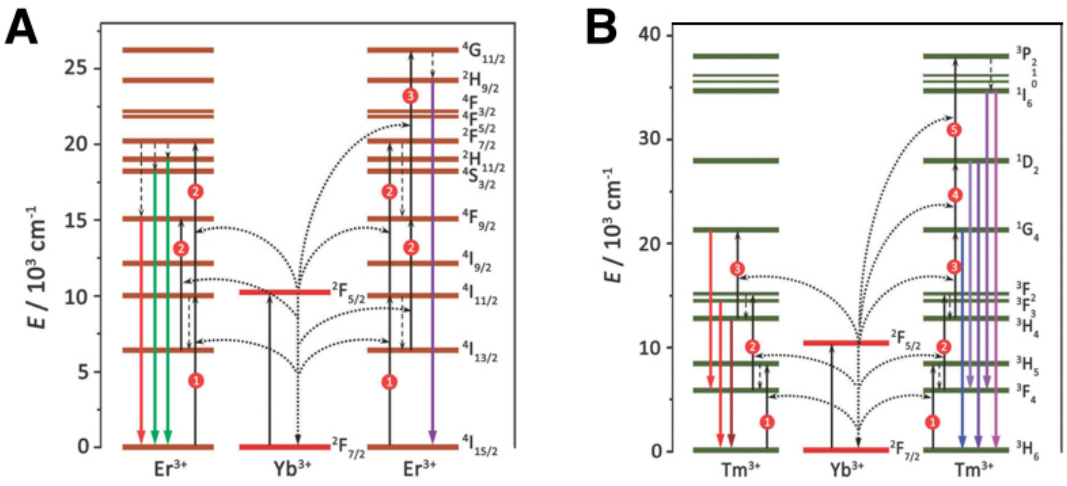

Figure I.2.3.3. Energy transfer steps in ETU process for the different upconversion emissions of Yb^{3+}/Er^{3+} (a) and Yb^{3+}/Tm^{3+} (b) pairs. Adapted from Ref. [25] with permission from The Royal Society of Chemistry.

As one can deduce from this figure, each upconversion emission involves a certain number of energy transfer steps or, in other words, they are processes that require two, three, four or more low energy photons, to emit one single high energy photon, depending on the region of the spectra where the emission is located at. For example, the UV (345 nm) emission obtained with the Yb^{3+}/Tm^{3+} pair ($^1I_6 \rightarrow {}^3F_4$ transition in Tm^{3+}) is a five-photon process. The nature of these ETU processes implies that the upconverting materials are going to show a non-linear optical behaviour. This means that the upconversion emissions are not going to show a linear excitation power-dependance, but a dependance that will follow an "n" power law, where "n" is the number of photons involved in that specific upconversion emission. Thus, in contrast to the reporters exposed in previous sections, the upconversion photoluminescence power-dependence of these materials can be generally expressed as:

$$I_{UCPL} = K \cdot P^n \qquad \text{Ec. I.2.1.4}$$

where "I_{UCPL}" is the upconversion photoluminescence intensity of the specific emission peak, "K" is the material-related coefficient, "P" is the laser pump excitation power, and "n" is the number of excitation photons required to produce that specific upconversion emission.

In addition to the use of proper Ln^{3+} pairs, whose energy levels need to suitably match each other to allow the ETU process, another major requisite is the integration of these trivalent ions at the right concentrations in a proper host matrix, in the form of dopants. It is important to mention that not any material is suitable for this purpose. In fact, the host matrices need to be as resistant to photodamage as possible, transparent in the spectral region of interest, chemically stable, and most importantly, to posses the lowest possible phonon cutoff energy value and a local crystal field that favors the process. The low phonon cutoff is of key importance, as phonon-induced non-radiative processes are the main energy loss mechanism of upconversion. This can be explained because the energy difference between higher and lower energy levels is turned into lattice phonons, dissipating the excitation energy by multiphonon-assisted relaxations. The larger

the number of phonons needed, the lower the efficiency of this non-radiative process.

While the cutoff phonon energy associated to the host lattice is a good indicator of the number of phonons that are needed for relaxation, a way to enhance the upconversion efficiency is to use host matrices with very low frequency phonons (low cutoff phonon energy). Thus, a higher number of phonons would be required to achieve the relaxed state by the non-radiative multiphonon-assisted relaxation pathway.

The local crystal field also has an important influence on the upconversion efficiency, as the local crystal geometry surrounding the lanthanide ions conditions the intermixing of ion's f orbital states. In fact, less symetric crystal phases generally increases upconversion efficiency as the intermixing of Ln^{3+}'s f states with higher electronic configurations is more favored.[26]

Meeting these criteria, the hexagonal or "β" phase of $NaYF_4$ stands out as one of the most efficient host matrices to date for green (Yb^{3+}/Er^{3+}) and blue (Yb^{3+}/Tm^{3+}) upconversion emissions. Thus, although the search for new host lattices is under active investigation, most of the upconverting nanoparticles (UCNPs) used in research consist of Ln^{3+}-doped β-$NaYF_4$ crystals (see Figure I.2.3.4).

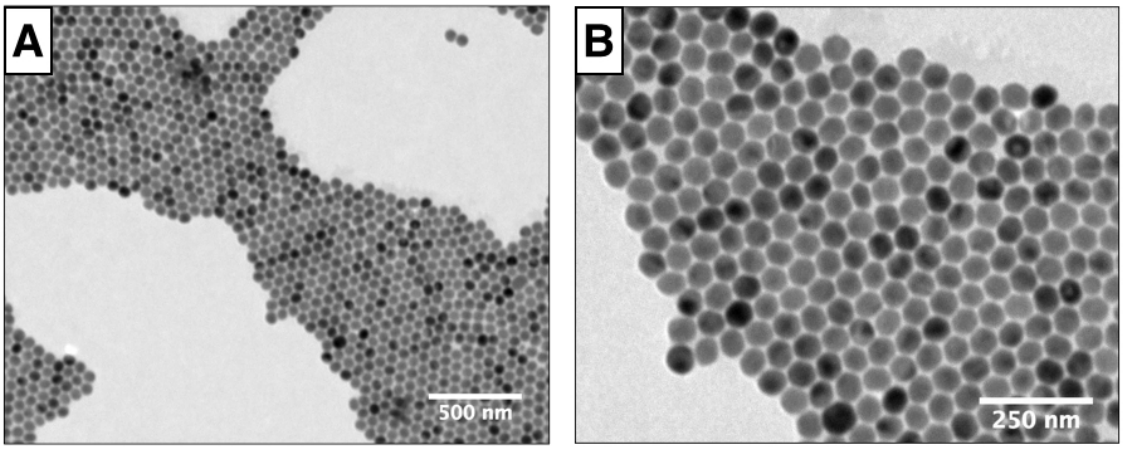

Figure I.2.3.4. A) Transmission electron microscopy (TEM) of β-$NaYF_4$ nanocrystals doped with Yb^{3+} (20% wt) and Er^{3+} (2% wt) synthesized in our laboratory. B) Magnification of TEM Image. Scale bars are 500 nm and 250 nm, respectively.

Interestingly, the distinct properties showed by upconverting nanoparticles (UCNPs) permit to meet most of the desirable characteristics that are pursued when using photoluminescent techniques in fields such as imaging or biodetection. In fact, these materials show superior performance, compared with organic dyes or Q-dots, in most of the previously discussed features from photoluminescent reporters. For example, they show remarkably high photostability due to the inorganic nature and photoresistance of Ln^{3+} ions and the dielectric host matrix, with some authors reporting stable emissions even under 1 hour of continuous 980 nm irradiation at $5 \cdot 10^6$ W/cm^2.[27] This permits to partially overcome their main limitation, the low quantum yields due to the natural inefficiency of the multi-photon requirements for upconversion processes. Another examples are the stability of their emission intensity through time (lacking of fluorescence intermittency, as opposed to organic dyes and Q-dots),[27] their distinct and clean emissions due to their huge anti-Stokes shifts (which can be hundreds of nanometers away from the excitation wavelength at 980 nm, see Figure I.2.3.5), their long lifetimes (up to tens of miliseconds), the lack of autofluorescence when using these reporters (as there is no known biomolecule capable of harvest 980 nm photons and turn them into visible light), their potential in multiplexed assays by introducing different dopants and tuning their concentrations to achieve different emissions and different lifetimes,[28,29] and more.[30]

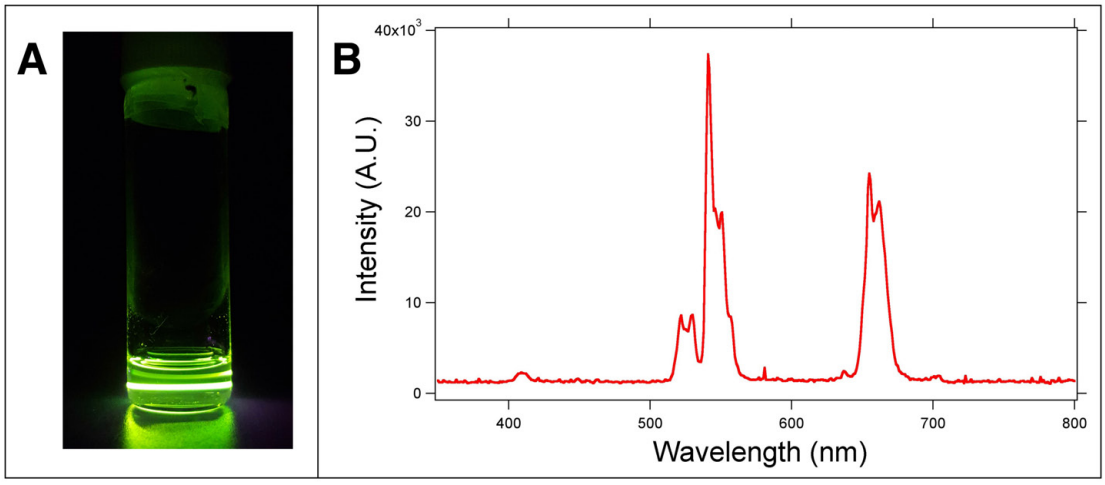

Figure I.2.3.5 A) Emission of β-$NaYF_4$:Yb^{3+}(20%);Er^{3+}(2%) UCNPs upon excitation with a 980 nm CW laser. The laser beam wavelength is invisible to human eye. B) Emission spectrum of the same UCNPs.

Thus, UCNPs properties have the potential to prompt a new generation of systems based on anti-stokes photoluminescence, which can be able to improve resolution and sensitivity in fields like bioimaging, but especially in biodetection.

References

(1) Rubio Retama, J.; López Cabarcos, E.; Mecerreyes, D.; López-Ruiz, B. Design of an Amperometric Biosensor Using Polypyrrole-Microgel Composites Containing Glucose Oxidase. *Biosens. Bioelectron.* **2004**, *20*, 1111.

(2) Tyagi, S.; Kramer, F. R. Molecular Beacons: Probes That Fluoresce upon Hybridization. *Nat. Biotechnol.* **1996**, *14*, 303.

(3) Sirkka, N.; Lyytikäinen, A.; Savukoski, T.; Soukka, T. Upconverting Nanophosphors as Reporters in a Highly Sensitive Heterogeneous Immunoassay for Cardiac Troponin I. *Anal. Chim. Acta* **2016**, *925*, 82.

(4) Rye, H. S.; Dabora, J. M.; Quesada, M. A.; Mathies, R. A.; Glazer, A. N. Fluorometric Assay Using Dimeric Dyes for Double- and Single-Stranded DNA and RNA with Picogram Sensitivity. *Anal. Biochem.* **1993**, *208*, 144.

(5) Melby, L. R.; Rose, N. J.; Abramson, E.; Caris, J. C. Synthesis and Fluorescence of Some Trivalent Lanthanide Complexes. *J. Am. Chem. Soc.* **1964**, *86*, 5117.

(6) Lakowicz, J. R. *Principles of Fluorescence Spectroscopy*; Lakowicz, J. R., Ed.; Springer US: Boston, MA, 2006.

(7) Würth, C.; Grabolle, M.; Pauli, J.; Spieles, M.; Resch-Genger, U. Relative and Absolute Determination of Fluorescence Quantum Yields of Transparent Samples. *Nat. Protoc.* **2013**, *8*, 1535.

(8) Song, L.; Hennink, E. J.; Young, I. T.; Tanke, H. J. Photobleaching Kinetics of Fluorescein in Quantitative Fluorescence Microscopy. *Biophys. J.* **1995**, *68*, 2588.

(9) Bernas, T.; Robinson, J. P.; Asem, E. K.; Rajwa, B. Loss of Image Quality in Photobleaching during Microscopic Imaging of Fluorescent Probes Bound to Chromatin. *J. Biomed. Opt.* **2005**, *10*, 64015.

(10) ThermoFisher Scientific. Photobleaching Principles

https://www.thermofisher.com/es/es/home/life-science/cell-analysis/cell-analysis-learning-center/molecular-probes-school-of-fluorescence/fluorescence-basics/fluorescence-fundamentals/photobleaching-principles.html#.

(11) Cerovic, Z. G.; Ounis, A.; Cartelat, A.; Latouche, G.; Goulas, Y.; Meyer, S.; Moya, I. The Use of Chlorophyll Fluorescence Excitation Spectra for the Non-Destructive in Situ Assessment of UV-Absorbing Compounds in Leaves. *Plant, Cell Environ.* **2002**, *25*, 1663.

(12) Zipfel, W. R.; Williams, R. M.; Christie, R.; Nikitin, A. Y.; Hyman, B. T.; Webb, W. W. Live Tissue Intrinsic Emission Microscopy Using Multiphoton-Excited Native Fluorescence and Second Harmonic Generation. *Proc. Natl. Acad. Sci.* **2003**, *100*, 7075.

(13) Georgakoudi, I.; Jacobson, B. C.; Müller, M. G.; Sheets, E. E.; Badizadegan, K.; Carr-Locke, D. L.; Crum, C. P.; Boone, C. W.; Dasari, R. R.; Van Dam, J.; et al. NAD(P)H and Collagen as in Vivo Quantitative Fluorescent Biomarkers of Epithelial Precancerous Changes. *Cancer Res.* **2002**, *62*, 682 LP.

(14) Gallas, J. M.; Eisner, M. Fluorescence of Melanin-Dependence upon Excitation Wavelength and Concentration. *Photochem. Photobiol.* **1987**, *45*, 595.

(15) Hill, S. C.; Mayo, M. W.; Chang, R. K. *Fluorescence of Bacteria , Pollens , and Naturally Occurring Airborne Particles : Excitation / Emission Spectra*; 2009.

(16) Absorption and emission data of tryptophan https://omlc.org/spectra/PhotochemCAD/html/091.html.

(17) Menter, J. M. Temperature Dependence of Collagen Fluorescence. *Photochem. Photobiol. Sci.* **2006**, *5*, 403.

(18) Nikon microscopy. Corn Kernel Autofluorescence https://www.microscopyu.com/gallery-images/corn-kernel-autofluorescence-1.

(19) El-Sayed, M. A. Small Is Different: Shape-, Size-, and Composition-Dependent Properties of Some Colloidal Semiconductor Nanocrystals. *Acc. Chem. Res.* **2004**, *37*, 326.

(20) Smith, A.; Nie, S. Semiconductor Nanocrystals: Structure, Properties, and Band Gap Engineering. *Acc. Chem. Res.* **2009**, *43*, 190.

(21) Brichkin, S. B.; Razumov, V. F. Colloidal Quantum Dots: Synthesis, Properties and Applications. *Russ. Chem. Rev.* **2016**, *85*, 1297.

(22) Algar, W. R.; Susumu, K.; Delehanty, J. B.; Medintz, I. L. Semiconductor Quantum Dots in Bioanalysis: Crossing the Valley of Death. *Anal. Chem.* **2011**, *83*, 8826.

(23) Resch-Genger, U.; Grabolle, M.; Cavaliere-Jaricot, S.; Nitschke, R.; Nann, T. Quantum Dots versus Organic Dyes as Fluorescent Labels. *Nat. Methods* **2008**, *5*, 763.

(24) Auzel, F. Upconversion and Anti-Stokes Processes with F and D Ions in Solids. *Chem. Rev.* **2004**, *104*, 139.

(25) Dong, H.; Sun, L.-D.; Yan, C.-H. Energy Transfer in Lanthanide Upconversion Studies for Extended Optical Applications. *Chem. Soc. Rev.* **2015**, *44*, 1608.

(26) Chen, G.; Qiu, H.; Prasad, P. N.; Chen, X. Upconversion Nanoparticles: Design, Nanochemistry, and Applications in Theranostics. *Chem. Rev.* **2014**, *114*, 5161.

(27) Wu, S.; Han, G.; Milliron, D. J.; Aloni, S.; Altoe, V.; Talapin, D. V.; Cohen, B. E.; Schuck, P. J. Non-

Blinking and Photostable Upconverted Luminescence from Single Lanthanide-Doped Nanocrystals. *Proc. Natl. Acad. Sci.* **2009**, *106*, 10917.

(28) Zhang, F.; Shi, Q.; Zhang, Y.; Shi, Y.; Ding, K.; Zhao, D.; Stucky, G. D. Fluorescence Upconversion Microbarcodes for Multiplexed Biological Detection: Nucleic Acid Encoding. *Adv. Mater.* **2011**, *23*, 3773.

(29) Lu, Y.; Zhao, J.; Zhang, R.; Liu, Y.; Liu, D.; Goldys, E. M.; Yang, X.; Xi, P.; Sunna, A.; Lu, J.; et al. Tunable Lifetime Multiplexing Using Luminescent Nanocrystals. *Nat. Photonics* **2013**, *8*, 32.

(30) Mendez-Gonzalez, D.; Lopez-Cabarcos, E.; Rubio-Retama, J.; Laurenti, M. Sensors and Bioassays Powered by Upconverting Materials. *Adv. Colloid Interface Sci.* **2017**, *249*, 66.

I.3 Sensors and bioassays powered by upconverting materials

I.3.1 Introduction

A general classification can be made within biosensing platforms attending to the way assays are carried out: Homogeneous assays are those that proceed by simply mixing solutions and taking measurements to read the result, without any separation or washing procedure. This kind of assays is often based on energy transfer processes between donor and acceptor pairs. A widely known example of homogeneous assay is the use of molecular beacons, where a DNA hairpin is marked with a fluorophore (donor) that faces a quencher molecule (acceptor), see Figure I.3.1.1. In this situation, when the organic dye is excited no fluorescence is observed, as its excitation energy is transferred to the quencher by a non-radiative process. On the other hand, when a complementary (target) sequence is present, it hybridizes with the probe, opening the hairpin. This moves the fluorophore away from the quencher, now being able to fluoresce and thus permitting to detect the presence of the target sequence.

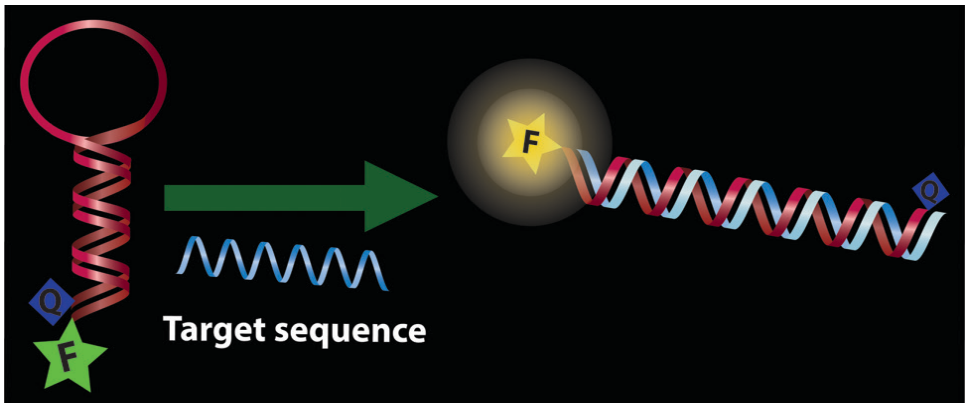

Figure I.3.1.1 Example of homogeneous assay: Molecular beacon. When the fluorophore (F) faces the quencher (Q), it is no able to fluoresce, as the energy from its excited state is transferred to the quencher, non-radiatively. When the target sequence is present, the hairpin opens upon hybridization with it. This moves the organic dye away from the quencher, allowing it to fluoresce.

As contrast, heterogeneous assays are multi-step based assays in which separation, analyte capture, and washings are carried out, often using solid supports. This usually results in the reduction of background signals and other advantages, due to the separation and washing steps, although this may turn the assays less time-effective in comparison with other strategies. Sandwich immunoassays using microwell plates, lateral flow assays, or DNA chips are some common examples of heterogeneous assays (see Figure I.3.1.2).

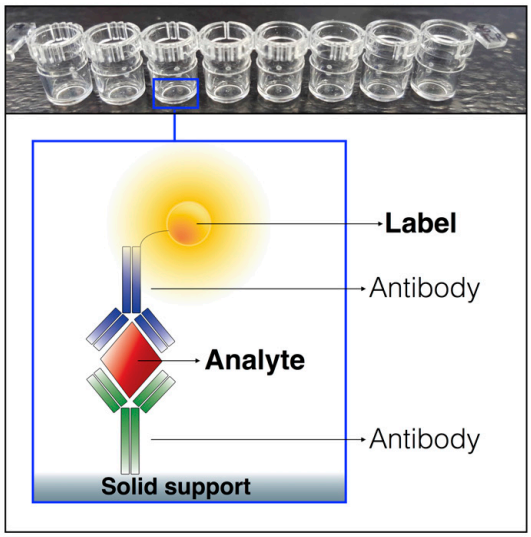

Figure I.3.1.2 Example of heterogeneous assay (inset) using microwells as solid support (real image). A molecule like an antibody, which can capture the analyte of interest, is previously fixed to the solid support. When adding the sample, the analyte is selectively captured from the solution by the antibody. Finally, another molecule is added to reveal the presence of the analyte, like a secondary antibody that is marked with a label and showing affinity for the analyte.

The use of UCNPs as reporters is starting to be widely applied to traditional detection platforms, as well as to brand new conceptual biosensing systems. The advantages derived from their use as labels are being exploited in both homogeneous and heterogeneous assays, as a way to improve sensitivities, increase the reliability and the reproducibility under reanalysis of results, or simply to build and investigate new concepts for biosensing. A review on the state of the art in this field is presented next.

I.3.2
Sensors and bioassays powered by upconverting materials

(Publication 1)

https://www.sciencedirect.com/science/article/pii/S0001868617300842

Advances in Colloid and Interface Science 249 (2017) 66–87

Contents lists available at ScienceDirect

Advances in Colloid and Interface Science

journal homepage: www.elsevier.com/locate/cis

Historical perspective

Sensors and bioassays powered by upconverting materials

Diego Mendez-Gonzalez, Enrique Lopez-Cabarcos, Jorge Rubio-Retama, Marco Laurenti*

Department of Physical Chemistry II, Faculty of Pharmacy, Complutense University of Madrid, Plaza Ramon y Cajal, Madrid 28040, Spain

A B S T R A C T

In recent years, considerable efforts have been done to better understand the peculiar emission properties of upconverting materials due to their widespread applications in different and important technological fields such as upconversion-based photoactivated cancer therapies, photoactivated drug-delivery, magnetic resonance imaging contrast agents, bioimaging. However, one of the most promising applications of upconverting materials concerns the field of sensing, due to their unique emission properties. In fact, the minimal autofluorescence, blinking, photo-bleaching, and high photostability makes them an excellent alternative to organic dyes or quantum dots. This article reviews the state-of-the-art, design, and sensing strategies of upconversion-based sensing platforms, with special attention to upconverting nanoparticles, as well as how the incorporation of these materials into pre-existing diagnostic tests and bioassays have improved their capabilities for the detection of different kinds of analytes.

1. Introduction

The detection and analysis of specific molecules is of tremendous importance in different fields such as biology, medicine, and life sciences, and typically most luminescent reporters used for this purpose are detected by means of their fluorescent characteristics. Common fluorescence is based on the absorption of photons at a certain specific wavelength, and the emission of photons at longer wavelengths (i.e. lower energy photons) [1]. Fluorescence is a process that can occur very efficiently, with some fluorophores showing very high quantum yields close to 90% [2,3]. Although this characteristic has permitted the development of sensitive assays and sensors, these labels have some inherent drawbacks that put a limit in the sensitivity that can be achieved when used in these sensing platforms. In fact, organic dyes suffer photobleaching [4], a photodegradation process of the fluorophore that makes them no longer able to fluoresce. This phenomenon can specially take place when high excitations energies are used in order to resolve the presence of small quantities of the fluorescent label (i.e. when very sensitive detection systems are pursued). Quantum dots can overcome this limitation, as they exhibit higher photostability and high quantum yields. However under continuous excitation, together with organic dyes, they can suffer from blinking (also called fluorescence intermittency), which is based on the competition of radiative and non-radiative processes and it manifests as the random activation and deactivation of the fluorescent emission [5]. Blinking effect gains influence when a small concentration of label is being analyzed, yielding high and random variability in the results, and thus limiting again the sensitivity of these sensing platforms. In addition the fluorescence coming from biomolecules (e.g. proteins, cofactors) also known as autofluorescence, is an important source of background noise that normally limits the quantity of fluorescent reporters that can be detected [6].

Nanotechnology is a field of research in continuous growth. The synthesis, properties and applications of nanomaterials and devices have prompted the development of different nanoprobes as diagnostic tools. Recently a new kind of nanoprobes have attracted attention, as they could solve some of the limitations previously described when more sensitive sensing platforms are pursued [7,8]. These new kind of reporters based on upconverting materials are named after the special luminescence process that they are able to carry out. Contrary to normal fluorescence, upconverting materials are able to absorb two or more low energy photons, typically from the near-infrared region (NIR), and emit one photon of higher energy in the ultraviolet (UV) and/or visible (vis) regions [9]. In general, these materials consist in a host matrix doped with lanthanide ions. Nevertheless, for the upconverting processes to occur, they must meet certain criteria. First, although different matrices can be used as the host material (e.g. fluorides, oxides, oxysulfides), they are dielectric materials displaying very low frequency phonons, a necessary feature to cut down the non-radiative processes and allow the upconversion phenomenon to take place [10]. Among the different matrices, hexagonal or β-$NaYF_4$ matrix stands out as one of the most efficient host for green and blue emissions [11]. Second, the low frequency matrix must be doped with specific Ln^{3+} ions responsible for the upconversion process due to their 4f-4f

* Corresponding author.
E-mail address: mlaurent@ucm.es (M. Laurenti).

http://dx.doi.org/10.1016/j.cis.2017.06.003
Received 31 January 2017; Received in revised form 2 June 2017; Accepted 2 June 2017
Available online 10 June 2017

orbital electronic transitions. Although it is not mandatory, a specific pair of Ln^{3+} ions can be used for the Energy Transfer Upconversion (ETU) process [9,12,13]. In ETU, one ion acts as sensitizer absorbing the NIR light and successively transfers the energy to the activator Ln^{3+} ion that is responsible for the emission. An example of a pair of Ln^{3+} ions commonly used is represented by Yb^{3+}/Er^{3+} and Yb^{3+}/Tm^{3+} (for green and blue emissions, respectively), where Yb^{3+} acts as sensitizer and the other Ln^{3+} ion as activator [12]. The unique nature of the upconversion process, the fact that their excitation wavelength locates within the NIR optical window of tissues (where light is able to achieve the maximum penetration) [14–17] and their discrete emissions in the UV–vis, have permitted the design of very interesting systems for photoactivated drug delivery [18], photodynamic therapy [19], in vitro and in vivo bioimaging [15,20,21], or magnetic resonance imaging contrast agents just to mention a few [22,23]. Although the nature of the upconversion process itself is inherently inefficient [11], it is in the field of sensing where upconverting phosphors (UCP) have probably best evidenced their potential thanks to the large anti-Stokes shifts, long lifetimes, and reduced background noise that significantly enhance the limit of detection (LOD) of sensing platforms based on UCP or upconverting nanoparticles (UCNPs). In addition, the high photostability showed by upconverting materials permits to use very intense power density irradiations without photobleaching, making possible to detect a few or even a single upconverting nanoparticles [24,25]. Contrary to organic dyes and quantum dots, the lack of blinking in UCPs makes possible to detect little amounts of UCP thanks to their signal stability. UCNPs show also great potential for bioimaging applications thanks to some attractive features such as greater tissue penetration depth, less damage to tissues during imaging, and minimal autofluorescence of biological samples [14–17,26]. In fact, no biosamples show anti-Stokes emission in the visible range after exposure to NIR light, thus reducing the autofluorescence of biological samples and the background interference [15,27]. However, there are also some disadvantages that are limiting the application of UCNPs in bioimaging. Water has a strong absorption of light at 980 nm producing a heating effect that should be taken into account during bioimaging of biological specimens [15,26]. In addition, the luminescence emission of UCNPs is related to the power density of the excitation NIR laser and with the size [13,15]. The American National Standard established that a conservative limit for human skin exposure at 980 nm is around 730 mW cm^{-2} [28], and for this reason in most studies a more conventional power density of 100–200 mW cm^{-2} at 980 nm is applied [14,15]. However, at this power density the luminescence emission of UCNPs is weak, making difficult their visualization [27].

The synthesis of UCNPs can be achieved using different methods that usually afford hydrophobic nanoparticles. This makes necessary the surface modification of UCNPs for their subsequent applications as sensors or bioapplications in general [10,12,13,29]. UCNPs can be obtained using the thermal decomposition of organometallic compounds, which decompose at elevated temperature in a high boiling point organic solvent such as oleic acid, oleylamine, tri-n-octylphosphine oxide and 1-octadecene. Another well-known method for the synthesis of UCNPs is the high-temperature co-precipitation method, which compared to the thermal decomposition is expected to be more convenient due to a simple protocol and short reaction time [10,12,13,29]. An interesting alternative to the previous methods is represented by the hydro(solvo)thermal synthesis that allows to obtain highly crystalline nanomaterials under relatively mild conditions when compared to the other synthetic routes [10,12,13,29]. By carefully tailoring all the experimental variables, all these methods allow to obtain UCNPs with a narrow size distribution, good crystallinity and optical properties. However, some recent works have described several issues such as chemical stability in water or buffer solutions that need to be addressed for their future in vivo and in vitro applications [30–33]. All these features have paved the way to the development of efficient assay methods based on UCNPs, all discussed in this review article.

2. Homogenous assays and resonance energy transfer

2.1. Resonance energy transfer

The energy transfer from the excited state of a donor to the ground state of an acceptor can occur in two different ways, either radiatively or non-radiatively. The energy transfer by radiative mechanism needs the emission of a photon from the donor and the following absorption of the photon by the acceptor [1]. On the other hand, non-radiative energy transfer does not require the emission and re-absorption of photons. The energy is transferred due to the "resonance" between the donor and the acceptor through specific interactions such as Resonance Energy Transfer (RET) [1]. This process is distance dependent and it occurs usually when the distance between the donor and acceptor is comprised between 2 and 10 nm, and there is overlap of the emission spectrum of the donor and the absorption spectrum of the acceptor [1,34]. RET refers to Fluorescence Resonance Energy Transfer (FRET) or to lanthanide-based Luminescence Resonance Energy Transfer (LRET). Although LRET can be considered as an extension of FRET, the luminescence emission of Ln^{3+} arise from 4f-4f transition, and hence should not be called fluorescence, whose emission comes from singlet to singlet transition. LRET offers some advantages over FRET such as strong energy transfer even at relatively large distance, and longer donor-lifetime that increase the sensitivity and reduces the background [34,35]. Moreover, the acceptor can be activated only by the energy transferred from the donor (the UCNP) that is excited in the NIR region, where the acceptors are barely absorptive [35]. Fluorescent sensors based on FRET or LRET are efficient and robust sensing platforms, and they are usually based on three different approaches: [1] energy transfer between donor (UCNP) and acceptor followed by the emission of the acceptor, [2] the luminescence turn-off of the donor induced by RET, and [3] the luminescence turn-on of the donor induced by the restoration of the original properties of the UCNPs. In the next section, we report some examples that describe these three different mechanisms and approaches to build a sensor using UCNPs and LRET.

2.2. Emission turn-off/on induced by luminescence resonance energy transfer

UCNP-based LRET systems use the nanoparticles as the energy donor due to their large anti-Stokes shifts and sharp-band emissions while organic dyes and quantum dots (QDs) are used as energy acceptors for their excellent absorption capacity. Besides, the possibility to tune their emission, together with their high luminescence intensity and quantum yield makes them excellent acceptors to be used in the construction of LRET-based biosensors [13,29,36]. To achieve a highly efficient LRET process, organic dyes or QDs are linked with the energy donor UCNPs through specific interaction provided by biological molecules such as biotin-streptavidin, antigen–antibody, or two complementary DNA/RNA target sequences. These sensors are based on the fact that LRET between UCNPs and dyes/QDs will take place only after the introduction of the specific analyte, bringing them in close proximity, and trigger the LRET from the energy donor UCNPs to the energy acceptors, as shown in the example of Fig. 1.

Chen and co-workers have reported one of the first examples of LRET based biosensor using UCNPs as donor and a DNA functionalized with carboxytetramethylrhodamine (TAMRA) as organic dye acceptor [37]. As shown in Fig. 2, the DNA sensor was developed using as energy donor nanoparticles of $NaYF_4$:Yb^{3+}, Er^{3+} functionalized with streptavidin and DNA-TAMRA as the energy acceptor. Upon addition of the specific target-DNA, the corresponding emission of the TAMRA gradually appears, and the signal intensities of green emissions of UCNPs significantly decrease indicating the resonance energy transfer from the UCNPs to TAMRA with a LOD ranging from 10 to 60 nM.

Yan and co-workers used tetramethylrhodamine isothiocyanate (TRITC) molecules, which had an absorption peak in the green region,

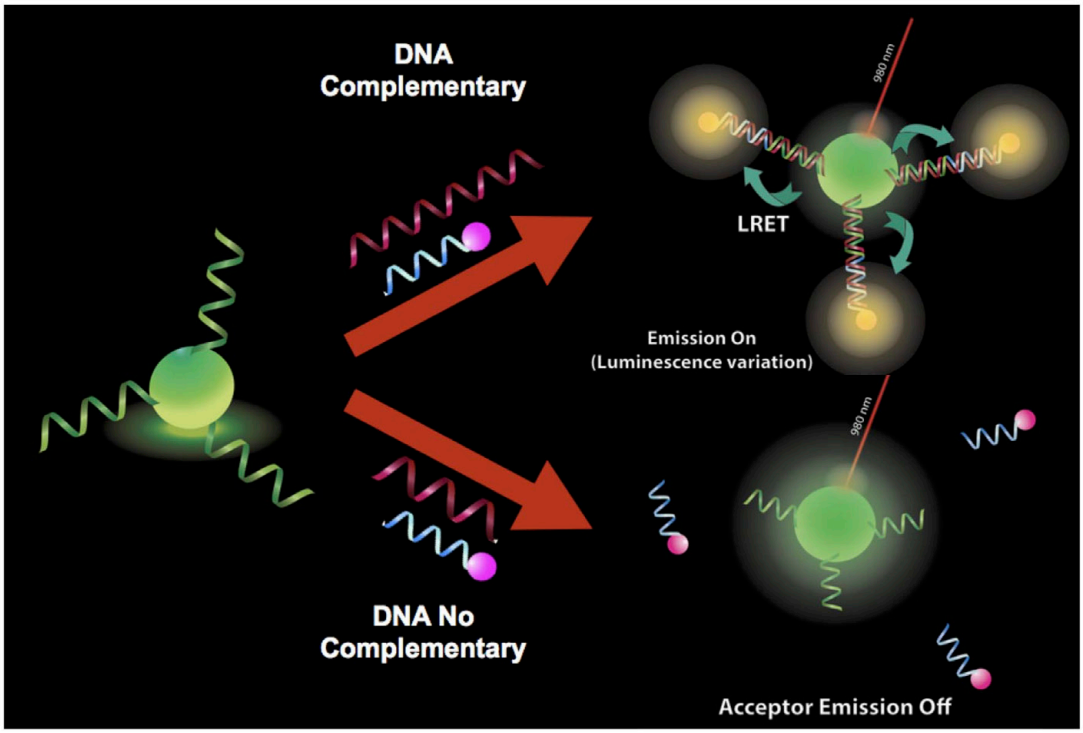

Fig. 1. Schematic representation of a sensor based on LRET mechanism between a donor (UCNP) and an acceptor (e.g. QD). In this example the presence of a target sequence induces the hybridization of the single strand DNA (ssDNA) with the donor and the acceptor making possible the LRET only with the specific DNA/RNA sequence. On the other hand, when no complementary DNA is present there is no link between the fluorophore and the UCNPs and there is no emission from the acceptor.

as a potential energy acceptor to absorb the green upconversion emission of the UCNPs donor. As expected, the green emission of Er^{3+} was quenched due to the overlaps with the absorption of TRITC that enables RET, while the red emission at 655 nm is not changed because there is no spectral overlap. Since the emission of TRITC molecules cannot be observed using NIR light as excitation source, the observed luminescence at 600 nm is produced by LRET. In addition, the luminescence lifetime of UCNPs shortened, while that of TRITC greatly lengthened indicating that the LRET process occurred from UCNPs to TRITC [38]. By combining UCNPs and QDs, both functionalized with a thrombin-specific aptamer, Krull's group developed a heterogeneous thrombin assay (Fig. 3) [39].

They immobilized amine capped UCNPs onto glass coverslips, which was previously functionalized with aldehyde groups, via the formation of an imine bond between the amine and the aldehyde. They found that a high surface density of UCNPs is important to obtain a more efficient assay based on LRET. In fact, the increased donor density improved the probability in which a single acceptor can interact with multiple donors. The presence of thrombin led to the assembly of UCNPs with QDs, causing the efficient LRET process where both the UV and the blue emission of the UCNPs were absorbed by the QDs to give its emission at 614 nm. Due to the low noise, the sensor showed a low LOD of 230 fmol (in buffer solution), being also one of the first examples of covalent immobilization of UCNPs for bioassays.

The luminescence turn-off or quenching of upconverting materials can be exploited to develop nanosensors as shown in Fig. 4. In this example the surface of UCNPs is functionalized with a specific ssDNA, whose free nucleobases can interact with the surface of Graphene Oxide (GO). This brings the UCNPs close to the GO, resulting in the quenching of their luminescence due to the LRET between UCNPs and GO [40]. On the other hand, the presence of the complementary target DNA hinders the interaction of the previously free nucleobases with GO upon hybridization, resulting in an upconversion signal that is proportional to the amount of target ssDNA in the media.

Our group developed a DNA biosensor platform to detect ssDNA in buffer media using ad-hoc functionalized UCNPs, exploiting the LRET pair between UCNPs and GO [41]. As shown in Fig. 4, the ssDNA-UCNPs can interact with the surface of the GO through π-π interaction between the DNA bases and the GO, and as result the luminescence of the UCNPs was quenched. The presence of the complementary DNA produces the hybridization of the ssDNA, resulting in a weaker interaction between GO and UCNPs with almost no luminescence quenching. The emission intensity was correlated to the concentration of complementary DNA and the detection limit was in the nM range. Ye and coworkers developed a biosensor made of $BaGdF_5$:Yb^{3+}, Er^{3+} UCNPs and Au nanoparticles for the detection of avian influenza virus H7 subtype. The biosensor relies on the specific functionalization of the Au nanoparticles and the UCNPs functionalized respectively with the H7 hemagglutinin gene sequence-modified oligonucleotide and the complementary ssDNA of H7 hemagglutinin gene. The hybridization of the oligonucleotides of these two nanoparticles induce the quenching of the green emission at 540 nm due to the LRET process from the UCNPs to the Au nanoparticles. Interestingly, the LOD of the proposed detection system was 7 pM [42]. Besides sensor probes based on the luminescence quenching of UCNPs a novel approach can be based on the emission enhancement of upconverting nanoparticles. Our group presented a microRNA (miRNA) sensor based on graphene oxide quantum dots and UCNPs functionalized with ssDNA (ssDNA-UCNPs) [43]. The sensor exploits the π-π stacking interaction between the graphene QDs and the DNA nucleobases that brings the QDs in close proximity to the surface of the UCNPs enhancing the upconversion emission. The introduction of the complementary miRNA sequence blocks the ability of the ssDNA-UCNPs to interact with the graphene QDs, reducing the enhancement of the emission in a miRNA concentration-dependent manner. Wilhelm and coworkers used UCNPs to follow and monitor enzymatic redox reactions utilizing nanoparticles made of $NaYF_4$:Yb^{3+},Tm^{3+}@$NaYF_4$ [44]. They exploited the reaction between the coenzyme of flavin adenine dinucleotide (FAD) and nicotinamide

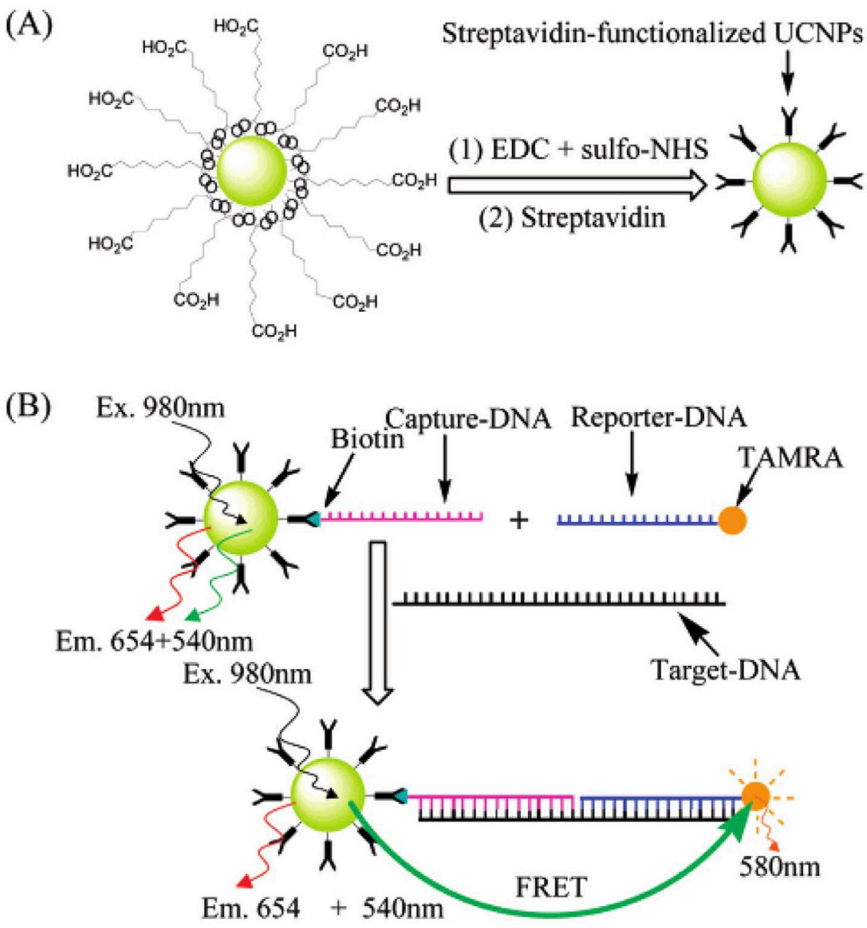

Fig. 2. Synthesis of streptavidin-functionalized UCNPs (A) and schematic of DNA nanosensor based on UCNPs. Reprinted with permission from reference 37. Copyright 2008 American Chemical Society.

adenine dinucleotide (NADH) that can be followed using the turn off/on of the emission at 360 and 475 nm of the UCNPs which serves as UV–vis source (Fig. 5).

In fact, the absorbance of FAD and NADH matches with the blue emission of Tm^{3+}, while their $FADH_2$/NAD counterparts produce a blue-shift in the absorption resulting in the restoration of the blue emission at 475 nm and quenching of the emission at 360 nm [44]. Apart from the detection of biological samples, UCNPs can be used for the detection of heavy metal ions. Saleh and coworkers showed the luminescence quenching of UCNPs by heavy metal ions in aqueous solution without external quenchers [45]. In fact, quite surprisingly heavy metal ions can affect the luminescence of upconverting nanoparticles. For this reason they can be used to detect these ions by simply following the change of the luminescence emission intensity of one of the emission bands. At low concentration the quenching mechanism is governed by dynamic quenching due to the collisions between the heavy metal ions and the UCNPs, while at higher concentration the quenching mechanism is due to the static quenching. They studied the luminescence quenching of the UCNPs produced by several metal ions such as Cu^{2+}, Hg^{2+}, Pb^{2+}, Cd^{2+}, Co^{2+}, Ag^{+}, Fe^{3+}, and Zn^{2+}. The obtained Stern-Volmer constant was higher for Hg^{2+}, however, compared to other systems such as QDs, the Stern-Volmer constants were smaller for UCNPs [45]. Mercury and most of its compounds are recognized as extremely toxic. They can cause serious environmental and health problems due to their bio-accumulative nature and the United States Environmental Protection Agency sets the maximum permitted level in drinking water at 2 ppb [46,47]. Gu et al. developed thiazole-derivative functionalized UCNPs able to detect Hg^{2+} ions in living cells. Measuring as signal the ratio of the upconversion emission intensity at 540 nm and 803 nm (I_{540}/I_{803}), they were able to detect Hg^{2+} in living cells with high selectivity and a LOD of 0.21 μM [48]. It is worth to mention that the approach based on a ratiometric calculation permits an accurate quantification of the concentration of the target species. Fig. 6 shows the working mechanism behind the sensor proposed by Gu et al. It is interesting to observe that the change of the emission is caused by the resonance energy transfer from the UCNPs to an antenna that is highly responsive to the presence of the desired analyte, while the interaction between the target species and the antenna provokes a change in the optical absorption/emission properties of the antenna.

Fluorescent nanoprobes based on rhodamine derivatives have demonstrated to be a promising candidate for the detection of Cu^{2+} ions. However, one of the problems encountered in this kind of fluorescent probes is that some of them were not able to distinguish Cu^{2+} from Hg^{2+}. Recently, Xu et al. developed a fluorescent nanoprobe based on a rhodamine B derivative (RBH) grafted to silica coated upconversion nanoparticles. RBH itself is non-fluorescent, however, its complex with Cu^{2+} can absorb the green emission of the UCNPs that provokes the emission at 580 nm of the RBH derivative while the upconversion emission intensity at 545 nm decreased due to the LRET from the UCNPs to the RBH-Cu^{2+} complex. The LOD of the proposed sensor was of 0.82 μM in absolute ethanol solution and, most importantly, was able to detect Cu^{2+} even in the presence of Hg^{2+} [49]. Liu et al. reported one of the first examples of sensor that was selective toward Hg^{2+} combining in one system a chromophoric nanoprobe of Ru(II) complex conjugated with an upconversion nanoparticle made of $NaYF_4$:Yb^{3+},Er^{3+},Tm^{3+} (Fig. 7) [50].

As shown in Fig. 7b the addition of Hg^{2+} change the λ_{max} absorbance of the resulting complex N719-Ru(II) that blue-shifts from 541 to

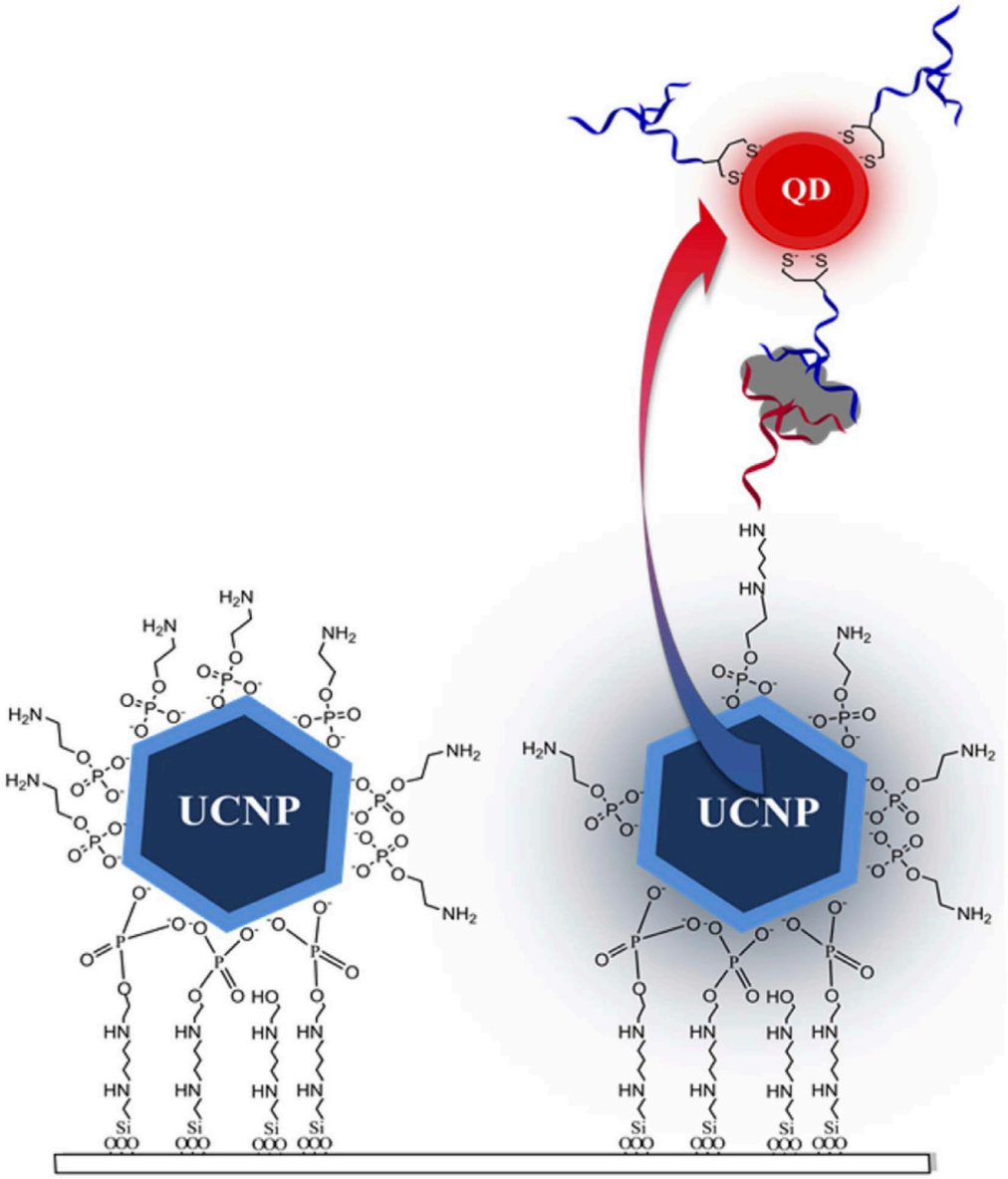

Fig. 3. Illustration of the sensor developed by Krull's group. Reprinted with permission from reference 39. Copyright 2014 American Chemical Society.

485 nm as a result of the complex formation. In this way the addition of Hg^{2+} modulates the energy transfer, between the donor and acceptor, leading to a decrease in the spectral overlap between the green emission band of the UCNPs and the absorption band of the complex N719-Ru(II) resulting in a recovery of the luminescence emission of the UCNPs at 541 nm. The detection of Hg^{2+} was achieved by using the ratio intensity of the Er^{3+} emission band of the UCNPs at 541 nm and the Tm^{3+} emission band at 801 nm. The selectivity of the system was confirmed by the simultaneous measurement of several metal ions such as Cd^{2+}, Zn^{2+}, Mn^{2+}, Cu^{2+}, Ni^{2+}, Pb^{2+}, Pd^{2+}, Cu^{2+}, Co^{2+}, Cr^{3+}, and Fe^{3+} among others together with Hg^{2+}. The LOD of the system in water was incredibly low with a measured concentration of mercury of 1.95 ppb [50]. Recently, Li et al. developed a similar approach through the turn-off/on emission of the green band of UCNPs. The sensor was made of UCNPs functionalized with Rhodamine B thiolactone (RBT) and it is based on the rapid turn-on upconversion luminescence for the selective detection of Hg^{2+}. The presence of Hg^{2+} induces the formation of a derivative RBT-Hg that provokes the LRET transfer from the UCNPs to the RBT with a LOD of Hg^{2+} in water of 0.7 ppb, being in addition ultrasensitive and selective toward Hg^{2+} among other metal ions over a broad range of pH [51]. Liu et al. reported a LOD for Hg in water of 0.1 ppb by using a system made of graphene oxide (GO) and $NaYF_4$:Yb^{3+},Er^{3+} functionalized with thymine and specific oligonucleotides for Hg^{2+} detection. Without the presence of Hg^{2+} ions, UCNPs interact with GO via $\pi-\pi$ stacking interaction between the bases of the ssDNA ligand on the UCNPs and GO inducing the luminescence quenching of the nanoparticles. On the other hand, the presence of Hg^{2+} transforms the Hg^{2+}-specific ssDNA into its double-stranded DNA counterpart, resulting in a weaker interaction between GO and UCNPs [40]. Zhang and coworkers reported the detection of Pb^{2+} in water by using poly(ethyleneimine) coated $NaYF_4$:Yb^{3+},Tm^{3+} UCNPs and gold nanoparticles capped with 11-mercaptoundecanoic acid (MUA). The electrostatic interaction between the positively charged UCNPs and the negatively charged gold nanoparticles produces the nanoparticles assembly that quenched the green emission of the UCNPs. The presence of Pb^{2+} provokes the aggregation of the gold

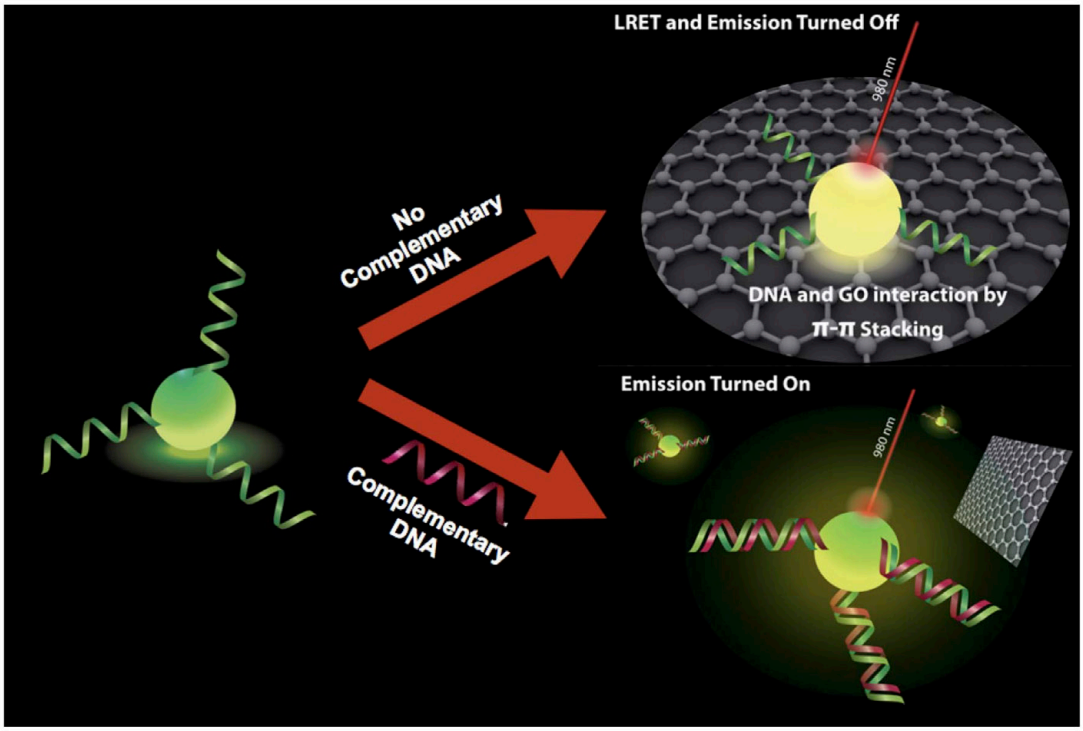

Fig. 4. Schematic representation of a DNA sensor exploiting the emission turn-off mechanism.

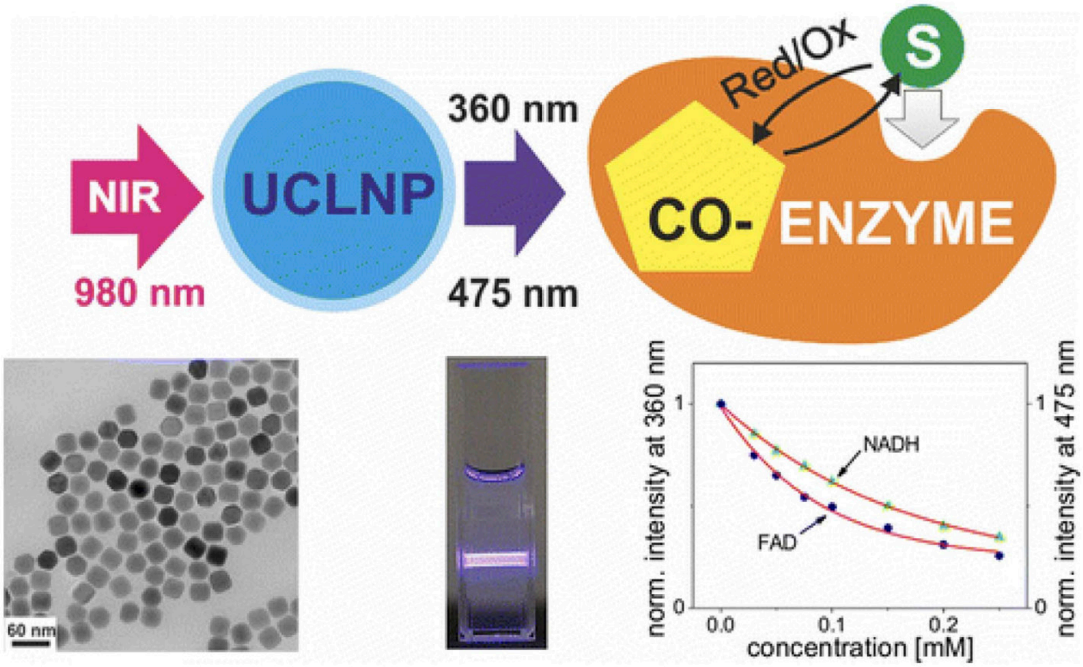

Fig. 5. Upon NIR excitation at 980 nm, the UCNPs display emission bands peaking at 360 and 475 nm with a perfect match to the absorption bands of the enzyme co-substrate NADH and the coenzyme FAD. Reprinted with permission from reference 44. Copyright 2014 American Chemical Society.

nanoparticles induced by the chelation of Pb^{2+} ions by the MUA ligands, causing their detachment from the UCNPs and the restoration of the green emission [52]. Xu et al. developed a sensor based on LRET for the detection of Pb^{2+} in human serum with an LOD of 80 nM [53]. UCNPs and QDs were assembled together via the electrostatic interaction between the positively charged polyethyleneimine ligands on the surface of the UCNPs and the negatively charged thioglycolic acid ligands on the surface of the QDs, which enables the LRET process from the donor UCNPs to the acceptor QDs. A good linear relationship was obtained from the Pb^{2+} concentration and the fluorescent intensity of the QDs. Moreover, the autofluorescence of serum under visible light can also be overcome by the NIR excitation of the nanoprobe.

Another interesting application of UCNPs and LRET is their use as nanoprobes for pH imaging, showing the flexibility of UCNPs as

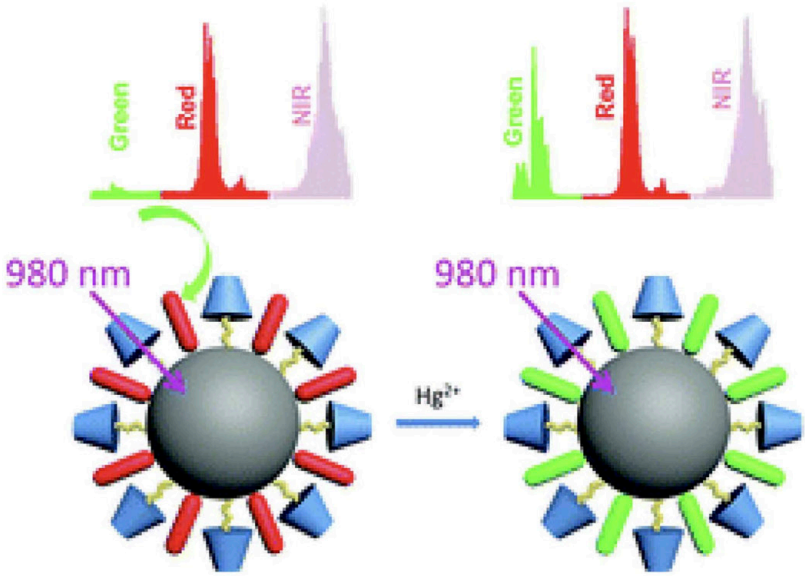

Fig. 6. Schematic representation of the nanoprobe based on LRET quenching caused by the thiazole moiety that upon addition of mercury decreased the energy transfer of the green emission Er^{3+} bands. Reproduced with permission from reference 48. Copyright 2015 Royal Society of Chemistry. (For interpretation of the references to color in this figure legend, the reader is referred to the web version of this article.)

platforms detection [54,55]. The development of pH nanosensors is of particular interest for the optical sensing of intracellular pH to study membrane dynamics and intracellular trafficking, and the bioimaging of acidic pH inside living cells might indicate cellular dysfunctions such as cancer. A simple and effective way to develop a pH sensor using UCNPs is to modulate their emission intensity by linking them to a pH indicator or chromogenic reactions. As explained in Section 2.1, one basic requirement to observe luminescence resonance energy transfer is that the emission of the UCNPs overlaps with the absorbance of the indicator probe. Using this approach Arppe et al. introduced a nanosensor based on LRET between UCNPs and a pH-dependent dye pHrodo™ Red [54]. The dye was covalently bound to the aminosilane surface of the nanoparticles and its fluorescence was strongly dependent by pH changes. By referencing the pH-dependent emission of pHrodo™ Red with the pH-insensitive upconversion photoluminescence of the UCNP, the developed pH-sensor exhibits a dynamic range from pH 7.2 to 2.5. More importantly they applied the pH nanoprobe by imaging the two emission wavelengths of the nanosensor in living HeLa cells with a confocal fluorescence microscope upon 980 nm excitation. However, the direct measurement of pH inside the HeLa cells needs extensive calibration experiments and further optimization of the particles have to be performed to be able to use the ratiometric signal for a quantitative determination of pH inside cells. A more recent publication from the same group reported the measuring and imaging of intracellular pH using UCNPs coated with poly(ethylenimine) and functionalized with pHrodo™ Red [55]. The coating ensures a high positive surface charge that enhances the cellular uptake and colloidal stability. At the same time it provides a high number of primary amino groups for its functionalization with the pH sensitive dye pHrodo™ Red. The dye shows a broad dynamic range from pH 8 to pH 4 and its absorption perfectly matches the green upconversion emission of the UCNPs allowing LRET. Living cells were imaged with a confocal scanning microscope using 980 nm excitation wavelength that facilitates high resolution and penetration depth into the specimen and low phototoxicity. After 16 h, the UCNPs with a concentration of 10 μg mL^{-1} were internalized by cells and no cytotoxic effect was observed over a period of 24 h. However, one of the conclusions of their study is that the exact pH determination of an intracellular compartment is not possible. This is because in endosomes and lysosomes the proton pumping vacuolar ATPase does not stop at a given pH but maintains a steady state with a counterion transport. For this reason any probes measuring the pH in such small volume will also affect the steady state by absorbing protons making impossible to obtain the exact pH determination.

3. Heterogeneous assays

3.1. Competitive and non-competitive heterogeneous assays

Heterogeneous assays are usually multi-step consisting tests, in which the analyte of interest is specifically captured from a complex mixture onto a solid support, incubated with a reporter, and finally detected. These tests usually integrate incubation and washing steps, permitting in the latter step to remove unbound molecules and labels. This usually translates in improved sensitivities compared with homogeneous assays. We could classify heterogeneous assays as competitive and non-competitive as illustrated in Scheme 1.

In the first approach the unlabeled analyte competes with a reporter for specifically binding to the support, yielding a signal that will be inversely proportional to the analyte concentration. On the other hand, in non-competitive heterogeneous assays the analyte will be captured onto the support and further labeled, obtaining a proportional relationship between the reporter signal and the analyte concentration. An example of a common non-competitive assay are sandwich immunoassays, in which the analyte is captured by an antibody, for instance, and then a labeled antibody showing affinity for the captured analyte is used to reveal its presence. The better sensitivity compared with other reporters, due to the inherent minimal autofluorescence when UCP are used, can improve even more the performance of heterogeneous assays. As it has been proved, their combination, together with different solid supports (magnetic beads, microwells, capillary) permits to develop assays detecting very small quantities of the targeted analyte, while demonstrating absence of photobleaching when scanning the surface and long term photo-stability when reanalyzing assay results at high excitation powers [56–58]. As the emission intensity of the UCP increases by the square or cube (for 2 or 3-photon upconversion processes, respectively) of the excitation power, while the nonspecific binding is proportional to the capture surface area, the detection sensitivity of UCP based assays should improve, in principle, when the size of the capture surface used in the assay is small. There is not any reporter that shows this feature apart from UCP, which makes them ideal candidates for the development of portable and small diagnostic devices. In fact, based on this concept, Wright and coworkers designed a capillary wick immunoassay containing up to five small capture

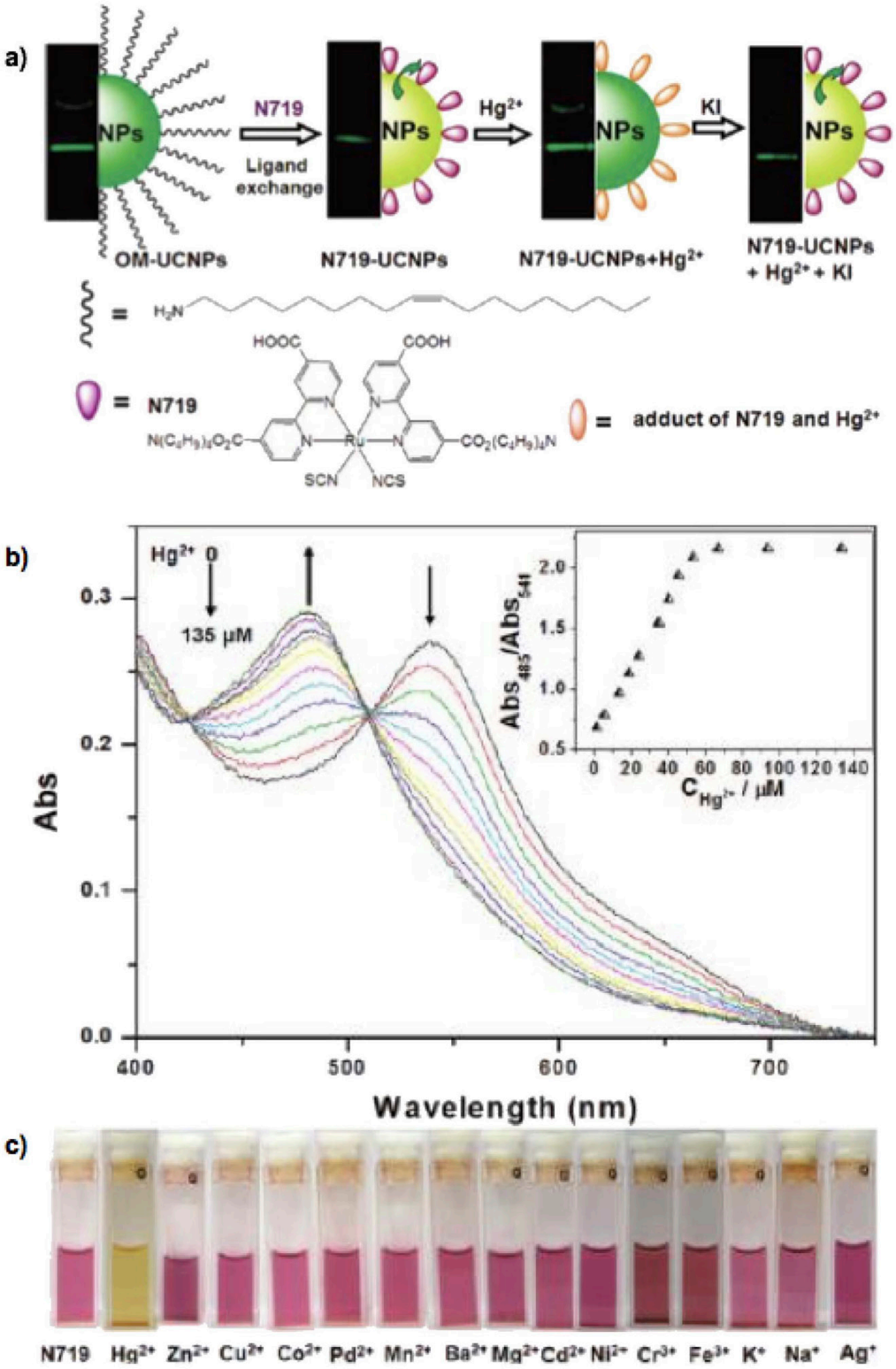

Fig. 7. Schematic representation of the sensor proposed by Liu et al. a) The UCNP functionalized with the complex N719-Ru(II) able to quench the green emission of the UCNP by LRET. b) UV–vis spectra showing the addition effect of Hg^{2+} that modulates the LRET luminescence of the UCNPs due to the blue-shift from 541 to 485 nm of the complex formed between N719-Ru(II) and Hg^{2+}. c) Cuvettes showing the color change of the aqueous solution of N719-UCNPs after the addition of different metal ions. Reproduced and adapted with permission from reference [50]. Copyright 2011 American Chemical Society. (For interpretation of the references to color in this figure legend, the reader is referred to the web version of this article.)

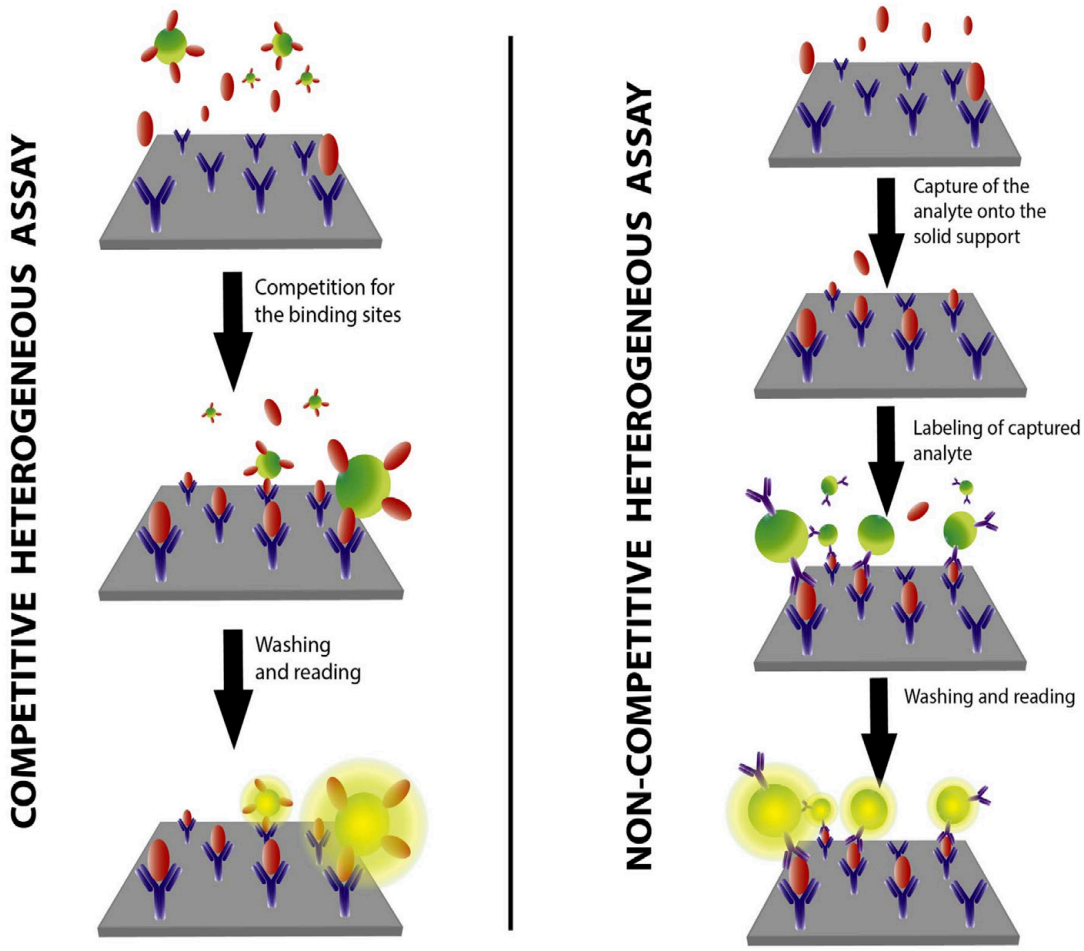

Scheme 1. Schematic representation of a competitive heterogeneous assay (left), and a non-competitive heterogeneous assay (right).

surfaces (each representing an individual assay spot to study variability within the test) for the detection of Staphylococcal enterotoxin B, which showed a sensitivity of 1 ng (10 ng mL^{-1}) [56].

The direct use of UCP as reporters in heterogeneous assays can improve their results, making them comparable to those from enzymatically amplified ones, like conventional ELISAs (Enzyme-Linked ImmunoSorbent Assays), where a measurable signal from a substrate is generated when the enzyme is present. For example, in a competitive heterogeneous assay for the detection of the anti-inflammatory drug Diclofenac, Hlaváček et al. obtained a limit of detection that was 5 times higher than the one obtained with an ELISA assay (170 pM compared with 34 pM) [59]. On the other hand, the direct detection when using UCNPs permits to avoid the enzymatic amplification step, making the assay quicker and more straightforward. In a highly sensitive non-competitive heterogeneous assay Sirkka and coworkers achieved to detect very small amounts of Cardiac Troponin I [60]. The use of a two-steps sandwich approach onto the bottom of microwells permitted to detect 3.14 ng L^{-1} of analyte (fM concentrations), while the calibration curve showed a linear behavior along 4–5 orders of magnitude. Up to now, this work shows to be one of the most sensitive heterogeneous immunoassays using UCNPs, while depicting the potential of these reporters for the direct detection of minute amounts of analyte when the non-specific binding of UCNPs labels is reduced. Although nowadays $NaYF_4$ is still one of the most commonly used host materials for upconversion processes due to its efficiency, new host matrices are continuously under study for the development of new upconverting materials. Ai et al. synthesized upconversion nanoparticles made of $NaScF_4$, with different sizes, and applied for the detection of avidin in a non-competitive heterogeneous assay [61]. They modified the surface of the nanoparticles with biotin while different concentrations of avidin were incubated in microplate wells for their further detection with the bioconjugated reporters. The assay showed a linear relationship between upconversion intensity and analyte concentration in the range of 0 to 9 nm, while exhibited a LOD of 180 pM. The early detection of biomarkers for diseases is of tremendous importance for in-time diagnosis and therapy. In a recent work, Huang and coworkers presented a biosensor for the detection of the β subunit of human chorionic gonadotropin. They synthesized core/shell UCNPs based on $LiLuF_4:Yb^{3+},Er^{3+}@LiLuF_4$ for their use as efficient upconverting bioprobes [62]. The resulting nanoparticles were conjugated with avidin, and used to detect the β subunit of human chorionic gonadotropin (β-hCG), after targeting the analyte with a biotinylated β-hCG antibody. The resulting LOD showed to be around 3.8 ng mL^{-1}. The possibility to carry out enzymatic amplifications of nucleic acids in order to increase the signal of a DNA target analyte, while using upconversion nanoparticles as reporters to improve the sensitivity and the signal-to-noise ratio, can be used to develop highly sensitive heterogeneous assays, as showed by Lan and coworkers [63].

After the catalyzed degradation of certain regions in a hairpin sequence by ExoIII, which was only possible when the target analyte (T1) was present to open the loop after hybridization, the remaining single stranded capture probes were able to initiate a long-range assembly of DNA concatamers (AP1 and AP2). These concatamers, in which DNA surface modified UCNPs participated by providing DNA sequences that

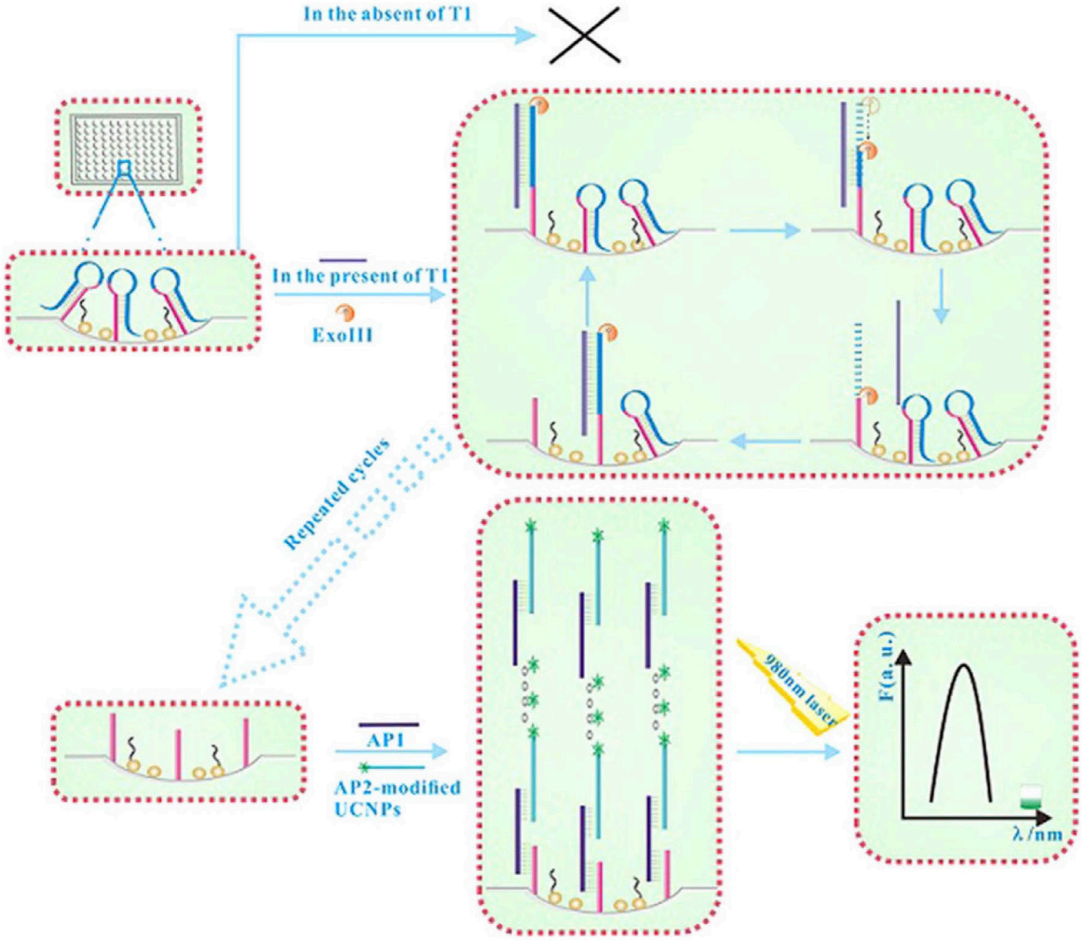

Fig. 8. Scheme of the designed biosensor based on dual signal amplification of Exo III for the detection of c-erbB-2 oncogene (T1). When T1 is present the first amplification is achieved with the aid of Exo III. The addition of two auxiliary probes AP1 and AP2 trigger the formation of super sandwich DNA concatamers which generate a strong upconversion luminescence signal when being excited at 980 nm. The detection of T1 is performed by measuring the intensity changes of the upconversion luminescence signal in the presence or absence of T1. Reprinted with permission from reference [63]. Licensed under CC by 4.0.

were necessary for the assembly (AP2) permitted to amplify the signal. At the same time, the target-specific catalyzed hairping degradation of the capture probes, which are grafted onto the bottom of microplate wells, allowed to selectively fix these concatamers to the solid support (Fig. 8). The assay showed high specificity and sensitivity, detecting aM concentrations of the target in spiked serum samples.

Among the different analytes that can be used in diagnostics, miRNAs are gaining importance as promising biomarkers for the detection of different diseases (e.g. Virus infections, Alzheimer disease or cancer), as they are present in serum at relatively high concentrations. Nevertheless, the detection of these biomolecules implies to face several challenges: Their small size (around 22 nucleotides) makes difficult to design successful probes for their amplification, while compromises their detection in hybridization assays because of their low melting temperatures. The latter, in turn, limits the stringency that can be used for their detection, while washing steps may be avoided or limited (i.e. using homogeneous assays). In addition, the efficiency of the miRNA isolation method from serum may compromise the detection in the assay and, as RNA is prompt to degradation, it would be desirable to reduce the total isolation and assay time. Taking this drawbacks into account, our group have very recently developed an heterogeneous assay for the sensitive detection of miRNA, in which the target is able to catalyze a DNA templated click-chemistry ligation also known as Strain promoted alkyne-azide cycloadditon (SPAAC) [64,65]. This target mediated reaction yields a covalent bond between 3′ Azide-modified oligonucleotides grafted to the surface of silica coated UCNPs, and 5′ DBCO-modified oligonucleotides (also containing a biotin modification at the opposite end), which are free in the solution (Fig. 9). The resulting biotin modified UCNPs are finally revealed by incubation in streptavidin coated microtiter wells. By this method, it was possible to use stringent and harsh wash conditions (e.g. Low ionic strength or high temperature), permitting to detect around 100 attomoles of target, while a linear range over four orders of magnitude was demonstrated.

Compared with planar surfaces, magnetic beads offer several advantages in heterogeneous assays [66,67]. First, the specific surface is higher than in a 2D solid support, which allows capturing an increased amount of analyte. The analyte is concentrated at the surface of the beads, as in normal 2D planar supports, so it is possible to achieve a high local analyte concentration. Second, although some processes like nucleic acid hybridization are kinetically impeded when carried out on solid supports compared with nucleic acid hybridizations in solution, their high surface area and 3D surface configuration makes this process less limited that in 2D planar surfaces. Third, the ability to magnetically manipulate the beads permits to quickly isolate, wash and concentrate the microbeads in a small surface. All these factors allow increasing the sensitivity of the assay, avoiding, in certain cases, the necessity of polymerase chain reaction (PCR) amplification. As an example, Wang et al. prepared magnetic nanoparticles and upconversion nanoparticles that were bioconjugated with DNA probes for the detection of a target DNA sequence. The possibility to capture the target sequences with the

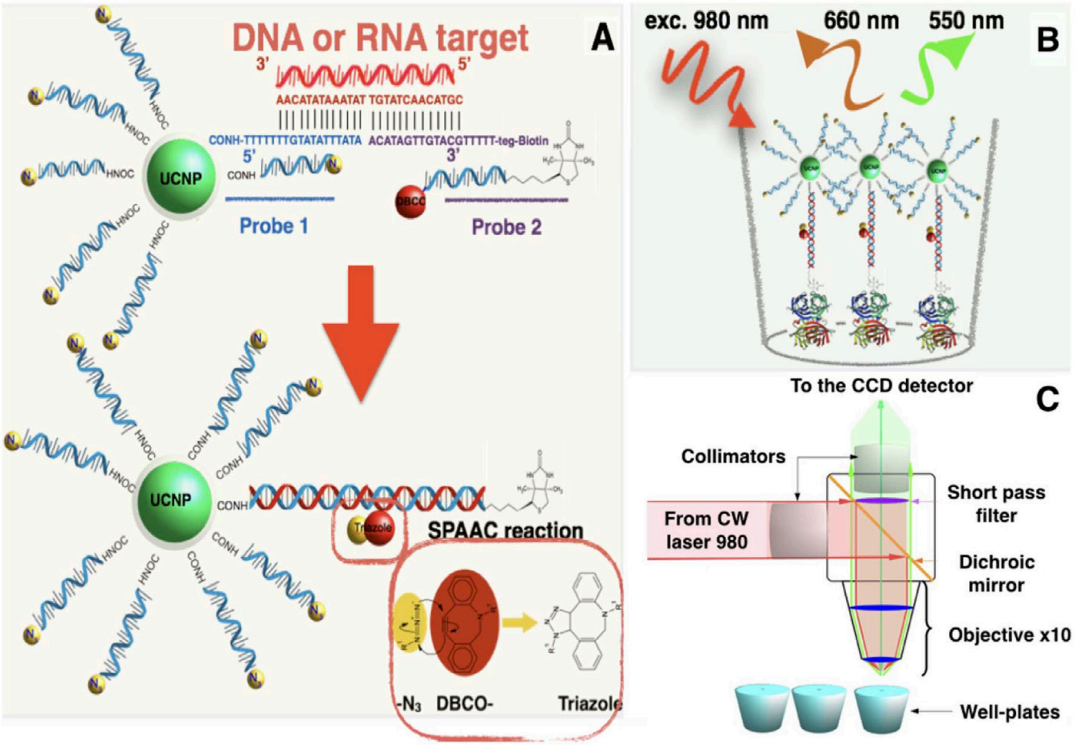

Fig. 9. General scheme of the click-chemistry based miRNA detection assay. A) SPAAC reaction mechanism between UCNPs functionalized with "3' Azide-modified oligonucleotide" and "5′ DBCO, 3′ biotinylated modified-oligonucleotide" in the presence of target miRNA. B) Incubation and detection of the biotinylated UCNPs in microwells after SPAAC reaction. C) General scheme of the microwell reader. Reproduced with permission from reference 65. Copyright 2017 American Chemical Society, Licensed under CC by 4.0.

magnetic nanoparticles, permitted to magnetically separate and wash them repeatedly, further hybridize the captured probes with the UCNPs for 12 h and ultimately wash and concentrate them again to improve the sensitivity of the assay. This approach allowed the detection of the DNA target in a linear range comprised between 7.8 and 78 nM [68]. Using a similar approach, Wollenberger and coworkers achieved to detect M13mp18(+) DNA sequences at pM concentrations using this kind of system [57]. In this work, they optimized the buffer that was used in the assays to improve the signal/noise ratio, aiming to obtain a sensitive and selective detection of the target. The components of the optimized buffer consisted of a mixture of Tris·HCl, $MgCl_2$, polyethylene glycol (PEG with Mn 6000 g mol^{-1} or 8000 g mol^{-1}) and sodium dodecyl sulfate. In another work, Li and coworkers used efficient core/shell upconversion nanoparticles in a similar system [69]. In this work, they synthesized $NaYF_4$:Yb^{3+};Er^{3+}@$NaYF_4$ nanoparticles with a core/shell structure which provided a 40-fold emission enhancement compared with the original cores (per unit mass). These UCNPs were then conjugated with an anti-CEA (Carcinoembryonic Antigen) antibody while magnetic beads were functionalized with the same antibody to carry out the sandwich immunoassays. After capturing the CEA antigen by the magnetic beads, and washing the particles several times, the anti-CEA modified UCNPs were added. After incubation, washing of label excess, and concentration of the resulting complexes, the assay demonstrated a linear range comprised between 0.05 and 20 ng mL^{-1} in buffer, and 0.1–20 ng mL^{-1} in human serum samples.

3.2. Arrays and multiplexed heterogeneous assays

The possibility to detect different analytes in a single assay is very attractive, since it can be used to measure simultaneously their relative concentrations and identify certain diseases or biological states that show specific analytical profiles (e.g. expression levels of miRNA). In addition, this simultaneous detection is interesting for screening applications, high sample throughput, and because its cost-effectiveness. There are several ways to carry out these heterogeneous assays, being the most common ones the spatial multiplexing using microarrays (where the detection of every analyte is delimited to specific spatial coordinates or "spots" in a solid support) and by spectral multiplexing (where the detection of different spectral signatures are associated to specific analytes with different fluorescent labels). This last strategy is commonly used in homogeneous multiplexed assays, where the detection is carried out directly from changes in the labels' spectra after mixing with a complex solution [70]. Upconversion phosphors are excellent candidates for their use in this kind of assays due to the emission of multiple and narrow bands, which can be used individually for the multiplexed detection of analytes. It is important to highlight that both approaches (microarrays and spectral multiplexing) can be also combined [71].

The use of UCP as labels can improve the sensitivity of microarrays, which is usually limited by the use of conventional fluorescent reporters. This have been demonstrated by van de Rijke and coworkers, who took advantage of the lack of autofluorescence of green-emitting UCP upon excitation with NIR light [7]. In this work they achieved a 4-fold greater sensitivity (allowing the detection of 1 ng μL^{-1} probe DNA), compared with Cy5 used as labels. In fact, the sensitivity of the system was limited only by non-specific hybridization and/or adsorption of the UCP reporters. The zero autofluorescence permitted as well to use relatively long integration times (5 min), which was necessary since a Xenon lamp was used as the IR excitation light source. Because the excitation of these green emitting UCP is based on a two-photon process, their emission will increase following a second power function with excitation energy, which would permit to improve sensitivity and scanning speed (i.e. reducing integration times) by using IR-emitting lasers.

The design of a single probe that perfectly matches within a

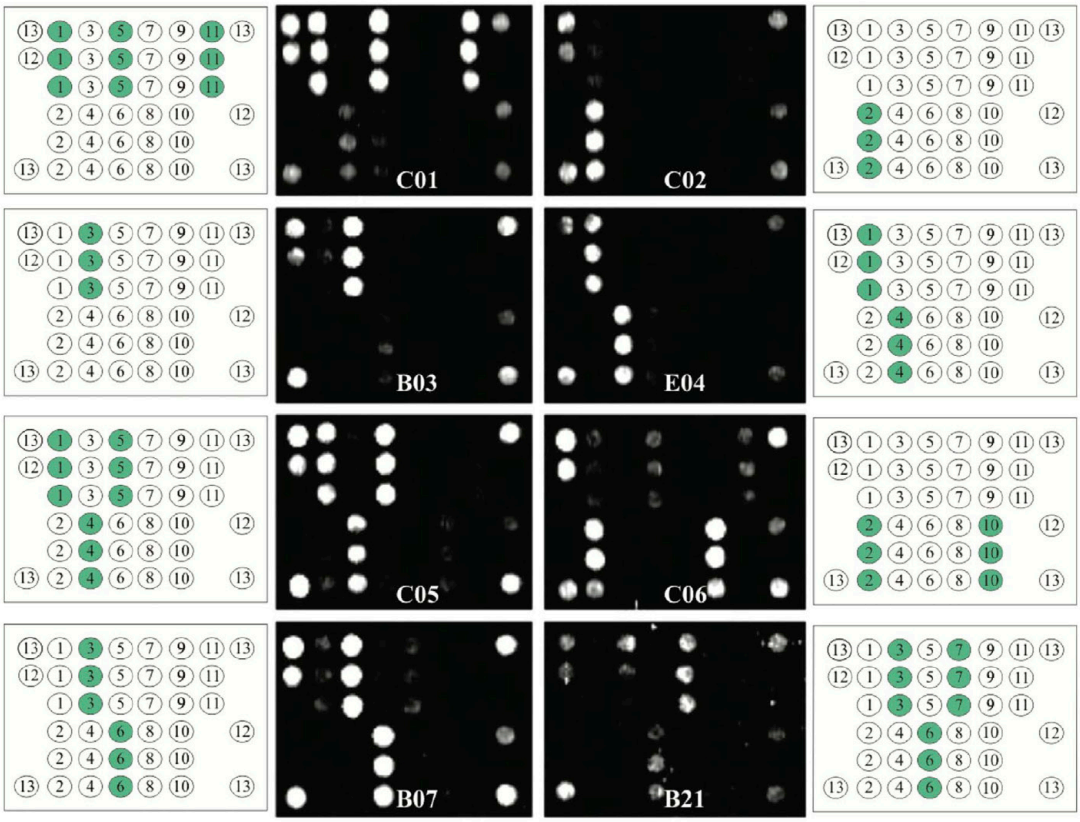

Fig. 10. Hybridization patterns of the different adenovirus genotypes tested on the array. The detection of each genotype results in a unique pattern that is displayed as a sort of "bar code". Reprinted with permission from reference 72. Copyright 2011 American Chemical Society.

microorganism's genotype for its complete identification is not a trivial task. In these cases, increasing the number of probes for targeting different genomic sequences by using a microarray-like assay can be the key to determine the presence of specific genotypes. Using this strategy, Ylihärsilä and coworkers were able to design an array-in-well assay to detect and genotype different human Adenoviruses employing UCP as labels [72]. First, genotype specific probes were printed at the bottom of microplate wells to build an array. Then, biotinylated Adenovirus genotype-specific amplicons were hybridized onto the array, and further revealed using UCP-Streptavidin modified labels (Fig. 10).

The spatial luminescence patterns produced by these multiplexed assays permitted to identify the different Adenovirus genotypes (Fig. 9). A correlation was found between the hybridization intensity from the array and the calculated thermodynamic behavior (ΔG) for the oligonucleotide capture probes. In fact, this is proposed as a useful rule to predict the behavior of oligonucleotide microarray probes. In this direction, this group also built a multiplexed serological array-in-a-well for the simultaneous detection of serum IgG antibodies against human Adenovirus and Parvovirus [73]. To construct the array, Human Parvovirus B19 virus-like particles, Adenovirus hAdV2, and hAdV5 hexon antigens were spotted at the bottom of microwells, together with positive and negative controls. UCNPs modified with anti-hIgG were used to reveal the presence of serum antibodies interacting specifically with the spotted antigens in the assay. Real serum samples from patients were used in the assays, and some of the samples were extracted at different infection times to study the evolution of the host immune response. The latter resulted in a time-dependent increase in the signal corresponding to IgG antibodies against B19 in acute phase infections. Another quantitative microarray was constructed by Päkkilä and coworkers, this time for the detection of prostate specific antigen (PSA), thyroid-stimulating hormone (TSH) and luteinizing hormone (LH) as models for a multianalyte detection assay [74]. The array was designed to work as a sandwich immunoassay: a monoclonal anti-PSA mouse antibody, a monoclonal recombinant anti-TSH antibody fragment, a monoclonal anti-LH and polyclonal rabbit anti-mouse immunoglobulins (which served as positive control) were printed as individual spots, while UCNPs were conjugated with the corresponding antibodies to reveal the analytes that were specifically captured at the array spots during the assay. Whole wells were used as reference for comparison with the array-in-well assay results, showing similar performance. The limit of detection and the dynamic range (about two orders of magnitude) were within clinically relevant ranges (except for the TSH), although the non-specific binding of the reporter limited the assay sensitivity. The authors also demonstrated the long-term stability of the performed assays storing them at 4 °C for up to 2 months, after which the signals were 96%, 99% and 100% of the original ones. Apart from spatial multiplexing, combining this strategy with spectral multiplexing can increase the information output in array-like assays, which is desirable from the point of view of assay time and sample consumption. Using this approach, Kale and coworkers were able to build a dual-mode array-in-well assay that was able to simultaneously detect serum IgG and IgM antibodies (which serve to distinguish between past infection and immunity, and acute infection, respectively) against influenza A and human adenoviruses, depending on the color and position of the upconversion signals on the array [71]. Two reporters were used, anti-human IgM coated blue emitting UCNPs, and anti-human IgG coated green emitting UCNPs, which demonstrated negligible cross-reactivity between their surface conjugated antibodies, and limited spectral crosstalk due to their narrow emission bands. Besides, as the excitation of the reporters occurs at the same wavelength (980 nm), it was possible to use just one excitation source, simplifying the required instrumentation for spectral multiplexing, which usually needs several

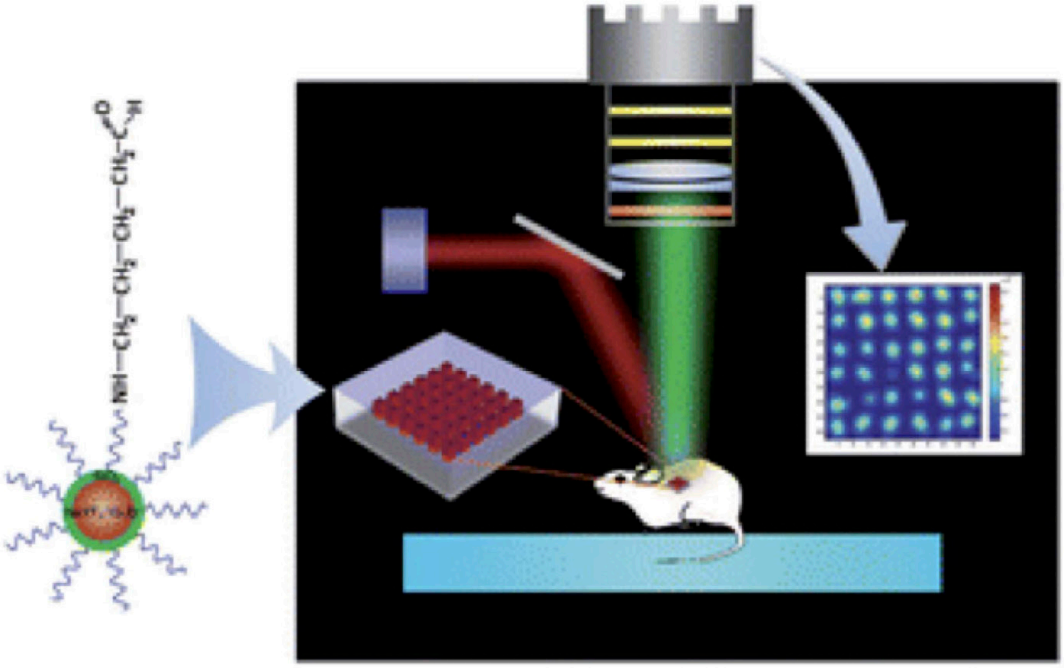

Fig. 11. Schematic representation of the in vivo imaging system using UCNPs and microarrays proposed by Li et al. Reprinted with the permission from reference [75]. Copyright 2013 Royal Society of Chemistry.

sources for the excitation of the different fluorophores. Microarray based assays are normally designed to work first extracting a sample from a living organism, and next analyzing it (i.e. the analyses are carry out in vitro). Nevertheless, a different approach has been evaluated by Li and coworkers [75]. As a proof of concept, they combined in vivo imaging with a microarray-like platform as a possible way to detect biomarkers inside the body, expecting to be applicable to the measure of altered cellular protein profiles in the tissue interstitial fluid. Different microarrays (containing UCNPs in 25 × 25, 50 × 50, and 100 × 100 μm micropits) were first tested in vitro using fresh skin of a Balb/c nude mouse, in order to study the feasibility to resolve the spots (Fig. 11).

The fluorescence images were de-noised using a signal enhancement algorithm, which permitted to resolve the 100 μm and most of the 50 μm micropits. To further improve the spatial resolution, an optical clearing agent, which consisted of a mixture of PEG-400 g mol^{-1} and thiazone, was used to treat the mouse skin in vivo in order to enhance its transparency. Under these conditions, they achieved to resolve the upconversion signals of a subcutaneous array of 25 × 25 μm spots.

3.3. Immunochromatographic and lateral flow strip assays

Lateral flow (LF) strips are assay formats in which a complex solution usually flows by capillary forces across a porous matrix like nitrocellulose. These assays achieve to separate and detect analytes through specific interactions with biomolecules (e.g. antibodies, enzymes or nucleic acids) that are previously immobilized at specific regions of the matrix. A lateral flow strip can be usually divided into four different regions: A "sample pad" (where the sample is dropped), a "conjugate pad" (containing a label and a receptor for the analyte), a "detection pad" (where the "test line" and "control line" are located) and an "absorption pad". As ideal point of care diagnosis and home test devices, LF assays fulfill the majority of the requirements, such as low cost, portability, low weight, fast diagnosis capabilities, good sensitivity and specificity, and the fact that do not require trained operators. Still, they present certain limitations yielding qualitative results (semi-quantitative if using reading devices) or issues concerning flowing capabilities due to parameters such as viscosity, obstruction of the matrix pores and non-specific adsorptions. Another drawback is the oversaturation by concentrated analyte solutions of receptors, due to the limited detection area, which can distort the results [76]. As the use of upconversion phosphors as labels could improve this field due, in part, to the minimal autofluorescence and high photo-stability, the demand for devices that permit to read upconversion based assays have prompted the construction and implementation of UCP readers [77,78]. These optical readers have permitted to expand the advantages of these labels to LF assays, contributing to solve some of the limitations of this technique, like permitting to quantify the analyte along a rather wide dynamic range (e.g. 3 orders of magnitude), improving the sensitivity compared with other labels, making possible to carry out multiplexed LF assays, or removing the need to read the assay immediately after carrying it out while permitting to do it anytime after [79–81]. Taking into account the features of LF devices, their application to pathogen-specific nucleic acid detection shows great interest, as it can be more advantageous in certain circumstances than antigen/antibody determination. Corstjens et al. used upconverting phosphors in a LF assay for the sensitive determination of human papillomavirus type 16 (HPV16), which is a screening marker for the detection of cervical cancer [79]. Two approaches were compared: one for quick screening, based on a PCR amplification step to yield haptenized amplicons for direct detection with the LF device, and another one in which not haptenized amplicons were specifically hybridized to haptenized probes and finally revealed. Results showed that patients who led to positive signals in the screening approach were correctly diagnosed while the ones that fell into the established cutoff values (i.e. indeterminate result) were further properly diagnosed by using the second approach. The detection limit of the first method was about 2000 copies of HPV16 per 10 ng of total DNA extracted from cells, whereas the detection of 10 pg of target (c.a. 30 attomoles) was possible by the second approach. The possibility to adapt these assays to direct pathogen detection, bypassing the requirement of PCR amplification, is very appealing for point of care diagnosis, otherwise impossible without properly equipped laboratories. Thus, Zuiderwijk et al. were able to use the high sensitivity given by up-converting phosphors for the direct detection of

S. pneumonie [82]. In this work, genomic DNA from the bacteria was isolated and digested with *Alu* I to generate two specific DNA fragments. To improve specificity and sensitivity each single strand from each fragment was made to hybridize with two different probes, one labeled with a digoxigenin (Dig) hapten and the other with a biotin hapten, both at 5′ end, which yielded four dual-labeled fragments. After hybridization, the fragments were labeled with anti-Dig-functionalized UCP, and these samples were applied to the lateral flow strips. Results showed that it was possible to detect the targeted fragments using only 1 ng of S. pneumoniae DNA.

In another work, direct detection of ssDNA was achieved mimicking non-optimal field laboratory conditions (i.e. using ambient temperature hybridization) [83]. Capture probes were covalently grafted onto UCPs and used, together with another biotinylated probe, to specifically hybridize with the target. As a sandwich-like hybridization was required from the two probes with the same target strand for the detection, specificity of the results were ensured. The hybridization step, the LF assay plus the read out required a minimum of 20–30 min, while exhibiting a LOD of 100 amol of target (3 pg). LF assays have demonstrated not being limited to the detection of just macromolecules like proteins or nucleic acids. Instead, they can be used to detect much smaller or bigger analytes as well, such as drugs or even bacteria. In this direction, core/shell UCNPs have been used as smaller and efficient reporters to detect the antibiotic cephalexin [84]. A visual detection limit of 10 ng mL^{-1} was achieved, while a sensitivity close to 0.6 ng mL^{-1} within a linear detection range from 0.5 to 100 ng mL^{-1} was obtained with further quantitative analysis. Despite yielding similar results as a LF assay based on gold nanoparticles, the advantages coming from the minimal autofluorescence when reading out up-conversion emissions are expected to outperform the results from gold nanoparticles in complex biological samples. Niedbala et al. used blue and green emitting UCPs to design a multiplexed LF strip containing up to 12 spatially separated test bands to detect different drugs, simultaneously, from saliva as biological fluid (Fig. 12) [85]. The detection limit was found to be less than 5 ng mL^{-1}. In the same work, another LF assay was design, this time to detect bigger analytes, like the bacteria strain *Escherichia coli* O157:H7. It was possible to determine the presence of this strain in a background of 10^9 other organisms mL^{-1} of culture medium. This assay could distinguish 10^3 organisms mL^{-1} with a 95% confidence in just 10 min.

In another study, a fluorescence signal that was proportional to the concentration of bacteria that was present in the original samples (*Vibrio anguillarum*) was obtained along seven orders of magnitude ($2{\cdot}10^3$ – $2{\cdot}10^9$ CFU mL^{-1}) [86]. The LF assay seemed to be very specific to *V. anguillarum*, while showing a detection limit close to 10^2–10^3 CFU mL^{-1}. The application of the LF-upconversion technology for the diagnosis of neurocysticercosis using patients' serum has been recently investigated by Corstjens and coworkers [87]. This assay consisted in detecting antibodies that showed reactivity with bacterial-expressed recombinant antigen (r) T24H. In this work, Protein A (which shows affinity for antibodies' Fc region) was covalently grafted to UCP (400 nm) and UCNPs (40 nm), and their performance in the assay was compared; given the assumption that the smaller the particles are, the fewer the capture molecules they will need to successfully bind to the test line. UCP particles were made of $Y_2O_2S{:}Yb^{3+}$, Tm^{3+} and coated with a silica shell, while the UCNPs $NaYF_4{:}Yb^{3+}$, Er^{3+} were coated with poly-acrylic acid (Fig. 13).

Their emission intensities were practically the same per unit mass upon NIR excitation. Under the selected test conditions, the obtained results suggest that the use of UCNPs increases the signal strength in the 1–10 units range (regarding quantification of infection grade). Nevertheless, the differences were not significant and a silica coating instead of poly-acrylic acid was suggested as a way to further improve the performance of the 40 nm UCNPs. The authors highlight that the use of control groups (healthy individuals) with different cultural behavior/ethnicity, as well as the use of banked serum samples collected, pre-treated and stored at different locations, might affect the analytical sensitivity of these assays. The LF assay together with the lightweight LF strip reader are presented as a good alternative to current methods for the point of care diagnosis of neurocysticercosis. In addition, the authors point out the use of finger-stick blood or saliva as direct and less invasive biological samples to explore, aiming at field-testing.

Urine stands out as another desirable biological fluid to be analyzed by UCP based LF assays since it is present in large volumes and can be obtained in a non-invasive way. As an example of the possibilities of this biological fluid, in a recent work the sensitivity of a urine CAA (worm circulating anodic antigen) LF assay for the detection of Schistosoma infections have been improved, using a urine concentration strategy [88]. Instead of running directly 20 μL of sample (from 10 μL urine), larger volumes of urine (0.25 mL and 2 mL) were concentrated to 20 μL and then the assay was performed and compared. This step allowed the detection of 0.3 pg mL^{-1} of CAA (from 2 mL urine) and increased the clinical sensitivity from 44% to 98%. As described along this section, multiple examples demonstrate the

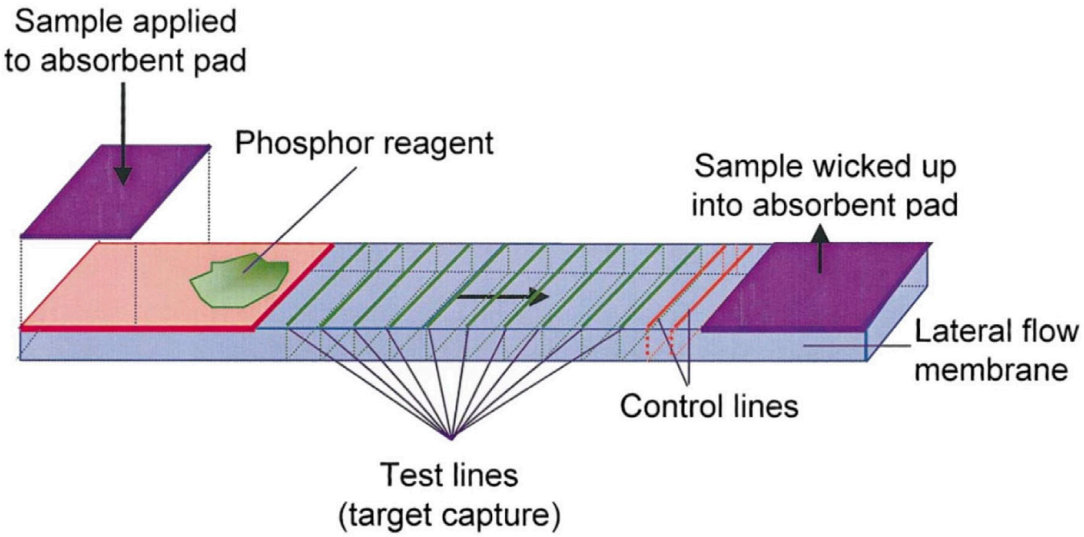

Fig. 12. Schematic illustration of the multiplexed lateral flow strip containing up to 12 spatially separated test bands to detect different drugs simultaneously and based on upconversion phosphors. Reprinted with the permission from reference [85]. Copyright 2001 Elsevier B. V.

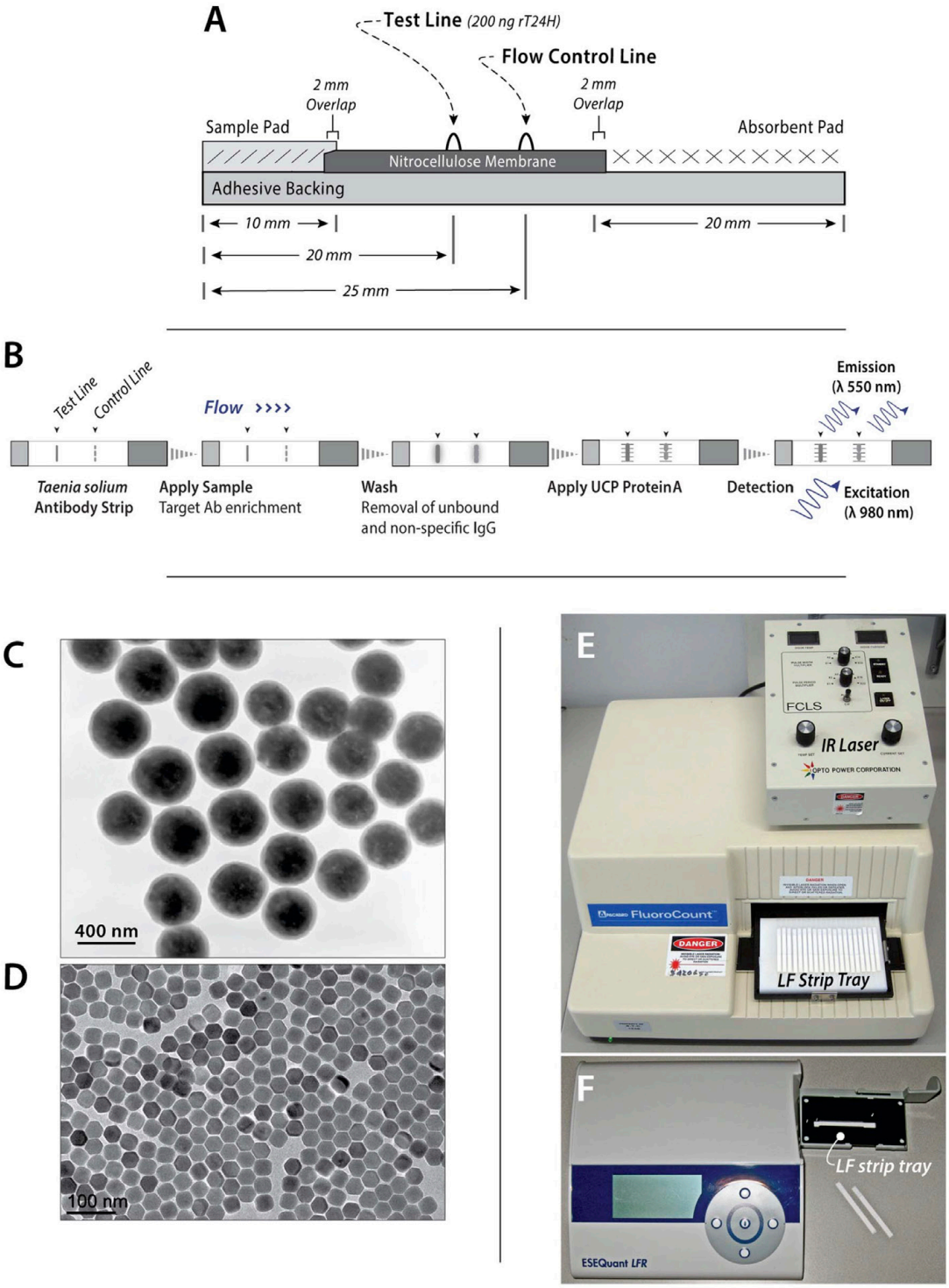

Fig. 13. A) and B) illustrate the lateral flow strip assay for the detection of recombinant antigen (r) T24H. C) TEM image of the UCPs, D) TEM image of the UCNPs. E) and F) Instrumentation used for the lateral flow strip assay. Reprinted from reference [87] with permission of the Creative Commons CC0 public domain dedication.

applicability of LF strips to the detection of proteic targets, nucleic acids, drugs/therapeutics or even direct pathogens. Upconverting materials have alleviated some of the drawbacks that were inherent to this technique (e.g. sensitivity and quantification of analytes along a wide dynamic range) while demonstrating real applicability in non-optimal/field laboratory conditions [87–89]. Advantages such as robustness, or not requiring to keep assay reagents refrigerated, as well as other previously commented features from LF strips, augur an optimistic future for this kind of upconversion based assays, specially taking into account the development and improvement of upconversion readers [90]. Nevertheless, requiring these kind of devices to read the strips is certainly accompanied with an increase in the overall price of the technique. There will be cases when requirements like high sensitivity or robustness will be mandatory (e.g. early stage detection of HIV, Zika,

Ebola), or when the volume of assays to be analyzed will be high enough to compensate the investment. On the contrary, other techniques may be better cost-effectively suited. However, as promising as results from UP incorporation into these platforms are showing, the development of smaller, lighter and cheaper readers may worth to be researched in order to alleviate this initial investment.

3.4. Microfluidics based sensors

Microfluidics refers to the control and manipulation of fluids at microliter or lower scales. It is a very wide field in which many disciplines meet (e.g. Physics, Nanotechnology, Engineering, Biochemistry) to design systems in which low volumes of fluids are controlled and processed by different means to achieve detection, automation, multiplexing, and high-throughput screening. In these systems, fluids are normally made to flow as droplets, separated, mixed, incubated and/or analyzed depending on the specific application the device is aimed to. To achieve all of this, different components like microvalves, microchannels, microfluidic mixers, and others are usually integrated in these devices. As a very general classification, attending to how fluids are made to move within these systems we could distinguish between active microfluidics (e.g. in which certain components such as micropumps are used) or passive microfluidics (e.g. using capillary forces). Development of microfluidics technologies is deeply impacting fields related to biomedicine, molecular biology and clinical pathology as the automated integration of assay operations, the detection of biomolecules such as DNA or proteins, and applications such as point-of-care (POC) diagnosis using small sample volumes start to be a reality by employing devices based on this concept [91,92]. Joining this technology with the advantages of using UCPs as reporters translates in the development of even more promising POC devices. For instance, the possibility to automate and couple together different laboratory operations such as DNA extraction, amplification, labeling and detection have been addressed by Chen and coworkers using a microfluidic system and UCP labels for the detection of *B. cereus* in saliva as pathogen model [93]. In this work, the device was designed as a credit-card sized plastic cassette, which contained the microfluidic components that worked as follows (Fig. 14): first, the sample is introduced in the loading port, and then aliquoted in a metering chamber, where it is subjected to two different lysis steps. Then, the lysate is made to move through a porous silica membrane, where the chaotropic salts from previous steps induce nucleic acids to bind to the membrane. After that, they are rinsed with ethanol-based solutions to remove the debris, and further desorbed from the silica membrane. Subsequently, an aliquot is mixed with PCR reagents and sealed in a PCR chamber where is thermally cycled. Finally, the resulting amplicons are labeled with avidin-conjugated UCP particles, applied to the sample pad of a LF-strip, captured by immobilized anti-DIG antibodies at the test line and scanned by an UPlink™ reader. The use of this system made possible to detect ca. 10^6 cells mL^{-1}.

In a more recent work, they developed a versatile and disposable microfluidic cassette for the detection of nucleic acids from bacteria or viruses using unprocessed samples of body fluids, or other liquids [94]. It performed automatically the sample lysis, nucleic acid extraction, concentration, purification, amplification and detection using UCP technology. The cassette included pouch-based liquid storage (for minimizing cross-contamination), valves, reaction chambers for fluid pumping, lysis and solid-phase nucleic acid purification as well as thermal cycling, dry storage of reverse transcription polymerase chain reaction (RT-PCR) reagents (depending on the cassette), lateral-flow strip for detection and waste storage. The microfluidic system was made to work by an analyzer, which compressed the cassette's pouches in a controlled manner for liquid dispensing, and actuated the valves to control the flow. It included as well thermoelectric units for the PCR chamber, heaters, a vibrator for mixing, a vacuum pump and a microprocessor to time and control the sequence of operations. The performance of the system was tested with saliva samples containing *B. cereus* bacteria to demonstrate the DNA detection capabilities. To demonstrate its performance for RNA detection, samples with Armor RNA HIV, and a few experiments with saliva samples containing HIV virus, were carried out. Under these conditions, the automated system permitted to detect down to 1000 pathogen particles in the sample. The integration of different analyses simultaneously in a same microfluidic automated system can be of clinical interest when there exist the possibility of various infections (e.g. opportunistic pathogens in HIV) that could be assayed in a single test [95]. The construction of these kinds of devices opens new possibilities for multiplexing, not only for the one-assay detection of different pathogens, but for the simultaneous detection of analytes of different nature that belong to the same microorganism. Quick tests for appropriate screenings are available for many infectious diseases, but they usually require a second confirmatory test, which usually demands well-equipped facilities. Besides, as a second visit to the clinic is required, patients often do not carry out this confirmatory test. Having this in mind, Chen and coworkers developed a POC microfluidic device that combined a HIV screening serological diagnostic with a nucleic acid detection confirmatory test using saliva as biological fluid [96]. The dual-path prototype has a modular design aiming to gain versatility accommodating different on-demand disease targets. After loading the saliva sample with an oral collector, an aliquot of phosphate buffer saline (PBS) diluted saliva is transferred to a compartment and further mixed and diluted with an assay buffer while flowing to an antibody detection LF strip. After that, a second flow step takes place for washing the strip, and finally a third flow step containing UCP reporters coated with Protein A is carried out for the antibody detection. These three steps LF-protocol is known as consecutive flow (CF). Simultaneously, the remaining diluted saliva sample is processed in a similar way as previously described for the automated RNA detection using cassette-like microfluidic devices, and finally detected by CF protocol. The serological results were available in less than 30 min, while the confirmatory test took another 60 min. As showed in this section, microfluidic devices can be adapted to carry out a plethora of different processes that can facilitate and save time in essential assay steps, such as isolation, purification and detection. The application of these advantages to circulating tumor cells isolation has been explored by Wang et al. [97] Their strategy consisted, first, in conjugating magnetic and upconversion nanoparticles (MUCNPs) with anti-EpCAM (Epithelial cell adhesion molecule) antibodies for the specific recognition of tumor cells in blood samples. Next, the cells were washed to remove unbound MUCNPs, suspended in PBS, and further applied to a microfluidic silicon nanowire array under the influence of a magnet to separate the labeled cancer cells from the whole blood. PBS was used again to wash the microfluidic chip twice, and finally the presence of cells was analyzed measuring the upconversion signals. The captured cells could be later released for further analyses, re-cultured, or stained for imaging. This system was applied to test lung cancer in real clinical samples, achieving very good consistency with clinical outcomes (staging) (Fig. 15).

4. Nanoprobes based on upconverting nanoparticles

During the past few years, considerable work has been done to find potential applications of UNCPs in the field of nanotechnology, which demonstrates their flexibility as reporter for sensing applications such as oxygen, ammonia, and temperature measurements [98]. Nanotechnology has provided new tools and materials to sense different analytes. The temperature measurement of a single living cell is not an easy task, and an alternative method to sensing temperature is to use luminescent nanoparticles whose emission band shape, peak position, intensity, or lifetimes can be affected by temperature [99–101]. In this context the work presented by Vetrone et al. demonstrate for the first time the possibility to determine the temperature of a single living cell in solution, as well as in HeLa cancer cells [102]. The accurate

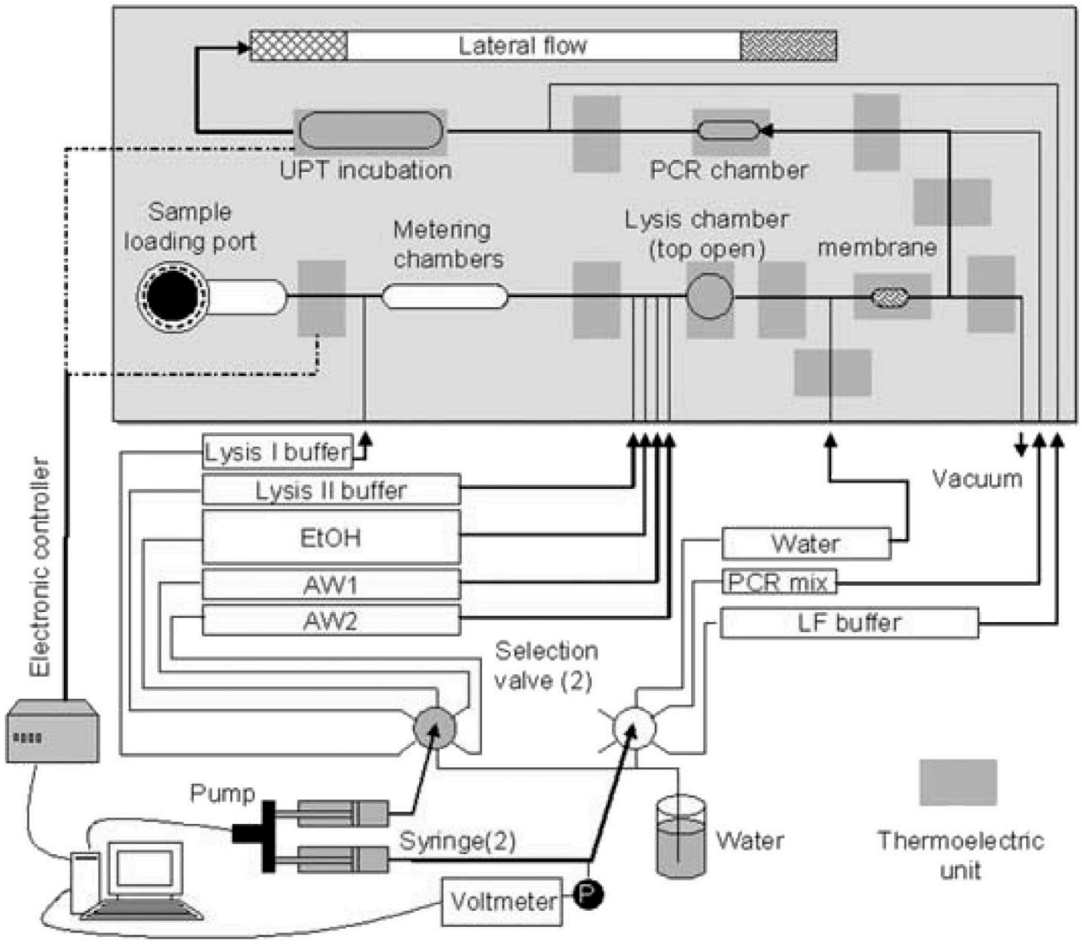

Fig. 14. Schematic representation of the microfluidic based sensor proposed by Chen et al. for the detection of *B. cereus* in saliva. Reprinted with permission from reference 93. Copyright 2007 Wiley-VCH Verlag GmbH & Co. KGaA.

determination was done using a nanothermometer based on the temperature-sensitive emission of $NaYF_4$:Yb^{3+},Er^{3+} nanoparticles. In fact the intensity ratio of the green emission bands of Er^{3+} changes with the temperature and thus was used to obtain thermal profiles created by heating a solution of UCNPs by means of confocal fluorescence [102,103].

Chen et al. proposed a more recent and advanced nanothermometer [104]. They generated a hybrid complex made of UCNPs and a rhodamine dye molecule that improved the temperature sensitivity of the complexes due to resonance energy transfer whose efficiency was temperature dependent. Dye molecules possess a stronger temperature-dependent absorption and emission than rare earth ions, so these hybrid complexes exhibited better sensitivity than pristine UCNPs to temperature measurements. Xiao et al. proposed a hybrid complex system based on LRET. They linked UCNPs as donor and Au nanoparticles as acceptor with the thermal responsive polymer poly(N-isopropylacrylamide) (PNIPAM) as a spacer between them in order to modulate the distance. PNIPAM possesses a lower critical solution temperature of 32 °C with a reversible phase transition from a hydrophilic swollen state to a hydrophobic collapse state [105]. The collapse/swollen state of the PNIPAM chain regulates and tunes the distance between the donor and acceptor, causing the emission quenching of the green bands of the UCNPs through the modulation of the energy transfer efficiency [106].

Another example of the versatility of UCNPs as sensing platform is represented by the work published by Mader and Wolfbeis [107]. They developed an ammonia sensor based on the green emission of UCNPs of $NaYF_4$:Yb^{3+},Er^{3+} and the pH probe phenol red immobilized in a polystyrene matrix. The sensor exploited the inner filter effect of the dye and it was insensitive to the pH changes because the UCNPs were coated with the polystyrene matrix that was impermeable to protons or hydroxyl groups. By contrast, ammonia was able to penetrate the polystyrene matrix and the exposure of the system to ammonia causes a strong increase in the absorption of the pH probe phenol red at 560 nm that exerts an inner filter effect over the green emission of the UCNPs. On the other hand the red emission of the UCNPs remains unaffected and was used as internal control. The ratio between the intensity of the green and red band emission was used for the quantification of the ammonia. One of the biggest advantages of the use of 980 nm as excitation source is that the obtained signal was free of background of visible luminescence of the sample and scattered light, which can be highly advantageous for the sensing of ammonia in complexes matrixes. Upconverting materials can be also used as optical biosensors for oxygen detection. An oxygen sensor based on this kind of technology presents some attractive features such as no oxygen consumption, fast response, easily miniaturized. In general, the sensor is based on the dynamic quenching of the luminescence by molecular oxygen, and the degree of quenching is related with the amount of oxygen [1]. Presley et al. combined UCPs made of Y_2O_2S:Yb^{3+},Tm^{3+} with a complex of tris-(4,7-diphenyl-1,10-phenanthroline) ruthenium(II) dichloride ($Ru(dpp)_3Cl_2$) [108], which is one of the most widely used luminescent oxygen-sensitive molecules [109]. The $Ru(dpp)_3Cl_2$ complex was indirectly excited by the $^1D_2 \rightarrow {}^3F_4$ and $^1G_4 \rightarrow {}^3H_6$ Tm^{3+} upconversion emission. The bilayer configuration of the sensor has thickness of μm

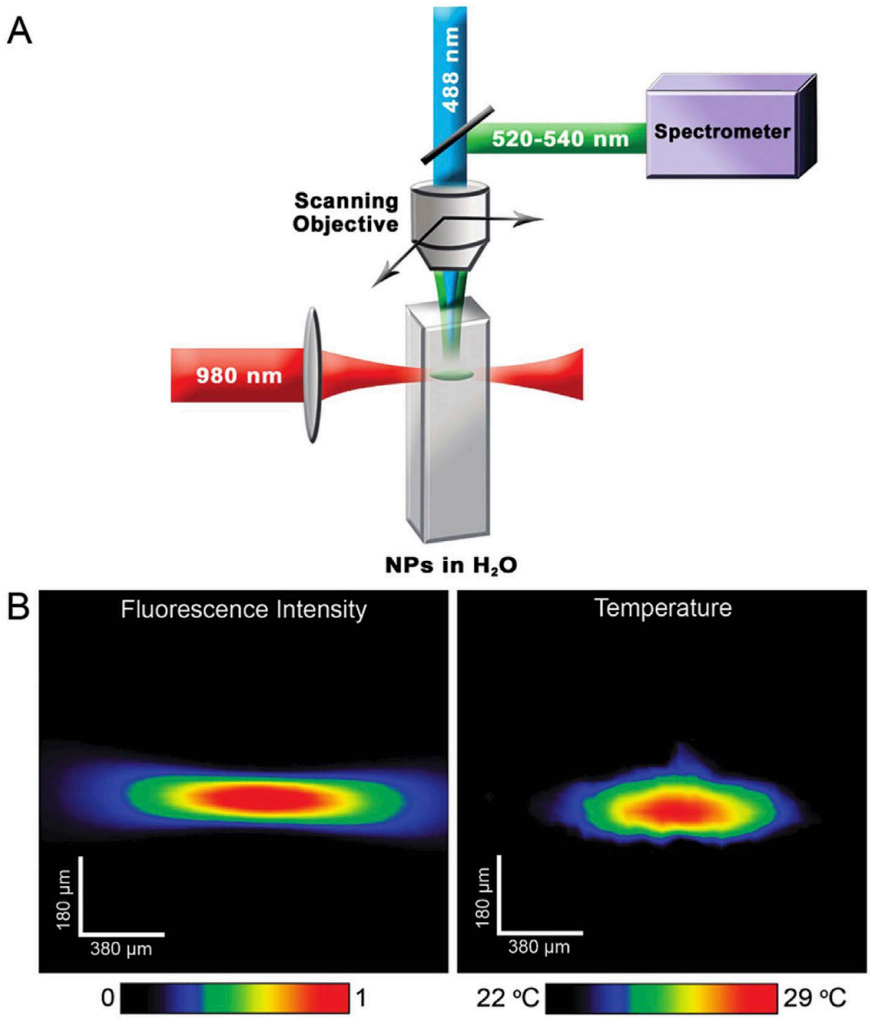

Fig. 15. (A) Schematic illustration of the setup used by Vetrone et al. to measure the temperature profile. (B) Confocal image of the upconverted luminescence (left), and thermal image of the spot created by the 980 nm pump beam (right). Reprinted with the permission from reference 102. Copyright 2010 American Chemical Society.

that hampers the possibility of LRET, which takes places within 10 nm. For this reason they proposed a handshake interaction between UCPs and the oxygen-sensitive complex $Ru(dpp)_3Cl_2$ to explain the local stimulation of these oxygen-sensitive molecules by the UCPs following external NIR excitation. The excited Ru(II)* complex was effectively quenched by O_2 and the emission of the Ru(II) complex was found to vary between exposure to pure N_2 and O_2 conditions with a very fast response time of only 0.118 s.

5. Brief comparison with other reporters, commercial potential of upconversion-based assays, and toxicity of upconverting nanoparticles

Despite the previously exposed potential of upconverting reporters in sensing, it is true that literature is missing a higher number of comparative studies with well-established detection techniques. Although some works can be found on this regard [81,110], showing promising results, more studies need to be focused on this subject in order to assess in a more accurate way at which point research on upconverting bioassays and sensing platforms is, and how far new improvements can be realistically expected to advance the field while allowing to see this technology finally introduced into the clinical practice. In an effort to compare the state of the art of upconversion-based assays with current luminescent and colorimetric assays, different reporters were compared with upconverting labels within the same detection platforms to try getting an objective picture of their impact and performance (Table 1).

As shown in Table 1, platforms using upconverting reporters give results comparable to the best labels under research found in literature for the reviewed analytes, and in some cases outperform commercially available systems, or are close to the LODs of well established "gold standard" techniques. It is important to highlight that detection using UCNPs is normally carried out in a "direct" and straightforward way, while several techniques included in the table are based on amplification strategies. Upconverting biolabels are a relatively new technology that, in a little more than a decade of research since the first efficient upconverting nanocolloids were developed [122], rival the performance in bioassays of reporters such as quantum dots or amplified detection techniques such as ELISAs. While the commercial and clinical potential of this technology seems obvious, there are a few reasons that explain the slow exploitation and incorporation into the clinical practice. The nature of the upconversion process, together with the requirement of a 980 nm high power excitation source, implies that most of the commercial instrumentation normally used to read common fluorescence based assays (e.g. plate readers) are not compatible with the upconversion technology. This may be due to the optical setup of the device (e.g. short pass filters instead of the long pass filters are required to collect the visible upconverted emissions), the absence of an adequate excitation source, or other particular reasons [123]. Lacking this basic instrumentation not only hampers the incorporation and application of upconverting materials into different fields, but it slows down their investigation and development at the research level as well.

Table 1
Comparison of Upconversion based assays performance with different label technologies on the detection of the same analyte within similar detection platforms.

Analyte	Reporter	Platform and detection method	Sample type	Dynamic range	LOD*1	Ref.
cTnI*2	UCNPs	Solid support (microwell) Direct	Plasma	4–5 orders of magnitude	3.14 ng L^{-1}	Sirkka et al. [60]
cTnI*2	FITC (Metal enhanced fluorescence)	Solid support (glass slide) Direct	Buffer and whole blood	3 orders of magnitude	5 ng L^{-1} (buffer) and 50 ng L^{-1} (whole blood)	Aslan et al. [111]
cTnI*2	Eu^{III} polystyrene nanoparticles	Solid support (microwell) Direct	Plasma	4 orders of magnitude	2 ng L^{-1}	Järvenpää et al. [112]
cTnI*2	UCNPs	Lateral flow Direct	Serum	3–4 orders of magnitude	41 ng L^{-1}	Juntunen et al. [113]
cTnI*2	ELISA	Lateral flow Amplified	Serum	2 orders of magnitude	27 ng L^{-1}	Cho et al. [114]
cTnI*2	Gold NPs	Lateral flow Amplified	Serum	–	10 ng L^{-1}	Choi et al. [115]
Hg^{2+}*3	UCNPs	Quenching FRET Direct	Tris-HCl Buffer	3 orders of magnitude	100 ng L^{-1}	Liu et al. [40]
Hg^{2+}*3	Ag clusters	Quenching Direct	Ammonium acetate buffer	2 orders of magnitude	$1{\cdot}10^3$ ng L^{-1}	Guo et al. [116]
Hg^{2+}*3	Carbon nanoparticles	FRET Direct	Lake water spiked-in with Hg^{2+}	2 orders of magnitude	46 ng L^{-1}	Lu et al. [117]
Pb^{2+}*4	UCNPs	FRET (solution) Direct	Tris-HCl Buffer	5 orders of magnitude	$4{\cdot}10^3$ ng L^{-1}	Zhang et al. [52]
Pb^{2+}*4	Graphene quantum dots	Quenching (solution) Direct	River water Spiked-in with Pb^{2+}	2 orders of magnitude	$14{\cdot}10^3$ ng L^{-1}	Dong et al. [118]

*1 LOD defined as the 0 target concentration signal + 3-fold its standard deviation, *2 LOD of most sensitive current cTnI commercial assay using solid support (beads) is 6 ng L^{-1}. [119] *3 LOD of Hg^{2+} using the cold vapor fluorescence atomic spectroscopy is 0.5 ng L^{-1}. [120] and *4 LOD of Pb^{2+} using inductively plasma coupled mass spectroscopy is 470 ng L^{-1} [121].

The presence of this instrumental gap on the market demands an additional effort from the researchers committed to this task, which are often forced to build their own custom made instrumentation. As the outcome of research carried out with different setups may be sometimes hardly comparable (especially if not all the details from the setup are specified), a reduction in results robustness is also encountered, which slows down the development of the field from the very first steps.

Besides the lack of technology that limits the application of UCNPs, another critical issue that limits their commercial application is the assessment of the UCNPs toxicity. In fact, the increased number of potential commercial applications based on UCNPs raised the important question about their toxicity. To date numerous studies report negligible or low toxicity of UCNPs [124–127]. Nevertheless, their use in vivo is still questionable as pointed out in a recent review published by Gnach et al. [128]. They tried to elucidate the potential toxicity of this kind of nanoparticles, however, after an extensive literature review they were not able to conclude that UCNPs are without health risks. In addition there is a lack of complex long-term (i.e. a few animal generations) toxicity. There is also a need to understand how and where the UCNPs accumulate, and what time is indispensable to clear the NPs from the various organs (e.g. liver, spleen, lungs). The lack of systematic fundamental research on the toxicological aspects of UCNPs may be one more reason to explain the delay on their commercial exploitation.

6. Summary and outlook

In summary, among all the desirable characteristics that should exhibit an ideal reporter, compared with other kinds of labels, upconverting materials outstand in many of these features. First, the great anti-Stoke shift that exists between the wavelength used to excite the upconverting material, and their highly characteristic discrete emissions is long enough to avoid any noise from the excitation source during the signal detection. In addition, the high photostability of upconverting materials makes possible to use extremely high excitation power densities due to their lack of photobleaching or blinking, which would be inconceivable for other reporters. Second, as biomolecules are unable to carry out upconversion processes, this results in minimal autofluorescence, thus being the non-specific absorption of the upconverting reporter the only source of background signal. Third, their characteristic and discrete emission bands can be tuned to obtain distinct emission spectra, which in turn can be used to widen their applications and possibilities as reporter libraries. All these features have been experimentally demonstrated by numerous works and exposed in this review, showing how in a few years they have been investigated and incorporated in new and pre-existing sensing platforms. Upconverting materials have demonstrated to improve the sensitivity and photostability of LF-strips and other POC detection devices, simplified and extended the possibilities of multiplexing as well as homogeneous assays using and tuning their emissions, as well as achieving low LODs in a multitude of sensors and assays.

Despite their numerous advantages, in the last years several works have raised some concerns regarding their use as biolabels that need to be addressed when reliable and sensitive assays are targeted. One limitation is the solubility of the particles in water when a low concentration of UCNPs is used as reporters in the assays (i.e. pursuing better sensitivities). Their use at low concentration, if we also consider their high surface area, translates into the partial dissolution and reduction of the upconversion signal, until the solubility equilibrium is reached. The effects of particle dissolution can be alleviated by taking advantage of the common-ion effect, but still, this limits the conditions in which the assays may be developed. In addition, when a low concentration of UCNPs is used in phosphate buffer even the common ion effect has no longer influence on the colloidal and chemical stability of these nanoprobes. Thus, extra care must be taken into consideration to decide which buffers and chemicals may be used during the assays, in order to avoid those that could harm these reporters. As non-specific binding is practically the only source of background noise in upconversion based assays, a deeper research on surface chemistry aiming to enhance the specific recognition of analytes by the upconverting material, while minimizing the non-specific adsorption of the reporters, may be a way to improve the performance of current assays using this

technology. In fact, non-specific binding of upconverting reporters may be one of the reasons why the potential of these reporters have not shown yet the high improvements in sensitivity that could be expected from their optical advantages compared with other luminescent labels. Apart from the aforementioned reasons, research on surface chemistry is crucial to guarantee the integrity and colloidal stability of these reporters, an important matter, if we consider that upconversion based homogeneous assays are currently in the spotlight for many researchers.

The possibility to detect just a few upconverting phosphors encourages the development of miniaturized and very sensitive assays. Nevertheless, as some researchers have found spectral differences when analyzing individual nanoparticles synthesized from a same batch, the question of if this issue could be addressed from a synthetic point of view, and to which extent this could compromise the results from these assays arises.

Besides the aforementioned, several drawbacks are inherent to the current upconverting technology when it is used in aqueous media (e.g. in homogeneous assays). It has been reported that certain OH-vibrational modes from water and other molecules are main contributors to the intense luminescence quenching that UCNPs suffer upon transfer to aqueous media via excited state Yb^{3+} relaxations. Thus, improvements in surface passivation methods or isolation of the reporters from the environment may be one interesting research topic, in order to overcome this important reduction in luminescence. Furthermore, as the maximum absorption of Yb^{3+} is located at 980 nm, where water molecules also have an absorption band, overheating processes on the irradiated aqueous media can take place during the excitation of the upconverting materials when long irradiation times and/or high power densities are used. This may have implications over the stability of biomolecules, biological processes, the reproducibility of different measurements, etc. Although it is always recommendable to specify the power density that has been used in the different experiments, it is especially relevant in these cases (e.g. homogeneous assays). The fact that water considerably absorbs at 980 nm also implies that, as the laser beam travels through the solvent, its power density is significantly reduced. This will affect the amount of photons that will be absorbed by the upconverting material, varying their luminescence intensity and spectra depending on the position where the detector will be located respect to the laser beam path through the sample (i.e. depending on the design of the setup). For these reasons during the last years many efforts have been devoted to shift the excitation wavelength of UCNPs from 980 nm to a more suitable wavelength for in vitro and in vivo biological applications. It is possible to use Nd^{3+} as a primary sensitizer that is able to absorb radiation at 800 nm. The excitation energy is transferred from Nd^{3+} to Er^{3+} or Tm^{3+} activator by using Yb^{3+} ions as a bridging sensitizer. For in vivo applications this is highly desirable since local overheating is greatly reduced by using 800 nm rather than 980 nm excitation light, and simultaneously increase the penetration depth into biological tissue. However, the preparation of such nanoparticles is a nontrivial task due to the energy transfer processes from Er^{3+} to Nd^{3+} via cross-relaxations, resulting in lack, or reduction, of upconversion emissions. Therefore, the design of core-shell architectures is needed to separate these ions, in order to avoid these cross-relaxations to occur. Although the controlled synthesis of UCNPs with a defined composition in the core and the shell is challenging, the shift in the excitation wavelength from 980 nm to 800 nm could be a huge improvement, having a special impact on their in vivo bioimaging applications. Thus Nd^{3+} sensitized UCNPs could be the next generation of upconverting nanomaterials for future in vivo application in bioimaging, biosensors and theranostic systems in general.

Acknowledgments

The authors acknowledge the Spanish Ministry MINECO (MAT2014-55065R) and Santander-UCM (PR26/16-12B-3) for funding.

References

[1] Lakowicz JR. Principles of Fluorescence Spectroscopy. Springer; 2006.
[2] Hua C, Zhang K, Xin M, Ying T, Gao J, Jia J, et al. High quantum yield and pH sensitive fluorescence dyes based on coumarin derivatives: fluorescence characteristics and theoretical study. RSC Adv 2016;6:49221–7.
[3] Cai Y, Samedov K, Dolinar BS, Albright H, Song Z, Zhang C, et al. AEE-active cyclic tetraphenylsilole derivatives with ~100% solid-state fluorescence quantum efficiency. Dalton Trans 2015;44:12970–5.
[4] Diaspro A, Chirico G, Usai C, Ramoino P, Dobrucki J. Photobleaching. Handb Biol Confocal Microsc 2006:690–702.
[5] Efros AL, Nesbitt DJ. Origin and control of blinking in quantum dots. Nat Nanotechnol 2016;11:661–71.
[6] Monici M. Cell and tissue autofluorescence research and diagnostic applications. Biotechnol Annu Rev 2005;11:227–56.
[7] van De Rijke F, Zijlmans H, Li S, Vail T, Raap AK, Niedbala RS, et al. Up-converting phosphor reporters for nucleic acid microarrays. Nat Biotechnol 2001;19:273–6.
[8] Corstjens PLAM, Li S, Zuiderwijk M, Kardos K, Abrams WR, Niedbala RS, et al. Infrared up-converting phosphors for bioassays. IEE Proceedings-Nanobiotechnology 2005;152:64–72.
[9] Haase M, Schäfer H. Upconverting nanoparticles. Angew Chem Int Ed 2011;50:5808–29.
[10] Liu Y, Tu D, Zhu H, Chen X. Lanthanide-doped luminescent nanoprobes: controlled synthesis, optical spectroscopy, and bioapplications. Chem Soc Rev 2013;42:6924–58.
[11] Boyer J-C, van Veggel FCJM. Absolute quantum yield measurements of colloidal $NaYF_4$: Er^{3+}, Yb^{3+} upconverting nanoparticles. Nanoscale 2010;2:1417–9.
[12] Chen G, Qiu H, Prasad PN, Chen X. Upconversion nanoparticles: design, nanochemistry, and applications in theranostics. Chem Rev 2014;114:5161–214.
[13] Dong H, Du SR, Zheng XY, Lyu GM, Sun LD, Li LD, et al. Lanthanide nanoparticles: from design toward bioimaging and therapy. Chem Rev 2015;115:10725–815.
[14] Zhu X, Su Q, Feng W, Li F. Anti-stokes shift luminescent materials for bio-applications. Chem Soc Rev 2017;46:1025–39.
[15] Jing Z, Liu Z, Li F. Upconversion nanophosphors for small-animal imaging. Chem Soc Rev 2012;41:1323–49.
[16] Li X, Zhang F, Zhao D. Lab on upconversion nanoparticles: optical properties and applications engineering via designed nanostructure. Chem Soc Rev 2015;44:1346–78.
[17] Kim D, Lee N, Park II Y, Hyeon T. Recent advances in inorganic nanoparticle-based NIR luminescence imaging: semiconductor nanoparticles and lanthanide nanoparticles. Bioconjug Chem 2017;28:115–23.
[18] Alonso-Cristobal P, Oton-Fernandez O, Mendez-Gonzalez D, Diaz JF, Lopez-Cabarcos E, Barasoain I, et al. Synthesis, characterization, and application in HeLa cells of an NIR light responsive doxorubicin delivery system based on $NaYF_4$:Yb,Tm@SiO_2-PEG nanoparticles. ACS Appl Mater Interfaces 2015;7:14992–9.
[19] Lin M, Gao Y, Hornicek F, Xu F, Lu TJ, Amiji M, et al. Near-infrared light activated delivery platform for cancer therapy. Adv Colloid Interface Sci 2015;226:123–37.
[20] Shen J, Sun L-D, Yan C-H. Luminescent rare earth nanomaterials for bioprobe applications. Dalton Trans 2008;9226:5687–97.
[21] Prodi L, Rampazzo E, Rastrelli F, Speghini A, Zaccheroni N. Imaging agents based on lanthanide doped nanoparticles. Chem Soc Rev 2015;44:4922–52.
[22] Johnson NJJ, Oakden W, Stanisz GJ, Scott Prosser R, Van Veggel FCJM. Size-tunable, ultrasmall NaGdF4 nanoparticles: insights into their T1 MRI contrast enhancement. Chem Mater 2011;23:3714–22.
[23] Zhang F. Photon Upconversion Nanomaterials. Springer; 2015.
[24] Rodriguez-Sevilla P, Labrador-Paez L, Wawrzynczyk D, Nyk M, Samoc M, Kar AK, et al. Determining the 3D orientation of optically trapped upconverting nanorods by in situ single-particle polarized spectroscopy. Nanoscale 2016;8:300–8.
[25] Nam SH, Bae YM, Park II Y, Kim JH, Kim HM, Choi JS, et al. Long-term real-time tracking of lanthanide ion doped upconverting nanoparticles in living cells. Angew Chem Int Ed 2011;50:6093–7.
[26] Sun L-D, Wang Y-F, Yan C-H. Paradigms and challenges for bioapplication of rare earth upconversion luminescent nanoparticles: small size and tunable emission/excitation spectra. Acc Chem Res 2014;47:1001–9.
[27] Wolfbeis OS. An overview of nanoparticles commonly used in fluorescent bioimaging. Chem Soc Rev 2015;44:4743–68.
[28] Li Z, Zhang Y, La H, Zhu R, El-Banna G, Wei Y, et al. Upconverting NIR photons for bioimaging. Nanomaterials 2015;5:2148–68.
[29] Sedlmeier A, Gorris HH. Surface modification and characterization of photon-upconverting nanoparticles for bioanalytical applications. Chem Soc Rev 2015;44:1526–60.
[30] Lahtinen S, Lyytikäinen A, Päkkilä H, Hömppi E, Perälä N, Lastusaari M, et al. Disintegration of hexagonal $NaYF_4$:Yb^{3+},Er^{3+} upconverting nanoparticles in aqueous media: the role of fluoride in solubility equilibrium. J Phys Chem C 2017;121:656–65.
[31] Lisjak D, Plohl O, Ponikvar-Svet M, Majaron B. Dissolution of upconverting fluoride nanoparticles in aqueous suspensions. RSC Adv 2015;5:27393–7.
[32] Lisjak D, Plohl O, Vidmar J, Majaron B, Ponikvar-Svet M. Dissolution mechanism of upconverting AYF_4:Yb,Tm (A = Na or K) nanoparticles in aqueous media. Langmuir 2016;32:8222–9.
[33] Plohl O, Kraft M, Kovac J, Belec B, Ponikvar-Svet M, Würth C, et al. Optically detected degradation of $NaYF_4$:Yb,Tm based upconversion nanoparticles in phosphate buffered saline solution. Langmuir 2017;33:553–60.
[34] Christ S, Schäferling M. Chemical sensing and imaging based on photon

upconverting nano- and microcrystals: a review. Methods Appl Fluoresc 2015;3:34004.
[35] Selvin PR. Lanthanide-based resonance energy transfer. IEEE J Sel Top Quantum Electron 1996;2:1077–87.
[36] Yuan L, Lin W, Zheng K, Zhu S. FRET-based small-molecule fluorescent probes: rational design and bioimaging applications. Acc Chem Res 2013;46:1462–73.
[37] Chen Z, Chen H, Hu H, Yu M, Li F, Zhang Q, et al. Versatile synthesis strategy for carboxylic acid-functionalized upconverting nanophosphors as biological labels. J Am Chem Soc 2008;130:3023–9.
[38] Sun LD, Gu JQ, Zhang SZ, Zhang YW, Yan CH. Luminescence resonance energy transfer based on Beta-$NaYF_4$:Yb,Er nanoparticles and TRITC dye. Sci China Ser B-Chemistry 2009;52:1590–5.
[39] Doughan S, Han Y, Uddayasankar U, Krull UJ. Solid-phase covalent immobilization of upconverting nanoparticles for biosensing by luminescence resonance energy transfer. ACS Appl Mater Interfaces 2014;6:14061–8.
[40] Liu C, Wang Z, Jia H, Li Z. Efficient fluorescence resonance energy transfer between upconversion nanophosphors and graphene oxide: a highly sensitive biosensing platform. Chem Commun 2011;47:4661–3.
[41] Alonso-Cristobal P, Vilela P, El-Sagheer A, Lopez-Cabarcos E, Brown T, Muskens OL, et al. Highly sensitive DNA sensor based on upconversion nanoparticles and graphene oxide. ACS Appl Mater Interfaces 2015;7:12422–9.
[42] Ye WW, Tsang MK, Liu X, Yang M, Hao J. Upconversion luminescence resonance energy transfer (LRET)-based biosensor for rapid and ultrasensitive detection of avian influenza virus H7 subtype. Small 2014;10:2390–7.
[43] Laurenti M, Paez-Perez M, Algarra M, Alonso-Cristobal P, Lopez-Cabarcos E, Mendez-Gonzalez D, et al. Enhancement of the upconversion emission by visible-to-near-infrared fluorescent graphene quantum dots for miRNA detection. ACS Appl Mater Interfaces 2016;8:12644–51.
[44] Wilhelm S, Del Barrio M, Heiland J, Himmelstoß SF, Galbán J, Wolfbeis OS, et al. Spectrally matched upconverting luminescent nanoparticles for monitoring enzymatic reactions. ACS Appl Mater Interfaces 2014;6:15427–33.
[45] Saleh SM, Ali R, Wolfbeis OS. Quenching of the luminescence of upconverting luminescent nanoparticles by heavy metal ions. Chem - A Eur J 2011;17:14611–7.
[46] Clarkson TW, Magos L. The toxicology of mercury and its chemical compounds. Crit Rev Toxicol 2006;36:609–62.
[47] Morel FMM, Kraepiel AML, Amyot M. The chemical cycle and bioaccumulation of mercury. Annu Rev Ecol Syst 1998;29:543–66.
[48] Gu B, Zhou Y, Zhang X, Liu X, Zhang Y, Marks R, et al. Thiazole derivative-modified upconversion nanoparticles for Hg^{2+} detection in living cells. Nanoscale 2015;8:276–82.
[49] Xu Y, Li H, Meng X, Liu J, Sun L, Fan X, et al. Rhodamine-modified upconversion nanoprobe for distinguishing Cu^{2+} from Hg^{2+} and live cell imaging. New J Chem 2016;40:3543–51.
[50] Peng Q, Sun L, Li F. High-efficiency upconversion luminescent sensing and bioimaging of Hg(II) by chromophoric ruthenium complex-assembled nanophosphors. ACS Nano 2011;5:8040–8.
[51] Li H, Wang L. $NaYF_4$:Yb^{3+}/Er^{3+} nanoparticle-based upconversion luminescence resonance energy transfer sensor for Mercury(II) quantification. Analyst 2013;138:1589–95.
[52] Zhang Y, Wu L, Tang Y, Su Y, Lv Y. An upconversion fluorescence based turn-on probe for detecting Lead(II) ions. Anal Methods 2014;6:9073–7.
[53] Xu S, Xu SH, Zhu YS, Xu W, Zhou PW, Zhou CY, et al. A novel upconversion, fluorescence resonance energy transfer biosensor (FRET) for sensitive detection of lead ions in human serum. Nanoscale 2014;6:12573–9.
[54] Arppe R, Näreoja T, Nylund S, Mattsson L, Koho S, Rosenholm JM, et al. Photon upconversion sensitized nanoprobes for sensing and imaging of pH. Nanoscale 2014;6:6837–43.
[55] Näreoja T, Deguchi T, Christ S, Peltoma R, Prabhakar N, Fazeli E, et al. Ratiometric sensing and imaging of intracellular pH using polyethylenimine-coated photon upconversion nanoprobes. Anal Chem 2017;89:1501–8.
[56] Wright WH, Mufti NA, Tagg NT, Webb RR, Schneider LW. High-sensitivity immunoassay using a novel upconverting phosphor reporter. Proc SPIE 1997;2985:248–55.
[57] Wollenberger LV, Yao YMM, Mufti NA, Schneider LV. Detection of DNA using upconverting phosphor reporter probes. Proc SPIE 2985, Ultrasensitive Biochem Diagnostics II, 100 1997;2985:100–11.
[58] Ukonaho T, Rantanen T, Jämsen L, Kuningas K, Päkkilä H, Lövgren T, et al. Comparison of infrared-excited up-converting phosphors and europium nanoparticles as labels in a two-site immunoassay. Anal Chim Acta 2007;596:106–15.
[59] Hlaváček A, Farka Z, Hübner M, Horňáková V, Němeček D, Niessner R, et al. Competitive upconversion-linked immunosorbent assay for the sensitive detection of diclofenac. Anal Chem 2016;88:6011–7.
[60] Sirkka N, Lyytikäinen A, Savukoski T, Soukka T. Upconverting nanophosphors as reporters in a highly sensitive heterogeneous immunoassay for cardiac troponin I. Anal Chim Acta 2016;925:82–7.
[61] Ai Y, Tu D, Zheng W, Liu Y, Kong J, Hu P, et al. Lanthanide-doped $NaScF_4$ nanoprobes: crystal structure, optical spectroscopy and biodetection. Nanoscale 2013;5:6430–8.
[62] Huang P, Zheng W, Zhou S, Tu D, Chen Z, Zhu H, et al. Lanthanide-doped $LiLuF_4$ upconversion nanoprobes for the detection of disease biomarkers. Angew Chem Int Ed 2014;53:1252–7.
[63] Lan J, Liu Y, Li L, Wen F, Wu F, Han Z, et al. A upconversion luminescene biosensor based on dual-signal amplification for the detection of short DNA species of c-ERBB-2 oncogene. Sci Rep 2016;6:24813.
[64] El-Sagheer A, Brown T. Click chemistry with DNA. Chem Soc Rev 2010;39:1388–405.
[65] Mendez-Gonzalez D, Laurenti M, Latorre A, Somoza A, Vazquez A, Negredo AI, et al. Oligonucleotide sensor based on selective capture of upconversion nanoparticles triggered by target-induced DNA interstrand ligand reaction. ACS Appl Mater Interfaces 2017;9:12272–81.
[66] Mani V, Chikkaveeraiah BV, Rusling JF. Magnetic particles in ultrasensitive biomarker protein measurements for cancer detection and monitoring. Expert Opin Med Diagn 2011;5:381–91.
[67] Verpoorte E. Beads and chips: new recipes for analysis. Lab Chip 2003;3:60–8.
[68] Wang L, Li Y. Green upconversion nanocrystals for DNA detection. Chem Commun 2006:2557–9.
[69] Li Y, Wu Z, Liu Z. An immune sandwich assay of carcinoembryonic antigen based on the joint use of upconversion phosphors and magnetic beads. Analyst 2015;140:4083–8.
[70] Zhang F, Shi Q, Zhang Y, Shi Y, Ding K, Zhao D, et al. Fluorescence upconversion microbarcodes for multiplexed biological detection: nucleic acid encoding. Adv Mater 2011;23:3775–9.
[71] Kale V, Päkkilä H, Vainio J, Ahomaa A, Sirkka N, Lyytikäinen A, et al. Spectrally and spatially multiplexed serological array-in-well assay utilizing two-color upconversion luminescence imaging. Anal Chem 2016;88:4470–7.
[72] Ylihärsilä M, Valta T, Karp M, Hattara L, Harju E, Hölsä J, et al. Oligonucleotide array-in-well platform for detection and genotyping human adenoviruses by utilizing upconverting phosphor label technology. Anal Chem 2011;83:1456–61.
[73] Ylihärsilä M, Alaranta S, Lahdenperä S, Lahtinen S, Arku B, Hedman K, et al. Array-in-well serodiagnostic assay utilizing upconverting phosphor label technology. J Virol Methods 2015;222:224–30.
[74] Päkkilä H, Ylihärsilä M, Lahtinen S, Hattara L, Salminen N, Arppe R, et al. Quantitative multianalyte microarray immunoassay utilizing upconverting phosphor technology. Anal Chem 2012;84:8628–34.
[75] Li X, Li Z, Gan W, Wang T, Zhao S, Lu Y, et al. Sensitive and high resolution subcutaneous fluorescence in vivo imaging using upconversion nanoparticles and microarrays. Analyst 2013;138:3711–8.
[76] Quesada-González D, Merkoçi A. Nanoparticle-based lateral flow biosensors. Biosens Bioelectron 2015;73:47–63.
[77] Li JJ, Ouellette AL, Giovangrandi L, Cooper DE, Ricco AJ, Kovacs GTA. Optical scanner for immunoassays with up-converting phosphorescent labels. IEEE Trans Biomed Eng 2008;55:1560–71.
[78] Huang L, Zhou L, Zhang Y, Xie C, Qu J, Zeng A, et al. A simple optical reader for upconverting phosphor particles captured on lateral flow strip. IEEE Sens J 2009;9:1185–91.
[79] Corstjens P, Zuiderwijk M, Brink A, Li S, Feindt H, Niedbala RS, et al. Use of up-converting phosphor reporters in lateral-flow assays to detect specific nucleic acid sequences: a rapid, sensitive DNA test to identify human papillomavirus type 16 infection. Clin Chem 2001;47:1885–93.
[80] Hampl J, Hall M, Mufti NA, Yao YM, MacQueen DB, Wright WH, et al. Upconverting phosphor reporters in immunochromatographic assays. Anal Biochem 2001;288:176–87.
[81] Corstjens PLAM, Van Lieshout L, Zuiderwijk M, Kornelis D, Tanke HJ, Deelder AM, et al. Up-converting phosphor technology-based lateral flow assay for detection of schistosoma circulating anodic antigen in serum. J Clin Microbiol 2008;46:171–6.
[82] Zuiderwijk M, Tanke HJ, Niedbala RS, Corstjens PLAM. An amplification-free hybridization-based DNA assay to detect streptococcus pneumoniae utilizing the up-converting phosphor technology. Clin Biochem 2003;36:401–3.
[83] Corstjens PLAM, Zuiderwijk M, Nilsson M, Feindt H, Niedbala RS, Tanke HJ. Lateral-flow and up-converting phosphor reporters to detect single-stranded nucleic acids in a sandwich-hybridization assay. Anal Biochem 2003;312:191–200.
[84] Liu C, Ma W, Gao Z, Huang J, Hou Y, Xu C, et al. Upconversion luminescence nanoparticles-based lateral flow immunochromatographic assay for cephalexin detection. J Mater Chem C 2014;2:9637–42.
[85] Niedbala RS, Feindt H, Kardos K, Vail T, Burton J, Bielska B, et al. Detection of analytes by immunoassay using up-converting phosphor technology. Anal Biochem 2001;293:22–30.
[86] Zhao Peng, Wu Yuanyuan, Zhu Yihua, Yang Xiaoling, Jiang Xin, Xiao Jingfan, et al. Upconversion fluorescent strip sensor for rapid determination of *Vibrio anguillarum*. Nanoscale 2014;6:3804–9.
[87] Corstjens PLAM, de Dood CJ, Priest JW, Tanke HJ, Handali S. Feasibility of a lateral flow test for neurocysticercosis using novel up-converting nanomaterials and a lightweight strip analyzer. PLoS Negl Trop Dis 2014;8:e2944.
[88] Corstjens PL, Nyakundi RK, de Dood CJ, Kariuki TM, Ochola EA, Karanja DM, et al. Improved sensitivity of the urine CAA lateral-flow assay for diagnosing active schistosoma infections by using larger sample volumes. Parasit Vectors 2015;8:241.
[89] Corstjens PLAM, Tjon Kon Fat EM, de Dood CJ, van der Ploeg-van Schip JJ, Franken KLMC, Chegou NN, et al. Multi-center evaluation of a user-friendly lateral flow assay to determine IP-10 and CCL4 levels in blood of TB and non-TB cases in Africa. Clin Biochem 2016;49:22–31.
[90] Sedlmeier A, Hlavacek A, Birner L, Mickert MJ, Muhr V, Hirsch T, et al. Highly sensitive laser scanning of photon-upconverting nanoparticles on a macroscopic scale. Anal Chem 2016;88:1835–41.
[91] Erickson D, Li D. Integrated microfluidic devices. Anal Chim Acta 2004;507:11–26.
[92] Tudos AJ, Besselink GJ, Schasfoort RB. Trends in miniaturized total analysis systems for point-of-care testing in clinical chemistry. Lab Chip 2001;1:83–95.
[93] Chen Z, Mauk MG, Wang J, Abrams WR, Corstjens PL, Niedbala RS, et al. A microfluidic system for saliva-based detection of infectious diseases. Ann N Y Acad Sci 2007;1098:429–36.
[94] Chen D, Mauk M, Qiu X, Liu C, Kim J, Ramprasad S, et al. An integrated microfluidic cassette for isolation, amplification, and detection of nucleic acids. Biomed

Microdevices 2010;12:705–19.
[95] Abrams WR, Barber CA, McCann K, Tong G, Chen Z, Mauk MG, et al. Development of a microfluidic device for detection of pathogens in oral samples using upconverting phosphor technology (UPT). Ann N Y Acad Sci 2007;1098:375–88.
[96] Chen Z, Abrams WR, Geva E, De Dood CJ, González JM, Tanke HJ, et al. Development of a generic microfluidic device for simultaneous detection of antibodies and nucleic acids in oral fluids. Biomed Res Int 2013:543294.
[97] Wang C, Ye M, Cheng L, Li R, Zhu W, Shi Z, et al. Simultaneous isolation and detection of circulating tumor cells with a microfluidic silicon-nanowire-array integrated with magnetic upconversion nanoprobes. Biomaterials 2015;54:55–62.
[98] Prodi L, Montalti M, Zaccheroni N. Luminescence Applied in Sensor Science. Springer; 2011.
[99] Binnemans K. Lanthanide-based luminescent hybrid materials. Chem Rev 2009;109:4283–374.
[100] Wang S, Westcott S, Chen W. Nanoparticle luminescence thermometry. J Phys Chem B 2002;106:11203–9.
[101] Jaque D, Vetrone F. Luminescence nanothermometry. Nanoscale 2012;4:4301–26.
[102] Vetrone F, Naccache R, Zamarrón A, De La Fuente AJ, Sanz-Rodríguez F, Maestro LM, et al. Temperature sensing using fluorescent nanothermometers. ACS Nano 2010;4:3254–8.
[103] Jaque D, del Rosal B, Rodríguez EM, Maestro LM, Haro-González P, Solé JG. Fluorescent nanothermometers for intracellular thermal sensing. Nanomedicine 2014;9:1047–62.
[104] Chen Rui, Ta Van Duong, Xiao Fen, Zhang Qinyuan, Sun H. Multicolor hybrid upconversion nanoparticles and their improved performance as luminescence temperature sensors due to energy transfer. Small 2013;9:1052–7.
[105] Laurenti M, Lopez-Cabarcos E, Garcia-Blanco F, Frick B, Rubio-Retama J. Interpenetrated PNIPAM-polythiophene microgels for nitro aromatic compound detection. Langmuir 2009;25:9579–84.
[106] Xiao Q, Li Y, Li F, Zhang M, Zhang Z, Lin H. Rational design of a thermal responsive-polymer-switchable FRET system for enhancing the temperature sensitivity of upconversion nanophosphors. Nanoscale 2014;6:10179–86.
[107] Mader HS, Wolfbeis OS. Ammonia sensor based on upconverting luminescent nanoparticles. Anal Chem 2010;82:5002–4.
[108] Presley KF, Cheong S, Cochran A, Tilley RD, Collins JE, Lannutti JJ. Chemical upconverter-powered oxygen sensing in electrospun polymeric bilayers. Sens Actuators B 2016;235:197–205.
[109] Zhou P, Zhou D, Tao L, Zhu Y, Xu W, Xu S, et al. 320-Fold luminescence enhancement of $[Ru(dpp)_3]Cl_2$ dispersed on PMMA opal photonic crystals and highly improved oxygen sensing performance. Light Sci Appl 2014;3:1–9.
[110] Mokkapati VK, Niedbala RS, Kardos K, Perez RJ, Guo M, Tanke HJ, et al. Evaluation of UPlink-RSV: prototype rapid antigen test for detection of respiratory syncytial virus infection. Ann N Y Acad Sci 2007;1098:476–85.
[111] Aslan K, Grell T. Rapid and sensitive detection of Troponin I in human whole blood samples by using silver nanoparticle films and microwave heating. Clin Chem 2011;57:746–52.
[112] Järvenpää ML, Kuningas K, Niemi I, Hedberg P, Ristiniemi N, Pettersson K, et al. Rapid and sensitive cardiac Troponin I immunoassay based on fluorescent europium(III)-chelate-dyed nanoparticles. Clin Chim Acta 2012;414:70–5.
[113] Juntunen E, Arppe R, Kalliomäki L, Salminen T, Talha SM, Myyryläinen T, et al. Effects of blood sample anticoagulants on lateral flow assays using luminescent photon-upconverting and Eu(III) nanoparticle reporters. Anal Biochem 2016;492:13–20.
[114] Cho IH, Paek EH, Kim YK, Kim JH, Paek SH. Chemiluminometric enzyme-linked immunosorbent assays (ELISA)-on-a-chip biosensor based on cross-flow chromatography. Anal Chim Acta 2009;632:247–55.
[115] Choi DH, Lee SK, Oh YK, Bae BW, Lee SD, Kim S, et al. A dual gold nanoparticle conjugate-based lateral flow assay (LFA) method for the analysis of Troponin I. Biosens Bioelectron 2010;25:1999–2002.
[116] Guo W, Yuan J, Wang E. Oligonucleotide-stabilized ag nanoclusters as novel fluorescence probes for the highly selective and sensitive detection of the Hg^{2+} ion. Chem Commun 2009;23:3395–7.
[117] Lu W, Qin X, Liu S, Chang G, Zhang Y, Luo Y, et al. Economical, green synthesis of fluorescent carbon nanoparticles and their use as probes for sensitive and selective detection of Mercury(II) ions. Anal Chem 2012;84:5351–7.
[118] Dong Y, Tian W, Ren S, Dai R, Chi Y, Chen G. Graphene quantum dots/L-cysteine coreactant electrochemiluminescence system and its application in sensing Lead (II) ions. ACS Appl Mater Interfaces 2014;6:1646–51.
[119] Tate JR, Bunk DM, Christenson RH, Katrukha A, Noble JE, Porter RA, et al. Standardisation of cardiac Troponin I measurement: past and present. Pathology 2010;42:402–8.
[120] US-EPA. Method 1631: Mercury in Water by Oxidation, Purge and Trap, and Cold Vapor Atomic Fluorescence Spectrometry. EPA 821-R-96-012. Washington, DC: US EPA, Off. Water; 2002https://www.epa.gov/sites/production/files/2015-08/documents/method_1631e_2002.pdf.
[121] Standard Operating Procedure for Determination of Lead in TSP by Inductively Coupled Plasma Mass Spectrometry (ICP-MS) with Hot Block Dilute Acid and Hydrogen Peroxide Filter Extraction. https://www3.epa.gov/ttnamti1/files/ambient/pb/EQL-0512-201.pdf.
[122] Heer S, Kömpe K, Güdel HU, Haase M. Highly efficient multicolour upconversion emission in transparent colloids of lanthanide-doped $NaYF_4$ nanocrystals. Adv Mater 2004;16:2102–5.
[123] Gnach A, Bednarkiewicz A. Lanthanide-doped up-converting nanoparticles: merits and challenges. Nano Today 2012;7:532–63.
[124] Wang K, Ma J, He M, Gao G, Xu H, Sang J, et al. Toxicity assessments of near-infrared upconversion luminescent LaF_3:Yb,Er in early development of zebrafish embryos. Theranostics 2013;3:258–66.
[125] Zhou J, Yu M, Sun Y, Zhang X, Zhu X, Wu Z, et al. Fluorine-18-labeled Gd^{3+}/Yb^{3+}/Er^{3+} co-doped $NaYF_4$ nanophosphors for multimodality PET/MR/UCL imaging. Biomaterials 2011;32:1148–56.
[126] Yang Y, Sun Y, Liu Y, Peng J, Wu Y, Zhang Y, et al. Long-term in vivo biodistribution and toxicity of $Gd(OH)_3$ nanorods. Biomaterials 2013;34:508–15.
[127] Cheng L, Yang K, Shao M, Xinhua L, Liu Z. In vivo pharmacokinetics, long-term biodistribution and toxicology study of functionalized upconversion nanoparticles in mice. Nanomedicine 2011;6:1327–40.
[128] Gnach A, Lipinski T, Bednarkiewicz A, Rybka J, Capobianco JA. Upconverting nanoparticles: assessing the toxicity. Chem Soc Rev 2015;44:1561–84.

II. Aims of the work

II) Aims of the work

1) Synthesis and characterization of monodisperse nanoparticles based on β-$NaYF_4$ doped with Yb^{3+}/Er^{3+} and Yb^{3+}/Tm^{3+} pairs.

2) Surface functionalization of upconverting nanoparticles to make them water-dispersible and with desired surface characteristics for bioconjugations and subsequent studies.

3) Bioconjugation of water-dispersible upconverting nanoparticles with DNA probes to obtain UC-labels that show a specific response to targeted oligonucleotide sequences.

4) Fundamental study of a system based on upconverting nanoparticles and quantum dots, aiming to find optimal conditions for the potential development of oligonucleotide sensors.

5) Systematic study on the effect of gold nanoparticles' size on upconversion luminescence, searching for optimal sizes to develop oligonucleotide sensors based on luminescence quenching or enhancement.

6) Exploration of an oligonucleotide target-induced ligation between capture probes, based on click chemistry, for the development of a highly sensitive heterogeneous assay using upconverting nanoparticles as labels.

7) Design of a highly sensitive oligonucleotide detection heterogeneous assay based on the target-induced photochemical ligation between capture probes using UV light as external stimuli and upconverting nanoparticles as labels.

8) Temporal and spatial-control of photochemical ligation using Yb^{3+}/Tm^{3+} doped upconverting nanoparticles as local UV source and near infrared (NIR) light as external excitation source.

II. Objetivos del trabajo

II) Objetivos del trabajo

1) Síntesis y caracterización de nanopartículas monodispersas basadas en β-$NaYF_4$ dopado con pares Yb^{3+}/Er^{3+} and $Yb^{3}+/Tm^{3+}$.

2) Funcionalización superficial de las nanopartículas de conversión ascendente para conseguir que se dispersen en agua y posean características superficiales deseadas para bioconjugaciones y estudios subsiguientes.

3) Bioconjugación de las nanopartículas de conversión ascendente dispersables en agua con sondas de DNA tradicionales o modificadas para obtener UC-labels que muestren una respuesta específica hacia secuencias de oligonucleótidos diana.

4) Estudio básico de un sistema basado en nanopartículas de conversión ascendente y puntos cuánticos, con el objetivo de encontrar condiciones óptimas para el potencial desarrollo de sensores de oligonucleótidos.

5) Estudio sistemático del efecto del tamaño de las nanopartículas de oro sobre la luminiscencia de conversión ascendente, en busca de tamaños óptimos para el desarrollo de sensores de oligonucleótidos basados en desactivación o incremento de la fluorescencia.

6) Exploración de una ligación entre sondas de captura, basada en química click e inducida por el oligonucleótido diana, para el desarrollo de un ensayo heterogéneo altamente sensible usando nanopartículas de conversión ascendente como etiquetas.

7) Diseño de un ensayo heterogéneo altamente sensible para la detección de oligonucleótidos basado en la ligación fotoquímica entre sondas de captura inducida por diana y usando luz UV como estímulo externo y nanopartículas de conversión ascendente como etiquetas.

8) Control del tiempo y la localización espacial de la ligación fotoquímica usando nanopartículas de conversión ascendente dopadas con Yb^{3+}/Tm^{3+} como fuente local de UV, y luz de la región del infrarrojo cercano (NIR) como fuente externa de excitación.

III. Experimental

III.1

Fundamental study of UCNPs/Q-dots and UCNPs/AuNPs pairs

III.1.1) Introduction

The fact that homogeneous assays can be performed in the absence of separation and washing steps makes them ideal candidates for the automatized, real-time, and quick detection and quantification of analytes. As they usually require just a simple solution "mixing" step to carry out the detection, they make it possible to bypass the necessity of well-equipped laboratories and facilities, as well as trained operators, making them suitable alternatives as point-of-care (POC) tools for the diagnosis of diseases in hardly accessible areas or countries with little resources. As shown in the previous review, UCNPs are receiving a lot of attention for their potential use as donors in this kind of assays, which usually rely on resonance energy transfer (RET) processes. The fundamental study of specific donor / acceptor pairs may permit a better comprehension of the advantages and limitations of the particular systems, as well as finding optimal conditions to build effective assays and sensors.

With this in mind, investigations were carried out on the optimal conditions to develop homogeneous assays using UCNPs as donors, and either CdTe Q-dots (Publication 2) or gold nanoparticles (Publication 3) as acceptors. Both studies will be treated in this section: "*Förster resonance energy transfer distance dependence from upconverting nanoparticles to quantum dots*" (Publication 2), and "Control of upconversion luminescence by gold nanoparticle size: from quenching to enhancement" (Publication 3).

As a first step for both studies, β-$NaYF_4$ nanoparticles doped with Yb^{3+} (20%wt relative to [Y^{3+} + Yb^{3+} + Er^{3+}] = 100%) and Er^{3+} (2%wt) were synthesized, which resulted in green/red-emitting UCNPs. Among the different methods existing to synthesize these nanomaterials (thermal decomposition, Ostwald-ripening, ionic liquid-based, and solvothermal methods) the Ostwald ripening method was chosen due to its advantages: relatively mild conditions, non-toxic by-products, more environmentally friendly chemicals, relatively simple protocols, and highly crystalline hexagonal (β)-phase nanoparticles with decreased defects as products.[1] This synthetic approach is based on the *in situ* formation of small sacrificial cubic (α)-phase $NaYF_4$ nanoparticles, by the reaction of rare earth (RE) oleates with

sodium fluoride (NaF) at high temperature. Subsequently, highly crystalline β-phase UCNPs are grown at the expense of the initial (α)-phase nanoparticles by heating at 300ºC for 1h due to a Ostwald-ripening process.[2] This ripening phenomenon is based on the fact that big particles are thermodynamically favored in comparison with smaller ones, due to a lower surface-to-volume ratio of the former ones. Thus, the high temperatures used in this synthesis favors the dissolution of small α-$NaYF_4$ nanoparticles (due in part to their high specific surface area) and their crystallization and growth at the surface of β-UCNPs (whose crystalline phase is less soluble and more stable in these conditions). Once the synthetic process has finished, all α-$NaYF_4$ nanoparticles are consumed and highly crystalline oleate-capped β-UCNPs are obtained. Note that the oleate molecules acting as capping agent make the resulting UCNPs hydrophobic. A general scheme of the synthetic procedure is depicted in Figure III.1.1.1. Interestingly, another different mechanism for β-$NaGdF_4$ formation has been recently proposed.[3]

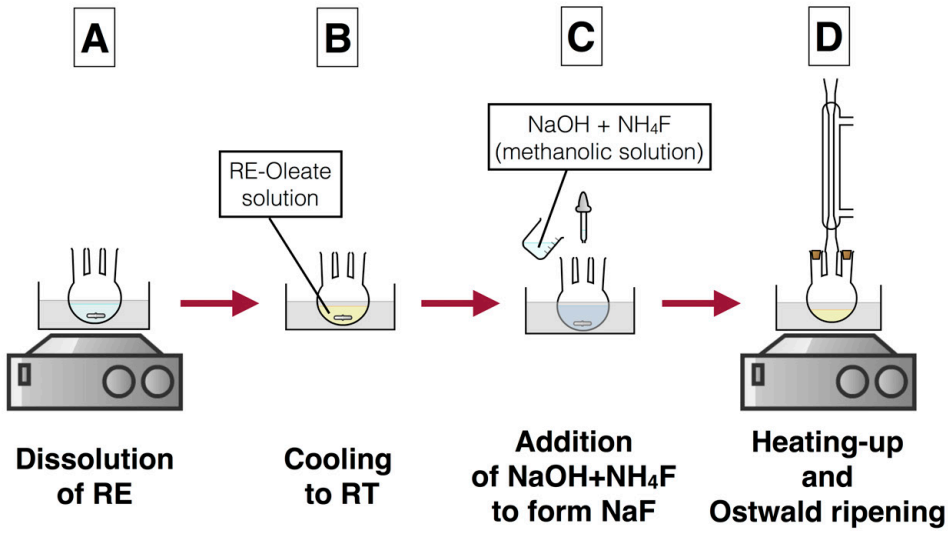

Figure III.1.1.1. Synthetic steps to obtain UCNPs by the Ostwald ripening approach. A) Dissolution of YCl_3, $YbCl_3$, and $ErCl_3$ in oleic acid and 1-octadecene at 160ºC. B) After the dissolution of the salts, the mixture is cooled down to room temperature (RT). C) Addition of methanolic solution containing NaOH and NH_4F. Precipitation of NaF after methanol removal. D) The resulting solution is heated up to 300ºC under N_2 atmosphere to give sacrificial α-phase $NaYF_4$ nanoparticles during the process, from which β-phase UCNPs will form by Ostwald ripening.

Once the UCNPs were obtained, a silica (SiO_2) shell was grown around the UCNPs as a first step to turn them hydrophillic and further modify their surface. This was achieved by a reverse-microemulsion method, using tetraethyl orthosilicate (TEOS) as silica precursor, Igepal CO-520 as surfactant, hexane as continuous phase, and ammonium hydroxide (NH_4OH) as catalyst and dispersed phase (see Figure III.1.1.2) . In this method, hydrolized TEOS molecules exchange at the surface of UCNPs with their capping agent (Igepal instead of oleic acid, at this point).[4–6] During this process the nanoparticles are transferred to the interior of the aqueous domains (i.e. water droplets), where TEOS molecules condense due to the alkaline media provided by NH_4OH. The condensation of TEOS molecules around the UCNPs eventually results in the formation of a concentric silica shell around the UCNPs, yielding "UCNPs@SiO_2" nanoparticles.

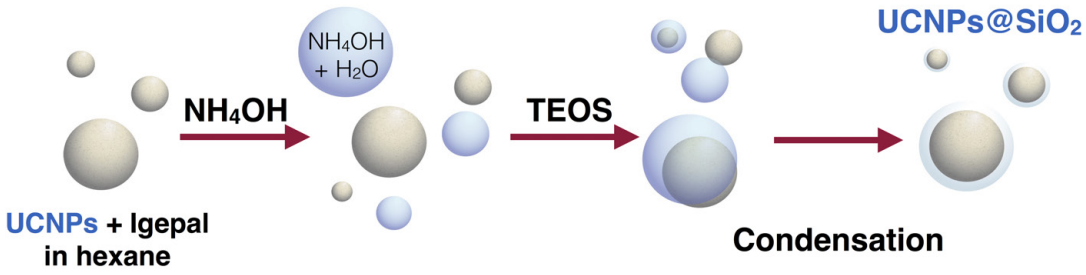

Figure III.1.1.2. Scheme of silica shell growth onto UCNPs' surface by the reverse-microemulsion method.

To study the distance-dependence of Förster resonance energy transfer (FRET) from UCNPs to Q-dots (Publication 2), different SiO_2 thicknesses were grown around the UCNPs to act as a "spacer" between the two nanomaterials. The reverse microemulsion method allowed a tight control of the silica coating: By using different amounts of TEOS, controlled thicknesses at the nanometric scale could be obtained (Figure III.1.1.3). Stopping the reaction at different times (i.e. a kinetic control), while keeping constant the amount of TEOS, is another effective way to control the shell thickness.

In the case of publication 3, UCNPs coated with a fixed SiO_2 thickness were used instead.

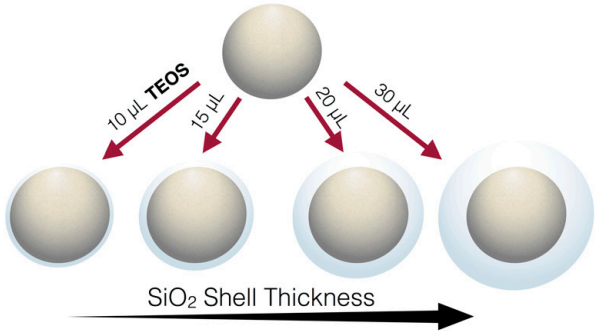

Figure III.1.1.3. The addition of different amounts of SiO_2 precursor (TEOS) permits to effectively control the shell thickness, making it an ideal spacer to study the FRET distance-dependence between UCNPs and Q-dots.

As a final step, the resulting UCNPs@SiO_2 (core@shell) nanoparticles were further modified using their silanol (-SiOH) surface groups as anchoring points for the attachment of "(3-aminopropyl) triethoxysilane" (APTES), an organosilane molecule that yields an amine-modified surface, see Figure III.1.1.4. Amino-modified UCNPs are able to interact with 3-mercaptopropionic acid capped CdTe Q-dots and citrate-stabilized gold nanoparticles (AuNPs), by electrostatic interactions and complexation, as amines are positively charged at neutral to acidic pHs and also present a high affinity to the surface of gold (Au)[7]. This allowed to study how the proximity of Q-dots/AuNPs influence the photoluminescence of UCNPs, permitting to establish general guidelines to follow when aiming to design homogeneous assays based on UCNPs/Q-dots and UCNPs/AuNPs pairs for the detection of small biomolecules such as oligonucleotides.

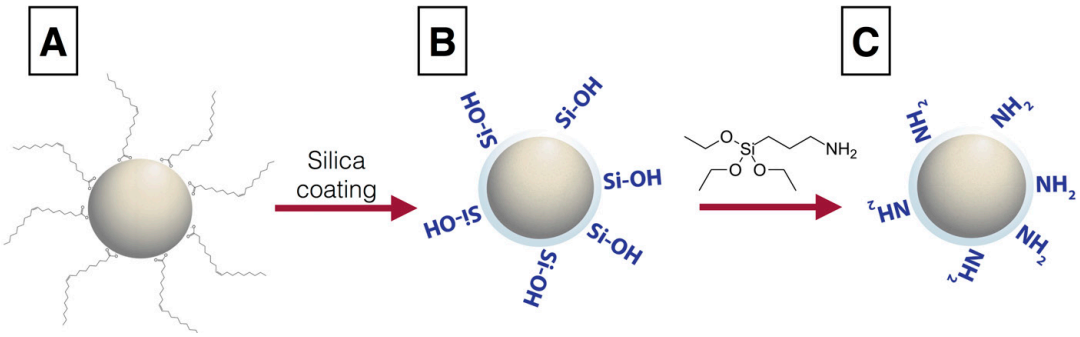

Figure III.1.1.4. A) UCNPs with oleic acid as capping agent. B) Silica shell growth by the reverse microemulsion method, yielding silanol (Si-OH) surface groups. C) The reaction of the UCNPs@SiO_2 with APTES allowed the functionalization of their surface with primary amines.

As discussed previously in section I.3 (publication 1), FRET is a non-radiative process that occurs between two light-sensitive entities (e.g. fluorophores), usually named as "donor" and "acceptor", under specific circumstances: the emission spectrum of the donor must overlap the absorption spectrum of the acceptor (Figure III.1.1.5), while the donor and the acceptor needs to be close enough for this phenomenon to happen (within 1-10 nm).[8, 9] In this situation, and upon absorption of light by the donor, the energy from its excited state is transferred to the acceptor, which is commonly named "quencher" as it deactivates the luminescence from the donor by these means. The received energy can be partially dissipated by the acceptor in the form of emitted photons at higher wavelengths (as it happens with Q-dots), or entirely as heat, in the case of a "dark quencher" (e.g. dyes lacking native fluorescence).

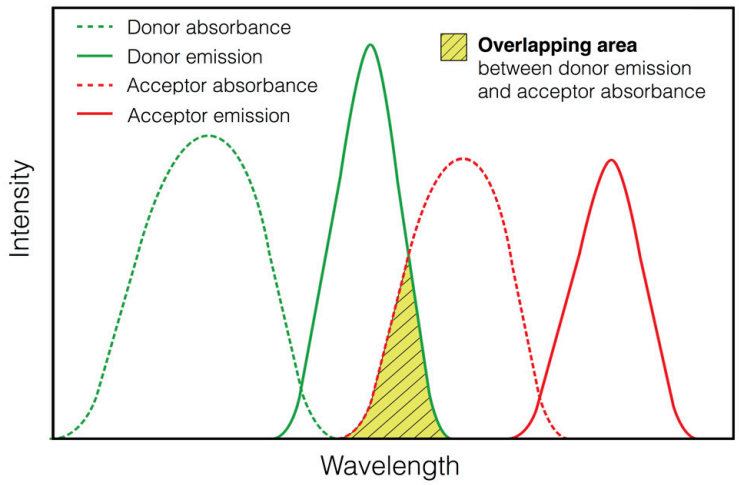

Figure III.1.1.5. FRET requires the spectral overlap between the donor emission and acceptor absorption spectra.

The non-radiative nature of FRET processes is explained by the long-range dipole-dipole interaction between the donor (whose excited electron creates a momentary dipole) and the acceptor. Thus, the energy transfer occurs without the emission/re-absorption of photons. The energy transfer rate is dependent on factors such as relative orientation of the donor to the acceptor transition dipoles, degree of spectral overlap between donor emission and acceptor absorbance, quantum yield of the donor, and distance between donor and acceptor. Once understood the mechanism of this phenomenon, it is evident that bringing in close proximity the quencher to the donor by means of a specific biological interaction

(e.g. antigen-antibody, hybridization of complementary oligonucleotides, etc) will cause a "switch off" behavior on donor's luminescence, which will make possible the detection of the targeted analyte behind this interaction (e.g. antigen, antibody, DNA strand, miRNA, etc), see Figure III.1.1.6.

When designing this kind of sensors, some considerations must be taken into account to maximize their detection performance, such as characteristics of the donor (e.g. size, specific surface area, spectroscopic features, surface bioconjugation, etc), characteristics of the acceptor, distance between donor / acceptor when interacting with the targeted analyte, relative donor / acceptor orientation, etc. As an example, FRET only occurs with high efficiency if donor and acceptor are located within the "Förster radius", which is defined as the distance where half the excitation energy of the donor is transferred to the acceptor. Thus, calculating this distance as well as other parameters for a specific system (e.g. UCNPs/Q-dots) will make it possible to improve its response towards a desired analyte, which is the motivation behind the study presented in publication 2.

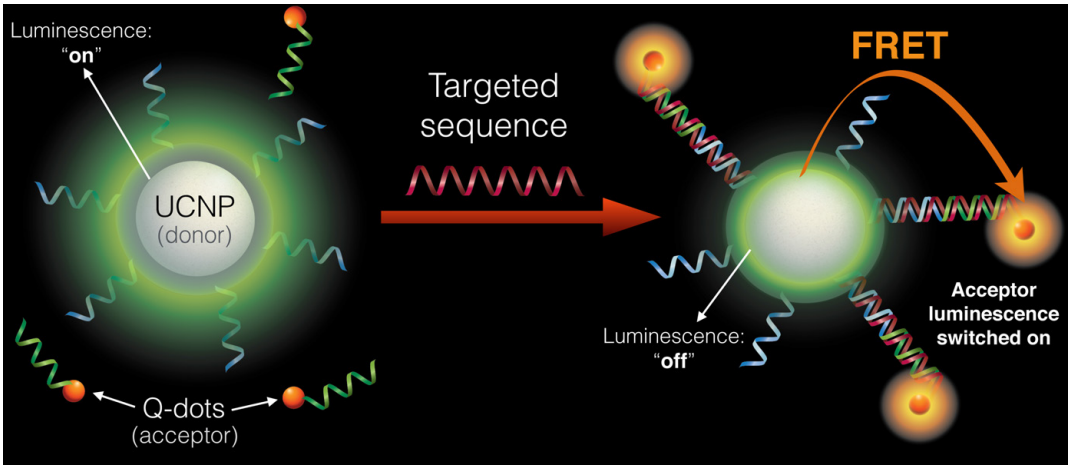

Figure III.1.1.6. Ideal model of UCNP/Q-dots FRET system for the detection of a specific oligonucleotide: The targeted sequence brings in close proximity, upon hybridization, the target-complementary DNA-functionalized UCNP and Q-dots. In the presence of the targeted sequence, the UCNP luminescence is quenched due to a successful FRET process to the nearby Q-dots (acceptors). As result, the Q-dots luminescence is activated when exciting the system at UCNPs' absorption wavelength (980 nm).

A similar kind of system based on upconversion luminescence quenching by non-radiative energy transfer processes can be built using UCNPs/AuNPs pairs. On the other hand, the existence of numerous works reporting either quenching or enhancement of upconversion luminescence by AuNPs deserves attention.[10–15]

Although β-$NaYF_4$ doped with Ln^{3+} are UCNPS commonly used due to the advantages previously discussed in this thesis, AuNPs featuring different size, shape, surface functionality, and spacing for the reported UCNPs/AuNPs systems, makes it difficult to qualitatively and quantitatively compare the described phenomena. In addition, the use of UCNPs with different sizes, which affects their luminescence and quantum yield even when dopant concentrations and host matrix are kept constant, is another factor to take into account in the design of these systems, as we and other groups have anticipated.[16,17] Thus, the need of a systematic study to shed light on the interaction between UCNPs/AuNPs aiming to better design sensors, was the motivation for the study presented in publication 3. In this work, UCNPs (20 nm in diameter) coated with a constant SiO_2 thickness as spacer (i.e. 3.8 nm) were used as donor, while the size-effect of spherical AuNPs on the luminescence of UCNPs was studied.

Typically, the proximity of a fluorophore to a metallic nanoparticle (MNP) can be accompanied of different effects, which will depend on factors such as proximity to the metallic surface, size and shape of the metallic nanostructure, orientation of the excited fluorophore (oscillating dipole) regarding the nanoparticle, etc. For example, the high proximity to a metallic surface (e.g. 0-20 nm) usually results in strong fluorescence quenching by non-radiative mechanisms like resonance energy transfer (RET) processes and other phenomena.[8,18,19]

On the other hand, fluorescence enhancement can also occur at certain distances from metallic surfaces. This can be explained by the increase of fluorophore's rate of excitation and/or of its radiative decay rate, which can occur due to the modification of the local electromagnetic field around the emitter by the localized surface plasmon resonance from a nearby MNP.[8,19,20]

Emission quenching or enhancement effects can be expressed in terms of the modification of both the non-radiative decay rate (K_{nr}) and the radiative decay rate (Γ) of the fluorophore. Thus, for example, when the fluorophore is in close proximity to the metallic surface, K_{nr} will rise substantially by the increase in non-

radiative relaxation pathways (e.g. RET), having a quenching effect on the overall luminescence quantum yield (Q) and a reduction of lifetime (τ):

In close proximity to a metallic surface:

$\mathbf{K_{nr}} \uparrow$

Therefore: $Q \downarrow$; $\tau \downarrow$

Quenching

$$Q = \frac{\Gamma}{\Gamma + K_{nr}}$$

$$\tau = \frac{1}{\Gamma + K_{nr}}$$

On the other hand, the enhancement of fluorescence emission can be ascribed to a higher rate of excitation, which will result in an increased brightness but without any change in quantum yield or lifetime, or to an increase in the radiative decay rate by what is called Purcell effect. In the latter case, we can account for the increment of the radiative decay rate due to the MNP as the decay rate due to the metal "Γ_m". In this situation the quantum yield will rise, while the lifetime will be reduced:

Proximity to a metallic surface:

$(\Gamma + \mathbf{\Gamma_m}) > \Gamma$

Therefore: $Q \uparrow$; $\tau \downarrow$

Enhancement

$$Q = \frac{\Gamma + \Gamma_m}{\Gamma + \Gamma_m + K_{nr}}$$

$$\tau = \frac{1}{\Gamma + \Gamma_m + K_{nr}}$$

The proximity to the metallic surface is not the only parameter permitting one of the two effects (i.e. quenching or enhancement) to become dominant. In fact, the size of the MNP can have a major role in this regard. According to Mie theory, small MNP, up to ~40 nm in diameter, are expected to quench fluorescence as absorption is dominant over scattering phenomena. Above this size, scattering starts to gain importance over absorbance, consequently starting to exert an enhancement effect over the fluorophore emission.[19]

Thus, establishing the optimal AuNP size that yields the highest quenching of UCNPs' luminescence is important for the proper design of sensors based on UCNPs/AuNPs pairs. Besides, finding AuNPs' sizes that can increase the luminescence of UCNPs is interesting to design new kinds of sensors based on upconversion luminescence enhancement, and as a way to raise upconversion

efficiency by the use of plasmonic nanostructures. To carry out these studies, we synthesized citrate-stabilized AuNPs with increasingly bigger diameters by a seeded mediated growth method reported by Bastús et al.[21]

This strategy consists in the formation of small gold nanoparticles in an initial step, by the addition of chloroauric acid ($HAuCl_4$) to a boiling solution of sodium citrate. From this point on, the sequential addition of chloroauric acid ($HAuCl_4$) and sodium citrate permits to deposit gold atoms onto the surface of the previously formed nanoparticles in a controlled way (i.e. avoiding secondary nucleation and formation of new small AuNPs), which allows the growth of the original formed AuNPs used as seeds (Figure III.1.1.7). The completion of each growth step is accompanied by the extraction and storage of 55 mL from the reaction flask, while this volume is substituted by 53 mL water and 2 mL sodium citrate (60 mM) for the new growth step. Thus, this method is ideal to obtain AuNPs of increasingly bigger sizes from the same exact synthesis, which is very desirable for the kind of study that we carried out in publication 3.

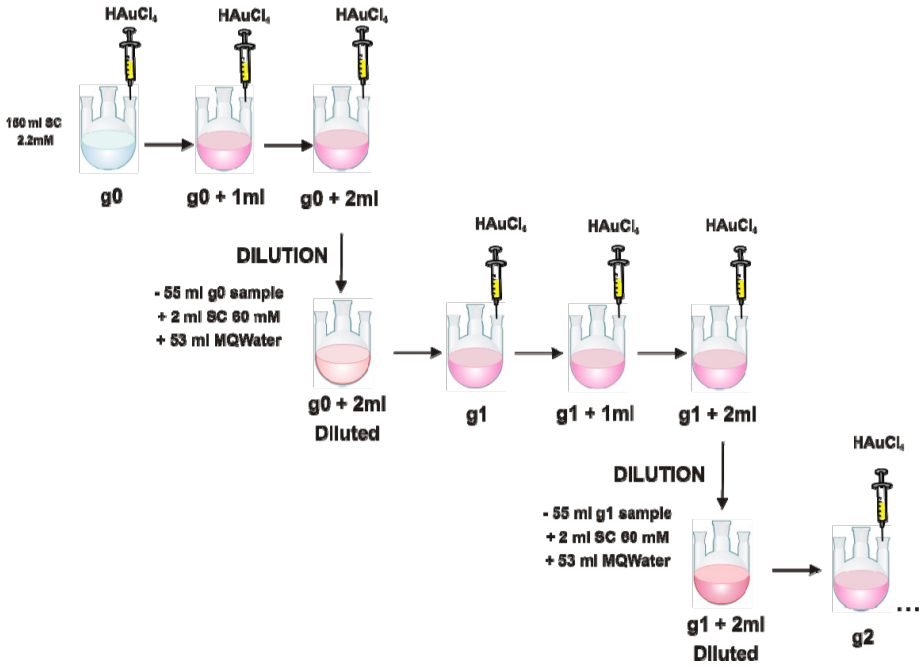

Figure III.1.1.7 General scheme for the seed-mediated growth method used for the synthesis of different sized AuNPs. The injection of $HAuCl_4$ to a boiling solution of sodium citrate generates the original Au seeds, which are subsequently grown by two more additions at 90 ºC of $HAuCl_4$ to a final size of around 20 nm (G0, G0 + 1 mL and G0 + 2 mL, respectively). From this point, 55 mL of the synthesis are extracted, 53 mL of water and 2 mL of citrate 60 mM are added to regenerate the reducing agent, and a new growth step is started.

References

(1) Chen, G.; Qiu, H.; Prasad, P. N.; Chen, X. Upconversion Nanoparticles: Design, Nanochemistry, and Applications in Theranostics. *Chem. Rev.* **2014**, *114*, 5161.

(2) Suter, J. D.; Pekas, N. J.; Berry, M. T.; May, P. S. Real-Time-Monitoring of the Synthesis of β-NaYF 4 :17% Yb,3% Er Nanocrystals Using NIR-to-Visible Upconversion Luminescence. *J. Phys. Chem. C* **2014**, *118*, 13238.

(3) Hudry, D.; Abeykoon, A. M. M.; Dooryhee, E.; Nykypanchuk, D.; Dickerson, J. H. Probing the Crystal Structure and Formation Mechanism of Lanthanide-Doped Upconverting Nanocrystals. *Chem. Mater.* **2016**, *28*, 8752.

(4) Ding, H. L.; Zhang, Y. X.; Wang, S.; Xu, J. M.; Xu, S. C.; Li, G. H. Fe3O4@SiO2 Core/Shell Nanoparticles: The Silica Coating Regulations with a Single Core for Different Core Sizes and Shell Thicknesses. *Chem. Mater.* **2012**, *24*, 4572.

(5) Darbandi, M.; Thomann, R.; Nann, T. Single Quantum Dots in Silica Spheres by Microemulsion Synthesis. *Chem. Mater.* **2005**, *17*, 5720.

(6) Vogt, C.; Toprak, M. S.; Muhammed, M.; Laurent, S.; Bridot, J.-L.; Müller, R. N. High Quality and Tuneable Silica Shell–magnetic Core Nanoparticles. *J. Nanoparticle Res.* **2010**, *12*, 1137.

(7) Kumar, A.; Mandal, S.; Selvakannan, P. R.; Pasricha, R.; Mandale, A. B.; Sastry, M. Investigation into the Interaction between Surface-Bound Alkylamines and Gold Nanoparticles. *Langmuir* **2003**, *19*, 6277.

(8) Lakowicz, J. R. *Principles of Fluorescence Spectroscopy*; Lakowicz, J. R., Ed.; Springer US: Boston, MA, 2006.

(9) Piston, D. W.; Kremers, G.-J. Fluorescent Protein FRET: The Good, the Bad and the Ugly. *Trends Biochem. Sci.* **2007**, *32*, 407.

(10) Li, Z.; Wang, L.; Wang, Z.; Liu, X.; Xiong, Y. Modification of NaYF4:Yb,Er@SiO2nanoparticles with Gold Nanocrystals for Tunable Green-to-Red Upconversion Emissions. *J. Phys. Chem. C* **2011**, *115*, 3291.

(11) Qian, L. P.; Zhou, L. H.; Too, H. P.; Chow, G. M. Gold Decorated NaYF4:Yb,Er/NaYF4/silica (Core/shell/shell) Upconversion Nanoparticles for Photothermal Destruction of BE(2)-C Neuroblastoma Cells. *J. Nanoparticle Res.* **2011**, *13*, 499.

(12) Liu, S.; Chen, G.; Ohulchanskyy, T. Y.; Swihart, M. T.; Prasad, P. N. Facile Synthesis and Potential Bioimaging Applications of Hybrid Upconverting and Plasmonic NaGdF4: Yb3+, Er3+/silica/gold Nanoparticles. *Theranostics* **2013**, *3*, 275.

(13) Liu, N.; Qin, W.; Qin, G.; Jiang, T.; Zhao, D. Highly Plasmon-Enhanced Upconversion Emissions from Au@β-NaYF 4:Yb,Tm Hybrid Nanostructures. *Chem. Commun.* **2011**, *47*, 7671.

(14) Clarke, C.; Liu, D.; Wang, F.; Liu, Y.; Chen, C.; Ton-That, C.; Xu, X.; Jin, D. Large-Scale Dewetting Assembly of Gold Nanoparticles for Plasmonic Enhanced Upconversion Nanoparticles. *Nanoscale* **2018**, *10*, 6270.

(15) Deng, W.; Sudheendra, L.; Zhao, J.; Fu, J.; Jin, D.; Kennedy, I. M.; Goldys, E. M. Upconversion in NaYF4:Yb, Er Nanoparticles Amplified by Metal Nanostructures. *Nanotechnology* **2011**, *22*.

(16) Melle, S.; Calderón, O. G.; Laurenti, M.; Mendez-Gonzalez, D.; Egatz-Gómez, A.; López-Cabarcos, E.; Cabrera-Granado, E.; Díaz, E.; Rubio-Retama, J. Förster Resonance Energy Transfer Distance Dependence from Upconverting Nanoparticles to Quantum Dots. *J. Phys. Chem. C* **2018**, *122*, 18751.

(17) Marin, R.; Labrador-Paéz, L.; Skripka, A.; Haro-González, P.; Benayas, A.; Canton, P.; Jaque, D.; Vetrone, F. Upconverting Nanoparticle to Quantum Dot Förster Resonance Energy Transfer: Increasing the Efficiency through Donor Design. *ACS Photonics* **2018**, *5*, 2261.

(18) Barnes, W. L. Fluorescence near Interfaces: The Role of Photonic Mode Density. *J. Mod. Opt.* **1998**, *45*, 661.

(19) Swierczewska, M.; Lee, S.; Chen, X. The Design and Application of Fluorophore–gold Nanoparticle Activatable Probes. *Phys. Chem. Chem. Phys.* **2011**, *13*, 9929.

(20) Gersten, J.; Nitzan, A. Spectroscopic Properties of Molecules Interacting with Small Dielectric Particles. *J. Chem. Phys.* **1981**, *75*, 1139.

(21) Bastús, N. G.; Comenge, J.; Puntes, V. Kinetically Controlled Seeded Growth Synthesis of Citrate-Stabilized Gold Nanoparticles of up to 200 Nm: Size Focusing versus Ostwald Ripening. *Langmuir* **2011**, *27*, 11098

III.1.3

Förster resonance energy transfer distance dependence from upconverting nanoparticles to quantum dots

(Publication 2)

https://pubs.acs.org/doi/10.1021/acs.jpcc.8b04908

THE JOURNAL OF PHYSICAL CHEMISTRY C

Article

Cite This: J. Phys. Chem. C 2018, 122, 18751−18758

pubs.acs.org/JPCC

Förster Resonance Energy Transfer Distance Dependence from Upconverting Nanoparticles to Quantum Dots

Sonia Melle,*[†] Oscar G. Calderón,[†] Marco Laurenti,[‡] Diego Mendez-Gonzalez,[‡] Ana Egatz-Gómez,[§] Enrique López-Cabarcos,[‡] E. Cabrera-Granado,[†] Elena Díaz,[∥] and Jorge Rubio-Retama*[,‡]

[†]Department of Optics, Complutense University of Madrid, E-28037 Madrid, Spain

[‡]Department of Chemistry in Pharmaceutical Sciences and [∥]GISC, Department of Materials Physics, Complutense University of Madrid, E-28040 Madrid, Spain

[§]Center for Applied Structural Discovery, Biodesign Institute, Arizona State University, Tempe, Arizona 85287, United States

Supporting Information

ABSTRACT: Förster resonant energy transfer (FRET) with upconverting nanoparticles (UCNPs) as donors and quantum dots (QDs) as acceptors has been regarded as a promising tool for biosensing applications. In this work, we use time-resolved luminescence spectroscopy to analyze the UCNP-to-QD FRET and we focus on the most relevant parameter of the FRET phenomenon, UCNP−QD distance. This distance is controlled by a nanometric silica shell around the UCNP surface. We theoretically reproduce the experimental results applying FRET theory to the distribution of emitting erbium ions in the UCNP. This simple model allows us to estimate the contribution of every erbium ion to the final FRET response and to explore different strategies to improve FRET efficiency.

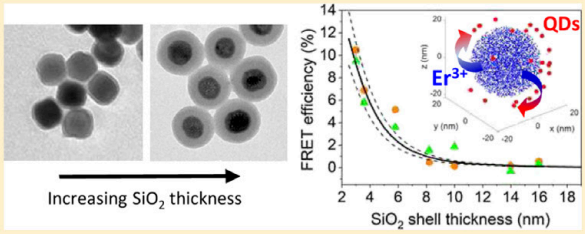

INTRODUCTION

Förster resonant energy transfer (FRET) is a physical process whereby the energy of a chromophore in the excited state (donor) can be transferred to a neighbor molecule that is in the ground state (acceptor), over a distance larger than the collisional radii. This phenomenon occurs when the donor and the acceptor are in close proximity, allowing the energy to be transferred without generation of any photons, through long-range dipole−dipole interactions.[1] The rate of the energy transfer depends on many different parameters, such as the extent of the spectral overlap between the emission spectrum of the donor and the absorption spectrum of the acceptor, the quantum yield of the donor, the relative orientation of the donor regarding the acceptor transition dipoles, and the distance between the donor and the acceptor.[2] The FRET's distance dependency has been crucial to detect two species in close proximity, enabling molecular rulers that can measure the distance between two specific molecules.[3] Such a feature in combination with the wide range of techniques for molecules and biomolecule functionalization with organic dyes has been applied to study the interaction between DNA, antigens, and proteins in vivo at the nanometer scale.[4]

During the last decades, advances in the synthesis of upconverting nanoparticles (UCNPs) with outstanding luminescence properties and higher photochemical stability than that of classical organic dyes have paved the way for analytical platforms using UCNP-based FRET systems.[5−12] Lanthanide-doped UCNPs are a special type of materials that are able to absorb low energy photons, typically in the near-infrared (NIR) wavelength, and emit UV−vis photons. Samples can be illuminated with high power densities of NIR light, with a high light penetration depth and without the risk of degradation or photobleaching, which is of especial interest for in vivo analyses.[12−15] Furthermore, the large anti-Stokes shift and the long lifetime allow us to separate the upconverting luminescence signal from biological sample autofluorescence, thus removing the background noise.[16] The narrow absorption and emission bands of UCNPs simplify the instrumentation for detecting and analyzing FRET processes.[17] However, the quantum efficiency in upconversion processes is rather low, and therefore, it is necessary to use an acceptor with high quantum yield and good spectral overlapping. Such requirements are fulfilled by quantum dots (QDs), which exhibit superb quantum yield and tunable absorption bands that can be adjusted to overlap with the emission band of the donor. Thus, the use of lanthanide-doped nanoparticles as donors and QDs as acceptors can be considered as ideal Förster pairs for bioassays.[18−21] Recently, Mattsson et al. have demonstrated a mix-and-measure UCNP-to-QD FRET system for rapid homogeneous bioassays for detecting analytes in aqueous solutions at nanomolar concentrations.[22]

A fundamental study of FRET between $NaYF_4:Er^{3+}/Yb^{3+}$ nanoparticles and CdSe QDs was reported by Bednarkiewicz et

Received: May 23, 2018
Revised: July 4, 2018
Published: July 10, 2018

al.[23] They observed an Er^{3+} upconversion luminescence lifetime decrease from 153 to 130 μs because of the presence of QDs. These authors suggested two strategies to increase FRET efficiency: (1) diminishing the size of the UCNPs and (2) distributing the lanthanide active ions only in the outer shell of a core/shell UCNP. In this context, Murh et al. have recently analyzed the efficiency of FRET from UCNPs to organic dyes for UCNPs of different sizes.[24] As the UCNP size decreases, two competing phenomena take place. On the one hand, an increasing percentage of the UCNP Er^{3+} ions becomes involved in FRET, increasing its efficiency. However, on the other hand, the surface-to-volume ratio increase leads to more luminescence quenching at the UCNP surface, which reduces FRET strength. They indeed found a maximum FRET efficiency for a 21 nm-sized UCNP. In addition, Bhuckory et al. have analyzed the efficiency of FRET between Er^{3+} ions distributed over either the core or the shell of UCNPs and Cy3.5 dye acceptors.[25] The authors use the FRET efficiency results to estimate parameters such as donor−acceptor (DA) distances and Er^{3+} donor quantum yields. Very recently, Marin et al.[26] have experimentally demonstrated enhanced FRET from $LiYF_4:Yb^{3+},Tm^{3+}$ UCNPs to $CuInS_2$ QDs by following two strategies: reducing the size of the UCNPs and doping the lanthanide active ions in the outer shell of a core/shell particle.

Despite these interesting works in UCNP-based FRET systems, to the best of our knowledge, no exhaustive studies of the FRET efficiency dependence on distance have been carried out. These systems are rather complex because the potential donors are distributed inside the UCNPs, which sizes are comparable to the length scale of FRET. This leads to a distribution of DA distances, a crucial key to the energy transfer phenomena. In this work, we present an in-deep study of the distance dependence of FRET in UCNP−QD systems with the aim of developing more efficient UCNP−QD FRET biosensors. To control the UCNP−QD distance, we cover the UCNPs with a nanometric silica shell. By varying the shell thickness, we analyze the change of the upconversion luminescence lifetime and, therefore, the FRET efficiency. Upconversion process involves many transitions and competing mechanisms, which makes it very difficult to isolate the real contribution of FRET to the energy transfer process. Here, we assume that energy transfer is most probably due to FRET. Then, the experimental results are interpreted by using FRET theory and taking into account the multiple distances between individual donor ions inside the UCNP and the FRET acceptors on its surface.

EXPERIMENTAL SECTION

Chemicals. $ErCl_3·6H_2O$ 99.9%, $YbCl_3·6H_2O$ 99.998%, $YCl_3·6H_2O$ 99.99%, oleic acid (OA) technical grade 90%, NH_4F 98%, NaOH 98%, methanol 99.9%, anhydrous *N*,*N*-dimethyl formamide 99.8%, 1-octadecene (1-ODE) technical grade 90%, *n*-hexane 97%, tetraethyl orthosilicate (TEOS) 98%, succinic anhydride 99%, NH_4OH ACS reagent 28−30%, IGEPAL CO-520, (3-aminopropyl)-triethoxysilane (APTES) 99%, and CdTe core-type QDs COOH functionalized (part number 777943) were acquired from Sigma-Aldrich and used as received.

Synthesis of $NaY_{0.78}F_4:Yb_{0.2},Er_{0.02}$. The synthesis of monodisperse UCNPs with a composition of $NaY_{0.78}F_4:Yb_{0.2},Er_{0.02}$ was performed by using the oleate route, which was first reported by Li and Zhang.[27] Briefly, 15 mL of 1-ODE and 6 mL of OA were mixed in a 100 mL round bottom flask with three necks. $YCl_3·6H_2O$ (233 mg; 0.78 mmol), 78 mg of $YbCl_3·6H_2O$ (0.2 mmol), and 7.9 mg of $ErCl_3·6H_2O$ (0.02 mmol) were mixed with the previous solution and heated up at 140 °C for 1 h under a constant magnetic stirring and N_2 flow to ensure the complete dissolution of the rare earths and obtain a transparent solution with a yellowish color. After this time, the solution is cooled down at room temperature and a fresh methanol solution is prepared by dissolving 100 mg of NaOH (2.5 mmol) and 148 mg of NH_4F (4 mmol). The methanol solution with NaOH and NH_4F is added dropwise to the rare earth solution and left stirring for 30 min at room temperature. Finally, the temperature is raised at 110 °C with a constant N_2 flow, kept for 15 min at this temperature and for other 10 min under vacuum to ensure the complete evaporation of methanol and water. The temperature of the resulting solution is then raised to 330 °C and kept at this temperature for 60 min. After this time, the reaction was quickly cooled down to room temperature. The UCNPs were separated by centrifugation: we split the product in four different centrifuge tubes and filled them with a solution 1/1 of H_2O and ethanol. Then, we centrifuged the tubes at 8000 rpm for 10 min. The supernatant was discarded and the nanoparticles were resuspended in 0.5 mL of *n*-hexane and then reprecipitated with ethanol and centrifuged again at 8000 rpm for 10 min. Finally the UCNPs were resuspended in 10 mL of *n*-hexane with a concentration of 12 g/L and stored for further experiments.

Preparation of $NaY_{0.78}F_4:Yb_{0.2},Er_{0.02}@SiO_2−NH_2$. The UCNPs were covered with different thicknesses of SiO_2, following the reverse microemulsion method.[28,29] IGEPAL CO-520 (240 μL) were mixed with 4 mL of *n*-hexane, 1 mL of UCNPs dispersed in the previous solution (12 g/L), and 40 μL of NH_4OH. The resulting solution was submitted to sonication until a transparent emulsion was formed. Different volumes of TEOS ranging from 10 to 30 μL were added depending on the desired SiO_2 shell thickness. The reaction was stopped after 18 h with the addition of methanol to disrupt the microemulsion, and then, it was centrifuged at 9000 rpm for 10 min, and the supernatant was discarded. This process was repeated three times to remove the excess of IGEPAL CO-520. Finally, the SiO_2 surface was functionalized with the amino groups by the addition of APTES (15 μL, 0.068 mmol) to the synthesized UCNPs@SiO_2 dispersed in 5 mL of ethanol. The heterogeneous solution was stirred overnight at room temperature, and the next day, the UCNPs@$SiO_2−NH_2$ were recovered by centrifugation at 9000 rpm for 10 min. The supernatant was discarded and the nanoparticles were redispersed in ethanol. This process was repeated three times.

Morphological Characterization. Transmission electron microscopy (TEM) images were acquired using a JEOL JEM 1010 microscope operated at 80 kV (JEOL, Japan; 80 kV) equipped with a digital camera Gatan MegaView II. High-resolution TEM (HRTEM) and low-angle annular dark field scanning TEM images were acquired using a JEOL JEM 3000F operated at 300 kV and a Gatan ADF detector.

Optical Characterization. Absorbance spectra of QDs water solutions at different concentrations were measured using a UV−vis spectrometer (Ocean Optics, Red Tide 650) with 3 mm path length cuvettes.

Upconversion luminescence spectra were recorded with a fluorescence home-built system. The excitation beam comes from a pigtailed 10 W CW laser (JDSU, L4-9897603) working at 976 nm and provided with a current and temperature controller (ILX Lightwave, LDX-36025-12 and LDT-5525B, respectively). The laser beam is transmitted through a long-pass dichroic filter

DOI: 10.1021/acs.jpcc.8b04908
J. Phys. Chem. C 2018, 122, 18751−18758

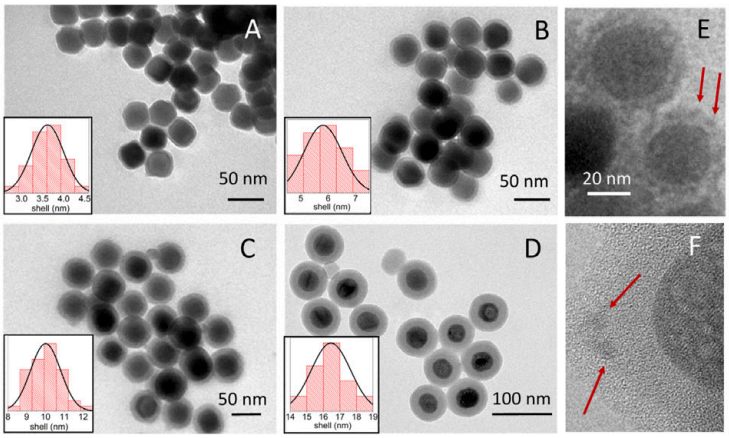

Figure 1. TEM micrographs of the synthesized $NaYF_4$:Yb,Er@SiO_2 nanoparticles with different SiO_2 shell thicknesses: (A) (3.6 ± 0.4), (B) (5.8 ± 0.7), (C) (10.0 ± 0.8), and (D) (16 ± 1) nm. (E) TEM and (F) HRTEM micrographs after attaching CdTe QDs (marked with arrows) on the surface of the $NaYF_4$:Yb,Er@SiO_2 nanoparticles.

(Semrock, FF757-Di01) and then focused on the sample with a 10× objective. The upconversion photoluminescence coming from the sample is reflected by the dichroic mirror toward a short-pass filter which blocks the IR reflected radiation (Semrock, FF01-775/SP). Then, it is focused into an optical fiber connected to a monochromator (HORIBA Jobin Yvon, iHR320). The monochromator is equipped with a photomultiplier tube (PMT) (HAMAMATSU, R928) and uses a 1200 g/mm grating blazed at 900 nm. To characterize the laser intensity in the sample, we measure the laser power with a thermal sensor power meter (Thorlabs, S310C) and the beam size using the slit scan technique.[30] The beam size (half width at half-maximum) is around 150 μm. In our measurements, we use excitation laser powers around 1.5 W, leading to laser intensities around 2 kW/cm^2. This allows us to ensure that the laser operates below the excitation saturation intensity of the transition $^2F_{7/2} \rightarrow {}^2F_{5/2}$ for the Yb^{3+} ions (see Figure 2B), which is $I_{sat} = \hbar\omega/(2\sigma\tau_{Yb}) = 3$ kW/cm^2, where $\tau_{Yb} = 2$ ms is the excited level lifetime, and $\sigma = 1.7 \times 10^{-20}$ cm^2 is the absorption cross-section.

Upconversion Emission Lifetime Measurements. Luminescence lifetimes were measured using the time-resolved photon counting method. Laser current is pulsed to generate excitation pulses of 40 μs with a repetition rate of 125 Hz. The luminescence emission at 540 nm is detected by the PMT, which is directly connected (without using a pre-amplifier) to a 50 Ω input of a digital oscilloscope (Agilent, DSO9104A). The signal from the laser current controller is used to trigger the oscilloscope. We developed a MATLAB program that analyzes directly in the oscilloscope each recorded signal in real-time. This code simulates the discriminator and the multichannel counter.[31] Upon analysis of more than 5000 trigger signals, we obtain a luminescence decay curve. Decay curve measurements were repeated at least three times for each sample under the same experimental conditions.

■ RESULTS AND DISCUSSION

To study the distance dependence of energy transfer between UCNP and QD pairs, we covered the surface of the UCNPs with a controlled thickness, uniform, amorphous silica layer. TEM micrographs from the as-synthesized UCNPs@SiO_2–NH_2 show highly monodisperse UCNPs with a mean diameter of (33 ± 3) nm (see Figure 1). We varied the SiO_2 shell thickness from 3 to 16 nm. As an example, Figure 1 shows TEM images for UCNPs@SiO_2–NH_2 with different silica shell thicknesses: (A) 3.6, (B) 5.8, (C) 10, and (D) 16 nm. After surface modification with amine groups, the $NaYF_4$:Yb,Er@SiO_2–NH_2 nanoparticles have a z-potential of +22 mV. CdTe QDs have an average diameter of 3 nm. QDs are functionalized with carboxylic groups and have a z-potential of −27 mV, so strong electrostatic interaction between positively charged UCNPs and negatively charged QDs will occur.

We prepared a solution containing UCNPs@SiO_2–NH_2 and CdTe–COOH QDs. First, the UCNPs@SiO_2–NH_2 were dispersed in ethanol at 5 g/L (1×10^{-7} M), while the CdTe–COOH QDs were dispersed in distilled water at 2.5 g/L (5×10^{-5} M). Then, we mixed equal volumes of the ethanol solution with the UCNPs@SiO_2–NH_2 and the aqueous solution with the CdTe–COOH QDs, so that an excess of QDs was used (QDs–UCNPs ratio of 478). A similar ratio has been used by Marin et al.[26] Negatively charged QDs were electrostatically adsorbed on the surface of positively charged UCNPs, as shown in the TEM and HRTEM images of Figure 1E,F, respectively. Single drops of this mixture were placed on a filter paper and allowed to dry at room temperature in air. The filter paper containing the mixture was set between two microscope glass slides for optical characterization.

As a reference, in the same way we prepared a filter paper with a drop of the ethanol solution containing UCNPs@SiO_2–NH_2 and distilled water without QDs mixed in equal volumes (hereafter named series I). In this reference sample, we use the same UCNP concentration than that of the sample with both UCNPs and QDs, while avoiding possible changes in the contributions to luminescence quenching due to water.[5] In a second experiment (hereafter, referred to as series II), the reference sample is made by using only the ethanol solution containing UCNPs@SiO_2–NH_2. In this last case, the possible effect of water was accounted for by taking into consideration that energy transfer between UCNPs and QDs should be negligible at very large UCNP–QD distances. This allows us to test the robustness of our experiments.

Figure 2A shows the optical characterization for the as-synthesized donors (UCNPs) and the acceptors (QDs) used in the FRET system under consideration. The upconversion

DOI: 10.1021/acs.jpcc.8b04908
J. Phys. Chem. C 2018, 122, 18751–18758

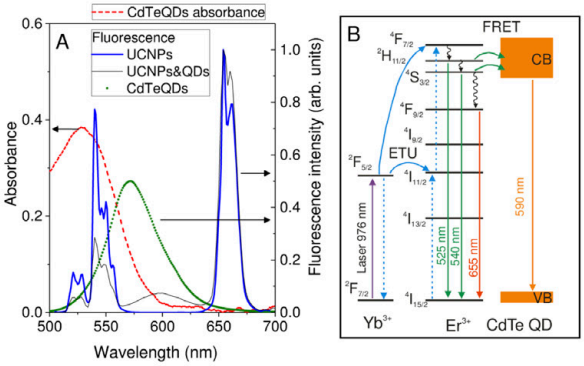

Figure 2. (A) (Left axis) Absorbance spectrum for 0.5 g/L water solution of CdTe QDs in a 3 mm cuvette (red curve). (Right axis) Fluorescence spectrum for: CdTe QDs water solution when excited at 455 nm (green curve), UCNPs@SiO_2 ethanol solution when excited at 976 nm (blue curve), and UCNPs@SiO_2 (3 nm-shell) with QDs dry sample when excited at 976 nm (black curve). (B) ETU scheme for populating the green emission levels $^2H_{11/2}$ and $^4S_{3/2}$ by a 976 nm laser and FRET scheme from these levels to the CdTe QD.

luminescence emission spectrum of $NaYF_4$:Yb,Er@SiO_2 nanoparticles under a 976 nm CW excitation laser is shown in Figure 2A (blue curve, right axis). Two green emission peaks near 525 and 540 nm are observed. These peaks correspond to $^2H_{11/2} \rightarrow {}^4I_{15/2}$ and $^4S_{3/2} \rightarrow {}^4I_{15/2}$ transitions of the Er^{3+} ions, respectively (see in Figure 2B, the energy transfer upconversion (ETU) mechanism populating these two levels). A red emission, with similar intensity, near 655 nm is also observed because of $^4F_{9/2} \rightarrow {}^4I_{15/2}$ transition (see Figure 2B). Figure 2A also shows the absorbance of a CdTe QDs water solution with 0.5 g/L in a 3 mm path length cuvette (red curve, left axis). Notice that the size of the QDs can be inferred from the position of their absorption peak.[32,33] In our case, we found an absorption peak around 529 nm, that gives us an estimation of the QDs size of 3 nm, in good agreement with that obtained from HRTEM images. Therefore, because the green emission bands of the UCNPs (donors) perfectly overlap with the absorption peak of the QDs (acceptors), the possibility of an efficient nonradiative energy transfer from UCNPs to QDs is ensured provided that both are close enough. Additionally, the QDs fluorescence emission spectrum under excitation by a LED radiation at 455 nm is shown in Figure 2A (green curve, right axis). The QDs orange emission band whose peak is around 572 nm does not overlap with the emission bands of the Er^{3+} ions avoiding mixed fluorescent emissions.

Now, let us test the interaction between UCNPs and QDs. Figure 2A shows the luminescence emission spectrum from the dry sample containing UCNPs with QDs electrostatically adsorbed on their surface (black curve, right axis). There, a new emission peak around 600 nm and a reduction of the green emission bands of the UCNPs are observed. Both features reveal that QDs are being excited by the $^4S_{3/2}$, $^2H_{11/2} \rightarrow {}^4I_{15/2}$ transitions of the Er^{3+} ions. Note that QDs cannot be excited with the IR radiation that excites the UCNPs. The emission peak arising from the QDs fluorescence appears as red-shifted respect to that obtained for the QDs solution excited under UV light. This is due to the inner filter effect that becomes relevant when increasing the QDs concentration during the drying process (see Figure S1). A similar shift was previously reported in UCNP−QD dried samples.[23]

Because the reduction of the UCNPs green luminescence intensity is due to both nonresonant energy transfer and reabsorption, to characterize in detail the Er^{3+} to QD FRET mechanism, luminescence lifetime studies are needed. Thus, luminescence decay signals for Er^{3+} ions at 540 nm ($^4S_{3/2} \rightarrow {}^4I_{15/2}$) were measured. As an example, Figure 3 shows the

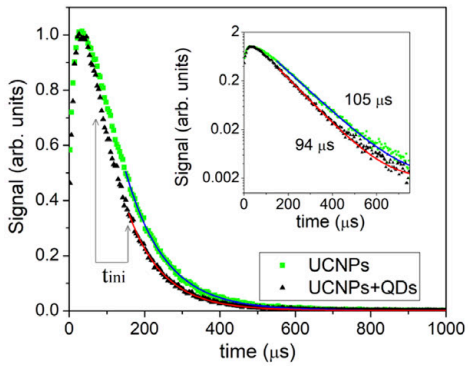

Figure 3. Normalized luminescence decay curves at 540 nm (transition $^4S_{3/2} \rightarrow {}^4I_{15/2}$) in the presence (black) or absence (green, series I) of CdTe QDs for UCNPs with a SiO_2 shell of 3 nm. Excitation laser at 976 nm with 40 μs pulses at 125 Hz. The arrows indicate the time range where the initial fitting time, t_{ini}, is varied. We set t_{final} = 1.2 ms. Inset: zoom of previous curves in a semilog scale.

luminescence intensity decay of UCNPs with a 3 nm silica shell, in the presence (black) and absence (green) of QDs. Fluorescence signals show an initial increase that is a signature of the upconversion process energy transfer from Yb^{3+} to Er^{3+} ions within the UCNPs, followed by an exponential decay. The luminescence decay time was obtained by fitting the decay curve to a single exponential function. For the fitting, we considered a time window from t_{ini} to t_{final}, where the final fitting time was set to t_{final} = 1.2 ms. For each experimental decay curve, we calculated around 25 fits by changing the initial fitting time t_{ini} within the range where the luminescence intensity varies from 70 to 30% of its maximum value. This fitting procedure gives us an average lifetime with its standard error. For the particular curve shown in Figure 3, the presence of the QDs reduces the luminescence lifetime from 104.7 ± 0.3 to 93.7 ± 0.2 μs. This decrease confirms the occurrence of nonradiative energy transfer from UCNPs to QDs. We have also corroborated that this energy transfer process produces a slow component (<100 μs) in the decay of the QD fluorescence at 590 nm, which otherwise would typically be in the nanosecond range (see the example in Figure S2 upper panel).

Once the FRET mechanism has been verified, its characterization is in order. FRET efficiency (E) can be computed from the experimental luminescence decay curves (as the ones shown in Figure 3) as

$$E = 1 - \frac{\tau_{DA}}{\tau_D} \quad (1)$$

where τ_D and τ_{DA} are the donor excited-state lifetime in the absence and in the presence of acceptor, respectively. For the particular case shown in Figure 3, an efficiency of E = (10.5 ± 0.4)% was achieved with a SiO_2 shell of 3 nm, which is quite high considering the relatively large diameter of the UCNPs (33 nm). Note that while luminescence emission comes from the Er^{3+} ions

DOI: 10.1021/acs.jpcc.8b04908
J. Phys. Chem. C 2018, 122, 18751−18758

distributed within the entire nanoparticle, ions far from the particle surface cannot participate in FRET.[22]

To analyze the behavior of FRET with the distance between the UCNPs and the QDs, we measured the luminescence decay times of UCNPs with different SiO_2 shell thicknesses, with and without QDs. The FRET efficiency as a function of shell thickness is plotted in Figure 4. The general trend is a fast

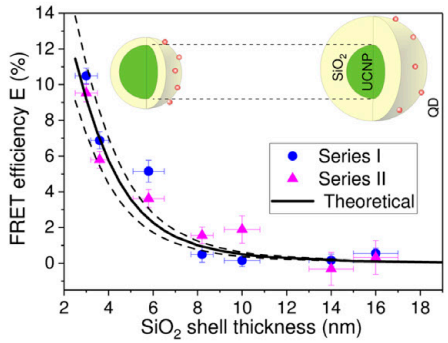

Figure 4. FRET efficiency, E, (eq 1) for different silica shell thicknesses on UCNPs with a diameter of 33 nm. Laser intensity: 1.7 kW/cm^2 (triangles), 2.4 kW/cm^2 (circles). Theoretical prediction of FRET efficiency (eq 7) for a Förster distance of R_0 = 5.5 nm and a number of QDs of 24 (solid line). Dashed lines correspond to the theoretical prediction under a variation of ±6 QDs.

decrease of the FRET efficiency for DA distances up to 12 nm, above which the energy transfer is negligible. A maximum FRET efficiency of around 10% is obtained, in agreement with the values reported in previous works.[23] We obtained similar results for the range of excitation laser intensities used in the experiments and also for the two reference samples, series I and II. Details on the method followed to take into account the water effect in series II are briefly described in the Supporting Information (see Table S1). The FRET efficiency curve calculated by measuring the luminescence decay signals at the QD emission channel, 590 nm, behaves as the one shown in Figure 4 (see Figure S2 lower panel).

Notice that our measurements do not show saturation of E as the silica shell thickness decreases, as it would be the case when dealing with a single DA pair. This feature is directly related to the fact of having a distribution of multiple donors (Er^{3+} ions) inside the UCNP as we will see later. Therefore, an estimation of the Förster radius R_0 from the experimental FRET efficiency curve cannot directly be obtained.

Theoretical FRET Efficiency. After analyzing the experimental data, let us now have a look at the theoretical counterpart for further interpretation of our results. The rate of energy transfer from a single donor to a single acceptor separated by a distance R is given by[2]

$$k_{ET} = \frac{9(\ln 10)}{128\pi^5 N_A n^4}\frac{\eta_D \kappa^2}{\tau_D R^6} J,$$
$$J = \int_{\Delta\lambda} F_D(\lambda)\epsilon_A(\lambda)\lambda^4 \, d\lambda \quad (2)$$

where N_A is the Avogadro's number, n is the refraction index of the medium surrounding the FRET pair, τ_D is the donor excited-state lifetime, and η_D is the intrinsic quantum yield of the donor in the absence of acceptor, that is, the quantum yield of the Er^{3+} ion excited state.[25] Note that $\eta_D = \tau_D/\tau_D^{rad}$, being τ_D^{rad} the radiative donor lifetime. Furthermore, κ^2 is a factor describing the relative orientation of the donor and the acceptor dipole moments, and the integral J measures the overlap between the donor emission spectrum and the acceptor absorption spectrum within the selected spectral donor emission region $\Delta\lambda$. Last, $F_D(\lambda)$ is the luminescence intensity of the donor normalized to the total intensity (i.e., $\int_{\Delta\lambda} F_D(\lambda)\, d\lambda = 1$), and $\epsilon_A(\lambda)$ is the molar extinction coefficient of the acceptor. In addition, the rate of energy transfer can be rewritten as

$$k_{ET} = \frac{1}{\tau_D}\left(\frac{R_0}{R}\right)^6 \quad (3)$$

where R_0 is the Förster distance defined as the distance at which half of the donor ions decay by transferring their energy to the acceptors, that is, the distance at which the energy transfer rate is equal to the donor decay rate in the absence of acceptor. By comparing eqs 2 and 3, one can obtain a closed expression for R_0 as follows

$$R_0 = 0.0211(\kappa^2 \eta_D n^{-4} J)^{1/6} \text{ [nm]} \quad (4)$$

where J is evaluated with the wavelength expressed in [nm] and the molar extinction coefficient in [M^{-1} cm^{-1}].

To estimate the Förster distance R_0, we calculate the overlap integral J from the experimental measurements of $\epsilon_A(\lambda)$ and $F_D(\lambda)$. The molar extinction coefficient of the QDs is obtained through the Beer–Lambert's law by measuring the absorbance at different concentrations and taking into account the cuvette path length (L = 3 mm). The result is shown in Figure 5. From

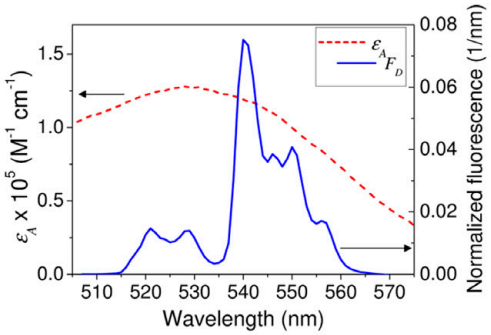

Figure 5. (Left axis) Molar extinction coefficient, $\epsilon_A(\lambda)$, of a 10^{-5} M QDs water solution in a cuvette with 3 mm path length. (Right axis) Upconversion luminescence intensity spectrum, $F_D(\lambda)$, (area under the curve in the green band region is normalized to unity) used to calculate the overlap integral J. Both represented as a function of the excitation wavelength λ.

the experimental data shown in Figure 5, the overlap integral results to be $J = 9.6 \times 10^{15}$ M^{-1} cm^{-1} nm^4. Note that this value can be roughly estimated by considering a nearly constant value of ϵ_A in the green region of the spectrum around $\lambda \simeq 540$ nm, which gives $J \simeq \epsilon_A \lambda^4 \simeq 10^{16}$ M^{-1} cm^{-1} nm^4.

Other important parameters necessary to evaluate eq 4 are κ, n, and η_D. The orientation factor of DA dipoles κ^2, is usually assumed to be 2/3; which corresponds to the dynamic random averaging. The material through which FRET mainly takes place is silica whose index of refraction is n = 1.46. Finally, the intrinsic quantum yield η_D, which measures the probability that donor de-excites radiatively in the absence of acceptor, has been estimated as around 20–30% by Bhuckory et al. from FRET measure-

DOI: 10.1021/acs.jpcc.8b04908
J. Phys. Chem. C 2018, 122, 18751–18758

ments of UCNPs with different core/shell architectures.[25] Note that this value is much larger than the one corresponding to the overall UCNP quantum yield. We estimate the intrinsic quantum yield by considering that the radiative lifetime for the excited-donor level ($^4S_{3/2}$) is in the millisecond range,[34] τ_D^{rad} = 0.5 ms and by using our experimental luminescence decay rate $\tau_D \simeq 105\ \mu s$. This leads to $\eta_D = \tau_D/\tau_D^{rad} \simeq 0.21$. For the sake of simplicity, we assume the quantum yield to be the same for all the UCNPs@SiO_2. This is reasonable because the donor lifetime obtained without QDs was quite similar throughout the range of silica shell thicknesses used in our experiments. Finally, by evaluating eq 4 with these parameters, our theoretical prediction for the Förster distance is $R_0 \simeq 5.5$ nm.

With this estimation in mind, to understand the observed dependency of the FRET efficiency on distance, we must consider the distribution of multiple DA pairs. First, let us express the transfer efficiency (i.e., the probability of de-excitation via energy transfer) of a single DA pair as

$$E_{Er-QD} = \frac{k_{ET}^{DA}}{1/\tau_D + k_{ET}^{DA}} = \frac{1}{1 + (R/R_0)^6} \quad (5)$$

From eq 5, we see how an Er^{3+} ion close to the UCNP external surface is able to transfer its energy to the QD for small silica shell thicknesses ($R < R_0$), whereas an ion close to the UCNP center will not be able to transfer its energy to the QD even in the absence of silica shell ($R > R_0$) (see Figure S3).

We consider that the energy transfer rate from each Er^{3+} ion inside the UCNP to all the QDs adsorbed onto its surface results from the sum of the single pair transfer rates: $k_{ET}^D = \sum_{A=1}^{N_{QD}} k_{ET}^{DA}(A)$, where N_{QD} is the total number of QD acceptors adsorbed onto the UCNP surface. Therefore, the FRET efficiency for each single Er^{3+} ion is

$$E_{Er-QDs} = \frac{\sum_{A=1}^{N_{QD}} k_{ET}^{DA}(A)}{1/\tau_D + \sum_{A=1}^{N_{QD}} k_{ET}^{DA}(A)} \quad (6)$$

Here, $k_{ET}^{DA}(A)$ results from the evaluation of eq 3 at the particular DA distance R for every case. Although we take N_{QD} as a fitting parameter in our simulations, we can roughly estimate this value from the TEM images as $N_{QD} \approx 20$. FRET efficiency is then calculated by averaging the efficiency of each Er^{3+} ion inside the nanoparticle

$$E = \langle E_{Er-QDs} \rangle_{N_{Er}} \quad (7)$$

Here, the number of Er^{3+} ions inside the nanoparticle is $N_{Er} = f_{Er} m_{NP} N_A / W = 4405$, where $f_{Er} = 0.019$ is the fraction of Er^{+3} ions, $W = 205.3$ g/mol is the molar weight of $NaYF_4$:Yb/Er, and $m_{NP} = 7.9 \times 10^{-17}$ g is the mass of the UCNP.

In our calculations, we generate a uniform random distribution of the Er^{3+} ions inside the UCNP,[35] and we compute the average FRET efficiency using eq 7 with the Förster distance calculated above, that is $R_0 = 5.5$ nm, and a number of QDs around the particle of 24. Our simulations result presented in Figure 4 (solid line) shows a very good agreement with the experimental data. We have also included in Figure 4 (dashed lines) theoretical curves with a different number of QDs, to account for the observed variation of the number of acceptors per UCNP in TEM images.

We conclude that the averaging process carried out when considering multiple DA configuration is needed to explain the FRET efficiency found in the experiments. For further analysis of this phenomenon, Figure 6 shows the distribution of FRET

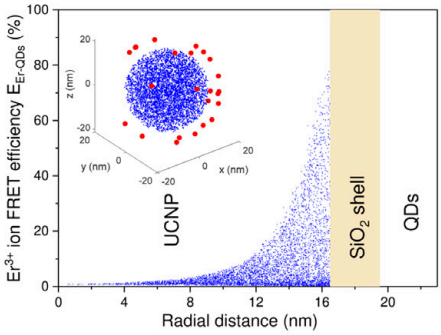

Figure 6. Distribution of the FRET efficiency achieved by each Er^{3+} ion inside an UCNP with 3 nm SiO_2 shell, E_{Er-QDs} (eq 6), as a function of the radial distance from the particle center. Inset: Distribution of Er^{3+} ions (blue points) inside a 33 nm UCNP with a SiO_2 shell of 3 nm and 24 QDs randomly adsorbed onto the particle-shell surface (red points).

efficiency for each Er^{3+} ion, E_{Er-QDs}, as a function of its radial distance to the particle center (blue points). Significant energy transfer, larger than 10%, occurs only for those ions placed farther than 11 nm from the UCNP center. This means that only the ions in close proximity to the UCNP external surface (≲5.5 nm) are susceptible to efficiently transfer their energy to the QDs. However, we observe a wide distribution on FRET efficiencies even for these superficial ions because the QDs are randomly distributed on the silica shell without completely covering the UCNP surface (see the inset in Figure 6).

Optimal Design of UCNPs for FRET Performance. As we mentioned in the Introduction, two different strategies have been used to increase the FRET efficiency in UCNP systems: reducing the UCNP size and developing inert-core/active-shell UCNP architectures.[25,26] In both cases, the fraction of active ions that can exhibit an efficient energy transfer increases. Marin et al.[26] have experimentally reported a two-fold FRET efficiency increase by applying these strategies to square-based bipyramidal shape UCNPs and QDs.

Let us use our theoretical approach to estimate the FRET efficiency that could be achieved under these two enhancement strategies for our particular UCNP−QD system. We consider UCNPs as the ones used in the experiments but with a tunable size inert-core, that is, particles with 33 nm of diameter, a silica shell of 3 nm, and we consider 24 QDs adsorbed onto the particle surface (see the particle scheme in Figure 7A). The quantum yield of particles with different inert-core diameters is expected to change. However, determining this magnitude is a challenging experimental problem, and as a first approximation, we consider here that all particles have roughly the same quantum yield, that is, the same Förster distance $R_0 = 5.5$ nm. Figure 7A shows the FRET efficiency and the number of Er^{3+} ions per nanoparticle as a function of the inert-core radius. We observe that to obtain a notable increase of FRET efficiency, an inert-core radius larger than half of the particle radius is required (see blue symbols in Figure 7A, left axis). Note that the reduction in the total number of Er^{3+} ions in a particle with an inert core is not significant until the inert core takes half of the particle radius (see black symbols in Figure 7A, right axis). We obtain a two-fold FRET efficiency increase when the inert radius is almost as large as the particle radius, that is, when the active shell is around 2 nm thick.

Finally, we now analyze the effect of the UCNP size on the FRET response. We consider UCNPs with diameter from 32 to

DOI: 10.1021/acs.jpcc.8b04908
J. Phys. Chem. C 2018, 122, 18751−18758

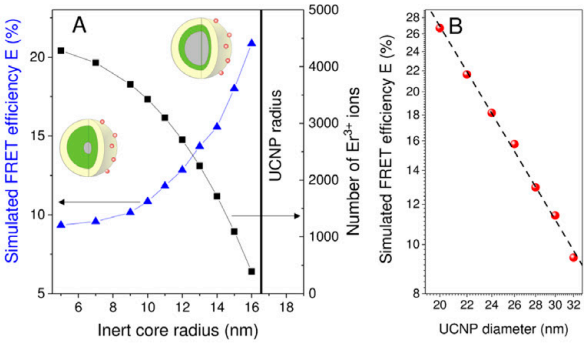

Figure 7. (A) Simulated FRET efficiency, E, from eq 7, (left axis) and total number of Er^{3+} ions inside each UCNP, N_{Er}, (right axis) as a function of the inert core radius for a particle with a diameter of 33 nm. (B) Simulated FRET efficiency, E, from eq 7, as a function of the UCNP diameter d_{NP} (symbols). The dashed line is the linear fit in the log−log plot.

20 nm, all particles with a 3 nm silica shell. The number of QDs adsorbed onto the UCNP surface and the donor quantum yield are properties that depend on the UCNP size; however, for the sake of simplicity, we consider the values previously used, that is, $N_{QD} = 24$ and $R_0 = 5.5$ nm. Figure 7B shows the FRET efficiency as a function of the UCNP size in a log−log plot. The linear fit shown in this figure (dashed line) indicates that the FRET efficiency follows a power law behavior with the UCNP diameter d_{NP} with an exponent close to minus 2, that is, $E \propto d_{NP}^{-2}$. Under these assumptions, the change of FRET efficiency is proportional to the nanoparticle area. For example, by reducing the UCNP diameter from 33 to 23 nm, therefore reducing the nanoparticle volume by 1/3, we calculate a FRET efficiency of around 20%, which is similar to our previously calculated efficiency for a 33 nm particle consisting of a 2 nm active-shell and a 31 nm inert-core and doubles the value measured in our experiments for the 33 nm diameter UCNPs. Similar increases in efficiency with reductions in the particle diameter have been experimentally reported in a previous work.[26]

CONCLUSIONS

We have studied the FRET phenomenon from UCNPs to QDs, which is a system with several advantages. The CdTe QDs exhibit a strong absorption band that perfectly overlaps with the luminescence emission band of the UCNPs. Furthermore, cross-excitation is avoided because the IR UCNP donor excitation does not produce fluorescence in the QD acceptors. We experimentally verified FRET between 33 nm diameter positively charged $NaYF_4$:Yb,Er@SiO_2−NH_2 particle donors and 3 nm diameter negatively charged CdTe−COOH QDs acceptors. In our system, several small CdTe QDs were adsorbed on each larger UCNP@SiO_2 surface by electrostatic interaction. This multiple acceptor configuration enhances the FRET response. The QD adsorption leads to a significant reduction of the upconversion luminescence lifetime, which clearly demonstrates that an additional decay pathway for the excited UCNPs takes place because of non-radiative energy transfer to the QDs. FRET is limited by the fact that the donor and acceptor must be in extreme close proximity. Considering the overlap between the donor emission spectrum and the acceptor absorption spectrum, we calculated a value for the Förster distance of $R_0 \simeq 5.5$ nm, assuming an intrinsic quantum yield of the Er^{3+} ions in the excited level $^4S_{3/2}$ of 0.21. This is a large value compared to the Förster radius characteristic of organic fluorophores of a few angstroms to 2 nm, but still small compared to the UCNP radius. We experimentally analyzed the effect of the UCNP−QD distance in the FRET efficiency by varying the thickness of the UCNPs silica shell from 3 to 16 nm. A maximum FRET efficiency of around 10% is achieved for the 3 nm silica shell, which is a remarkably large value if we take into account the distribution of all the potential donors, that is, Er^{3+} ions, inside the relatively large UCNP in comparison with the Förster distance. The UCNP-to-QD nonradiative interaction vanishes for distances above 12 nm.

We have theoretically explained the experimental results by calculating the FRET efficiency of each single Er^{3+} ion−QD pair and averaging the FRET response of every Er^{3+} ion inside the UCNP. Therefore, to theoretically obtain accurate values of the FRET efficiency in UCNP-based FRET systems, this averaging process is required. Indeed, we were able to establish that only Er^{3+} ions placed in close proximity to the UCNP surface, in a shell of around 5 nm (similar to the Förster distance), are able to participate in an energy transfer process with $E > 10\%$.

In summary, our work supports that the main physical characteristics governing the UCNP-to-QD energy transfer process is the relative spatial configuration of donors and acceptors. Our results show that the as-proposed UCNP−QD FRET system is a good potential platform for biosensing short biomolecules whose length of interaction is below the estimated Förster distance (≤6 nm). Nanoparticle systems with alternative architectures, as the ones discussed in this work, can be used to improve the distribution of DA distances for more efficient FRET-based biosensing applications.

ASSOCIATED CONTENT

Supporting Information

The Supporting Information is available free of charge on the ACS Publications website at DOI: 10.1021/acs.jpcc.8b04908.

Fluorescence spectrum of CdTe QDs excited at 455 nm: water solution and dried sample; FRET analysis at the acceptor QDs emission channel (590 nm); experimental FRET efficiency calculation from lifetimes; and theoretical FRET efficiency of a single Er^{3+} ion to a single QD (PDF)

AUTHOR INFORMATION

Corresponding Authors

*E-mail: smelle@fis.ucm.es (S.M.).
*E-mail: bjrubio@ucm.es (J.R.-R.).

ORCID

Sonia Melle: 0000-0002-9802-6908
Marco Laurenti: 0000-0002-0273-7423
Jorge Rubio-Retama: 0000-0002-1785-5844

Notes

The authors declare no competing financial interest.

ACKNOWLEDGMENTS

This work was supported by Universidad Complutense de Madrid and Santander Bank (PR26/16-12B), Ministerio de Economía y Competitividad-MINECO (MAT2016-75955, MAT2017-83111R), The European Upconversion Network COST Action CM1403 (2014-2018), and Comunidad de Madrid (B2017/BMD-3867 RENIM-CM) co-financed by European Structural and Investment Fund. D.M.-G. thanks

DOI: 10.1021/acs.jpcc.8b04908
J. Phys. Chem. C 2018, 122, 18751−18758

UCM-Santander for a predoctoral contract (CT17/17-CT18/17). TEM images were obtained at the National Center for Electron Microscopy (UCM, Madrid) facility.

REFERENCES

(1) Förster, T. Zwischenmolekulare Energiewanderung und Fluoreszenz. *Ann. Phys.* **1948**, *437*, 55−75.
(2) Lakowicz, J. R. *Principles of Fluorescence Spectroscopy*, 3rd ed.; Springer: New York, USA, 2006.
(3) Stryer, L.; Haugland, R. P. Energy Transfer: A Spectroscopic Ruler. *Proc. Natl. Acad. Sci. U.S.A.* **1967**, *58*, 719−726.
(4) Byrne, A. G.; Byrne, M. M., III; Gemmill, K. B.; Spillmann, C.; Medintz, I.; Sloan, S. L.; van der Meer, B. W. *FRET Förster Resonance Energy Transfer*; Wiley-Blackwell, 2013; Chapter 14, pp 655−755.
(5) Riuttamäki, T.; Hyppänen, I.; Kankare, J.; Soukka, T. Decrease in Luminescence Lifetime Indicating Nonradiative Energy Transfer from Upconverting Phosphors to Fluorescent Acceptors in Aqueous Suspensions. *J. Phys. Chem. C* **2011**, *115*, 17736−17742.
(6) Vetrone, F.; Naccache, R.; Morgan, C. G.; Capobianco, J. A. Luminescence Resonance Energy Transfer from an Upconverting Nanoparticle to a Fluorescent Phycobiliprotein. *Nanoscale* **2010**, *2*, 1185−1189.
(7) Kuningas, K.; Päkkilä, H.; Ukonaho, T.; Rantanen, T.; Lövgren, T.; Soukka, T. Upconversion Fluorescence Enables Homogeneous Immunoassay in Whole Blood. *Clin. Chem.* **2007**, *53*, 145−146.
(8) Jiang, S.; Zhang, Y. Upconversion Nanoparticle-Based FRET System for Study of siRNA in Live Cells. *Langmuir* **2010**, *26*, 6689−6694.
(9) Chen, N.-T.; Cheng, S.-H.; Liu, C.-P.; Souris, J.; Chen, C.-T.; Mou, C.-Y.; Lo, L.-W. Recent Advances in Nanoparticle-Based Förster Resonance Energy Transfer for Biosensing, Molecular Imaging and Drug Release Profiling. *Int. J. Mol. Sci.* **2012**, *13*, 16598−16623.
(10) Ding, Y.; Wu, F.; Zhang, Y.; Liu, X.; de Jong, E. M. L. D.; Gregorkiewicz, T.; Hong, X.; Liu, Y.; Aalders, M. C. G.; Buma, W. J.; et al. Interplay between Static and Dynamic Energy Transfer in Biofunctional Upconversion Nanoplatforms. *J. Phys. Chem. Lett.* **2015**, *6*, 2518−2523.
(11) Huang, Y.; Hemmer, E.; Rosei, F.; Vetrone, F. Multifunctional Liposome Nanocarriers Combining Upconverting Nanoparticles and Anticancer Drugs. *J. Phys. Chem. B* **2016**, *120*, 4992−5001.
(12) DaCosta, M. V.; Doughan, S.; Han, Y.; Krull, U. J. Lanthanide Upconversion Nanoparticles and Applications in Bioassays and Bioimaging: A Review. *Anal. Chim. Acta* **2014**, *832*, 1−33.
(13) Liu, J.; Liu, Y.; Bu, W.; Bu, J.; Sun, Y.; Du, J.; Shi, J. Ultrasensitive Nanosensors Based on Upconversion Nanoparticles for Selective Hypoxia Imaging in Vivo upon Near-Infrared Excitation. *J. Am. Chem. Soc.* **2014**, *136*, 9701−9709.
(14) Nyk, M.; Kumar, R.; Ohulchanskyy, T. Y.; Bergey, E. J.; Prasad, P. N. High Contrast in Vitro and in Vivo Photoluminescence Bioimaging Using Near Infrared to Near Infrared Up-Conversion in Tm3+and Yb3+Doped Fluoride Nanophosphors. *Nano Lett.* **2008**, *8*, 3834−3838.
(15) Zhou, J.; Liu, Z.; Li, F. Upconversion Nanophosphors for Small-Animal Imaging. *Chem. Soc. Rev.* **2012**, *41*, 1323−1349.
(16) Zwier, J. M.; Hildebrandt, N. In *Reviews in Fluorescence 2016*; Geddes, C. D., Ed.; Springer: Cham, 2016; pp 17−43.
(17) Mendez-Gonzalez, D.; Lopez-Cabarcos, E.; Rubio-Retama, J.; Laurenti, M. Sensors and Bioassays Powered by Upconverting Materials. *Adv. Colloid Interface Sci.* **2017**, *249*, 66−87.
(18) Charbonnière, L. J.; Hildebrandt, N.; Ziessel, R. F.; Löhmannsröben, H.-G. Lanthanides to Quantum Dots Resonance Energy Transfer in Time-Resolved Fluoro-Immunoassays and Luminescence Microscopy. *J. Am. Chem. Soc.* **2006**, *128*, 12800−12809.
(19) Doughan, S.; Han, Y.; Uddayasankar, U.; Krull, U. J. Solid-Phase Covalent Immobilization of Upconverting Nanoparticles for Biosensing by Luminescence Resonance Energy Transfer. *ACS Appl. Mater. Interfaces* **2014**, *6*, 14061−14068.
(20) Cui, S.; Xu, S.; Song, H.; Xu, W.; Chen, X.; Zhou, D.; Yin, Z.; Han, W. Highly Sensitive and Selective Detection of Mercury Ions Based on Up-conversion FRET from NaYF4:Yb3+/Er3+ Nanophosphors to CdTe Quantum Dots. *RSC Adv.* **2015**, *5*, 99099−99106.
(21) Hildebrandt, N.; Spillmann, C. M.; Algar, W. R.; Pons, T.; Stewart, M. H.; Oh, E.; Susumu, K.; Díaz, S. A.; Delehanty, J. B.; Medintz, I. L. Energy Transfer with Semiconductor Quantum Dot Bioconjugates: A Versatile Platform for Biosensing, Energy Harvesting, and Other Developing Applications. *Chem. Rev.* **2017**, *117*, 536−711.
(22) Mattsson, L.; Wegner, K. D.; Hildebrandt, N.; Soukka, T. Upconverting Nanoparticle to Quantum Dot FRET for Homogeneous Double-nano Biosensors. *RSC Adv.* **2015**, *5*, 13270−13277.
(23) Bednarkiewicz, A.; Nyk, M.; Samoc, M.; Strek, W. Up-conversion FRET from Er3+/Yb3+:NaYF4 Nanophosphor to CdSe Quantum Dots. *J. Phys. Chem. C* **2010**, *114*, 17535−17541.
(24) Muhr, V.; Würth, C.; Kraft, M.; Buchner, M.; Baeumner, A. J.; Resch-Genger, U.; Hirsch, T. Particle-Size-Dependent Förster Resonance Energy Transfer from Upconversion Nanoparticles to Organic Dyes. *Anal. Chem.* **2017**, *89*, 4868−4874.
(25) Bhuckory, S.; Hemmer, E.; Wu, Y.-T.; Yahia-Ammar, A.; Vetrone, F.; Hildebrandt, N. Core or Shell? Er3+ FRET Donors in Upconversion Nanoparticles. *Eur. J. Inorg. Chem.* **2017**, 5186.
(26) Marin, R.; Labrador-Paéz, L.; Skripka, A.; Haro-González, P.; Benayas, A.; Canton, P.; Jaque, D.; Vetrone, F. Upconverting Nanoparticle to Quantum Dot Förster Resonance Energy Transfer: Increasing the Efficiency through Donor Design. *ACS Photonics* **2018**, *5*, 2261−2270.
(27) Li, Z.; Zhang, Y. An Efficient and User-friendly Method for the Synthesis of Hexagonal-phase NaYF4:Yb, Er/Tm Nanocrystals with Controllable Shape and Upconversion Fluorescence. *Nanotechnology* **2008**, *19*, 345606.
(28) Alonso-Cristobal, P.; Lopez-Quintela, M. A.; Contreras-Caceres, R.; Lopez-Cabarcos, E.; Rubio-Retama, J.; Laurenti, M. Synthesis of Catalytically Active Gold Clusters on the Surface of Fe3O4@SiO2 Nanoparticles. *RSC Adv.* **2016**, *6*, 100614−100622.
(29) Zhelev, Z.; Ohba, H.; Bakalova, R. Single Quantum Dot-Micelles Coated with Silica Shell as Potentially Non-Cytotoxic Fluorescent Cell Tracers. *J. Am. Chem. Soc.* **2006**, *128*, 6324−6325.
(30) McCally, R. L. Measurement of Gaussian Beam Parameters. *Appl. Opt.* **1984**, *23*, 2227.
(31) Stacewicz, T.; Krainska-Miszczak, M. Time-resolved Photon Counting with Digital Oscilloscope. *Meas. Sci. Technol.* **1997**, *8*, 453−455.
(32) Yu, W. W.; Qu, L.; Guo, W.; Peng, X. Experimental Determination of the Extinction Coefficient of CdTe, CdSe, and CdS Nanocrystals. *Chem. Mater.* **2003**, *15*, 2854−2860.
(33) Dagtepe, P.; Chikan, V.; Jasinski, J.; Leppert, V. J. Quantized Growth of CdTe Quantum Dots; Observation of Magic-Sized CdTe Quantum Dots. *J. Phys. Chem. C* **2007**, *111*, 14977−14983.
(34) Weber, M. J. Radiative and Multiphonon Relaxation of Rare-Earth Ions inY2O3. *Phys. Rev.* **1968**, *171*, 283−291.
(35) Knuth, D. E. *The Art of Computer Programming, Vol. 2: Seminumerical Algorithms*, 3rd ed.; Addison-Wesley: Boston, USA, 1999.

DOI: 10.1021/acs.jpcc.8b04908
J. Phys. Chem. C 2018, 122, 18751−18758

Supporting Information:

FRET Distance Dependence from Upconverting Nanoparticles to Quantum Dots

Sonia Melle,*,† Oscar G. Calderón,† Marco Laurenti,‡ Diego Mendez-Gonzalez,‡ Ana Egatz-Gómez,¶ Enrique López-Cabarcos,‡ E. Cabrera-Granado,† Elena Díaz,§ and Jorge Rubio-Retama*,‡

†*Department of Optics, Complutense University of Madrid, E-28037 Madrid, Spain*

‡*Department of Chemistry in Pharmaceutical Sciences, Complutense University of Madrid, E-28040 Madrid, Spain*

¶*Center for Applied Structural Discovery, Biodesign Institute, Arizona State University, Tempe, Arizona 85287, USA*

§*GISC, Department of Materials Physics, Complutense University of Madrid, E-28040 Madrid, Spain*

E-mail: smelle@fis.ucm.es; bjrubio@ucm.es

Contents

Fluorescence spectrum of CdTe QDs excited at 455 nm: water solution and dried sample.

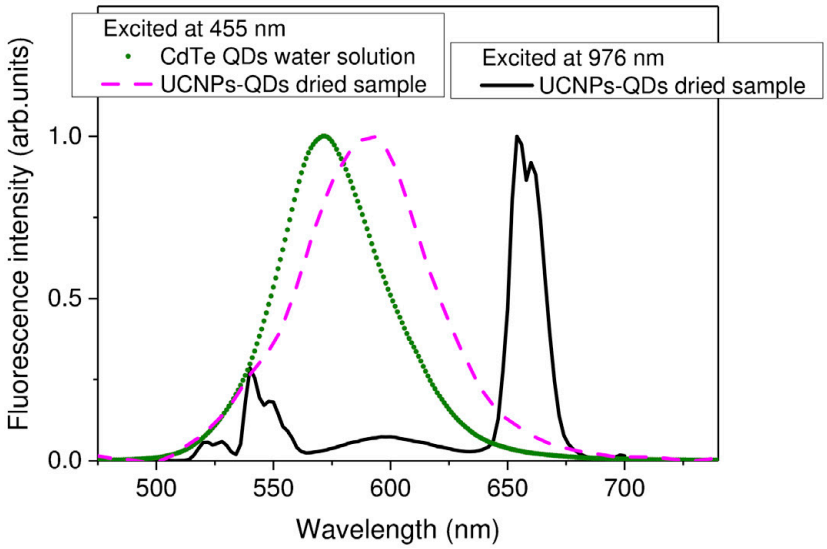

Figure S1: Fluorescence spectrum of the CdTe QDs water solution when excited at 455nm (dotted line). Luminescence spectrum of the dried sample containing UCNPs@SiO_2 (3 nm-shell) with QDs when excited at: 455 nm (dashed line), and 976 nm (solid line).

FRET analysis at the acceptor QDs emission channel (590 nm).

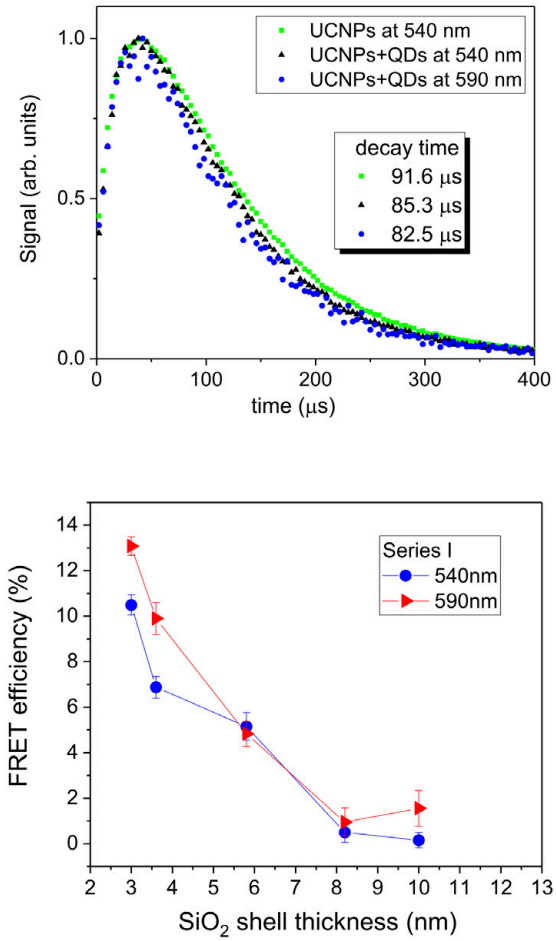

Figure S2: *Upper panel.* Normalized luminescence decay curves for UCNPs with a SiO_2 shell of 3.6 nm. Emission at 540 nm (transition $^4S_{3/2} \rightarrow {}^4I_{15/2}$ of Er^{3+} ion) in presence (black) or absence (green) of CdTe QDs. Emission at 590 nm (CdTe QD emission) (blue). *Lower panel.* FRET efficiency, E (equation 1), for different silica shell thicknesses. E calculated with the luminescence decay time at 540 nm (circle) and at 590 nm (triangle). Laser intensity 2.4 kW/cm^2 and series I.

Experimental FRET efficiency calculation from lifetimes.

FRET efficiency is computed from the experimental luminescence UCNP excited-state lifetimes in the absence (τ_D) and in the presence of QDs (τ_{DA}), as $E = 1 - \tau_{DA}/\tau_D$.

In series II, the reference sample was prepared without adding any water to the ethanol solution of UCNPs. However, the UCNP-QD sample was prepared using an aqueous solution of QDs. Thus, the decay time of the mixture sample includes the effect of water. By assuming that energy transfer is negligible at large SiO_2 shell thicknesses, both decay times at large thicknesses, with and without QDs, should match. We shifted down the decay time values of the reference sample $\tau_{D-nowater}$ to account for the reduction of the lifetime that could be associated to water.

In series I, the reference sample contains the same volume of water than the UCNP-QD sample. Thus, FRET efficiency is directly calculated from the decay times of the reference sample, τ_D, and the UCNP-QD sample, τ_{DA}. For example, for UCNPs with a silica shell thickness of 5.8 nm, we obtain $\tau_D = 92 \pm 1$ μs and $\tau_{DA} = 88 \pm 1$ μs, then $E = 5.2 \pm 0.6\%$.

Table S1: Experimental FRET efficiency calculation from time decays of series II

	3.6 nm	5.8 nm	8.2 nm	14 nm	16 nm
$\tau_{D-nowater}$ (μs)[a]	98 ± 1	97 ± 1	94.6 ± 0.9	91 ± 2	90 ± 2
τ_{DA} (μs)[b]	87.6 ± 0.6	89.0 ± 0.9	88.5 ± 0.8	86 ± 2	85 ± 2
τ_D (μs)[c]	93 ± 1	92 ± 1	90 ± 1	86 ± 2	85 ± 2
E (%)[d]	5.8 ± 0.5	3.6 ± 0.5	1.6 ± 0.5	-0.3 ± 0.9	0.3 ± 0.9

[a] Measured decay time for the reference sample (without QDs) without adding water;
[b] Measured decay time for the UCNP-QD sample;
[c] Corrected decay time for the reference sample to account for the effect of water. Both decay times, with and wihtout QDs, should match at large silica shell thicknesses (14 and 16 nm). $\tau_{D-nowater}$ is shifted down 4.7 μs;
[d] FRET efficiency calculated as $E = 1 - \tau_{DA}/\tau_D$.

Theoretical FRET efficiency of a single Er^{3+} ion to a single QD.

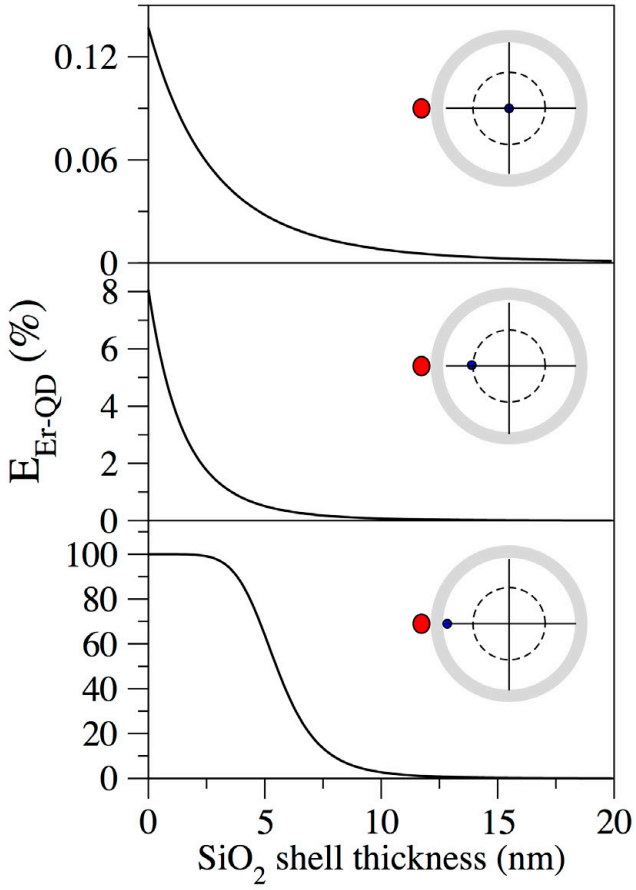

Figure S3: Theoretical FRET efficiency of a single Er^{3+} ion to a single QD calculated using equation 5 (E_{Er-QD}), versus the silica shell thickness. Different panels show different positions of the Er^{3+} ion inside the UCNP: at the center of the UCNP (upper panel), at half of the UCNP radius (center panel), at the external UCNP surface (lower panel). The ion is placed in the same direction as the QD.

III.1.4

Control of upconversion luminescence by gold nanoparticle size: from quenching to enhancement

(Publication 3)

Journal Name

ARTICLE TYPE

Cite this: DOI: 10.1039/xxxxxxxxxx

Control of upconversion luminescence by gold nanoparticle size: from quenching to enhancement†

Diego Mendez-Gonzalez,[a] Sonia Melle,*[b] Oscar G. Calderón,[b] Marco Laurenti,[a] E. Cabrera-Granado,[b] Ana Egatz-Gómez,[c,d] Enrique López-Cabarcos,[a] Jorge Rubio-Retama,[a] and Elena Díaz[e]

Received Date
Accepted Date

DOI: 10.1039/xxxxxxxxxx

www.rsc.org/journalname

Metallic nanostructures have the potential to modify the anti-Stokes emission of upconverting nanoparticles (UCNPs) by coupling their plasmon resonance with either the excitation or the emission wavelength of the UCNPs. In this regard gold nanoparticles (AuNPs) have been often used in sensors for UCNP luminescence quenching or enhancement, although systematic studies are still needed in order to design optimal UCNPs-AuNPs-based biosensors. Amidst mixed experimental evidence of these two phenomena, two key factors arise: nanoparticle distance and nanoparticle size. In this work, we synthesize AuNPs of different sizes to assess their influence on the luminescence of UCNPs. We find that strong luminescence quenching due to resonance energy transfer is preferentially obtained for small AuNPs, peaking at an optimal size. A further increase in AuNP size is accompanied by a reduction of luminescence quenching due to an incipient plasmonic enhancement effect. This enhancement counterbalance the luminescence quenching effect at the biggest tested AuNP size. The experimental findings are theoretically validated by studying the decay rate of the UCNP emitters near a gold nanoparticle using both a classical phenomenological model and the finite-difference time-domain method. Results from this study establish general guidelines to consider when designing sensors based on UCNPs-AuNPs as donor-quencher pairs, as well as suggest the potential of plasmon-induced luminescence enhancement as a sensing strategy.

Introduction

During the last years, lanthanide doped upconverting nanoparticles (UCNPs) have emerged as promising materials due to their capacity to exhibit photon upconversion.[1–4] UCNPs are able to absorb low-energy photons in the infrared or near infrared (NIR) range and emit high-energy photons in the UV-Vis range. This process can take place through different mechanisms, among them energy-transfer upconversion (ETU) and excited-state absorption (ESA) are by far the most common.[5–7]. These mechanisms involve multistep absorption of two or more photons by an intermediate meta-stable state that promotes the population of a highly excited state from which upconversion emission happens.[8]. That gives rise to a high conversion efficiency with no need for intense coherent excitation or ultra-fast laser sources, which are required for other nonlinear multiphoton processes. In addition, the large anti-Stokes shifts, and the lack of photo-bleaching and blinking provide special features to these nanoparticles that make them ideal candidates to create sensors and bioassays powered by UCNPs.[9,10] Many of these sensors exploit the so called resonance energy transfer (RET) as the action mechanism to detect a specific target molecule.[11,12] This is normally based on the energy transfer from the excited state of a UCNP (donor) to the ground state of a molecule or other material that acts as acceptor, resulting in a variation of the UCNP luminescence.[13]

Plasmonic nanostructures placed in close proximity to UCNPs have been demonstrated to be an excellent tool for tuning the upconversion luminescence by enhancing or quenching the luminescence intensity.[14] In the first case, the signal enhancement is

[a]Department of Chemistry in Pharmaceutical Sciences, Complutense University of Madrid, E-28040 Madrid, Spain
[b] Department of Optics, Complutense University of Madrid, E-28037 Madrid, Spain. E-mail: smelle@fis.ucm.es
[c] School of Molecular Sciences, Arizona State University, Tempe, Arizona 85287, United States.
[d] Center for Applied Structural Discovery, The Biodesign Institute, Arizona State University, Tempe, Arizona 85281, United States
[e] GISC, Department of Materials Physics, Complutense University of Madrid, E-28040 Madrid, Spain

† Electronic Supplementary Information (ESI) available: Analysis of the luminescence decay signals; Luminescence rise signals and absorbance spectra for dispersions containing 66nm-diameter AuNPs and APTES- and non-APTES-functionalized UCNPs; Description of the parameters used to simulate luminescence decay curves from UCNPs interacting with AuNPs. See DOI: 00.0000/00000000.

III.1.5 Conclusions

- Yb/Er doped UCNPs are suitable photoluminescent probes for the potential construction of homogeneous assays based on energy transfer processes using CdTe Q-dots or AuNPs as acceptors, as the green emission of the former suitably overlaps the absorption spectra of the latter.

- FRET between UCNPs and Q-dots has been demonstrated, achieving a maximum efficiency value of 10% for the thinner SiO_2 shell (3 nm) whereas a negligible value was obtained for distances above 12 nm.

- We obtained a Förster radius of R_0 = 5.5 nm, which is large if compared with R_0 from organic fluorophores but still small if compared with our UCNPs diameter (33 nm) to produce an effective FRET between most of the excited Er^{3+} ions and the Q-dots.

- Experimental results were successfully explained theoretically by calculating the FRET efficiency of each single Er^{3+}/Q-dot pair and averaging the response of each of these Er^{3+} ions inside the UCNP. We found out that only Er^{3+} ions within a 5 nm shell from the UCNPs' surface were able to experience a FRET efficiency > 10%.

- AuNPs of ~14 nm in diameter are optimum to efficiently quench luminescence from UCNPs by RET (i.e. ~40 % luminescence quenching).

- Increasingly bigger AuNPs raises the radiative decay rate from UCNPs' green level ($^4S_{3/2}$) by means of the Purcell effect, which translates in an upconversion luminescence enhancement of ~30% for 66 nm AuNPs, with the possibility to improve this effect with larger AuNP diameters.

III.2

Innovative strategies for heterogeneous assays with upconverting labels

III.2.1) Introduction

The use of heterogeneous assays is generally accompanied by several advantages over homogeneous assays: as they are usually based on the capture of analyte and reporter by a solid support, it is possible to use separation and washing steps that often translate in a sensitivity improvement. The fact that the analyte can be captured, labeled, and ultimately separated from the liquid sample also permits more reliable measurements, as it is measured in a "steady" instead of in a "dynamic" state, as it occurs with homogeneous assays. This also permits, especially when using upconverting nanoparticles as labels, a second measurement of the assay even months after the assay has been carried out.[1] Even more, the use of a 2D solid support allows to easily developing multiplexed detection assay formats, taking advantage of the spatial localization of different spots.

The unusual anti-stokes optical properties exhibited by UCNPs makes their non-specific binding the main source of background noise, as autofluorescence is directly avoided when using these as labels. This fact is in contrast to the vast majority of reporters, whose main sensitivity limitation comes from their detectability and which is constrained, for example, when their signal is hidden within the autofluorescence signal. Thus, the reduction of the amount of upconverting labels non-specifically bound to the solid support may potentially improve sensitivities in heterogeneous assays.
The use of stringent or even harsh washes may be used to reduce background noise by disrupting the non-specific interactions between UCNPs and the solid support. However, this will also lead to the denaturation between the capture probes and the target sequence aimed to be detected in oligonucleotide hybridization assays. As consequence, the specific signal coming from hybridization with the target will also be reduced, eventually avoiding an improvement of the signal-to-background ratio (Sg/bg ratio) and sensitivity (see Figure III.2.1.1).

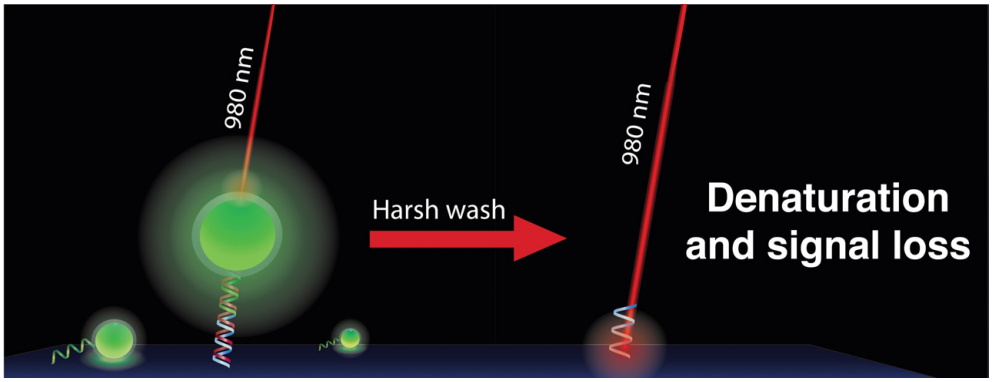

Figure III.2.1.1. Harsh washes can be used to reduce the background signal coming from non-specifically bound labels (UCNPs) to the solid support. However, it will also reduce the specific signal due to denaturation of the duplexes formed between the capture probes and the miRNA target sequence.

Nevertheless, if the presence of the target sequence could induce the formation of a covalent bond between the capture probes used for its detection, the situation would be different: The use of harsh washes would permit the reduction of the background signal while the specific signal coming from the target-induced covalent ligation of capture probes would be conserved, even when denaturation took place upon these washes (Figure III.2.1.2). This would translate in a higher Sg/Bg ratio and an improvement of the assay sensitivity.

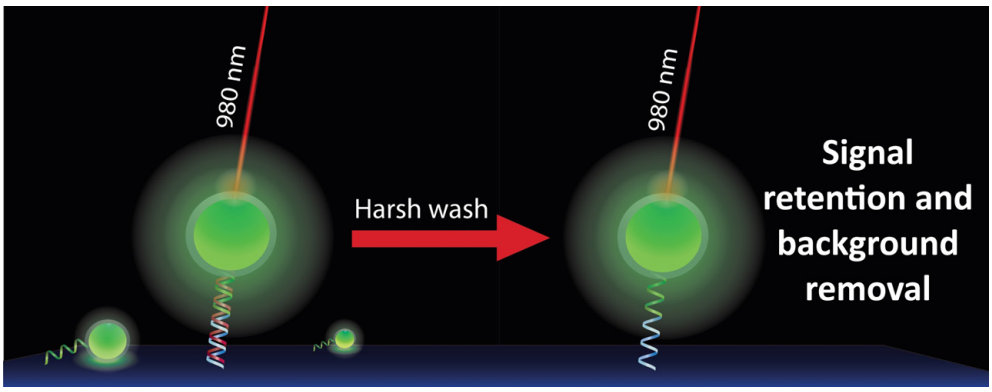

Figure III.2.1.2 The target-induced covalent ligation of capture probes upon hybridization would permit to use harsh washes to reduce the background signal, while conserving the specific signal generated by the target.

Two different heterogeneous assays using UCNPs as labels and different target-induced ligation strategies were developed and are presented in this section: "Oligonucleotide Sensor Based on Selective Capture of Upconversion Nanoparticles Triggered by Target-Induced DNA Interstrand Ligand Reaction" (Publication 4), and "Photochemical Ligation to Ultrasensitive DNA Detection with Upconverting Nanoparticles" (Publication 5).

In publication 4, the synthesis of UCNPs was carried out using the same strategy as the one described for publications 2 and 3. In brief, UCNPs were synthesized using the Ostwald ripening method, covered with a silica shell to turn them water-dispersible, and further modified with APTES. Aiming to use the resulting nanomaterials as upconverting labels (UC-labels), an additional synthetic step was performed: the reaction of the amino-modified UCNPs@SiO_2 with succinic anhydride to yield carboxylic acid surface-modified UCNPs. At this point, the carboxylated UCNPs were ready for their bioconjugation with single stranded DNA (ssDNA) probes by Sulfo-NHS/EDC coupling.

In this reaction, 1-ethyl-3-(3-dimethylaminopropyl)carbodiimide hydrochloride (EDC·HCl) was used to form an o-acylisourea with the carboxylic acid groups at the surface of UCNPs. This unstable intermediate allows the formation of an amide bond at room temperature between the activated carboxylic acids and the amine group from ssDNA (Figure III.2.1.3). As the o-acylisourea intermediate is unstable in water, it is common to use N-hydroxysulfosuccinimide (Sulfo-NHS) to prolong the EDC-mediated activation of the carboxylic acids, and thus improve the whole efficiency of the coupling process.

The conjugation of UCNPs with ssDNA was the last step on the synthesis of upconverting labels (UC-labels) for their use in the heterogeneous assays presented in this section.

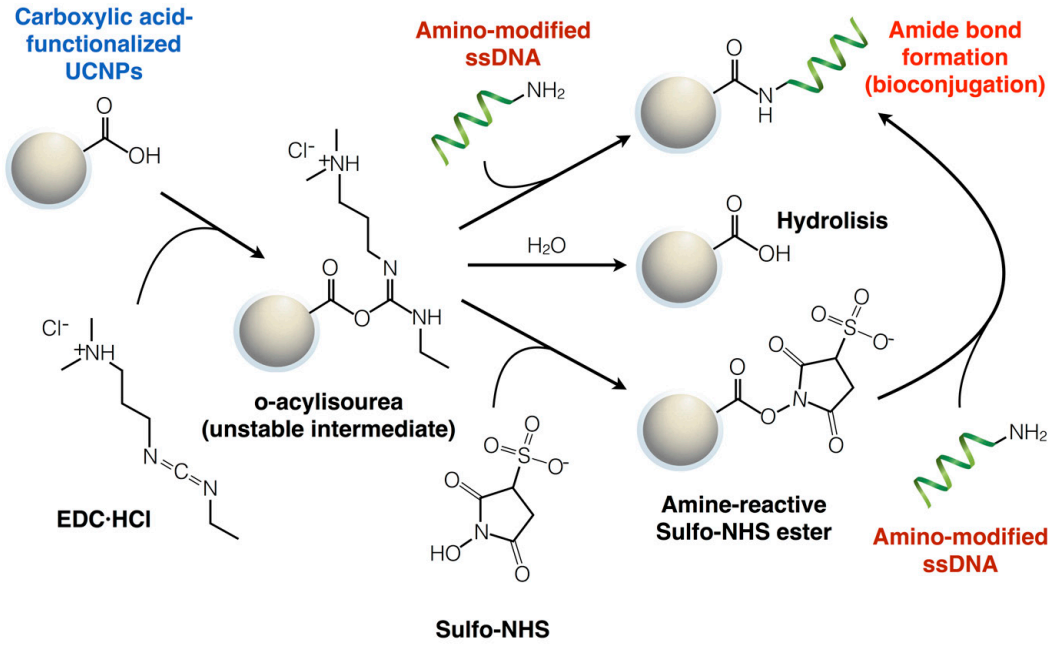

Figure III.2.1.3. Bioconjugation of carboxylic acid functionalized UCNPs with ssDNA-NH_2 via EDC·HCl/ Sulfo-NHS coupling reaction.

In contrast to the previous works, β-$NaYF_4$ nanoparticles with Yb^{3+} (40% wt relative to [Y^{3+} + Yb^{3+} + Tm^{3+}] = 100%) and Tm^{3+} (0.5% wt) as dopants, were synthesized by the Ostwald ripening method in publication 5, obtaining UV/blue-emitting upconverting nanoparticles. In this case, a second different strategy was used to make the resulting UCNPs water-dispersible, which was based on the ligand exchange of their capping agent (i.e. oleic acid) by poly-acrylic acid (PAA), see Figure III.2.1.4. This ligand exchange was carried out by first removing the oleate from the UCNPs' surface with HCl 0.1M. In this step, the acidic media allows the removal of oleate from the surface due to the formation of oleic acid, which is discarded in subsequent washes. After this, the resulting bare UCNPs are functionalized by the incorporation of a thin layer of PAA at pH=9. The fact that PAA is a polydentate ligand implies that once at the surface of the UCNPs, it will be strongly attached. Thus, the coating of UCNPs with a thin PAA layer is accompanied by certain advantages: A strongly bound coating, good colloidal stability in water, and the presence of carboxylic acid groups to eventually graft the ssDNA capture probes by Sulfo-NHS/EDC coupling.

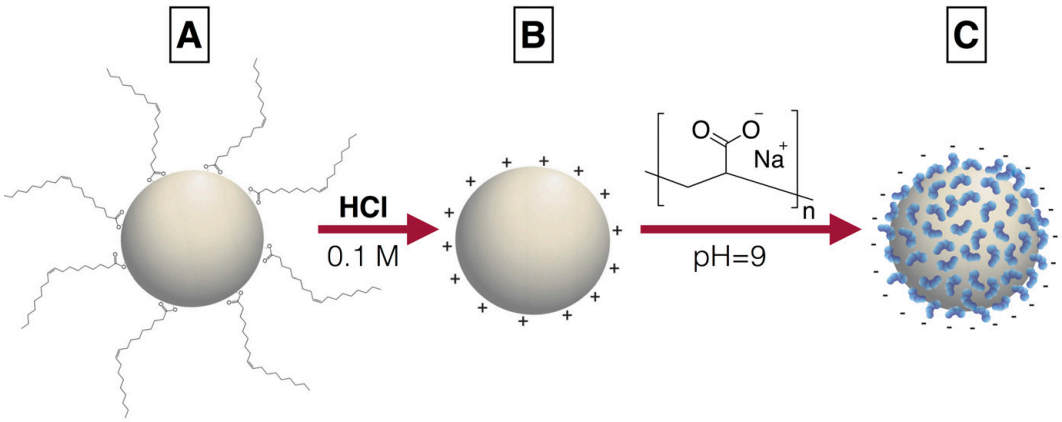

Figure III.2.1.4. Coating of UCNPs with a thin PAA layer. First, the hybrophobic UCNPs (A) are treated with an HCl solution to remove oleic acid from their surface. Then, the resulting bare UCNPs (B) are added to a solution of PAA (pH=9). After incubation, the PAA-coated UCNPs are obtained (C).

Once the UC-labels were obtained by Sulfo-NHS/EDC coupling, two different heterogeneous assays were developed and studied.

In "publication 4", a target-induced ligation strategy based on a Cu-free click chemistry reaction was explored. This reaction takes advantage of the strain contained within the alkyne moiety of a dibenzocyclooctine (DBCO) group to increase its reactivity towards azide groups (N_3), without requiring catalyzers. This kind of reaction is known as a "strain promoted alkyne-azide cycloaddition" or "SPAAC", and results in the formation of a covalent bond between both groups by yielding a triazole ring as product (see Figure III.2.1.5). SPAAC reactions are superior to other kind of chemistries due to their interesting advantages: they are bioorthogonal as they only occur by the reaction of DBCO and N_3 while being inert to functional groups commonly present in biological systems such as amines, thiols, carboxylic acids, etc. They are considered non-toxic, they cannot be digested by common cellular enzymes, do not require catalyzers, do not generate by-products, and occur at room temperature.[2] When these functional groups are incorporated to DNA capture probes, a complementary sequence can be used as a "template" to hold the DNA sequences, forcing the DBCO and N_3 groups to face each other (see Figure III.2.1.5). This results in a specific ligation of the probes containing these reactive groups, as the reaction rate between DBCO and N_3 accelerates by several orders of magnitude under these conditions.[3–5] Thus, the use

of this templated-SPAAC could be used to improve even more the sensitivity of bioassays that already employ UC-labels: Harsh washes could be used to reduce the background signal coming from non-specifically bound UC-labels, while the specific signal formed upon ligation would be conserved due to the presence of the covalent bond.

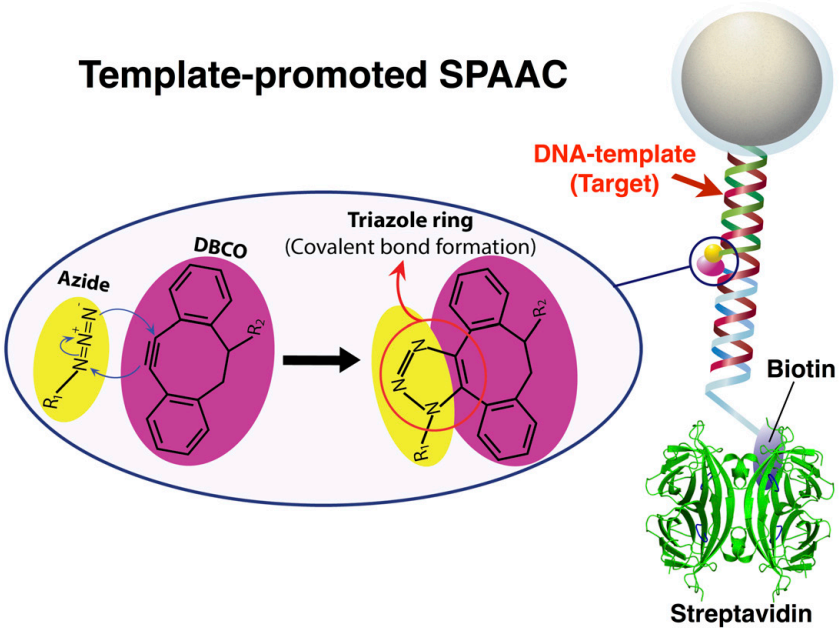

Figure III.2.1.5. Scheme of the oligonucleotide detction assay based on the template-promoted SPAAC. In the presence of the target sequence the SPAAC occurs, yielding UCNPs covalently functionalized with biotin. Upon incubation in streptavidin-coated microwells, the resulting biotinylated UCNPs are captured and subsequently washed to remove the non-specific bound labels.

To test this hypothesis, a novel oligonucleotide detection assay was developed using the DNA-analogue of a small RNA sequence as the target, which is specific from a ribosomal subunit of plasmodium falciparum. This sequence acted as the template that allowed the specific ligation of the capture probes (see Figure III.2.1.5). The assay was revealed by using streptavidin (SA) coated microwells, in which the biotinylated ligated-products could be trapped and washed in order to remove the non-specifically bound labels before reading the bottom of the wells.

A similar approach was used in "publication 5" to develop a highly sensitive detection assay. In this work, the specific formation of a covalent bond between the

capture probes in the presence of a target sequence was also pursued, in order to achieve high sensitivity by exploiting the aforementioned strategy. However, instead of the SPAAC, a photochemical ligation reaction between the DNA capture probes produced by 365 nm light was tested.[6,7] The presence of a special photoactivatable nucleotide in one of the capture probes is required for this photochemical ligation to occur, being 5'carboxyvinyl-2'-deoxyuridine (^{cv}U) the one used in this work. This nucleotide has a chemical modification compared with the natural deoxyuridine (Figure III.2.1.6.), which allows it to absorb 365 nm photons and subsequently react with a close cytidine or thymidine via a 2+2 cycloaddition, see Figure III.2.1.7.

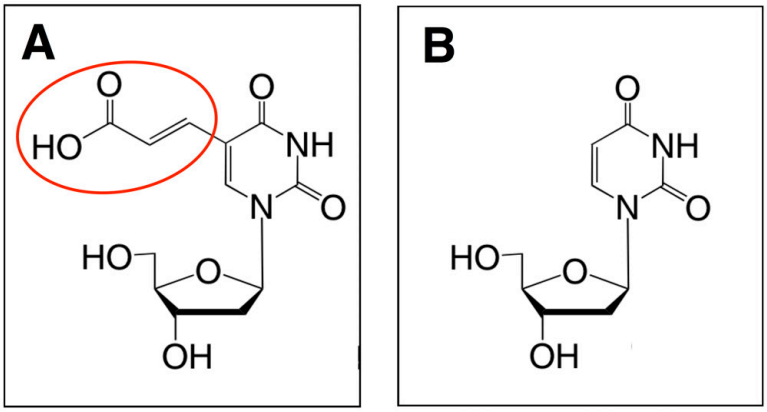

Figure III.2.1.6. Nucleotide structures. A) Synthetic photoactivatable nucleotide: 5'carboxyvinyl-2'-deoxyuridine (^{cv}U). The photoactivatable/reactive group is marked in red. B) Naturally occurring nucleotide: 2'-deoxiuridine.

This photochemical reaction is very specific: It requires a DNA/RNA sequence acting as template to progress, as upon hybridization this target sequence holds the cytidine located at the 3' end of the UC-label in a way that faces the ^{cv}U located at the 5' end of a second probe. Besides, the photoactivatable group also requires a specific spatial configuration towards the cytidine/thymidine in order to react, which is favored during hybridization and makes this reaction very target-specific. In addition, as photochemical ligation depends on the irradiation with 365 nm light it can be started and stopped at will, permitting a tighter control of the reaction progress.

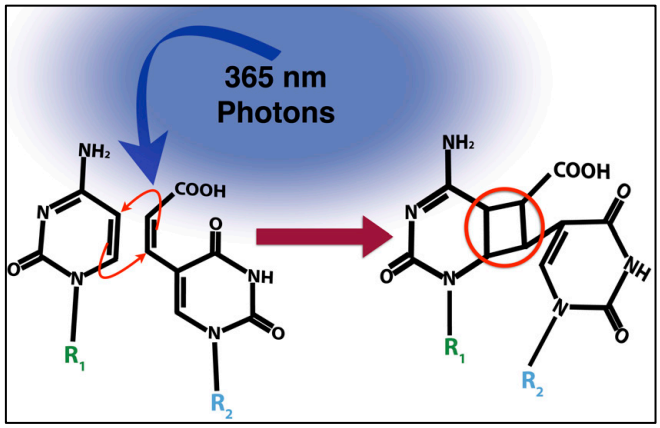

Figure III.2.1.7. Photochemical ligation. The photoactivatable nucleotide (^{cv}U), R_2, reacts with a close Cytidine (or Thymidine), R_1, via a 2+2 cycloaddition upon 365 nm UV irradiation. This photochemical ligation results in the formation of a cyclobutane (i.e. covalent bond) between R_1 and R_2, marked in red.

The fact that the photochemical ligation proceeds under 365 nm excitation, and that UCNPs doped with Yb^{3+} and Tm^{3+} also exhibit an upconverted emission peak at 365 nm when excited at 980 nm, led us to study if the photochemical ligation could be locally carried out at the surface of the UCNPs using 980 nm as the external excitation source (see Figure III.2.1.8).

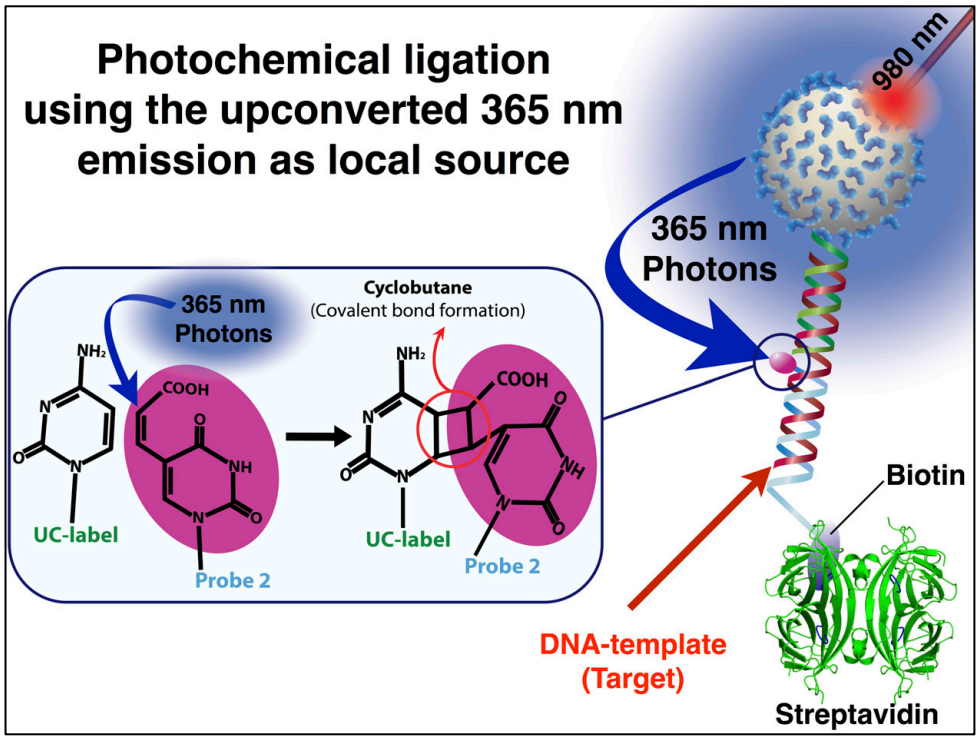

Figure III.2.1.8. NIR Photochemical ligation mechanism: upon 980 nm external excitation UC-labels act as the local source of 365 nm photons.

As a way to evaluate the feasibility of this new way to carry out the photochemical ligation of the DNA capture probes in the presence of a target sequence, the 980 nm laser used as external source was focused on the bottom of streptavidin-coated microwells, where the hybridized complexes formed by the UC-labels, the biotinylated probe and the target had been previously captured.

The fact that the laser photons can be concentrated in a small spot at the bottom of the microwells is of interest, as it opens the possibility to carry out the photochemical ligation at known spatial coordinates. This photoligated spot could then be easily revealed by performing a wash using denaturing conditions, which would led to the removal of UCNPs from the wells except for those from the photoligated spot (see Figure III.2.1.9).

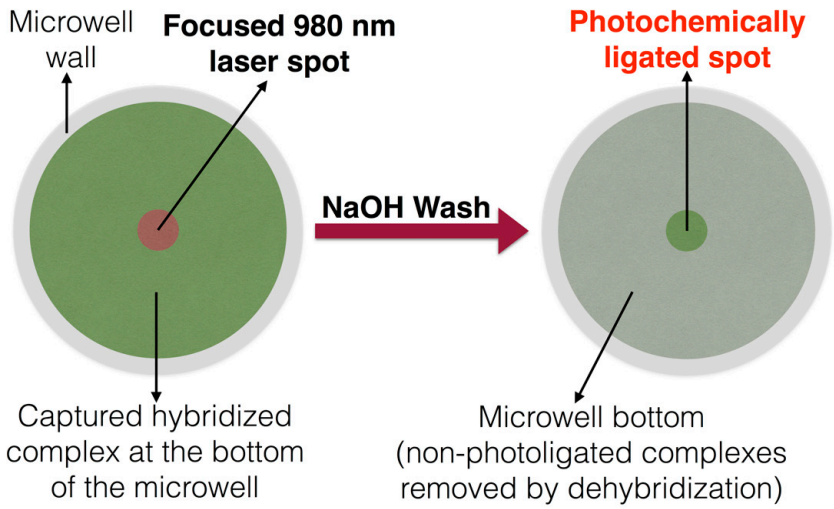

Figure III.2.1.9. Top view of microwell during photochemical ligation using UC-labels as local 365 nm light source. The complexes, formed by hybridization of the UC-label and the biotinylated probe with the target sequence, are first captured at the bottom of the SA-coated microwells. Then, a 980 nm laser beam is focused at a region of the microwell bottom, to carry out the photochemical ligation at that spot using the upconverted 365 nm emission from the captured UC-labels. After a denaturing NaOH wash, the non-photochemically ligated complexes are removed, while the photochemically ligated spot is revealed.

Interestingly, this strategy would make it possible to draw patterns of photochemically ligated UC-labels, using the bottom of the wells as canvas (Figure III.2.1.10). The fact that the spatial coordinates where the laser irradiation has taken place are known in advance implies that the presence of an "intensity pattern" may serve as a way to prove the presence of a targeted sequence.

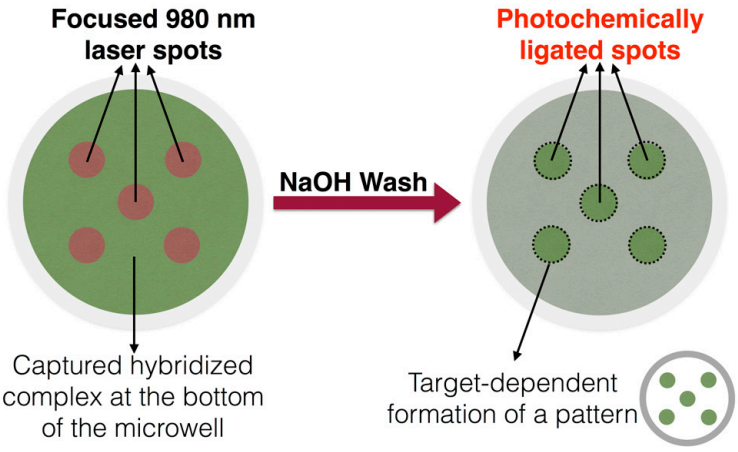

Figure III.2.1.10. Target-dependent formation of patterns upon NIR-photoligation. After denaturing the non-photoligated complexes and reading the bottom of the microwell, the intensity pattern appears.

As a final remark, it is worth saying that this strategy permits the specific spatial functionalization of a surface, in this case the bottom of the microwell, which can be exploited for different applications such as the development of arrays or to confer different spatial functionalities by using NIR light as external stimuli.

References

(1) Päkkilä, H.; Ylihärsilä, M.; Lahtinen, S.; Hattara, L.; Salminen, N.; Arppe, R.; Lastusaari, M.; Saviranta, P.; Soukka, T. Quantitative Multianalyte Microarray Immunoassay Utilizing Upconverting Phosphor Technology. *Anal. Chem.* **2012**, *84*, 8628.

(2) Jewett, J. C.; Bertozzi, C. R. Cu-Free Click Cycloaddition Reactions in Chemical Biology. *Chem. Soc. Rev.* **2010**, *39*, 1272.

(3) Shelbourne, M.; Chen, X.; Brown, T.; El-Sagheer, A. H. Fast Copper-Free Click DNA Ligation by the Ring-Strain Promoted Alkyne-Azide Cycloaddition Reaction. *Chem. Commun.* **2011**, *47*, 6257.

(4) Heuer-Jungemann, A.; Kirkwood, R.; El-Sagheer, A. H.; Brown, T.; Kanaras, A. G. Copper-Free Click Chemistry as an Emerging Tool for the Programmed Ligation of DNA-Functionalised Gold Nanoparticles. *Nanoscale* **2013**, *5*, 7209.

(5) Heuer-jungemann, A.; Kiessling, L.; Stratakis, E.; Kymakis, E.; El-sagheer, A. H.; Kanaras, A. G. Programming the Assembly of Gold Nanoparticles on Graphene Oxide Sheets Using DNA †. *J. Mater. Chem. C* **2015**, *3*, 9379.

(6) Nakamura, S.; Ogasawara, S.; Matuda, S.; Saito, I.; Fujimoto, K. Template Directed Reversible Photochemical Ligation of Oligodeoxynucleotides. *Molecules* **2011**, *17*, 163.

(7) Yoshimura, Y.; Noguchi, Y.; Sato, H.; Fujimoto, K. Template-Directed DNA Photoligation in Rapid and Selective Detection of RNA Point Mutations. *ChemBioChem* **2006**, *7*, 598.

III.2.3

Oligonucleotide sensor based on selective capture of upconversion nanoparticles triggered by target-induced DNA interstrand ligand reaction

(Publication 4)

https://pubs.acs.org/doi/10.1021/acsami.7b00575

ACS APPLIED MATERIALS & INTERFACES

Research Article

www.acsami.org

Oligonucleotide Sensor Based on Selective Capture of Upconversion Nanoparticles Triggered by Target-Induced DNA Interstrand Ligand Reaction

Diego Mendez-Gonzalez,[†] Marco Laurenti,[†] Alfonso Latorre,[§] Alvaro Somoza,[§] Ana Vazquez,[∥] Ana Isabel Negredo,[∥] Enrique López-Cabarcos,[†] Oscar G. Calderón,[‡] Sonia Melle,*[,‡] and Jorge Rubio-Retama*[,†]

[†]Department of Physical Chemistry II, Faculty of Pharmacy, Complutense University of Madrid, 28040 Madrid, Spain
[‡]Faculty of Optics and Optometry, Complutense University of Madrid, Arcos de Jalón 118, 28037 Madrid, Spain
[§]Nanobiotecnología (IMDEA-Nanociencia), Unidad Asociada al Centro Nacional de Biotecnología (CSIC), 28049 Madrid, Spain
[∥]Laboratorio de Arbovirus, Centro Nacional de Microbiología-Instituto de Salud Carlos III, Majadahonda, 28220 Madrid, Spain

Supporting Information

ABSTRACT: We present a sensor that exploits the phenomenon of upconversion luminescence to detect the presence of specific sequences of small oligonucleotides such as miRNAs among others. The sensor is based on $NaYF_4$:Yb,Er@SiO_2 nanoparticles functionalized with ssDNA that contain azide groups on the 3′ ends. In the presence of a target sequence, interstrand ligation is possible via the click-reaction between one azide of the upconversion probe and a DBCO-ssDNA-biotin probe present in the solution. As a result of this specific and selective process, biotin is covalently attached to the surface of the upconversion nanoparticles. The presence of biotin on the surface of the nanoparticles allows their selective capture on a streptavidin-coated support, giving a luminescent signal proportional to the amount of target strands present in the test samples. With the aim of studying the analytical properties of the sensor, total RNA samples were extracted from healthy mosquitoes and were spiked-in with a specific target sequence at different concentrations. The result of these experiments revealed that the sensor was able to detect 10^{-17} moles per well (100 fM) of the target sequence in mixtures containing 100 ng of total RNA per well. A similar limit of detection was found for spiked human serum samples, demonstrating the suitability of the sensor for detecting specific sequences of small oligonucleotides under real conditions. In contrast, in the presence of noncomplementary sequences or sequences having mismatches, the luminescent signal was negligible or conspicuously reduced.

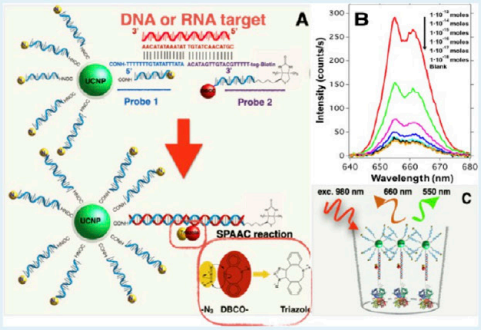

KEYWORDS: *upconversion, nanoparticles, DNA, sensor, interstrand ligation*

1. INTRODUCTION

In recent years, the advances in deep sequencing techniques have facilitated the discovery of the presence of noncoding nucleic acids, such as microRNAs (miRNAs), small-interfering RNAs (siRNAs), and Piwi-interacting RNAs (piRNAs), involved in the regulation of gene expression, modulating protein production,[1,2] and lately used as biomarkers for different diseases. Furthermore, these biomarkers appear at the very beginning of the disease, facilitating early diagnostics.[3,4] Among them, miRNAs are the best known due to their potential role as biomarkers in cancer, cardiovascular diseases,[5,6] as well as in many viral infections such as HIV-1,[7] Ebola,[8] and so forth. Other small RNAs like piRNAs, small nucleolar RNAs, and small nuclear RNAs are also gaining support as biomarkers for male infertility[9] or for viral infections like that produced by DENV2.[10] However, in most cases, proper diagnosis of disease requires the analysis of multiple sequences (multiplexing) by qRT-PCR or next-generation sequencing, limiting its application to wealthy regions as these techniques require specific labs, trained personnel, and expensive reagents. In addition, these techniques are time consuming and difficult to apply as a screening tool, especially in developing countries. These drawbacks have prompted scientists to investigate alternative methods that could be used as screening tools in the detection of these oligonucleotides without the requirement of enzymatic transcription and amplification. Among the new technologies, the use of molecular beacons based on upconversion nanoparticles has opened the possibility to create highly sensitive systems capable of analyzing the presence of these oligonucleotides at extremely

Received: January 12, 2017
Accepted: March 23, 2017
Published: March 23, 2017

DOI: 10.1021/acsami.7b00575
ACS Appl. Mater. Interfaces 2017, 9, 12272−12281

ACS Applied Materials & Interfaces Research Article

Table 1. Oligonucleotide Sequences Used in This Work

name	sequence
probe 1	5′ NH_2-C(6)-TTTTT-TT-GTA-TAT-TTA-TA-N_3 3′
probe 2	5′ DBCO-A-CAT-AGT-TGT-ACG-TTTTT-Bio-teg 3′
targets	*DNA 5′ CGT-ACA-ACT-ATG-TTA-TAA-ATA-TAC-AA 3′
	*RNA 5′ CGU-ACA-ACU-AUG-UUA-UAA-AUA-UAC-AA 3′
one mismatch (lateral)	5′ CGT-AAA-ACT-ATG-TTA-TAA-ATA-TAC-AA 3′
one mismatch (middle)	5′ CGT-ACA-ACT-ATG-TCA-TAA-ATA-TAC-AA 3′
three mismatches	5′ CGT-ACA-ACT-ATT-CCA-TAA-ATA-TAC-AA 3′
noncomplementary	5′ CAG-AAG-UCA-GGU-CGG-AUU-AAG-CC 3′

Scheme 1. Schematic Illustration of the Chemical Route for the Synthesis and Functionalization of $NaYF_4$:Yb,Er@SiO_2-DNA-N_3 Nanoparticles

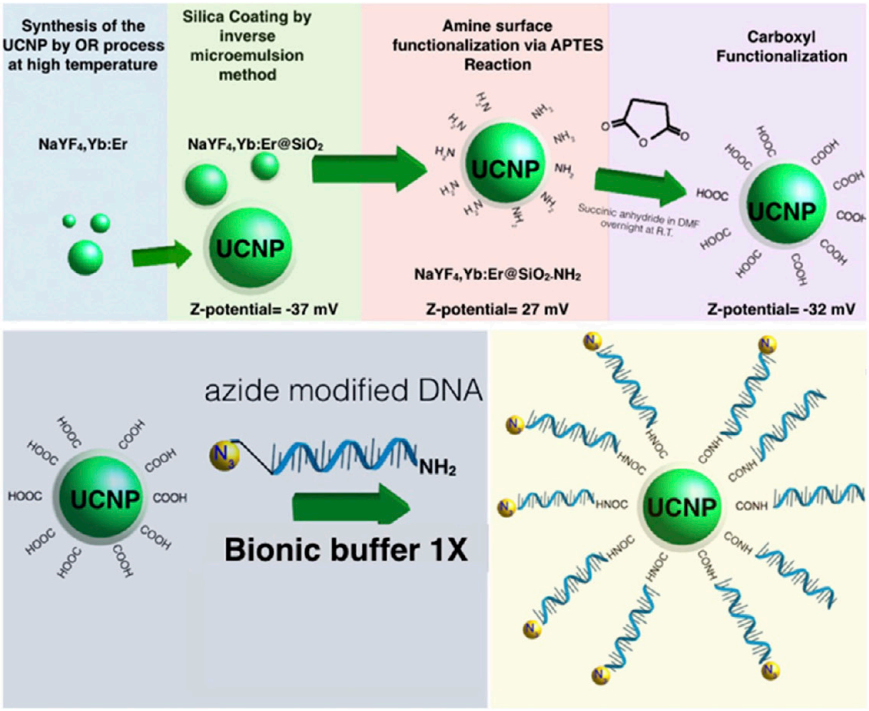

low concentrations in a fast, cheap and easy way.[11−18] These systems exploit the use of lanthanide-doped nanoparticles, which can absorb two or more low energy photons and emit one at higher energy.[19,20] In addition, these nanoparticles have interesting photoluminescent properties, like high photostability, the absence of blinking and photobleaching, along with large anti-Stokes shifts, which allow the creation of robust analytical systems with low backgrounds and high signal-to-noise ratios.[19,21−26] Furthermore, the narrow emission bands exhibited by these nanoparticles and the possibility to tune their emission wavelengths make them ideal candidates to be used for multiplexed analytical systems[27−29] in immunoassays (ULISA)[30] where the upconversion nanoparticles (UCNPs) are linked to antibodies or aptamers[25] as reporters. In these analytical systems, the target and the functionalized UCNP are captured on a solid support giving a signal proportional to the amount of target. The high affinity and specificity between the UCNPs and the targets yield highly thermodynamically stable complexes, which allows stringent cleaning processes of the capture-surface that permit washing away of any nonspecifically physisorbed UCNPs. This yields low detection limits comparable to those obtained by enzymatic amplification techniques like ELISA. However, when this strategy is applied to the detection of small oligonucleotides, like miRNAs (20−30 bp), a major problem related to the low thermodynamic stability of the complexes prevents the use of stringent cleaning steps, which in turn hampers target detection.

In this work, we present an analytical system that allows the detection of oligonucleotides (RNA or DNA) on a solid support, which is based on ssDNA functionalized $NaYF_4$:Yb,Er@SiO_2 nanoparticles that contain azide groups on the 3′ ends. In the presence of a target sequence, an interstrand ligand reaction occurs via a click-reaction between an azide of the upconversion probe and a DBCO-ssDNA-biotin probe present in the solution. As a result of this specific and selective reaction, biotin-functionalized upconversion nanoparticles are produced. After that, the biotin-functionalized upconversion nanoparticles are selectively captured on a streptavidin-coated surface, producing an upconversion emission intensity that is proportional to the target concentration present in the sample. The validity of the system was checked using samples containing total RNA extracted from mosquitoes or human

DOI: 10.1021/acsami.7b00575
ACS Appl. Mater. Interfaces 2017, 9, 12272−12281

ACS Applied Materials & Interfaces Research Article

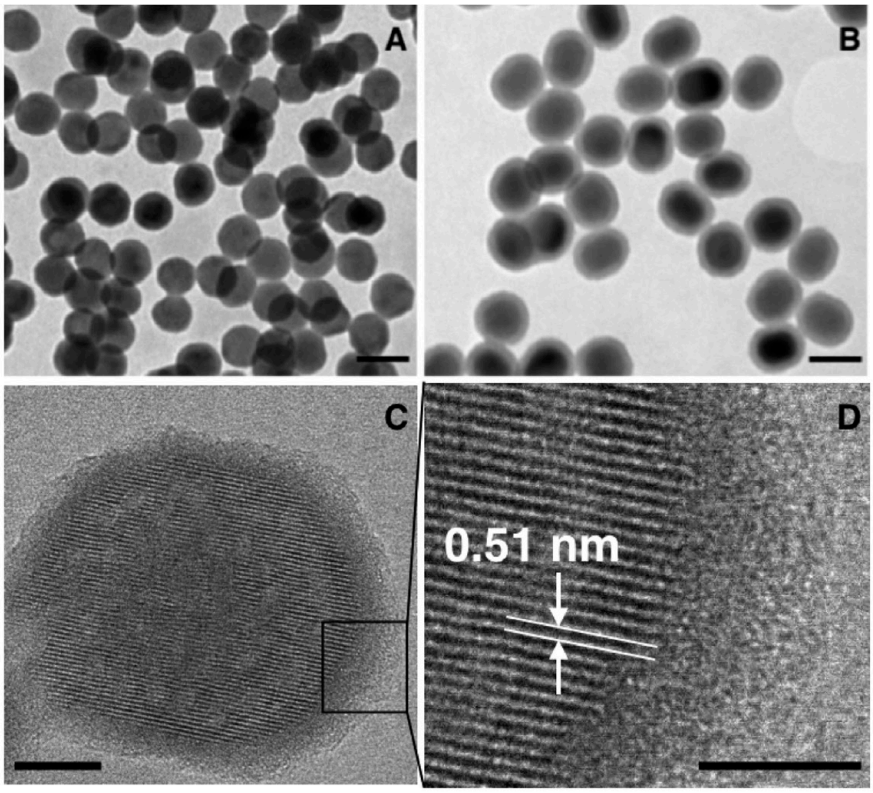

Figure 1. TEM micrographs of the synthesized $NaYF_4$;Yb,Er nanoparticles (A) and $NaYF_4$;Yb,Er@SiO_2 nanoparticles (B). (C) HRTEM image of a $NaYF_4$;Yb,Er@SiO_2 nanoparticle. (D) Magnification of the image in (C). The scale bars in (A) and (B) are 50 nm, whereas in (C) and (D) they are 10 and 5 nm, respectively.

serum samples that have been doped with a synthetic sequence that appears in the small subunit ribosomal RNA of the *Plasmodium falciparum* and which was used as a target model. The result of these experiments demonstrated an exceptionally low detection limit close to 1×10^{-17} moles per well (100 fM). The simplicity and potential of the presented system could allow its use as a screening tool for multiple RNA or DNA sequence analyses.

2. MATERIALS

Methanol (99.9%), *n*-hexane (95%), *N*,*N*-dimethylformamide anhydrous (99.8%), tetraethyl orthosilicate (99.999%), polyoxyethylene (5) nonylphenylether branched (IGEPAL CO-520), ammonium hydroxide solution (30%), (3-aminopropyl)triethoxysilane (99%), succinic anhydride (99%), Bionic buffer 10× concentrated, HEPES 99.5%, NaCl BioXtra 99.5%, dimethyl sulfoxide 99.9%, *N*-(3-(dimethylamino)propyl)-*N*′-ethylcarbodiimide hydrochloride (99%), and *N*-hydroxysulfosuccinimide sodium salt (Sulfo-NHS) (98%) were purchased from Sigma-Aldrich and used as received. The modified DNA sequences NH_2-ssDNA-N_3 probes 1 and 2 were purchased from ATDBio. The target strands and the noncomplementary strands were acquired from Invitrogen. The mismatch strands were acquired from Integrated DNA Technologies. A complete description of the sequences is given in Table 1. Streptavidin-coated well-plates (UniverSA96) were purchased from Kaivogen (Turku, Finland).

3. CHARACTERIZATION

Transmission electron microscopy (TEM) analyses were carried out using a JEOL JEM 1010 operated at 80 kV coupled with a digital camera GATAN MegaView II. High-resolution TEM (HRTEM) studies were performed in a JEOL JEM 2100 operated at 200 kV with a digital camera GATAN CCD Orius SC1000. *Z*-potential experiments were carried out using a Malvern Nano-ZS. Thermogravimetric experiments were performed using a TGA/DSC-1 (Mettler-Toledo) working under an air atmosphere. The upconversion emission spectra were collected from the well-plate using a homemade system as depicted in Scheme 2C. The light beam from a 3 W CW laser (MDL-H-980-3W) working at 980 nm was transmitted through a 200 μm core fiber, which was coupled to a collimator lens. Then, the laser beam was reflected toward the well-plate using a short-pass dichroic mirror (Thorlabs DMSP950R) and focused on the sample using a 10× objective. The upconversion luminescence coming from the well-plate passed through the short-pass dichroic mirror and through a short-pass filter (Thorlabs FES900), which blocks the excitation wavelength. A collimator lens focused the light into an optical fiber that goes to the spectrometer Glacier X (B&W Tek).

4. EXPERIMENTAL SECTION

The synthesis of the upconversion nanoparticles and their functionalization was carried out using sequential steps that are described in detail within the Supporting Information. Scheme 1 summarizes the chemical route followed to obtain the upconversion nanoparticles.

5. RESULTS AND DISCUSSION

5.1. Particle Preparation, Characterization, and Functionalization. The synthesis of the fluorescent nano-

DOI: 10.1021/acsami.7b00575
ACS Appl. Mater. Interfaces 2017, 9, 12272−12281

Scheme 2. Schematic Illustration of the Action Mechanism of the Proposed Sensor[a]

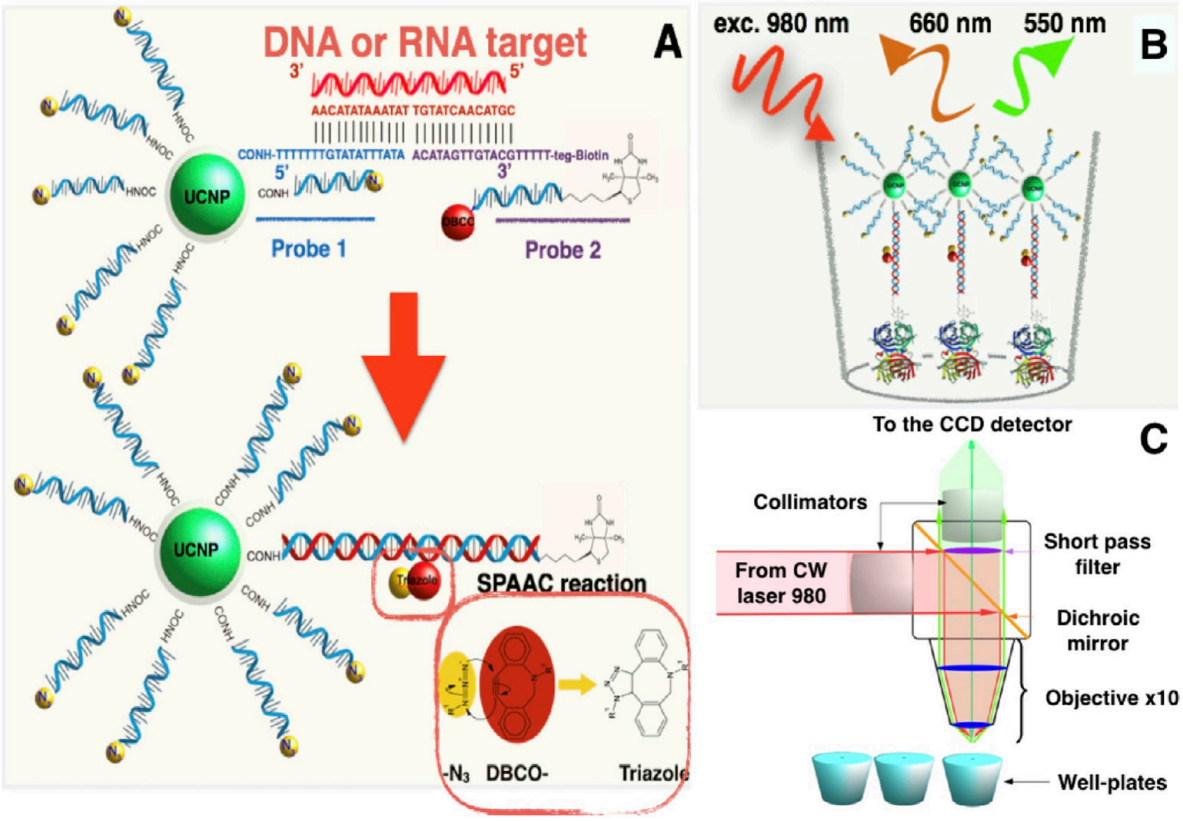

[a](A) The presence of the target sequence allows the hybridization and brings in close proximity the azide group on probe 1 and the DBCO groups on probes 1 and 2 producing the SPAAC reaction that gives $NaYF_4$;Yb,Er@SiO_2-dsDNA-biotin nanoparticles. (B) Biotin moieties on the surface of the UCNPs allow their immobilization on the surface of the streptavidin-coated well-plates. (C) The fluorescence detection was performed using the homemade device.

particles afforded monodisperse nanoparticles with a mean diameter of 36 ± 3 nm, as obtained from the TEM micrograph (see Figure 1A). X-ray energy dispersive spectroscopy analysis (Figure S1A) gave a composition of $NaY_{0.792}F_4$:$Yb_{0.189}$,$Er_{0.019}$ while the X-ray diffraction pattern of the particles (Figure S1B) demonstrated that they can be indexed to the hexagonal phase. In Figure 1B, one can observe a thin and homogeneous layer around each nanoparticle with a mean thickness of 7 nm, which was the result of the silica deposition reaction. Figure 1C,D depicts an HRTEM photograph of a $NaYF_4$:Yb,Er@SiO_2, nanoparticle, showing its crystalline structure in contrast with the amorphous silica shell. The silica layer confers hydrophilic behavior to the nanoparticles and permits their dispersion in aqueous media, as well as being a functional platform for their successive functionalization with ssDNA, as depicted in Scheme 1. A complete description of the nanoparticle functionalization and characterization is given in the Supporting Information. Figure S1C shows the upconversion luminescence spectrum of the $NaYF_4$:Yb,Er@SiO_2 nanoparticles under excitation with a 980 nm CW laser. We observed two green emission peaks near 525 and 545 nm due to the $^2H_{11/2} \rightarrow {}^4I_{15/2}$ and $^4S_{3/2} \rightarrow {}^4I_{15/2}$ transitions of the Er^{3+} ions, respectively. A red emission, with similar intensity, near 655 nm is also observed due to the $^4F_{9/2} \rightarrow {}^4I_{15/2}$ transition of the Er^{3+} ions.

5.2. Well-Plate Signal Detection and Protocol Optimization. *5.2.1. Interstrand Ligand Reaction.* The sensor is based on a hybridization process that renders an interstrand ligand reaction between the $NaYF_4$;Yb,Er@SiO_2-ssDNA-N_3 strand (probe 1) and the DBCO-ssDNA-biotin strand (probe 2). This hybridization requires the presence of a target sequence, which acts as splint strand bringing the probes 1 and 2 closer, yielding the strain-promoted alkyne−azide cycloaddition (SPAAC) reaction,[31] as seen in Scheme 2. This process permits in a subsequent step the selective capture of the resulting $NaYF_4$;Yb,Er@SiO_2-dsDNA-biotin nanoparticles on a streptavidin-coated surface. To analyze the performance of the sensor, we computed the intensity of the upconversion emission by integrating the emission spectra around the red band between 640 and 680 nm.

This strategy was designed to provide robustness to the sensor, because, in the absence of the click-reaction, any variation of the physicochemical properties of the media, like temperature or ionic strength, could revert the hybridization process, inducing the separation of probe 2 from probe 1, particularly when targets with low melting temperatures are involved in the hybridization. Therefore, the interstrand ligation stabilizes the incorporation of biotin moieties on the $NaYF_4$;Yb,Er@SiO_2-dsDNA nanoparticles and permits use of a stringent cleaning process to remove the physisorbed UCNPs

DOI: 10.1021/acsami.7b00575
ACS Appl. Mater. Interfaces 2017, 9, 12272−12281

ACS Applied Materials & Interfaces Research Article

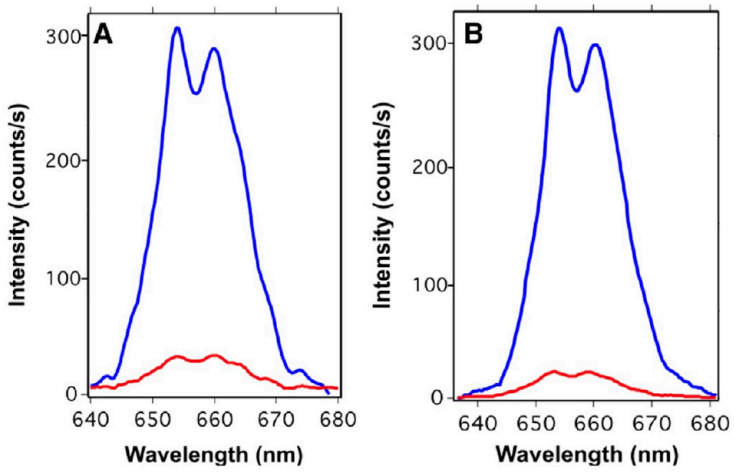

Figure 2. Luminescence spectra obtained from $NaYF_4$;Yb,Er@SiO_2-ssDNA-N_3 and DBCO-ssDNA-biotin able to produce interstrand ligation (blue line) and $NaYF_4$;Yb,Er@SiO_2-ssDNA-N_3 and ssDNA-biotin, which are unable to produce interstrand ligation (red line), in the presence of 10^{-13} moles per well (1 nM) of target sequence and after washing the solid support with 10 mM of HEPES buffer and different concentrations of NaCl at 50 °C: 150 mM in (A) and 50 mM in (B).

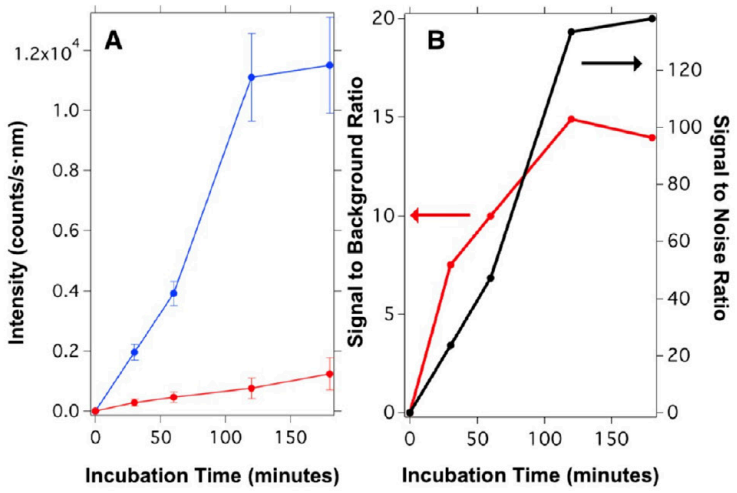

Figure 3. (A) Time evolution of the upconversion signal on the streptavidin-coated well-plate during the incubation process. The blue points correspond to the signal measured after incubating the biotin-functionalized UCNPs obtained from hybridization with 1 μg of probe 1 and 2×10^{-12} moles of probe 2 with 10^{-12} moles (10 nM) of target sequence per well. The red points represent the signal of the blank samples using the same procedure described before but without the target sequence. (B) Signal-to-background ratio (left axis) and signal-to-noise ratio (right axis) as a function of incubation time.

without the risk of removing the selectively captured UCNPs. To highlight the relevance of the click-reaction process, we compared the photoluminescence obtained from a system designed to enable the interstrand ligand reaction with another system unable to yield such a reaction (see Figure 2). In both cases, we washed the solid support with different cleaning protocols.

As one can observe from these experiments, there was a notable reduction of the photoluminescent intensity, when probes 1 and 2 were not able to yield the interstrand ligand reaction. This reduction could be attributed to a denaturalization of the double strands during the solid support cleaning process, which separates probes 1 and 2, washing away the UCNPs from the surface. When the interstrand ligand reaction takes place, probes 1 and 2 are still bound together after denaturalization and therefore remain attached on the well surface. Consequently, the $NaYF_4$;Yb,Er@SiO_2-dsDNA-biotin nanoparticles with inter-strand that have undergone the interstrand ligand reaction resist the cleaning steps with the buffer at 50 °C or with buffer with low ionic strength, which in principle could denaturalize the double strands constituted by the short oligonucleotides. Figure S2 depicts the results when the same experiments were carried out in the absence of target sequences. From these experiments we can observe that the background signals are basically the same and due to nonspecific physisorption.

5.2.2. Binding Kinetic Experiments. One of the parameters studied to optimize the signal of the sensor was the incubation time required by the streptavidin-coated well-plate to capture the maximum amount of biotin-functionalized nanoparticles.

DOI: 10.1021/acsami.7b00575
ACS Appl. Mater. Interfaces 2017, 9, 12272−12281

ACS Applied Materials & Interfaces Research Article

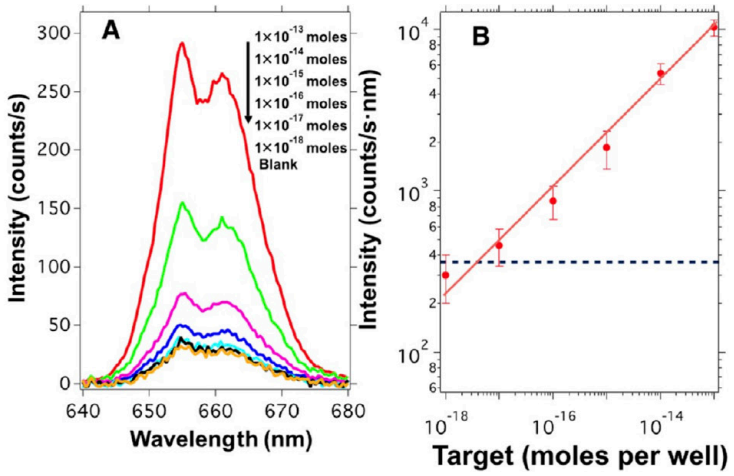

Figure 4. (A) Upconversion emission spectra collected from the multiwell-plate after being incubated with biotin-functionalized upconversion nanoparticles produced by hybridization with different amounts of target sequences. (B) Upconversion intensity collected from the multiwell-plate as a function of target concentration from 1×10^{-18} to 1×10^{-13} moles per well (10 fM to 1 nM). The signal intensity is blank subtracted. The error bars are the standard deviation obtained from measurements at 10 different positions on each well out of three independent samples for each target concentration. The blue dashed line indicates the LOD based on 3-fold SD of the blank samples.

These experiments were performed by measuring the fluorescence signal for three independent samples with a fixed target amount of 10^{-12} moles per well (10 nM) and comparing this signal with the one obtained from three blank samples. Figure 3 shows the luminescence signal collected from the streptavidin-coated surface after being incubated with 1 μg of UCNP@SiO_2-dsDNA-biotin produced by the hybridization of 10^{-12} moles of the target and 2×10^{-12} moles (20 nM) of probe 2. Figure 3A shows the increment of the luminescence signal as a function of time, reaching a plateau after 120 min. The time evolution of simple receptor−ligand interactions is usually described by a single exponential process with an observed rate constant k_{obs} that depends on the kinetic parameters, that is, the association (k_{on}) and dissociation (k_{off}) rate constants, and the ligand concentration (C), so that $k_{obs} = k_{off}(C/K_d + 1)$.[32] By fitting our data to an exponential function, we obtained a value of the rate constant of $k_{obs} = 3.8 \times 10^{-4}$ s^{-1}, which means that the half-time of the equilibrium reaction is nearly 30 min. Assuming an equilibrium dissociation constant of $K_d = K_{off}/K_{on} = 10^{-12}$ M,[33] and a ligand concentration of 10^{-10} M, the calculated k_{on} and k_{off} values for our system would be 3×10^6 M^{-1} s^{-1} and 3×10^{-6} s^{-1}, respectively. These values are similar to the ones found in other works.[34] Figure 3A also shows the signal obtained from the blank samples (background signal), which increases linearly with time (red line). Therefore, specific and nonspecific interactions exhibit different kinetics, which must be taken into account to optimize the system. For this reason, we analyzed the time evolution of the signal to background ratio and the result is shown in Figure 3B. We can observe that the signal to background ratio reaches a maximum value of 15 after 120 min (see red line). However, the signal-to-noise ratio (S/N = average signal/standard deviation of the blank) obtained from the measurements also reaches a plateau with a value of 140 after 120 min, as depicted in Figure 3B (black line). As a result of these kinetic experiments, we decided to use an incubation time of 120 min for all experiments.

5.2.3. Sensor Calibration. Figure 4A shows the red upconversion emission spectra collected from the multiwell-plates for different concentrations of target sequence. Here, we can see that the intensity of the emission spectrum collected from the multiwell-plate gradually increases with the amount of complementary target sequence added during the hybridization step. This result indicates that the presence of higher amounts of target sequences yields more biotin-functionalized UCNPs that can be captured on the streptavidin-coated wells during the incubation process. We computed the intensity of the upconversion emission by integrating the emission spectra around the red peak. The result versus the target concentration is shown in Figure 4B in a log−log plot demonstrating the feasibility of our sensor. Each point of this graph was obtained averaging the luminescence intensity of 10 different positions at each well from three independent samples; the shown intensities are blank subtracted.

As one can observe, the emission intensity collected from the well-plate roughly follows a straight line in the log−log plot of Figure 4B. From these data, we obtain the relative sensitivity changes with target concentration as S_r (%/moles per well) = $30/C_{target}$, which means a relative sensitivity of 0.3%/attomoles per well for a target concentration of 10^{-16} moles per well. The sensor shows high sensitivity and a large dynamic range, which spans over 4 orders of magnitude. Also, the blank value obtained was 950 counts/s nm with a standard deviation of 120 counts/s nm. This result defined the lowest target concentration (limit of detection, LOD) that the system can detect, which is close to 10^{-17} moles per well (100 fM). The LOD was calculated as 3-fold the standard deviation of the blank value.

With the aim of evaluating the specificity of the sensor, we analyzed the fluorescence signal in the presence of different amounts of total RNA obtained from healthy mosquitoes but in the absence of target sequences. This experiment can give us an idea about the proportion of true negatives identified as such under different amounts of total RNA. The results are presented in Figure 5A. Here, one can observe that independent of the amount of total RNA, the signal of the sensor is constant with an average value of 830 ± 102 counts/s nm, which is close to the background obtained in the absence of total RNA (950 ± 120 counts/s nm). This result

DOI: 10.1021/acsami.7b00575
ACS Appl. Mater. Interfaces 2017, 9, 12272−12281

ACS Applied Materials & Interfaces Research Article

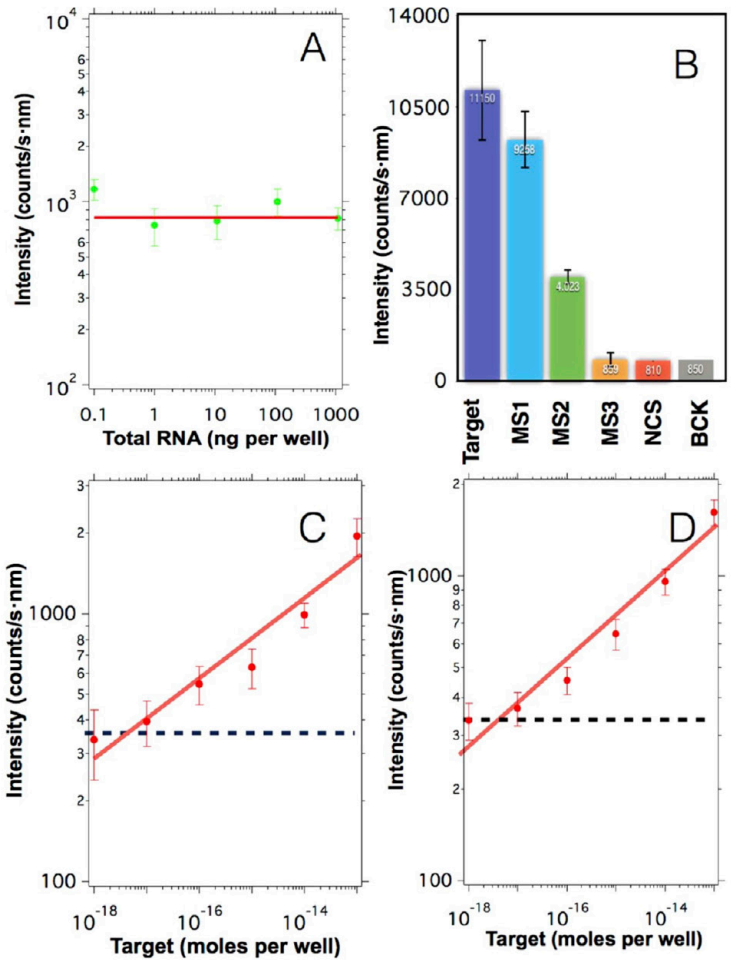

Figure 5. A) Upconversion emission obtained from blank samples prepared in the presence of different amounts of total RNA from healthy mosquitoes and in the absence of target sequences. The red line indicates the average value 830 counts/s nm. (B) Upconversion emission obtained after hybridizing 1 μg of upconversion nanoparticles with 10^{-12} moles per well of different sequences: full complementary sequences (Target), a sequence containing a single mismatch in the middle (MS1), a sequence containing three mismatches in the middle (MS2), a sequence containing a single mismatch in the first quarter of the strand (MS3), noncomplementary sequences (NCS), and in the absence of target sequences (BCK). The error bars indicate the standard deviation obtained from the experiments. (C) Upconversion intensity obtained after spiking samples containing 100 ng of total RNA with varying concentrations of target sequences. (D) Upconversion intensity obtained after spiking samples containing human serum with varying concentrations of target sequences. The intensities in (C) and (D) were blank subtracted and the blue dashed line indicates the threshold resulting from three times the standard deviation of the control signal. In all graphs, the error bars indicate the standard deviation.

demonstrates that in the presence of noncomplementary sequences, the sensor gives a signal similar to the negative control.

In addition, the capacity of the sensor to discriminate between target sequences and mismatched sequences was also studied. Figure 5B represents the upconversion emission obtained after hybridizing 1 μg of upconversion nanoparticles in the presence of 2×10^{-12} moles per well of biotin-functionalized probe 2 with 10^{-12} moles per well of different sequences: full complementary target sequences (Target), a sequence containing a single mismatch in the middle of the strand (MS1), a sequence containing three mismatches in the middle of the strand (MS2), a sequence containing a single mismatch in the first quarter of the strand (MS3), non-complementary sequences, and in the absence of target sequences (BCK). Scheme 3 illustrates the different mismatch sequences used in this experiment.

These experiments show that when the particles were hybridized with sequences that have a single mismatch placed on the center of the strand (MS1), the sensor signal decreases slightly with respect to the signal obtained with full complementary targets (see Figure 5B). This small reduction of the signal intensity could be attributed to the small hampering that this single mismatch introduces in the 3′ end of probe 1. In contrast, when the particles were hybridized with a sequence that has three mismatches located on the center of the strands (MS2), the signal decreased conspicuously due to the hybridization hindrance that under this scenario affects the 3′ and 5′ ends of probes 1 and 2, respectively. Finally, when the sensor was tested against a sequence that has a single mismatch that affected its hybridization with the central part of probe 2 (MS3), the signal obtained by the sensor was similar to those obtained with the noncomplementary sequences and blank, indicating that this mutation could completely hamper the

DOI: 10.1021/acsami.7b00575
ACS Appl. Mater. Interfaces 2017, 9, 12272−12281

Scheme 3. Graphical Representation of the Possible Duplexes Formed[a]

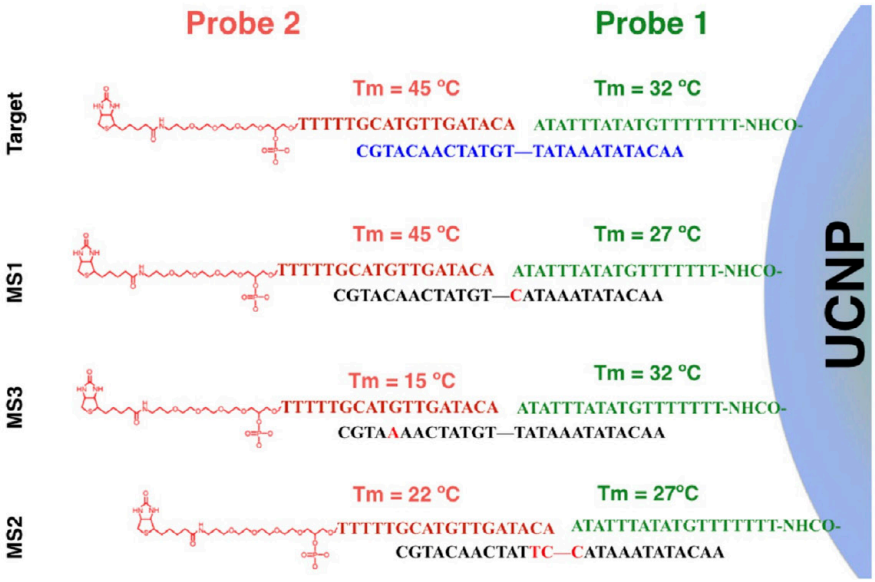

[a]The mismatches bases are colored in red. Melting temperatures (T_m) of probes 1 and 2 with the target DNA and the mismatches DNA sequences were calculated using IDT SciTools.

incorporation of the biotin moiety on the surface of the UCNP, which is the base of the sensor. These results demonstrate that the proposed sensor exhibits a selectivity that is dependent on the position of the mismatch.

Furthermore, the analytical properties of the system were studied by analyzing samples containing 100 ng of total RNA spiked with different amounts of target strands. As expected, we observed an increment of upconversion emission when the concentration of the target sequence was increased (see log−log curve of Figure 5C). In this case, the relative sensitivity is slightly lower with Sr of $20/C_{target}$%/moles per well, which means a sensitivity of 0.2%/attomoles per well for a target concentration of 10^{-16} moles per well. The small variation in the sensitivity of the sensor could be related to the high amount of total RNA added in the sample that somehow hampers the hybridization process, reducing the number of biotin-functionalized UCNPs. Nevertheless, under this condition, the sensor can detect the presence of small oligonucleotides with a LOD close to 10^{-17} moles per well (100 fM).

Finally, we studied the analytical properties of our sensor in the presence of human serum. For that, different serum samples obtained from humans were spiked with varying amounts of target containing small oligonucleotides and were analyzed without sample pretreatment. The result of these experiments is shown in Figure 5D. Here, one can observe that the system was able to detect the small oligonucleotides in the serum samples, with a LOD of around 10^{-17} moles per well, showing the capacity of the proposed sensor to work with raw samples, facilitating the measurement and reducing the cost that would involve the use of RNA extraction kits.

All of these results reveal that the detection limit of the proposed sensor is in the range of 10 attomoles per well (100 fM), indicating the potential of the proposed sensor to detect extremely low amounts of target sequences. This LOD is significantly smaller than the one found in other sensors based on the solid phase, which are summarized in Table 2.

Table 2. Comparison of the Sensor LOD for Different Techniques

sensor methodology[a]	linear range	LOD	reference
FRET	30 fmol to 30 pmol	30 fmol	34
EIS	1 pM to 500 nM	0.5 pM	35
SERS	10 pM to 10 nM	10 pM	36
ELC	50 pM to 10 nM	10 pM	37
PLGA	100 pM to 1 nM	100 pM	38
SCUP	100 fM to 10 nM	100 fM	this work

[a]FRET, fluorescence resonant energy transfer; EIS, electrochemical impedance spectroscopy; SERS, surface enhancement Raman spectroscopy; ELC, electrochemical redox detection; PLGA; photoluminescence graphene assay; SCUP, selective capture of upconversion nanoparticles.

6. CONCLUSIONS

In this work, we have synthesized upconversion nanoparticles conveniently functionalized with ssDNA strands to create a sensor able to detect the presence of specific target sequences on a solid support. The LOD of the proposed sensor was around 10^{-17} moles per well and the relative sensitivity at this target concentration was around 0.3%/attomoles per well. The signal produced by the sensor upon hybridization with sequences that have mismatches or noncomplementary sequences was significantly smaller than the one obtained for the full complementary sequence at the same concentration. Finally, spiked-in samples were prepared by adding different amounts of a synthetic target sequence in samples containing 100 ng of total RNA extracted from healthy mosquitoes or human serum samples. The results of these experiments demonstrate the capacity of the sensor to detect the target sequence with high selectivity and sensitivity. In addition, its capacity to directly detect the target sequence in serum samples demonstrates its suitability to be used as a low cost point-of-

DOI: 10.1021/acsami.7b00575
ACS Appl. Mater. Interfaces 2017, 9, 12272−12281

care diagnostic, as the use of RNA extraction kits or sample pretreatment are not necessary.

■ ASSOCIATED CONTENT

Supporting Information

The Supporting Information is available free of charge on the ACS Publications website at DOI: 10.1021/acsami.7b00575.

Materials, synthesis, characterization and detection method (PDF)

■ AUTHOR INFORMATION

Corresponding Authors

*E-mail: smelle@fis.ucm.es (S.M.).
*E-mail: bjrubio@ucm.es (J.R.-R.).

ORCID

Jorge Rubio-Retama: 0000-0002-1785-5844

Notes

The authors declare no competing financial interest.

■ ACKNOWLEDGMENTS

The authors are grateful for the financial support from the Bill & Melinda Gates Foundation, with Grant OPP1128411, Asociación Española Contra el Cáncer, Santander-Universidad Complutense project PR26/16-12B-3, and from the Spanish MINECO for the projects MAT2014-55065-R, SAF2014-56763-R, and FIS2013-41709-P.

■ REFERENCES

(1) Fire, A.; Xu, S.; Montgomery, M. K.; Kostas, S. A.; Driver, S. E.; Mello, C. C. Potent and Specific Genetic Interference by Double-Stranded RNA in *Caenorhabditis elegans*. *Nature* **1998**, *391*, 806−811.

(2) Hess, A. M.; Prasad, A. N.; Ptitsyn, A.; Ebel, G. D.; Olson, K. E.; Barbacioru, C.; Monighetti, C.; Campbell, C. L. Small RNA Profiling of Dengue Virus-Mosquito Interactions Implicates the PIWI RNA Pathway in Anti-Viral Defense. *BMC Microbiol.* **2011**, *11*, 45.

(3) Lopez, J. P.; Diallo, A.; Cruceanu, C.; Fiori, L. M.; Laboissiere, S.; Guillet, I.; Fontaine, J.; Ragoussis, J.; Benes, V.; Turecki, G.; Ernst, C. Biomarker Discovery: Quantification of microRNAs and Other Small Non-Coding RNAs Using next Generation Sequencing. *BMC Med. Genomics* **2015**, *8*, 35.

(4) Gilad, S.; Meiri, E.; Yogev, Y.; Benjamin, S.; Lebanony, D.; Yerushalmi, N.; Kushnir, M.; Cholakh, H.; Melamed, N.; Bentwich, Z.; Hod, M.; Goren, Y.; Chajut, A. Serum MicroRNAs Are Promising Novel Biomarkers. *PLoS One* **2008**, *3*, No. e3148.

(5) Calin, G. A.; Croce, C. M. MicroRNA Signatures in Human Cancers. *Nat. Rev. Cancer* **2006**, *6*, 857−866.

(6) Flemming, A. Targeting miRNA Pathology in Heart Disease. *Nat. Rev. Drug Discovery* **2014**, *13*, 336.

(7) Munshi, S. U.; Panda, H.; Holla, P.; Rewari, B. B.; Jameel, S. MicroRNA-150 Is a Potential Biomarker of HIV/AIDS Disease Progression and Therapy. *PLoS One* **2014**, *9*, No. e95920.

(8) Liang, H.; Zhou, Z.; Zhang, S.; Zen, K.; Chen, X.; Zhang, C. Identification of Ebola Virus microRNAs and Their Putative Pathological Function. *Sci. China: Life Sci.* **2014**, *57*, 973−981.

(9) Hong, Y.; Wang, C.; Fu, Z.; Liang, H.; Zhang, S.; Lu, M.; Sun, W.; Ye, C.; Zhang, C. Y.; Zen, K.; Shi, L.; Zhang, C.; Chen, X. Systematic Characterization of Seminal Plasma piRNAs as Molecular Biomarkers for Male Infertility. *Sci. Rep.* **2016**, *6*, No. 24229.

(10) Morazzani, E. M.; Wiley, M. R.; Murreddu, M. G.; Adelman, Z. N.; Myles, K. M. Production of Virus-Derived Ping-Pong-Dependent piRNA-like Small RNAs in the Mosquito Soma. *PLoS Pathog.* **2012**, *8*, No. e1002470.

(11) Alonso-Cristobal, P.; Vilela, P.; El-Sagheer, A.; Lopez-Cabarcos, E.; Brown, T.; Muskens, O. L.; Rubio-Retama, J.; Kanaras, A. G. Highly Sensitive DNA Sensor Based on Upconversion Nanoparticles and Graphene Oxide. *ACS Appl. Mater. Interfaces* **2015**, *7*, 12422−12429.

(12) Laurenti, M.; Paez-Perez, M.; Algarra, M.; Alonso-Cristobal, P.; Lopez-Cabarcos, E.; Mendez-Gonzalez, D.; Rubio-Retama, J. Enhancement of the Upconversion Emission by Visible-to-Near-Infrared Fluorescent Graphene Quantum Dots for miRNA Detection. *ACS Appl. Mater. Interfaces* **2016**, *8*, 12644−12651.

(13) Yang, X.; Yu, Y.; Gao, Z. A Highly Sensitive Plasmonic DNA Assay Based on Triangular Silver Nanoprism Etching. *ACS Nano* **2014**, *8*, 4902−4907.

(14) Tang, L.; Chun, I. S.; Wang, Z.; Li, J.; Li, X.; Lu, Y. DNA Detection Using Plasmonic Enhanced near-Infrared Photoluminescence of Gallium Arsenide. *Anal. Chem.* **2013**, *85*, 9522−9527.

(15) Tsang, M.-K.; Ye, W.; Wang, G.; Li, J.; Yang, M.; Hao, J. Ultrasensitive Detection of Ebola Virus Oligonucleotide Based on Upconversion Nanoprobe/Nanoporous Membrane System. *ACS Nano* **2016**, *10*, 598−605.

(16) Chen, Z.; Chen, H.; Hu, H.; Yu, M.; Li, F.; Zhang, Q.; Zhou, Z.; Yi, T.; Huang, C. Versatile Synthesis Strategy for Carboxylic Acid-Functionalized Upconverting Nanophosphors as Biological Labels. *J. Am. Chem. Soc.* **2008**, *130*, 3023−3029.

(17) Ma, W.; Kuang, H.; Xu, L.; Ding, L.; Xu, C.; Wang, L.; Kotov, N. A. Attomolar DNA Detection with Chiral Nanorod Assemblies. *Nat. Commun.* **2013**, *4*, No. 2689.

(18) Li, S.; Xu, L.; Ma, W.; Wu, X.; Sun, M.; Kuang, H.; Wang, L.; Kotov, N. A.; Xu, C. Dual-Mode Ultrasensitive Quantification of MicroRNA in Living Cells by Chiroplasmonic Nanopyramids Self-Assembled from Gold and Upconversion Nanoparticles. *J. Am. Chem. Soc.* **2016**, *138*, 306−312.

(19) Wang, F.; Liu, X. Recent Advances in the Chemistry of Lanthanide-Doped Upconversion Nanocrystals. *Chem. Soc. Rev.* **2009**, *38*, 976−989.

(20) Liu, C.; Wang, H.; Li, X.; Chen, D. Monodisperse, Size-Tunable and Highly Efficient β-NaYF4:Yb,Er(Tm) up-Conversion Luminescent Nanospheres: Controllable Synthesis and Their Surface Modifications. *J. Mater. Chem.* **2009**, *19*, 3546−3553.

(21) Liu, B.; Chen, Y.; Li, C.; He, F.; Hou, Z.; Huang, S.; Zhu, H.; Chen, X.; Lin, J. Poly(Acrylic Acid) Modification of Nd^{3+} -Sensitized Upconversion Nanophosphors for Highly Efficient UCL Imaging and pH-Responsive Drug Delivery. *Adv. Funct. Mater.* **2015**, *25*, 4717−4729.

(22) Zhang, C.; Yuan, Y.; Zhang, S.; Wang, Y.; Liu, Z. Biosensing Platform Based on Fluorescence Resonance Energy Transfer from Upconverting Nanocrystals to Graphene Oxide. *Angew. Chem., Int. Ed. Engl.* **2011**, *50*, 6851−6854.

(23) Wu, S.; Duan, N.; Ma, X.; Xia, Y.; Wang, H.; Wang, Z.; Zhang, Q. Multiplexed Fluorescence Resonance Energy Transfer Aptasensor between Upconversion Nanoparticles and Graphene Oxide for the Simultaneous Determination of Mycotoxins. *Anal. Chem.* **2012**, *84*, 6263−6270.

(24) Sedlmeier, A.; Gorris, H. H. Surface Modification and Characterization of Photon-Upconverting Nanoparticles for Bioanalytical Applications. *Chem. Soc. Rev.* **2015**, *44*, 1526−1560.

(25) Doughan, S.; Han, Y.; Uddayasankar, U.; Krull, U. J. Solid-Phase Covalent Immobilization of Upconverting Nanoparticles for Biosensing by Luminescence Resonance Energy Transfer. *ACS Appl. Mater. Interfaces* **2014**, *6*, 14061−14068.

(26) Sedlmeier, A.; Hlavek, A.; Birner, L.; Mickert, M. J.; Muhr, V.; Hirsch, T.; Corstjens, P. L. A. M.; Tanke, H. J.; Soukka, T.; Gorris, H. H. Highly Sensitive Laser Scanning of Photon-Upconverting Nanoparticles on a Macroscopic Scale. *Anal. Chem.* **2016**, *88*, 1835−1841.

(27) Kale, V.; Päkkilä, H.; Vainio, J.; Ahomaa, A.; Sirkka, N.; Lyytikäinen, A.; Talha, S. M.; Kutsaya, A.; Waris, M.; Julkunen, I.; Soukka, T. Spectrally and Spatially Multiplexed Serological Array-in-Well Assay Utilizing Two-Color Upconversion Luminescence Imaging. *Anal. Chem.* **2016**, *88*, 4470−4477.

(28) Ylihärsilä, M.; Valta, T.; Karp, M.; Hattara, L.; Harju, E.; Hölsä, J.; Saviranta, P.; Waris, M.; Soukka, T. Oligonucleotide Array-in-Well Platform for Detection and Genotyping Human Adenoviruses by

DOI: 10.1021/acsami.7b00575
ACS Appl. Mater. Interfaces 2017, 9, 12272−12281

Utilizing Upconverting Phosphor Label Technology. *Anal. Chem.* **2011**, *83*, 1456−1461.
(29) van de Rijke, F.; Zijlmans, H.; Li, S.; Vail, T.; Raap, A. K.; Niedbala, R. S.; Tanke, H. J. Up-converting Phosphor Reporters for Nucleic Acid Microarrays. *Nat. Biotechnol.* **2001**, *19*, 273−276.
(30) Hlaváček, A.; Farka, Z.; Hübner, M.; Horňáková, V.; Němeček, D.; Niessner, R.; Skládal, P.; Knopp, D.; Gorris, H. H. Competitive Upconversion-Linked Immunosorbent Assay for the Sensitive Detection of Diclofenac. *Anal. Chem.* **2016**, *88*, 6011−6017.
(31) El-Sagheer, A. H.; Brown, T. Click Chemistry with DNA. *Chem. Soc. Rev.* **2010**, *39*, 1388−1405.
(32) Hulme, E. C.; Trevethick, M. A. Ligand Binding Assays at Equilibrium: Validation and Interpretation. *Br. J. Pharmacol.* **2010**, *161*, 1219−1237.
(33) Broder, G. R.; Ranasinghe, R. T.; Neylon, C.; Morgan, H.; Roach, P. L. Kinetics and Thermodynamics of Biotinylated Oligonucleotide Probe Binding to Particle-Immobilized Avidin and Implications for Multiplexing Applications. *Anal. Chem.* **2011**, *83*, 2005−2011.
(34) Noor, M. O.; Krull, U. J. Camera-Based Ratiometric Fluorescence Transduction of Nucleic Acid Hybridization with Reagentless Signal Amplification on a Paper-Based Platform Using Immobilized Quantum Dots as Donors. *Anal. Chem.* **2014**, *86*, 10331−10339.
(35) Yang, Y.; Li, C.; Yin, L.; Liu, M.; Wang, Z.; Shu, Y.; Li, G. Enhanced Charge Transfer by Gold Nanoparticle at DNA Modi Fi Ed Electrode and Its Application to Label-Free DNA Detection. *ACS Appl. Mater. Interfaces* **2014**, *6*, 7579−7584.
(36) Kang, T.; Yoo, S. M.; Yoon, I.; Lee, S. Y.; Kim, B. Patterned Multiplex Pathogen DNA Detection by Au Particle-on-Wire SERS Sensor. *Nano Lett.* **2010**, *10*, 1189−1193.
(37) López, M. S.; Cabanillas, G. F.; Castañón, M. J. L.; López-Ruiz, B. Development of a Genosensor for Peanut Allergen ARA H 2 Detection and Its Optimization by Surface Response Methodology. *Biosens. Bioelectron.* **2014**, *62*, 350−356.
(38) Du, Y.; Guo, S.; Dong, S.; Wang, E. An Integrated Sensing System for Detection of DNA Using New Parallel-Motif DNA Triplex System and Graphene-Mesoporous Silica-Gold Nanoparticle Hybrids. *Biomaterials* **2011**, *32*, 8584−8592.

DOI: 10.1021/acsami.7b00575
ACS Appl. Mater. Interfaces 2017, 9, 12272−12281

Supporting Information

Oligonucleotide Sensor Based on Selective Capture of Upconversion Nanoparticles Triggered by Target Induced DNA Inter-Strand Ligand Reaction

Diego Mendez-Gonzalez[1], Marco Laurenti[1], Alfonso Latorre[3], Alvaro Somoza[3], Ana Vazquez[4], Ana Isabel Negredo[4], Enrique López-Cabarcos[1], Oscar G. Calderón[2], Sonia Melle[2]* and Jorge Rubio-Retama[1]*

[1]Department of Physical Chemistry II, Faculty of Pharmacy, Complutense University of Madrid, 28040 Madrid, Spain

[2]Faculty of Optics and Optometry, Complutense University of Madrid, Arcos de Jalón 118, 28037 Madrid, Spain

[3]Nanobiotecnología (IMDEA-Nanociencia), Unidad Asociada al Centro Nacional de Biotecnología (CSIC), Madrid, Spain

[4]Laboratorio de Arbovirus, Centro Nacional de Microbiología-Instituto de Salud Carlos III, Majadahonda, Madrid, Spain.

Correspondence to: bjrubio@ucm.es or smelle@fis.ucm.es

Index

1. Synthesis of the $NaYF_4$:Yb,Er@SiO_2-ssDNA-N_3 Nanoparticle

1.*a Synthesis of $NaYF_4$:Yb,Er Nanoparticles*

Upconverting nanoparticles (UCNPs) were synthesized by a modification of the Ostwald ripening method.[1] First, 0.78 mmol of YCl_3, 0.2 mmol of $YbCl_3$, and 0.02 mmol of $ErCl_3$ were dissolved with 6 mL of oleic acid and 15 mL of 1-octadecene in a three necked round bottom flask by heating the mixture to 160 ºC for 90 minutes under nitrogen atmosphere. After that, the mixture was cooled to room temperature and 10 mL

of a methanol solution containing 100 mg of NaOH (2.5 mmol) and 148.16 mg of NH_4F (4 mmol) were added drop-wise under vigorous stirring. The mixture was stirred for 30 min and finally the methanol was evaporated by heating at 100 ºC. Traces of methanol were extracted with a vacuum pump. The flask was placed on a heating mantle and heated up to 315 ºC at reflux for 60 minutes. After this time, the solution was transferred to a decantation funnel and cleaned 4 times with deionized water. Then, the oil phase was centrifuged with ethanol at 8500 rpm, 10 min. The pellets were redispersed with 1 mL of hexane, and centrifuged with ethanol again. Finally, the pellets were rinsed with ethanol, redispersed in 18 mL of hexane and stored for further use.

1.b Synthesis of $NaYF_4$:Yb,Er@SiO_2 Nanoparticles

A SiO_2 shell was grown on the surface of the UCNPs via the reverse microemulsion method.[2,3,4] Briefly, 240 mg of Igepal™ CO-520, 1.2 mL of UCNPs and 3.8 mL of hexane were mixed and dispersed using an ultrasonic bath. Next, 40 µL of Ammonia (30%) was added and the mixture was sonicated again until obtaining a homogeneous solution. Finally, 30 µL of TEOS (0.14 mmol) was added under stirring to start the reaction. After 8 h, the reaction was stopped and the microemulsion was destabilized using methanol. The resulting solution was centrifuged and the process was repeated three times using ethanol as solvent (9500 rpm, 10 min). Finally, the nanoparticles were collected and stored in 5 mL of ethanol. After this reaction, the z-potential of the particles was -37 mV.

1.c Synthesis of $NaYF_4$:Yb,Er@SiO_2-COOH Nanoparticles

$NaYF_4$:Yb,Er@SiO_2 nanoparticles were modified with amine (-NH_2) groups by adding 100 µL (0.45 mmol) of APTES to the UCNPs dispersed in 5 mL of ethanol and stirred overnight. After this time, the resulting product was centrifuged three times with ethanol at 9500 rpm for 10 min and once with anhydrous N,N-Dimethylformamide (DMF) at 10500 rpm during 12 min. After the surface modification with amine groups, the z-potential of the nanoparticles was +27 mV. The resulting pellet was dispersed with 3 mL of dry DMF and transferred to a vial, where it was kept under stirring. Then, a solution of 150 mg of succinic anhydride (1.5 mmol) in 2 mL of DMF was added dropwise to the $NaYF_4$:Yb,Er@SiO_2 dispersion and the reaction was allowed to progress overnight. Finally, the nanoparticles were recovered by centrifugation (11000 rpm, 12 min),

centrifuged twice with deionized water and stored in deionized water at a concentration of 2.2 mg mL^{-1}. After this reaction the z-potential of the nanoparticles change to -32 mV.

1.d. Immobilization of ssDNA-N_3 on the surface of UCNPS@SiO_2-COOH

Amine functionalized DNA strands (H_2N-C_6-TTTTTTTGTATATTTATA-N_3) were grafted on the surface of the upconversion nanoparticles using the EDC and sulfo-NHS coupling reaction. Hence, 4 mg of nanoparticles were transferred to an eppendorf tube and centrifuged. The resulting pellet was redispersed in 4 mL of Bionic (1X) and kept under stirring in a vial. Then, 60 µL of EDC·HCl 0.2 M and 120 µL of Sulfo-NHS 0.2 M were added, and the nanoparticles were let to activate for 1.5 h. Amine functionalized ssDNA (40 µL, 49µM) was added and the coupling reaction was allowed to progress for 3h. After this time, the nanoparticles were recovered by centrifugation, washed by centrifugation twice with Bionic (1x), and finally stored in DMSO at a concentration of 8 mg mL^{-1}. Thermogravimetric analysis indicated that the amount of DNA anchored on the surface of each nanoparticle is roughly 40 chains.

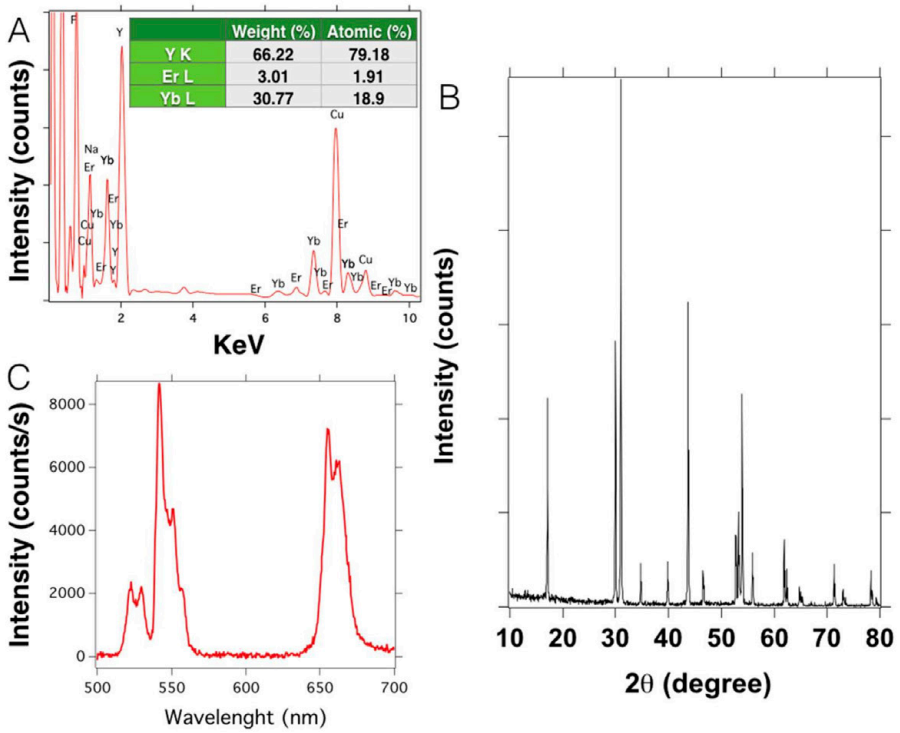

Figure S1. EDS spectrum of the bare $NaYF_4$;Yb,Er nanoparticles (A), X-Ray diffraction pattern of the as synthesized $NaYF_4$;Yb,Er nanoparticles (B) and emission spectrum of the silica coated upconversion nanoparticles in water after being excited with a CW laser at 980 nm. (C)

2. RNA Extraction and Target Detection

2.a Total RNA Extraction

The total RNA was extracted from healthy mosquitoes (Aedes albopictus) using the miRNeasy Mini Kit from Quiagen following the manufacturer's protocol.

2.b Target Detection

2.b.1. The standard process that was used for the detection assays was the following: First, 200 µL eppendorf tubes were filled with 90 µL of hybridization buffer (Hepes, 150 mM NaCl) containing a concentration of target sequence between 10^{-12} and 10^{-18} moles. In this work we have evaluated the response of the sensor against DNA and RNA targets obtaining similar results independently of the nature of the complementary strand. 1 µg of UCNPs-ssDNA-N_3 and $2x10^{-12}$ moles of biotinylated-oligo were added to the eppendorf giving a final volume of 100 µL. The resulting mixture was let to hybridize for 1 hour at room temperature. After this time, the content of the eppendorf was transferred to streptavidin-coated wells, and incubated at room temperature for 2 hours. Finally, the wells were washed six times with assay buffer and dried upside-down at room temperature, before reading. To analyze the reproducibility of the results, we run at least, three independent experiments measuring the luminescence intensity at 10 different positions for each well. All the experiments were compared with the background signal obtained from blank samples, which were produced as indicated above but without the addition of the target sequence.

2.b.2 The target detection in the presence of total RNA was performed follows; First, 200 µL eppendorf tubes were filled with 90 µL of hybridization buffer (HEPES, 150 mM NaCl) containing 100 ng of total RNA and from 10^{-12} to 10^{-18} moles of the target sequence. After that, 1 µg of UCNPs-ssDNA-N_3 and $2x10^{-12}$ moles of biotinylated-oligo were added to the eppendorf giving a final volume of 100 µL. The next steps that include the hybridization time and the incubation were the same as indicated above.

2.b.3. The target detection in spiked-in serum samples was performed as follows. First, 200 µL eppendorf tubes were filled with 50 µL of hybridization buffer (Hepes, 150 mM NaCl) and mixed with 40 µL of human serum containing a target sequence concentration from 10^{-12} to 10^{-18} moles. After spiking the serum samples, they were immediately measured in order to reduce degradation effects. The fraction of serum inside the whole sample was 50% v/v. After that, 1 µg of UCNPs-ssDNA-N_3 and $2x10^{-12}$ moles of biotinylated-oligo were added to the eppendorf giving a final volume of 100 µL. The next steps that include the hybridization time and the incubation were the same as indicated above.

The amount of target sequences presented in the calibration curves is referred to the moles of target strands spiked in the samples.

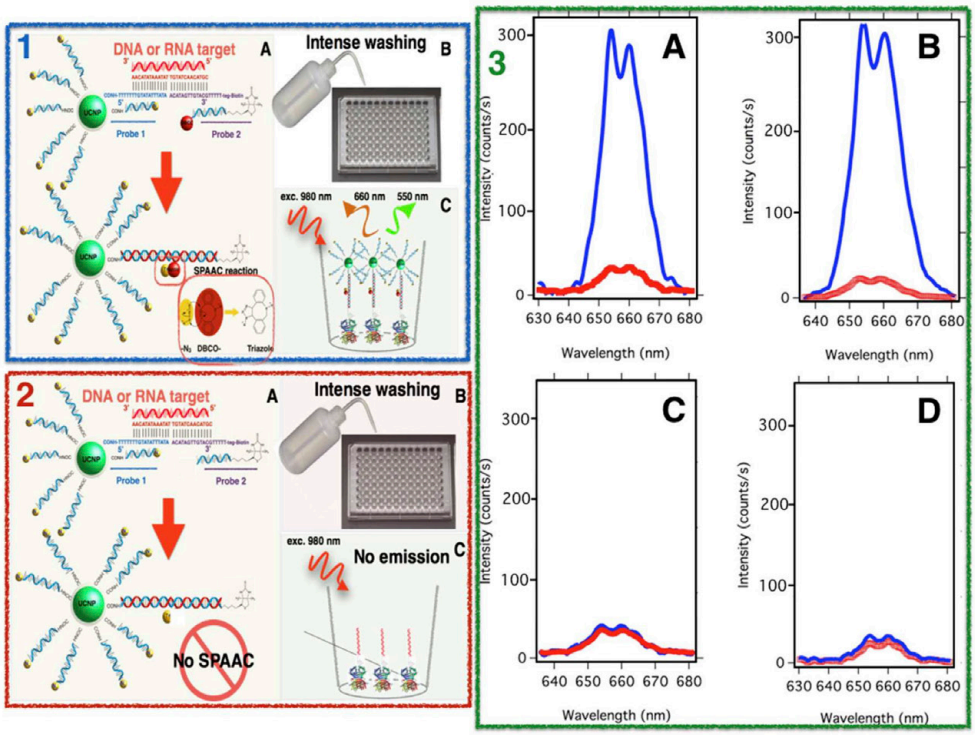

Figure S2. Panel 1 illustrates the measuring process where inter-strand ligand reaction is involved. Panel 2 depicts the same process in the absence of inter-strand ligand reaction. Panel 3 shows the photoluminescent spectra obtained from $NaYF_4$;Yb,Er@SiO_2-ssDNA-N_3 and DBCO-ssDNA-biotin able to produce inter strand ligation (blue) and $NaYF_4$;Yb,Er@SiO_2-ssDNA-N_3 and ssDNA-biotin, which are unable to produce inter-strand ligation (red) in the presence of 10^{-13} moles of target sequence and after washing the solid support with 10 mM HEPES buffer and different concentrations of NaCl at 50ºC, 150 mM in A) and 50 mM in B). C and D are the same experiments but in the absence of target sequence (control experiments).

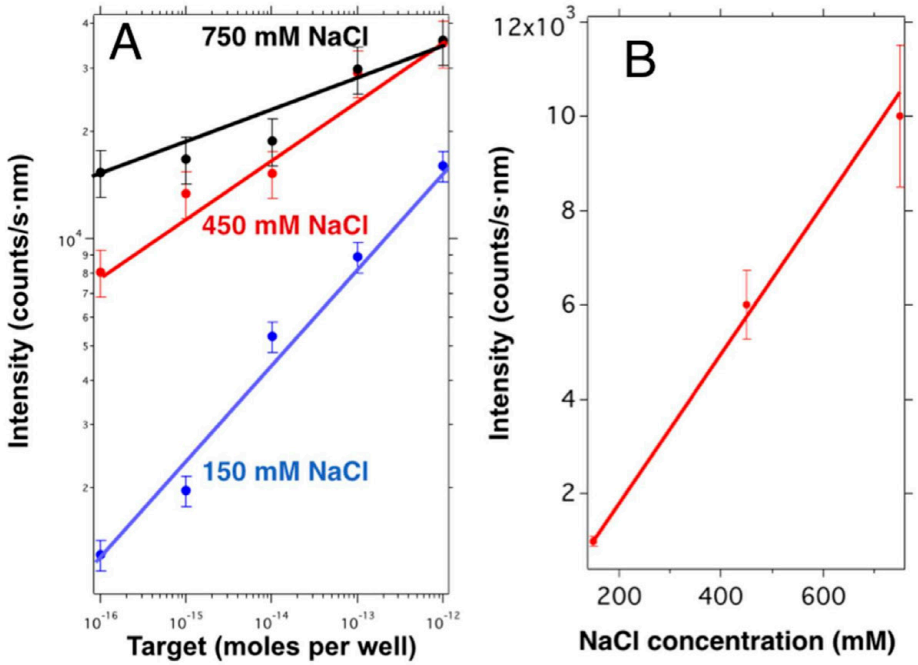

Figure S3. A) Calibration curve of the sensor using different ionic strength, B) signal intensity of the backgrounds as a function of the ionic strength. The results obtained from Figure S3 indicated that the best ionic strength was 150 mM of NaCl.

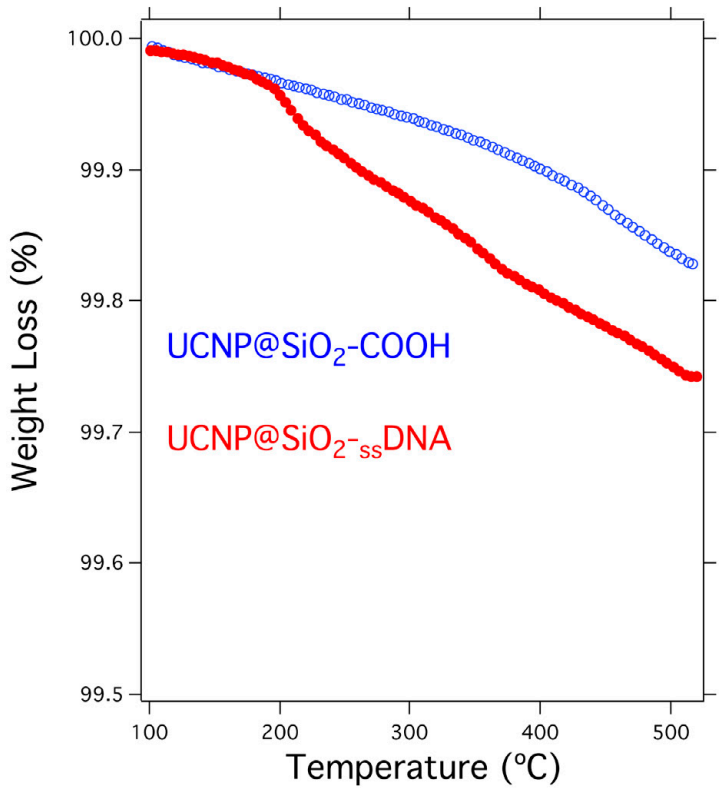

Figure S4. TGA experiment for UCNP@SiO_2-COOH and UCNP@SiO_2-ssDNA nanoparticles

References

(1) Voss, B.; Haase, M. Intrinsic Focusing of the Particle Size Distribution in Colloids Containing Nanocrystals of Two Di Ff Erent Crystal Phases. *ACS Nano* **2013**, No. 12, 11242–11254.

(2) Laurenti, M.; Paez-Perez, M.; Algarra, M.; Alonso-Cristobal, P.; Lopez-Cabarcos, E.; Mendez-Gonzalez, D.; Rubio-Retama, J. Enhancement of the Upconversion Emission by Visible-to-Near-Infrared Fluorescent Graphene Quantum Dots for miRNA Detection. *ACS Appl. Mater. Interfaces* **2016**, *8* (20), 12644–12651.

(3) Serrano-Ruiz, D.; Alonso-Cristobal, P.; Mendez-Gonzalez, D.; Laurenti, M.;

Olivero-David, R.; López-Cabarcos, E.; Rubio-Retama, J. Nanosegregated Polymeric Domains on the Surface of Fe3O4@SiO2 Particles. *J. Polym. Sci. Part A Polym. Chem.* **2014**, *52*, 2966–2975.

(4) Alonso-Cristobal, P.; Lopez-Quintela, M. A.; Contreras-Caceres, R.; Lopez-Cabarcos, E.; Rubio-Retama, J.; Laurenti, M. Synthesis of Catalytically Active Gold Clusters on the Surface of Fe_3O_4@SiO_2 Nanoparticles. *RSC Adv.* **2016**, *6* (102), 100614–100622.

III.2.4

Photochemical ligation to ultrasensitive DNA detection with upconverting Nanoparticles

(Publication 5)

https://pubs.acs.org/doi/10.1021/acs.analchem.8b03106

analytical chemistry

Article

Cite This: Anal. Chem. 2018, 90, 13385−13392

pubs.acs.org/ac

Photochemical Ligation to Ultrasensitive DNA Detection with Upconverting Nanoparticles

Diego Mendez-Gonzalez,[†] Satu Lahtinen,[‡] Marco Laurenti,[†] Enrique López-Cabarcos,[†] Jorge Rubio-Retama,*[,†] and Tero Soukka*[,‡]

[†]Department of Chemistry in Pharmaceutical Sciences, Faculty of Pharmacy, Complutense University of Madrid, Plaza Ramon y Cajal, No. 2, 28040, Madrid, Spain

[‡]Department of Biotechnology, University of Turku, Kiinamyllynkatu 10, FI-20520 Turku, Finland

Supporting Information

ABSTRACT: In this work, we explore a photochemical ligation reaction to covalently modify oligonucleotide-conjugated upconverting nanoparticles (UCNPs) in the presence of a specific target DNA sequence. The target sequence acts as a hybridization template, bringing together a biotinylated photoactivatable oligonucleotide probe and the oligonucleotide probe that is attached to UCNPs. The illumination of the UCNPs by NIR light to generate UV emission internally or illuminating the photoactivatable probe directly by an external UV light promotes the photochemical ligation reaction, yielding covalently biotin functionalized UCNPs that can be selectively captured in streptavidin-coated microwells. Following this strategy, we developed a DNA sensor with a limit of detection of 1×10^{-18} mol per well (20 fM). In addition, we demonstrate the possibility to create UCNP patterns on the surface of solid supports upon NIR illumination that are selectively formed under the presence of the target oligonucleotide.

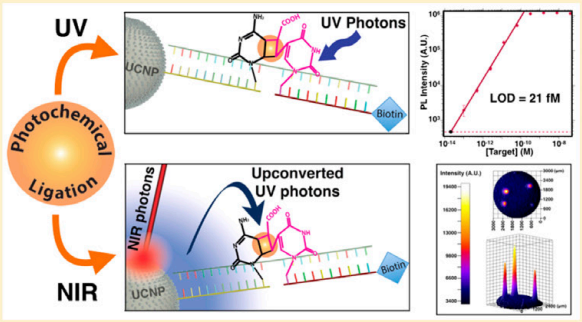

During last decades, short noncoding oligonucleotide sequences, particularly miRNAs, have been found to exert control over essential cell functions like proliferation, differentiation, and death.[1] Not surprisingly, the abnormal expression levels of many miRNAs have been related to different human diseases, such as cancer, Alzheimer disease, viral infections, and others.[2−6] For this reason, these biomolecules are nowadays under the spotlight as promising biomarkers for the early diagnosis, prognosis, and treatment of different human disorders.[2,7−9] Nevertheless, the small size of miRNAs imposes several limitations to their detection, due to the difficulty designing suitable probes and their low melting temperatures, among others.[10]

To face the problems inherent to miRNA detection and quantification, new detection strategies are needed if reliable diagnosis and prognosis of diseases using these biomarkers are to become a reality.[11,12]

In this direction, upconverting nanoparticles (UCNPs) are a new kind of photoluminescent material that are gaining attention in biomedical applications, specially for sensing and bioimaging,[13,14] as they are able to harvest near-infrared (NIR) light and to emit it in the UV−vis region. UCNPs exhibit several advantages over conventional dyes or quantum dots: the lack of autofluorescence, photobleaching, or blinking, together with a high photostability, permit the significant reduction of the background in imaging and detection applications, gaining sensitivity.[15,16] In addition, their long decay times allow one to create fluorescence resonance energy transfer systems that can be used as molecular rulers for analytical purposes.[17] Nevertheless, although having the potential to easily overcome the sensitivity limitations of other labels, there is little evidence that the UCNPs are currently showing much better performance in practical assays.[18]

As few or even single UCNPs can be imaged and detected using simple instrumentation,[16,19−21] nonspecific binding (NSB) of these reporters is the major limiting factor, since it elevates the background signals from blank samples, affecting the limit of detection (LOD) in bioaffinity binding assays.[18,22] Reducing the NSB could be solved in DNA/RNA sandwich hybridization assays by utilizing a target-specific formation of a covalent bond between the solid-phase capture probe and the UCNP-attached detection probe. That would allow the use of highly stringent washing protocols, reducing the NSB without affecting the selectively captured probes and improving the signal-to-background ratio and assay sensitivity.[23] This strategy would be particularly helpful to improve the detection limits in different sensing platforms, permitting one to find hard-to-

Received: July 11, 2018
Accepted: October 19, 2018
Published: October 19, 2018

DOI: 10.1021/acs.analchem.8b03106
Anal. Chem. 2018, 90, 13385−13392

Scheme 1. Action Mechanism of the Proposed Sensor[a]

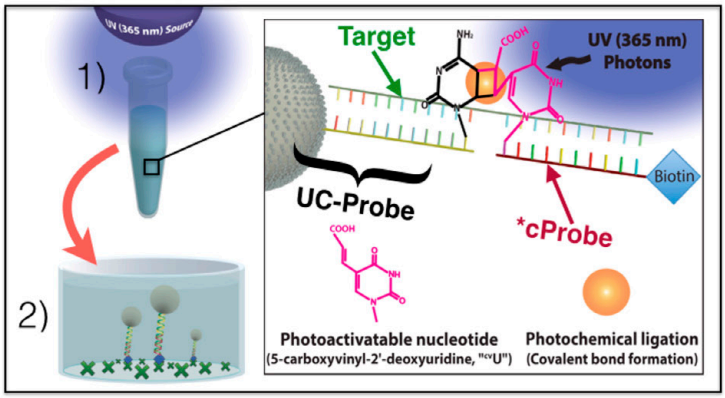

[a](1) In the presence of target sequence, UC-Probe and *cProbe are hybridized adjacently. Upon UV irradiation, a photochemical ligation occurs between the ^{cv}U photoactivatable nucleotide (pink) of *cProbe and the 3′-end cytosine of UC-Probe. (2) This yields biotin-functionalized UCNPs, which are then selectively captured on the surface of SA-coated microwells. The amount of UCNPs bound to the surface is proportional to the concentration of target sequence. Step 1 includes hybridization (30 min) and photochemical ligation (20 min). Step 2 involves the selective capture of the photoligated complexes (30 min), washing procedures (10-15 min), and drying of the microwells (30 min). As a result, the whole procedure could be carried out in about 2 h.

detect biomarkers such as miRNAs, which are present at low concentrations. With this in mind, we aimed to detect a DNA analogue of an important miRNA (miR-195) as the target sequence, the expression of which has been found to be almost 20-fold increased in breast cancer patients.[24] To do so, we have designed two oligonucleotide probes: a detection probe attached to UCNPs, "UC-Probe", and a capture probe containing a photoactivatable nucleotide (5-carboxyvinyl-2′-deoxyuridine or "^{cv}U") and a biotin moiety, "*cProbe". Although more efficient photoactivatable nucleotides have been reported,[25] we have chosen ^{cv}U as the photoactivatable nucleotide due to the relatively small size of the photoreactive moiety, which would permit efficient hybridization with the target sequence by minimizing possible steric hindrance issues, as well as its commercial availability. As opposed to enzymatic ligation strategies,[26−28] photochemical ligations permit one to avoid the stringent conditions required during use of ligase enzymes (e.g., temperature, ATP, $MgCl_2$, etc.), while nowadays showing comparable ligation times, allowing their potential application to more diverse conditions.[25] In addition, although much research is still necessary, the photochemical ligation reaction allows temporal and spatial control of the reaction that may permit the construction of new sensitive and robust direct-detection assay concepts, giving new opportunities in biosensing.

In our proposed system, UC-Probe and *cProbe are hybridized adjacently in the presence of the target sequence. As a result of the hybridization, a specific covalent bond between the two probes can be formed upon external irradiation with 365 nm light or by internal 365 nm upconverted emission upon 980 nm excitation.[29−32] Under these conditions, the UCNPs will be covalently modified with biotin and selectively captured on streptavidin (SA) coated microwells. After that, repeated washing cycles or harsh washes with NaOH solutions can be used to reduce the background and improve the detection limit of the assay. Scheme 1 summarizes the mechanism of action of the proposed methodology.

EXPERIMENTAL SECTION

Chemicals. All chemicals were purchased from Sigma-Aldrich and used as received. Bovine serum albumin was purchased from Bioreba. Assay buffer, washing buffer, and white and clear streptavidin-coated polystyrene microwells were purchased from Kaivogen (Turku, Finland). The photoactivatable probe (*cProbe) was obtained from Trilink Biotechnologies, the nonphotoactivatable probe (cProbe) was obtained from Biomers, and the other oligos were purchased from ThermoFisher Scientific. Table 1 describes the DNA sequences used in this work. In the Supporting Information (SI) there is a complete description of the chemicals used in this work.

Table 1. DNA Sequences Used in This Work

name	sequence
probe for bioconjugation with UCNPs, UC-Probe	5′-amino C6-GCCAATATTTC-3′
non-*photoactivatable* capture probe, cProbe	5′-TGTGCTGCTA-spacer-biotin-3′
photoactivatable capture probe, *cProbe	5′-^{cv}UGTGCTGCTA-spacer-biotin-3′
miR-195 DNA analogue, Target	5′-TAGCAGCACA**GAAATATTGGC**-3′

Characterization. Transmission electron micrographs were obtained using a JEOL JEM 1010 at 80 kV coupled to a GATAN MegaView II digital camera and a JEOL JEM 2100 at 200 kV coupled to a GATAN CCD Orius SC1000 digital camera. The transmission electron microscopy samples were prepared by putting a drop of the sample onto the grid and letting it to dry at room temperature. The microwell luminescence was analyzed using a Chameleon microplate reader (Hidex Ltd., Turku, Finland) modified with a near-infrared (980 nm) 0.5 W diode laser. A 8 W UV lamp (Spectroline model ENF-280C/F, 230 V, 50 Hz, 0.17 A, Spectronics Corp.) and a 2.7 W LED (Engin LZ1-00UV00 365 nm UV LED) with emission centered at 365 nm were used as UV light source for the photochemical ligation reaction. For the NIR-mediated photochemical ligation reaction, a home-

DOI: 10.1021/acs.analchem.8b03106
Anal. Chem. 2018, 90, 13385−13392

made illuminator was built combining a ~700 W/cm^2 CW laser (0.5 W continuous-wave laser power output focused in a ~300 μm diameter spot) at 980 nm with a microscope. More technical details about the light sources are given in the Supporting Information.

Synthesis of UCNPs ($NaYF_4$; 40% Yb, 0.5% Tm). The UCNPs were synthesized by the thermal coprecipitation method. Initially, 1.9 mg (0.005 mmol) of $TmCl_3$, 155 mg (0.4 mmol) of $YbCl_3$, and 182 mg (0.6 mmol) of YCl_3 were added to a three-necked round-bottom flask. Then, 15 mL of 1-octadecene and 6 mL of oleic acid were added, and the salts were dissolved with stirring at 180 °C for 1.5 h under a nitrogen atmosphere. After dissolution, the mixture was let to cool down to room temperature. In parallel, 100 mg of NaOH (2.5 mmol) and 150 mg of NH_4F (4 mmol) were dissolved in 10 mL of methanol. Next, the rare-earth solution was subjected to vigorous stirring while the methanolic solution was added dropwise. The mixture was stirred for 30 min, after which the temperature was fixed at 100 °C for another 30 min under a nitrogen atmosphere. After this, methanol and other traces were removed by vacuum for 15 min. Then, the flask was connected to a reflux system, purged with nitrogen, allowed to react for 1 h at 320 °C, and finally allowed to cool down to room temperature. The product was divided into centrifuge tubes, completed and mixed with deionized water, and centrifuged at 8000 rpm for 10 min. After this, the oily phase was removed, and the centrifuge tubes were completed with deionized water, vortexed, and ultrasonicated. After another centrifugation, the pellets were dried with acetone and finally dispersed and stored in hexane. The size, monodispersity, and SAED were studied by TEM, demonstrating the synthesis of β-$NaY_{0.64}F_4$;$Yb^{3+}_{0.32}Tm^{3+}_{0.04}$ (see section S2.1, Figures S4 and S5, and Table S1, SI). The Tm^{3+}-doped UCNPs exhibited the typical ultraviolet (365 nm), blue (475 nm), and near-infrared (800 nm) emission bands (Figure S4D, SI).

Coating of UCNPs with Poly(acrylic acid) (UCNPs@PAA). First, 5 mg of UCNPs in hexane was centrifuged at 16 873*g* for 30 min. Then, the resulting pellet was redispersed by ultrasonication in 1 mL of 0.1 M HCl. The UCNPs were slowly vortexed for 5 h. After this, the UCNPs were pelleted by centrifugation and washed with 1 mL of deionized water. A 1 mL portion of PAA (M_w ~ 2000 g/mol, 2.5 wt % solution, pH 9) was subsequently added, and the pellet was properly redispersed by vigorous ultrasonication and vortexing. After incubating this solution under slow vortexing for 16 h, the UCNPs@PAA were recovered by centrifugation. Next, the nanoparticles were washed twice with deionized water and once with 0.5 mL of 20 mM MES buffer, pH 6.1. Finally, UCNPs@PAA were redispersed in 250 μL of this buffer.

Oligonucleotide Conjugation of UCNPs@PAA. A 2.5 mg portion of UCNPs@PAA was centrifuged (20 237*g*, 10 min) and dispersed by ultrasonication in 230 μL of 20 mM MES (pH 6.5). Next, 10 μL (5 nmol) of UC-Probe oligonucleotide was added to the solution. Then, 5 μL of EDC·HCl (1 M, in MES buffer) and 5 μL of sulfo-NHS (3 M, in MES buffer) were added to the mixture, which was vortexed and ultrasonicated for 3 min. The final mixture was incubated for 2.5 h under slow rotation. After this, the reaction was quenched by adding 6.25 μL of glycine (2 M, pH 11), vortexed, and further incubated for 30 min. Then, the resulting UCNPs@PAA@ssDNA (UC-Probes) were centrifuged (20 237*g*, 10 min), redispersed in 500 μL of measurement buffer [10 mM Tris (pH 8.5), 0.1% Tween 20], and centrifuged again. Finally, the conjugated UCNPs were redispersed in 250 μL of storage buffer [5 mM Tris (pH 8.5), 0.2% Tween-80, 50 μM EDTA, 0.05 wt % NaN_3].

Optimization of DNA Denaturation Solution. First, the microwells were washed with a prewashing solution [5 mM Tris·HCl (pH 7.75), 150 mM NaCl, 0.05 g/L Tween-20, and 1 g/L Germall]. After that, 50 μL of an assay buffer [25 mM sodium tetraborate (pH 7.75), 1 M NaCl, 0.5% BSA, 0.1% Tween-20, 0.01% Tween-40, 0.05% NaN_3, 0.05% bovine γ-globuline, 20 μM DTPA] containing cProbe (26.1 nM) was added to the wells and incubated for 20 min under slow rotation (650 rpm) in a plate shaker. Then, the volume was retired, and 50 μL of assay buffer containing different target concentrations (0, 0.0013, 0.004, 0.012, 0.036, 0.11, 0.32, 0.97, and 2.9 nM) was incubated for 30 min. Later, 25 μL of UC-Probe was added to each well (final concentration of 7.5 μg/mL in a total volume of 75 μL/well), and the plates were incubated under shaking (650 rpm) at room temperature for 45 min. Later, the volume was aspirated from the wells, and 75 μL/well of assay buffer (control assay) and 75 μL/well of each denaturation solution (denaturation assays) were added to compare their effects. After incubating for 10 min, all the wells were washed four times with washing buffer [5 mM Tris-HCl (pH 7.75), 450 mM NaCl, 0.1% Tween-20, 1 g/L Germall], dried at room temperature, and their upconversion emission read.

Comparison of the Hybridization Process between Photoactivatable Capture Probe (*cProbe) and Non-photoactivatable Capture Probe (cProbe). Assay buffers containing 7.5 μg/mL of UC-Probe, 5 mM target sequence, and different concentrations of *cProbe or cProbe (0, 0.036, 0.11, 0.32, 0.97, 2.9, 8.7, 26.1, and 52.2 nM) were mixed and allowed to hybridize for 30 min under moderate shaking (950 rpm) at rt. Then, 50 μL of each sample was added into a prewashed microwell and incubated for 30 min (slow shaking, 650 rpm). Finally, the wells were washed four times with washing buffer and dried at rt, and the upconversion emission from the captured complexes was read.

UV Photochemical Ligation Assays. The study of the photochemical ligation kinetic was carried out as follows: An Eppendorf tube with 500 μL of buffer assay containing 7.5 μg/mL of UC-Probe, 5 nM target sequence, and 52.2 nM *cProbe (cProbe for the control experiment) was irradiated with a UV lamp or UV-LED for different times at 4 °C. After that, the solutions were added to prewashed streptavidin-coated microwells (50 μL/well, six replicas per studied point) and incubated for 30 min, and the solution was aspirated from the wells. Then, 75 μL per well of assay buffer was added to three (out of the six) replicas, while 75 μL per well of a 50 mM NaOH solution (denaturalizing solution previously optimized) was added to the other three replicas. The wells were incubated under slow shaking for 10 min. Finally, the wells were washed four times with washing buffer, dried at rt, and read. For DNA detection assays, the process was the same as indicated above but using a UC-Probe concentration of 3.75 μg/mL, a target concentration ranging from 1×10^{-13} to 60×10^{-8} M, and a fixed irradiation time of 2.5 vh (when using the UV lamp) or 20 min (when using the UV-LED) at 4 °C. The detection of the mismatched sequences was carried out using the same process as indicated above but with a fixed concentration of target or mismatched sequence of 50×10^{-12} M.

DOI: 10.1021/acs.analchem.8b03106
Anal. Chem. 2018, 90, 13385−13392

NIR Photochemical Ligation Reactions. UC-Probe, *cProbe, and target sequence were mixed in assay buffer to a final concentration of 7.5 μg/mL, 52.2 nM, and 5 nM, respectively, and allowed to hybridize for 30 min. Then, the solution was added to the prewashed white streptavidin-coated microwells (50 μL/well) and incubated for another 30 min. After this, the volume was aspirated, 50 μL/well of irradiation solution (0.5 M NaCl and 1 mM NaF in D_2O) was added, and the microplate was placed inside a platform containing an ice bath for irradiation. Then, the bottoms of the wells were irradiated with a focused NIR laser (0.5 W power imput, 700 W/cm^2 surface power density) for different times. Next, the volume from the wells was aspirated, and 75 μL/well of assay buffer was added to the control wells, while 75 μL/well of 10 mM NaOH was added to reveal the photoligated spots. The wells were then incubated for 10 min, after which they were washed four times with washing solution. The bottoms of the wells were revealed using the anti-Stokes photoluminescence imaging device. In the case of NIR photoligation detection assays, the process was the same as described above but using different target concentrations (0, 8, 40, and 200 pM) and using an NIR irradiation time of 10 min at 700 W/cm^2.

All the experiments were made at least in triplicate, and the results were used to calculate the mean values and the standard deviations.

■ RESULTS AND DISCUSSION

Influence of the Photoactivatable Nucleotide on Hybridization. The DNA target sequence detected in this work brings in close proximity the UCNP-attached probe oligonucleotide (UC-Probe) and the biotinylated photoactivatable probe (*cProbe) upon hybridization. Under this scenario, the cytosine at the 3′-end in UC-Probe faces the photoactivatable nucleotide 5-carboxyvinyl-2′-deoxyuridine (^{cv}U; see Figure S6A, SI), located at the 5′-end in *cProbe (see Scheme 1). After that, the spatial conformation of these nucleotides allows the photochemical reaction upon irradiation at 365 nm. The influence of the ^{cv}U moiety on the hybridization process has been studied, as it could hamper the performance of the assay by reducing the stability of the hybridized DNA strands. For that, *cProbe performance was compared with an equivalent nonphotoactivatable capture oligonucleotide (cProbe) in which ^{cv}U was substituted by a thymidine (see Figure S6C, SI). Different concentrations of *cProbe and cProbe were tested without irradiation at 365 nm to compare the signals obtained by hybridization and to establish the optimal *cProbe and cProbe concentration. Thus, UC-Probe and the target sequence were kept at a fixed concentration of 7.5 μg/mL and 5 × 10^{-9} M, respectively, while different *cProbe or cProbe concentrations were tested. Both probes resulted in the same signals at the tested concentrations, indicating that the structure of ^{cv}U did not affect the hybridization properties (Figure 1). The formation of a signal plateau at the higher *cProbe and cProbe concentrations led us to select 52 × 10^{-9} M as their optimal concentration to be used in further assays, since it yielded the highest signal for the detection of the desired target concentration. This indicated efficient hybridization to the target and the maximum capture of hybridized complexes onto the microwell surface.

Optimization of the Photochemical Ligation Reaction. The UV irradiation of the hybridized complexes allows a photochemical ligation reaction between UC-Probe and *cProbe, yielding a cyclobutane moiety that acts as covalent bridge between the two probes, as shown in Scheme 1. This process permits in a subsequent step a selective capture of the biotin-modified UCNPs on the streptavidin-coated microwell surface. In order to indirectly evaluate the efficiency of the process, which includes different stages like hybridization, irradiation, and [2 + 2] cyclization, we compared the signals obtained after capture when irradiating the samples for a fixed time (60 min), under different hybridization conditions (e.g., ionic strength, temperature), and with or without a denaturation treatment (50 mM NaOH) of the solid support for both *cProbe and cProbe (see Figure 2). The denaturation solution (50 mM NaOH) induces the denaturation of the DNA strands in the sandwich assay without substantially affecting the physicochemical properties of the streptavidin, as described in the Experimental Section (see Figure S7, SI). Therefore, the maximum signal (normalized to 1) presented the sum of the contributions of the photoligated and nonligated hybridized probes, while the retention of the upconversion luminescence signal after NaOH wash could be only attributed to the formation of a covalent bond between the probes (i.e., photoligated probes' contribution). Figure 2 depicts the results obtained during the optimization of this process.

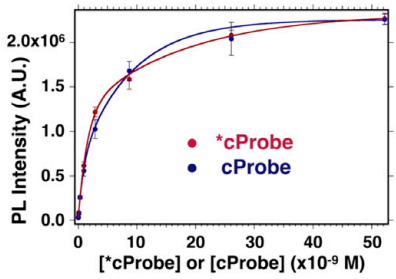

Figure 1. Upconversion photoluminescence intensity at 470 nm under 980 nm excitation, obtained using different concentrations of *cProbe or cProbe in the presence of 5 × 10^{-9} M target sequence and 7.5 μg/mL of UC-Probe in the sandwich hybridization assay.

Initially, the photochemical ligation reaction was carried out by illuminating the samples with a 8 W UV lamp with a maximum emission centered at 365 nm for 60 min using 7.5 μg/mL of UC-Probe, 5 × 10^{-9} M target sequence, and 52 × 10^{-9} M cProbe or *cProbe concentration. Under these conditions it was found that, in the assay using cProbe, practically all the UC-Probe dehybridized upon NaOH treatment, while in the assay with the *cProbe, around 40% of the UC-Probe remained anchored, indicating covalent bond formation upon photoligation (see Figure 2A). With the aim of improving the photochemical ligation process efficiency, we analyzed the influence of different parameters, like the ionic strength used during the hybridization process. As shown in Figure 2B, the highest signal was obtained when the concentration of NaCl used during the hybridization was 1 M. As expected, the increment of the ionic strength favors the hybridization of the probes, which enhances the efficiency of the photochemical ligation process by improving the stability of the DNA duplexes during the irradiation. In addition, charge screening of the carboxylate group in the photoactivatable moiety (see Figure S6A, SI) may allow a more favorable spatial configuration for the photochemical reaction to happen, giving higher reaction efficiency. In addition, we studied the influence

DOI: 10.1021/acs.analchem.8b03106
Anal. Chem. 2018, 90, 13385−13392

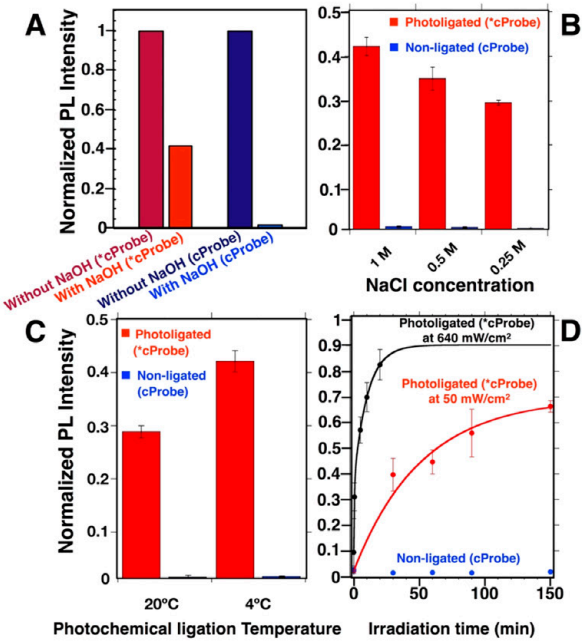

Figure 2. Assessment and optimization of the photochemical ligation process at 5×10^{-9} M target. The normalized photoluminescence (PL) intensities are presented for *cProbe and cProbe, evaluating the effect of using different conditions during UV irradiation (365 nm) on the photoligation reaction progress (A) Normalized signals after washing the solid support without or with NaOH treatment for *cProbe (dark red and light red, respectively) and for cProbe (dark blue and light blue, respectively). (B) Effect of ionic strength, (C) effect of temperature, and (D) effect of UV irradiation time at two different surface power densities on signals after washing the solid support with NaOH treatment. Light red and light blue colors indicate the relative signals after NaOH treatment of the solid support when using *cProbe and cProbe, respectively.

of the temperature on the photochemical ligation process, since overheating of the sample during irradiation could negatively affect the hybridization process of the reactive oligonucleotides. In fact, we observed that lower reaction temperatures resulted in a higher efficiency of the photoligation process, as seen in Figure 2C. Finally, we evaluated the influence of the irradiation time and the surface power density on the reaction progress (see Figure 2D). Here, we can observe that upon irradiation at 50 mW/cm^2 the yield of the *cProbe photoligation was around 0.4 after 60 min, while after 2.5 h a value close to 0.65 was obtained. To increase the photoligation reaction yield, we illuminated the samples using a 365 nm LED UV light (Figure S1, SI) with a surface power density of 640 mW/cm^2. This allowed increasing the value up to 0.83 after an illumination time of only 20 min (Figure 2D). It is important to highlight that similar optimized yields have been also reported by others,[33,34] although in our case higher sample volumes (up to 10-fold) have been successfully photoligated in a comparable time. Interestingly, RNA templates (i.e., RNA target sequences) seem to increase the efficiency of the photoligation, implying that an even shorter UV irradiation time is expected to be needed when detecting real miRNA target (miR-195).[34] Under such conditions, the irradiation time showed here to photoligate ^{cv}U to C should be applicable when aiming to photoligate ^{cv}U to T, as the irradiation time needed to achieve a comparable level of photoligation in this case would be slightly shorter.[34] Interestingly, instead of photoligating two DNA probes, the combination of an RNA probe containing a 3′-terminal U with a DNA probe containing a 5′-terminal ^{cv}U seems to be an alternative way to increase the efficiency of photoligation, apparently due to a special spatial configuration between the probes upon hybridization with a DNA template.[33] Unfortunately, the increased efficiency of this strategy has not been confirmed yet when using RNA sequences as (target) templates.

DNA Detection Assay Based on Photochemical Ligation Reaction. To find the best analytical conditions for the target detection, we plotted the different signal intensities collected from UV-irradiated DNA detection assays using *cProbe or cProbe (with and without NaOH treatment) in the presence of 5×10^{-12} M target sequence (see Figure 3A). The background signals provided by their negative controls (absent of target) and which arise from UC-Probe nonspecific binding were also plotted in Figure 3A. These parameters are tremendously important, since the former

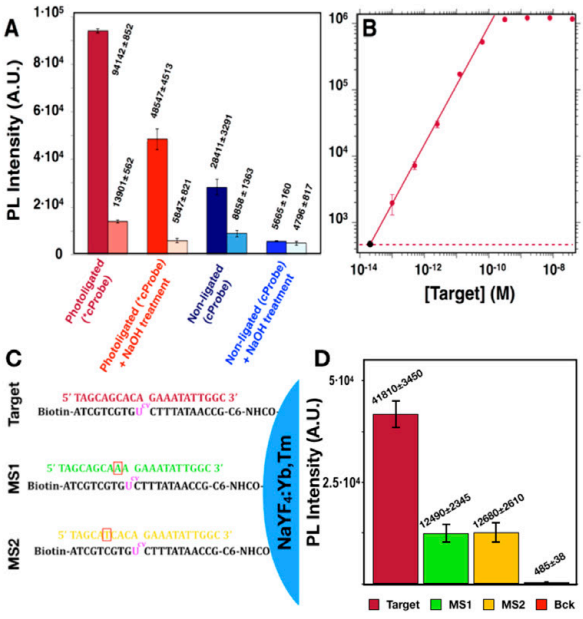

Figure 3. (A) Influence of *cProbe or cProbe and washing conditions on the signal intensity obtained with 5×10^{-12} M target concentration (columns with intense colors) and the absence of target (adjacent columns with faded colors). Photoligated assay without (dark red) and with (red) NaOH treatment. Nonligated assay without (dark blue) and with (blue) NaOH treatment. The intensity and the standard deviation values are depicted above each column as intensity ± SD. (B) Calibration curve obtained with the photoligated assay without NaOH treatment. The LOD is represented as the dotted line. (C) Representation of the possible duplexes formed, where the position of each mismatch is marked with red squares. (D) Upconversion emission obtained with photoligated assay without NaOH treatment of 7.5 μg/mL of UC-probe with 50×10^{-12} M per well of different sequences: full complementary sequence (Target), a sequence containing a single mismatch close to the photoactivatable moiety (MS1), and a sequence containing a single mismatch in the middle (MS2). The error bars indicate the standard deviation obtained from four independent replicas.

DOI: 10.1021/acs.analchem.8b03106
Anal. Chem. 2018, 90, 13385−13392

defines the sensitivity when compared to the background signal, while the latter is related to the LOD defined as the background signal plus three times the standard deviation (SD).

From these experiments, we observed that the maximum signal was obtained when the UC-Probes are photoligated, and repeated washes without NaOH treatment were used (incubation of the solid support with assay buffer followed by four cycles with washing buffer). By contrast, when the same process is applied to nonligated UC-Probes, there is an important loss of signal, which could be due to the low thermodynamic stability of the short DNA strands. This fact can contribute to the dehybridization of the probes during the assay buffer incubation and washing cycles, resulting in a reduction of the amount of captured UC-Probes. Interestingly, when the UC-Probes are photoligated and NaOH treatment is used (incubation with NaOH followed by four cycles with washing buffer), we observe a reduction not only of the background signal but also of the specific PL intensity when detecting 5×10^{-12} M target. This may be related to the loss of those UC-Probes that may have not been photochemically stabilized, together with some disruption of biotin−streptavidin interactions upon NaOH treatment.[35,36] Even so, it is remarkable that the signal obtained with photoligated UC-Probes using 5×10^{-12} M target after the NaOH treatment is still higher than the one obtained with the assay using nonligated UC-Probes without the NaOH treatment. In addition, photoligated UC-probes with NaOH treatment exhibit a higher signal to background ratio (Sg/Bg ratio) than the photoligated UC-probes without NaOH treatment, which evidence the capacity of the NaOH treatment to reduce the NSB and potentially enhance the analytical properties of the assay. Finally, it is important to highlight that the use of the NaOH treatment on the nonligated UC-Probes makes the signal drop down to a level comparable to that from its background signal. In summary, the aforementioned results indicate that photoligation avoids the loss of specific signal by denaturation of the probes during repeated washes, improving the Sg/Bg ratio and the sensitivity in comparison with traditional assays. This system also permits the use of very stringent solutions (e.g., NaOH) as a way to reduce the background signal and thus improve the Sg/Bg ratio, although the use of repeated washes seems to yield better assay performances under our studied conditions due to lower standard deviations.

The combination of optimal analytical conditions (i.e., for photoligation, washes, etc.) were used to build a calibration curve, as seen in Figure 3B. This graph shows how the proposed sensor allows the detection of different target concentrations along almost 4 orders of magnitude (linear range from 2×10^{-14} to 5×10^{-10} M), giving a saturation signal above 5×10^{-10} M. At the same time, the very high sensitivity of the sensor is demonstrated by its LOD (defined as the background signal + 3 × standard deviation), which corresponds to 2.1×10^{-14} M. Remarkably, this LOD (~12 600 copies/μL) is already within the concentration range of some low to moderately abundant circulating miRNAs (8910−133 970 copies/μL),[37] while it has been obtained by a direct (nonamplified) relatively quick strategy (~2 h assay). The excellent performance showed by the assay in terms of small standard deviations and wide linear range would permit one to accurately correlate the upconversion intensity yielded by an unknown sample to detect the presence or absence of the specific target, while the quantitative value for its concentration was obtained with high sensitivity. Additionally, the capacity of the sensor to discriminate the presence of mutations within the sequences was checked using sequences with a single mismatch located close to the photoactivatable moiety (MS1) or at the center of the strand (MS2) (see Figure 3C). In both cases, the presence of mismatches within the DNA strands was concomitant with a 70% signal reduction of the PL intensity compared with the full complementary target sequence at the same concentration (see Figure 3D). These results demonstrate that the proposed sensor also exhibits moderate selectivity besides its excellent sensitivity. It is important to highlight that the selectivity of the system could be easily improved by reducing the ionic strength of the buffer, which was kept at 1 M NaCl for consistency with previous experiments. Interestingly, the complex buffer used in this work already partially resembles the composition of serum due to the high amount of BSA and other proteins and components, giving relatively realistic detection conditions if compared with simple buffers consisting only of a saline solution with a buffering molecule. Finally, it is worth mentioning that the possibility to undo the photoligation between UC-Probe and *cProbe by using 311 nm light[30,34,38] potentially permits the reusability of the streptavidin-coated surfaces to which these sensors may be applied to as detection platforms.

Photoligation Using Near-Infrared (NIR) Excitation as External Source and Design of a Conceptual "Patterned-Intensity"-Based Biosensor. UCNPs doped with Yb^{3+} and Tm^{3+} have a narrow emission peak at 365 nm upon irradiation with a 980 nm NIR CW laser.[39] This property was utilized to carry out the photoligation reaction using focused NIR light as external stimuli. In these experiments, hybridization of UC-Probe and *cProbe with 2×10^{-10} M DNA target and further capture of the hybridized complexes in the microwell were carried out exactly as in previous experiments, but without irradiating the samples with UV light. Once in the microwells, the volume was replaced by D_2O containing 0.5 M NaCl and the microplate was introduced in an ice bath to keep the microwells refrigerated during NIR (980 nm) irradiation, as well as to increase the efficiency of the photochemical ligation process, as shown previously in Figure 2C. The laser was focused in a small area (~300 μm in diameter) to promote the 365 nm emission of the Tm-doped UCNPs (allowing photoligation to proceed at their surface), while permitting one to use a relatively low laser power (0.5 W) to ensure a minimum thermal loading during the experiments. A scheme of the device built to carry out these experiments is shown in Figure S2 (SI). After irradiation, a treatment with NaOH was used to denaturalize the nonligated complexes, permitting to reveal the possible NIR-mediated photoligated ones that should remain attached to the microwells. Finally, the imaging of the dry microwell was carried out by illuminating the whole surface with a 7.0 W 980 nm laser (see the complete scheme of the device in Figure S3, SI).

Figure 4 depicts schematically the photochemical ligation reaction initiated by NIR light as external stimuli and the surface plot intensity obtained from the bottom of the microwell, where the reaction took place. When imaging the resulting microwell, a defined region that exhibited upconverting emission was found. This region presented a size of around 300 μm in diameter and a circular shape, which stem from the NIR light focal point. The photoligation yield was estimated to

DOI: 10.1021/acs.analchem.8b03106
Anal. Chem. 2018, 90, 13385−13392

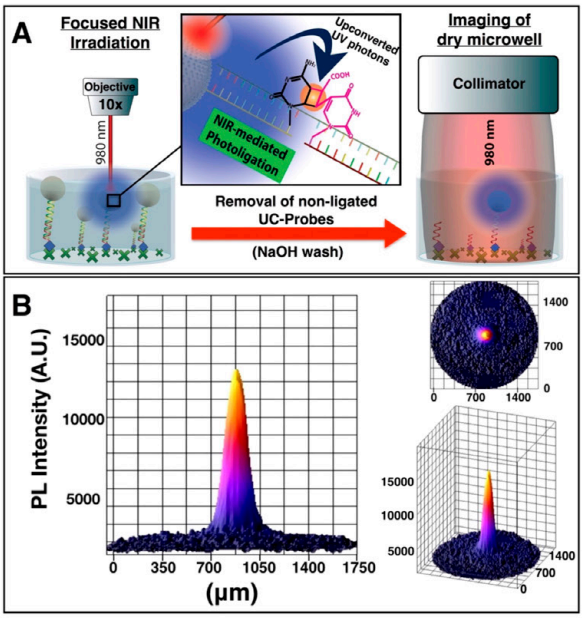

Figure 4. Photochemical ligation reaction initiated by NIR light. (A) Scheme of focused NIR irradiation on microwells for the local photoligation on the surface of UC-Probes by their upconverted 365 nm emission. When using a NaOH treatment, the nonligated UC-Probes are denatured, while the photoligated UC-Probe pattern remains and can be later revealed by illuminating the whole microwell at 980 nm. (B) Surface plot intensity of 470 nm upconverted emission, obtained after illuminating the bottom of a microwell where UC-Probes had been previously photoligated using NIR light in the presence of 2×10^{-10} M target sequence. From left to right and from top to bottom: Front, top, and side view of the photochemically ligated spot, respectively.

be around 30%. Control experiments comparing *cProbe with cProbe showed that a moderate level of signal remained in the latter upon laser exposition, due to an increase of the NSB (see Figure S8, SI). However, the signal intensity yielded by *cProbe in all the experiments was much higher and permits one to conclude that it is possible to initiate the photochemical ligation reaction also using NIR light as external stimuli.

Additional experiments where designed in order to assess the potential and possible applications of this NIR initiated photoligation modality. For example, we found that the intensity of the photoligated spots followed a proportional relationship with the concentration of target present in the media (Figure S9, SI). Thus, a reduction of the target concentration resulted in a proportional reduction of the photoligated spot signal, which potentially allows using this system for biosensing. This NIR-initiated strategy was also explored as a way to create patterns whose formation relied on the presence of the target sequence: upon hybridization and capture, the microwell surface is covered with hybridized complexes, which can be selectively irradiated at desired spatial coordinates. When irradiating the surface at different locations, the intensity of the spots (which collectively formed a pattern) could be individually controlled by varying the irradiation time, as this results in different photoligation yields (Figure S10A, SI). Finally, the shape of the photoligated spot could be controlled, as demonstrated, by changing the laser beam from a circular to a rectangular shape (Figure S10B). In summary, the NIR-initiated photoligation modality is an interesting approach that could be used to analyze samples sensitive to UV light.

■ CONCLUSIONS

In this work, we have constructed a highly sensitive DNA sensor based on the target-dependent covalent functionalization of ssDNA-functionalized UCNPs and their immobilization on a solid support. This covalent functionalization was based on a photochemical ligation, which permitted to biotinylate the UCNPs upon irradiation with 365 nm UV light when a specific DNA target sequence was present. Our strategy avoided the loss of signal by dissociation of the bound UCNPs when the microwells were repeatedly washed. As a result, a detection system with a LOD of 2×10^{-14} M and a linear range of 4 orders of magnitude was obtained. In addition, the sensor exhibited good selectivity toward single mismatched sequences. Furthermore, the possibility to carry out the photochemical ligation reaction using NIR light as external stimuli has been successfully tested, demonstrating its potential to create patterns for analytical purposes when the use of UV light is not recommended.

■ ASSOCIATED CONTENT

Supporting Information

The Supporting Information is available free of charge on the ACS Publications website at DOI: 10.1021/acs.analchem.8b03106.

Materials, description of the homemade instruments, methods, TEM images, and complementary analyses, including EDX, size-distribution, SAED, and UCNP photoluminescence spectrum, are described (PDF)

■ AUTHOR INFORMATION

Corresponding Authors

*J.R.-R.: e-mail, bjrubio@ucm.es; phone: +34913941751.
*T.S.: e-mail, tejoso@utu.fi; phone: +358294504589.

ORCID

Satu Lahtinen: 0000-0003-2816-7809
Marco Laurenti: 0000-0002-0273-7423
Jorge Rubio-Retama: 0000-0002-1785-5844

Notes

The authors declare no competing financial interest.

■ ACKNOWLEDGMENTS

The authors would like to thank the Spanish MINECO (project MAT2014-55065-R, MAT2017-83111-R), the Santander-UCM (PR26/16-12B-3), and Comunidad Autónoma de Madrid (B2017/BMD-3867 RENIM-CM). D.M.G. thanks UCM-Santander for a predoctoral contract (CT17/17-CT18/17) and T.S. and S.L. thank Tekes, the Finnish Funding Agency for Innovation, and the Doctoral Programme in Molecular Life Sciences for their financial support. Part of this work was supported by the COST Action CM1403 The European Upconversion Network From The Design of Photon-upconverting Nanomaterials To (Biomedical) Applications. The authors thank Kenzo Fujimoto and Shigetaka Nakamura for their scientific advice. The authors also would like to thank Juan Luis Méndez González for his essential role in the construction of the UV-LED prototype and Daniel Pascual Herranz for his continuous advice and useful information on 3D-printing and electronics fields.

DOI: 10.1021/acs.analchem.8b03106
Anal. Chem. 2018, 90, 13385−13392

REFERENCES

(1) Hwang, H.-W.; Mendell, J. T. *Br. J. Cancer* **2006**, *94* (6), 776–780.
(2) Hayes, J.; Peruzzi, P. P.; Lawler, S. *Trends Mol. Med.* **2014**, *20* (8), 460–469.
(3) Hu, Y.-B.; Li, C.-B.; Song, N.; Zou, Y.; Chen, S.-D.; Ren, R.-J.; Wang, G. *Front. Aging Neurosci.* **2016**, *8*, 13.
(4) Grundhoff, A.; Sullivan, C. S. *Virology* **2011**, *411* (2), 325–343.
(5) Hussain, M.; Asgari, S. *Proc. Natl. Acad. Sci. U. S. A.* **2014**, *111* (7), 2746–2751.
(6) Li, Y.; Kowdley, K. V. *Genomics, Proteomics Bioinforma.* **2012**, *10* (5), 246–253.
(7) Hennessey, P. T.; Sanford, T.; Choudhary, A.; Mydlarz, W. W.; Brown, D.; Adai, A. T.; Ochs, M. F.; Ahrendt, S. A.; Mambo, E.; Califano, J. A. *PLoS One* **2012**, *7* (2), e32307.
(8) Manterola, L.; Guruceaga, E.; Pérez-Larraya, J. G.; González-Huarriz, M.; Jauregui, P.; Tejada, S.; Diez-Valle, R.; Segura, V.; Samprón, N.; Barrena, C.; Ruiz, I.; Agirre, A.; Ayuso, Á.; Rodríguez, J.; González, Á.; Xipell, E.; Matheu, A.; López De Munain, A.; Tuñón, T.; Zazpe, I.; García-Foncillas, J.; Paris, S.; Delattre, J. Y.; Alonso, M. M. *Neuro. Oncol.* **2014**, *16* (4), 520–527.
(9) Iorio, M. V.; Visone, R.; Di Leva, G.; Donati, V.; Petrocca, F.; Casalini, P.; Taccioli, C.; Volinia, S.; Liu, C. G.; Alder, H.; Calin, G. A.; Ménard, S.; Croce, C. M. *Cancer Res.* **2007**, *67* (18), 8699–8707.
(10) Cissell, K. A.; Shrestha, S.; Deo, S. K. *Anal. Chem.* **2007**, *79* (13), 4754–4761.
(11) Qiu, X.; Guo, J.; Xu, J.; Hildebrandt, N. *J. Phys. Chem. Lett.* **2018**, *9* (15), 4379–4384.
(12) Jin, Z.; Geißler, D.; Qiu, X.; Wegner, K. D.; Hildebrandt, N. *Angew. Chem., Int. Ed.* **2015**, *54* (34), 10024–10029.
(13) Han, Y.; Noor, M. O.; Sedighi, A.; Uddayasankar, U.; Doughan, S.; Krull, U. J. *Langmuir* **2017**, *33* (45), 12839–12858.
(14) Hemmer, E.; Benayas, A.; Légaré, F.; Vetrone, F. *Nanoscale Horiz.* **2016**, *1* (3), 168–184.
(15) Chen, G.; Qiu, H.; Prasad, P. N.; Chen, X. *Chem. Rev.* **2014**, *114* (10), 5161–5214.
(16) Wu, S.; Han, G.; Milliron, D. J.; Aloni, S.; Altoe, V.; Talapin, D. V.; Cohen, B. E.; Schuck, P. J. *Proc. Natl. Acad. Sci. U. S. A.* **2009**, *106* (27), 10917–10921.
(17) Melle, S.; Calderón, O. G.; Laurenti, M.; Mendez-Gonzalez, D.; Egatz-Gómez, A.; López-Cabarcos, E.; Cabrera-Granado, E.; Díaz, E.; Rubio-Retama, J. *J. Phys. Chem. C* **2018**, *122* (32), 18751–18758.
(18) Mendez-Gonzalez, D.; Lopez-Cabarcos, E.; Rubio-Retama, J.; Laurenti, M. *Adv. Colloid Interface Sci.* **2017**, *249*, 66–87.
(19) Nam, S. H.; Bae, Y. M.; Park, Y. I; Kim, J. H.; Kim, H. M.; Choi, J. S.; Lee, K. T.; Hyeon, T.; Suh, Y. D. *Angew. Chem., Int. Ed.* **2011**, *50* (27), 6093–6097.
(20) Zhao, J.; Jin, D.; Schartner, E. P.; Lu, Y.; Liu, Y.; Zvyagin, A. V.; Zhang, L.; Dawes, J. M.; Xi, P.; Piper, J. A.; Goldys, E. M.; Monro, T. M. *Nat. Nanotechnol.* **2013**, *8* (10), 729–734.
(21) Rodríguez-Sevilla, P.; Labrador-Páez, L.; Wawrzyńczyk, D.; Nyk, M.; Samoć, M.; Kar, A. K.; Mackenzie, M. D.; Paterson, L.; Jaque, D.; Haro-González, P. *Nanoscale* **2016**, *8* (1), 300–308.
(22) Sirkka, N.; Lyytikäinen, A.; Savukoski, T.; Soukka, T. *Anal. Chim. Acta* **2016**, *925*, 82–87.
(23) Mendez-Gonzalez, D.; Laurenti, M.; Latorre, A.; Somoza, A.; Vazquez, A.; Negredo, A. I.; López-Cabarcos, E.; Calderón, O. G.; Melle, S.; Rubio-Retama, J. *ACS Appl. Mater. Interfaces* **2017**, *9* (14), 12272–12281.
(24) Heneghan, H. M.; Miller, N.; Lowery, A. J.; Sweeney, K. J.; Newell, J.; Kerin, M. J. *Ann. Surg.* **2010**, *251* (3), 499–505.
(25) Ami, T.; Fujimoto, K. *ChemBioChem* **2008**, *9* (13), 2071–2074.
(26) Bauer, R. J.; Jurkiw, T. J.; Evans, T. C.; Lohman, G. J. S. *Biochemistry* **2017**, *56* (8), 1117–1129.
(27) Huh, Y. S.; Lowe, A. J.; Strickland, A. D.; Batt, C. A.; Erickson, D. *J. Am. Chem. Soc.* **2009**, *131* (6), 2208–2213.
(28) Xue, X.; Xu, W.; Wang, F.; Liu, X. *J. Am. Chem. Soc.* **2009**, *131* (33), 11668–11669.
(29) Tagawa, M.; Shohda, K. I.; Fujimoto, K.; Sugawara, T.; Suyama, A. *Nucleic Acids Res.* **2007**, *35* (21), e140.
(30) Nakamura, S.; Ogasawara, S.; Matuda, S.; Saito, I.; Fujimoto, K. *Molecules* **2012**, *17* (1), 163–178.
(31) Prasad, P. N. *Introduction to Biophotonics*; John Wiley & Sons, Inc.: Hoboken, NJ, 2003.
(32) Ogasawara, S.; Fujimoto, K. *Angew. Chem.* **2006**, *118* (27), 4624–4627.
(33) Yoshimura, Y.; Noguchi, Y.; Fujimoto, K. *Org. Biomol. Chem.* **2007**, *5* (1), 139–142.
(34) Yoshimura, Y.; Noguchi, Y.; Sato, H.; Fujimoto, K. *ChemBioChem* **2006**, *7* (4), 598–601.
(35) Kilili, G. K.; Tilton, L.; Karbiwnyk, C. M. *BioTechniques* **2016**, *61*, 114–116.
(36) Marimuthu, C.; Tang, T. H.; Tominaga, J.; Tan, S. C.; Gopinath, S. C. B. *Analyst* **2012**, *137* (6), 1307–1315.
(37) Mitchell, P. S.; Parkin, R. K.; Kroh, E. M.; Fritz, B. R.; Wyman, S. K.; Pogosova-Agadjanyan, E. L.; Peterson, A.; Noteboom, J.; O'Briant, K. C.; Allen, A.; Lin, D. W.; Urban, N.; Drescher, C. W.; Knudsen, B. S.; Stirewalt, D. L.; Gentleman, R.; Vessella, R. L.; Nelson, P. S.; Martin, D. B.; Tewari, M. *Proc. Natl. Acad. Sci. U. S. A.* **2008**, *105* (30), 10513–10518.
(38) Ogasawara, S.; Fujimoto, K. *ChemBioChem* **2005**, *6* (10), 1756–1760.
(39) Beyazit, S.; Ambrosini, S.; Marchyk, N.; Palo, E.; Kale, V.; Soukka, T.; Tse Sum Bui, B.; Haupt, K. *Angew. Chem., Int. Ed.* **2014**, *53* (34), 8919–8923.

DOI: 10.1021/acs.analchem.8b03106
Anal. Chem. 2018, 90, 13385–13392

Supporting information

Photochemical ligation to ultrasensitive DNA detection with upconverting nanoparticles

Diego Mendez-Gonzalez[1], Satu Lahtinen[2], Marco Laurenti[1], Enrique López-Cabarcos[1], Jorge Rubio-Retama[1*], Tero Soukka[2*].

[1] Department of Chemistry in Pharmaceutical Sciences, Faculty of Pharmacy. Universidad Complutense de Madrid. Plaza Ramon y Cajal, s/n, 28040, Madrid, Spain.

[2] Department of Biotechnology, University of Turku, Kiinamyllynkatu 10, FI-20520 Turku, Finland.

Correspondence to: bjrubio@ucm.es or tejoso@utu.fi

Phone number: +34913941751 or +358294504589

Index

b. Plate washer

c. UV lamp (365 nm irradiation)

d. UV-LED Prototype (365 nm irradiation). Figure S1

e. Instrument for focused NIR-irradiation of microwells' bottom surface (980 nm NIR photoligation). Figure S2

f. Anti-Stokes photoluminescence imaging device (Imaging of microwells' bottom surface). Figure S3

S2. Results

S2.1 Characterization of $NaYF_4$:Yb(40%); Tm(0.5%) upconverting nanoparticles. Figure S4 and Figure S5 ; Table S1.

S2.2 Structure comparison of *photoactivatable* and non-*photoactivatable* nucleotides. Figure S6

S2.3 Selection of denaturation solution. Figure S7

S2.4 Comparison of *cProbe and cProbe under focused NIR photoligation. Figure S8.

S2.5 Target detection by focused NIR photoligation. Figure S9.

S2.6 Patterning, spot shape and intensity variation. Figure S10.

S3. References

S1. Materials

S1.1 Chemicals

Ytterbium (III) chloride hexahydrate (99.9%), yttrium (III) chloride hexahydrate (99.9%), thulium (III) chloride hexahydrate (99.9%), 1-octadecene (90%), oleic acid (90 %), sodium hydroxide (98%), ammonium

fluoride (99.9%), methanol (99.9%), n-hexane (95%), N-(3-(dimethylamino)propyl)-N'-ethylcarbodiimide hydrochloride (99%), N-hydroxysulfosuccinimide sodium salt (Sulfo-NHS) (98%), polyacrylic acid (Mw~2000; 50 wt% in H_2O), bovine gamma globuline, 2-(*N*-morpholino)ethanesulfonic acid (MES), Tween-20, Tween-40, and diethylenetriaminepentaacetic acid (DTPA) were purchased from Sigma Aldrich and used as received.

S1.2 Instrumentation and measurements

a) Reading of assays (Anti-stokes luminescence adapted microplate reader)

The microwells were analysed using a Chameleon microplate reader (Hidex Ltd., Turku, Finland) modified with a near infrared (980 nm) 0.5 W diode laser for the excitation of the upconverting nanoparticles. This setup has been previously described by Soukka et. al.[1] Emission from each well was measured with 470/20 nm emission filter (Chroma Technology, Rockingham, VT) by 3x3 point raster mode using 2-s excitation for each measurement point, and an average intensity was calculated.

b) Plate Washer, The washing of microtitration plate wells was performed using a plate washer by Wallac (Perkin Elmer, model 1296-026 Delfia Platewash).

c) UV lamp (365 nm irradiation)

A 8 W UV lamp in 365 nm emission mode was used (Spectroline model ENF-280C/F, 230 Volts, 50 Hz, 0.17 Amps, Spectronics corporation, Westbury, New York, USA) for simultaneous irradiation of multiple samples by placing it on top of the uncapped eppendorfs. The distance between the surface of the UV lamp and the surface of the samples was typically 1 cm.

d) UV-LED Prototype (365 nm irradiation)

Adaptors for UV-LED (365 nm) prototype were custom modeled using Autodesk Autocad 2015. They were then 3D printed by means of a Makerbot Replicator 2 series with a maximum layer resolution of 100 micrometers, loaded with RS Pro 1.75mm Natural PLA 3D Printer Filament. As UV light source, an LED (Engin LZ1-00UV00 365 nm UV LED) with 1200mW flux output at 2.7W power dissipation was used, placed on top of the sample at a distance of 1.3 cm. In order to minimize variations on LED's performance over time due to warming up, a passive oversized anodized aluminum heat sink (Advanced Thermal Solutions ATSEU-077A2-C1-R1) with a maximum dissipation power of 16 watts at ΔT = 65ºC was attached to it. Standard silicone based CPU thermal grease was used to optimize the thermal transfer across the interface.

The UV LED was powered using a stepdown Recom RCD-24-0.70 LED driver at 700 mA constant DC Current, which was PWM intensity controlled by a BLE compatible Arduino/Genuino 101 microcontroller. Custom firmware for Input/Output control and supervision, 8bit resolution PWM generation @500 Hz default frequency and auto timer-stop function where also developed for this purpose. Full real time serial communication was kept for double-check monitorization of the prototype well-functioning. Images of the prototype and the adaptors can be seen in Figure S1.

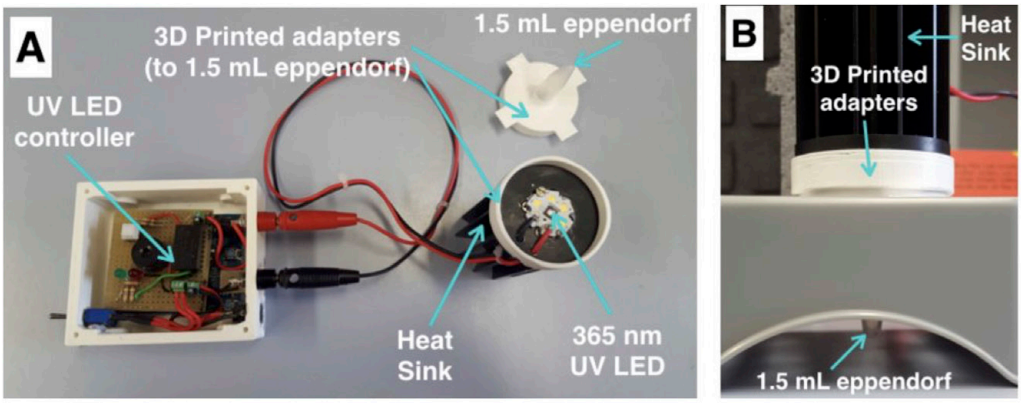

Figure S1. UV-LED prototype for time-effective photoligation. A) Main components of UV-LED prototype for the time-effective photoligation of samples. B) UV-LED prototype adapted to a 1.5 mL eppendorf, prepared to irradiate the sample.

e) Instrument for focused NIR-irradiation of microwells' bottom surface (980 nm NIR photoligation)

A 3W CW laser (MDL-H-980-3W) with emission at 980 nm was used as the excitation source. The laser beam was directed to the instrument using a 200 µm core fiber, which was coupled to a collimator lens at its end. Once collimated, the laser beam was reflected toward the microwells by means of a short-pass dichroic mirror (Thorlabs DMSP950R) and focused on the microwell's bottom surface using a 10× objective. The upconversion emission coming from the bottom of the well went through the short-pass dichroic mirror and a short-pass filter (Thorlabs FES900), which cleaned

the harvested signal by blocking the reflected 980 nm coming from the laser. Finally, it was splitted (beam splitter 400-700 nm, 30:70, BSS10R Thorlabs) simultaneously to a lens (LA1608 N-BK7, Thorlabs), which formed the image to a digital camera (DFC310 FX, Leica Microsystems), and a collimator lens, which harvested the light into an optical fiber, directing it to a spectrometer (Glacier X, B&W Tek). A scheme of the instrument is depicted in Figure S2

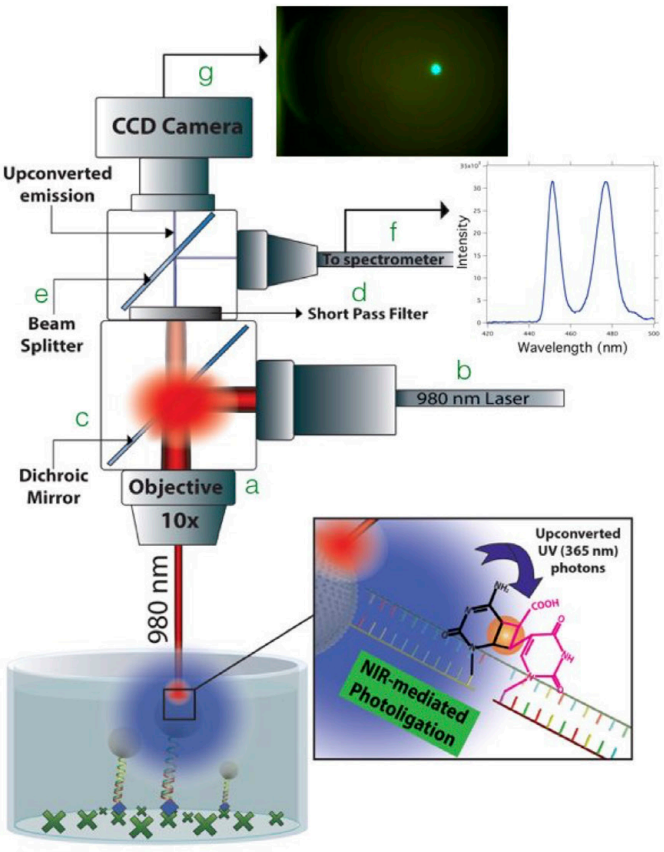

Figure S2. Instrument for focused NIR-irradiation of microwells' surface. The instrument consisted of an 10x objective (a), which focused the collimated beam of a 980 nm laser onto the microwell surface (b), after its reflection by a dichroic mirror (c). The upconverted emission from the well's

surface was filtered to remove the 980 nm reflected light (d), and splitted (e) to a spectrophotometer (f, see model spectra) and a CCD camera (g, see image of upconversion emitting-spot at the bottom of a microwell). A NIR irradiation power density of ~700 W/cm^2 (0.5 W continuous-wave laser power output focused in a ~300 μm diameter spot) was selected for having a negligible thermal effect on both 50 μL of H_2O or 50 μL D_2O (contained in microwells) after 10 min continuous irradiation in an ice-bath.

f) Anti-Stokes photoluminescence imaging device (Imaging of microwells' bottom surface)

The upconversion luminescence from microwells' bottom surface was imaged using a Chameleon microplate reader (Hidex Ltd., Turku, Finland) modified for near-infrared excitation and equipped with a cooled CCD camera. The setup has been described by Ylihärsilä et. al.[2] An infrared laser diode (DLS-976- 008, Optical Fiber Systems Inc., Massachusetts, USA) delivering 7.0 W radiant flux at 976 ± 2 nm out of an optical fiber (100 μm core diameter) was used as excitation source. The measurements were performed using 460/20 nm emission filter (Chroma Technology) using 2-s excitation per well.

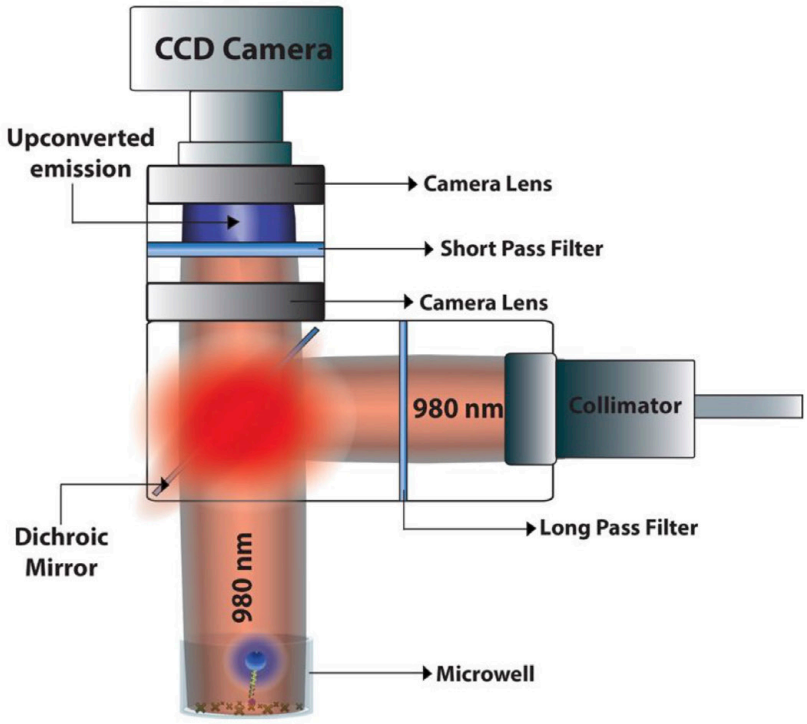

Figure S3. General scheme of the device used for imaging the surface of the dried microwells after NIR-mediated photoligation experiments. For more details see reference.

S2. Results

S2.1 Synthesis and characterization. The synthesis of the $NaYF_4$: Yb^{3+}, Tm^{3+} UCNPs gave as result monodisperse spherical nanoparticles with a mean diameter of 48 ± 3 nm as revealed by TEM (see Figure S4A). The selected-area electron diffraction (SAED) pattern depicts the polycrystalline diffraction rings corresponding to the (100), (110), (200), (201), (210), and

(211) planes of the β-phase $NaYF_4$ lattice (JCPDS card no. 16-0334), see Figure S4B. In the HRTEM image (Figure S4C), one can clearly distinguish a d-space of 0.51 nm corresponding to the (100) lattice plane. X-ray energy dispersive spectroscopy analyses demonstrated that these nanoparticles were formed by the following composition; β-$NaY_{0.64}F_4$; $Yb^{3+}_{0.32}Tm^{3+}_{0.04}$ (see Table S1). The synthesized UCNPs exhibit upconversion emission upon illumination with a CW laser at 980 nm, see Figure S4D. Here one can observe the emission peaks at 345, 365, 450, 475 and 800 nm corresponding to the $^1I_6 \rightarrow {}^3F_4$, $^1D_2 \rightarrow {}^3H_6$, $^1D_2 \rightarrow {}^3F_4$, $^1G_4 \rightarrow {}^3H_6$, and $^1G_4 \rightarrow {}^3H_5$ transitions of the Tm^{3+} ions, respectively.[3,4] The surface of the synthesized UCNPs was functionalized with polyacrylic acid (PAA, Mw~2000 g/mol) via ligand exchange reaction. This step yields a polymeric shell around the UCNP that provides colloidal stability in aqueous media as well as carboxylic groups that were further used for the coupling of an amino-modified DNA oligonucleotide using EDC/sulfo-NHS chemistry. The resulting oligonucleotide probe-attached UCNPs were employed as reporters and named as "UC-Probe".

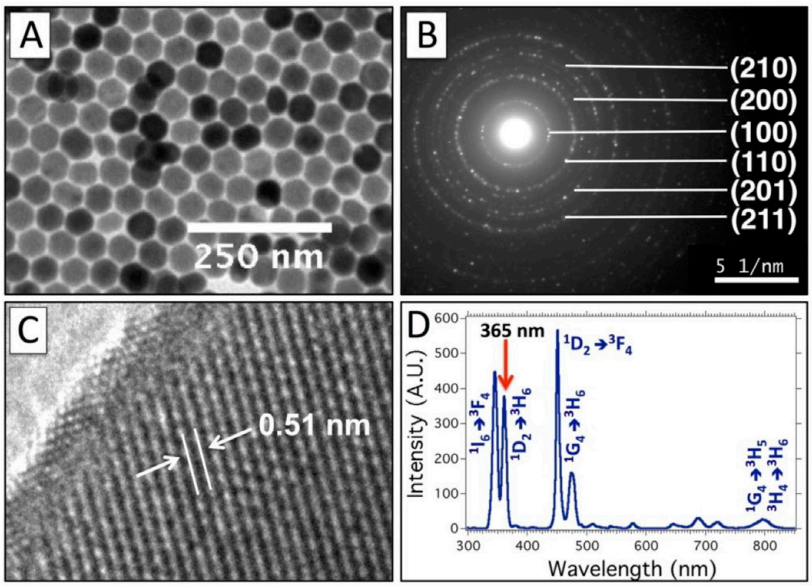

Figure S4. A) TEM image of as-synthesized hexagonal $NaY_{0.64}F_4$; $Yb^{3+}_{0.32}$ $Tm^{3+}_{0.04}$ UCNPs. B) Representative SAED pattern exhibiting highly crystalline structure of the UCNPs. C) HR-TEM image of a single UCNP showing the plane (100). D) Emission spectra of the nanoparticles upon irradiation with a CW laser at 980 nm with a power density of 300 W/cm^2.

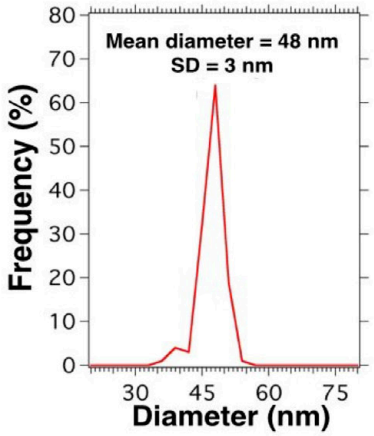

Figure S5. Size distribution analyses of UCNPs. The UCNPs showed a mean diameter of 48.7 nm, while having high monodispersity (SD = 2.8 nm).

Table S1. EDX analyse results regarding Y, Yb and Tm composition of UCNPs.

Element	Weight %	Atomic %
Y K	48.52	64.72
Yb L	50.84	34.86
Tm L	0.64	0.42
Total:	100	100

S2.2. Structure comparison of *photoactivatable* and non-*photoactivatable* nucleotides

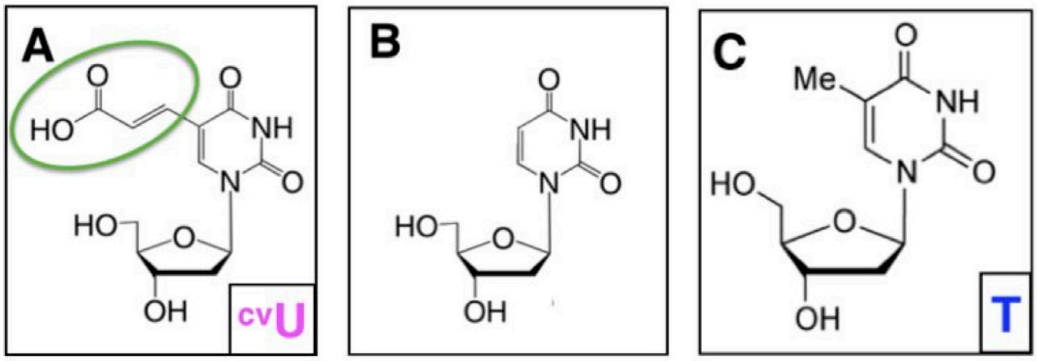

Figure S6. A) Chemical structure of 5-carboxyvinyl-2'-deoxyuridine (^{cv}U), the modified nucleotide used in the *photoactivatable* capture probe ("∗cProbe"). The photo-reactive moiety has been marked in green. B) Chemical structure of deoxyuridine for comparison. C) Chemical Structure of thymidine (T), the natural deoxi-nucleotide present within the traditional capture probe ("cProbe").

S2.3. Selection of denaturation solution to evaluate the photoligation process

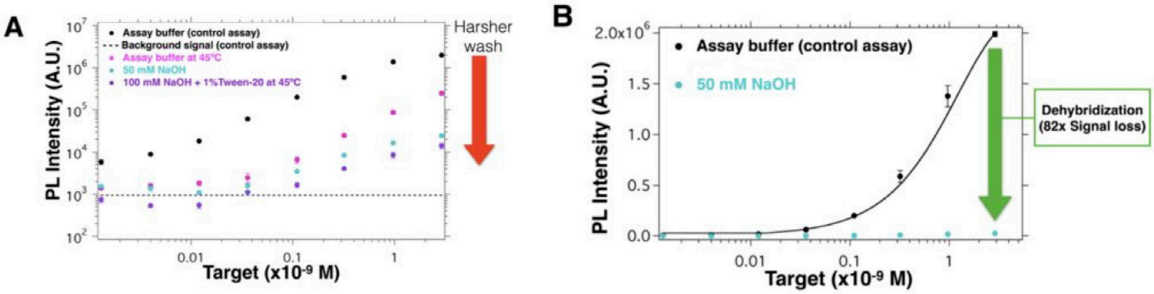

Figure S7. Selection of denaturation solution to evaluate the photoligation process A) Signal at different target concentrations after using several denaturation washes: Control Assay (black); Control Assay + "45º heating step" (pink); Control Assay + "50 mM NaOH" (light blue); Control Assay + "100 mM NaOH + Tween-20 at 45 ºC" (violet). B) Signal loss after using 50 mM NaOH. 50 mM NaOH was selected as the DNA denaturation solution due to its effectiveness (82x signal loss at the highest tested target concentration, 3 nM) and less harmfull effect (compared with the other studied solutions) on streptavidin and streptavidin-biotin interaction stability.

S2.4. Comparison of ∗cProbe and cProbe under focused NIR photoligation

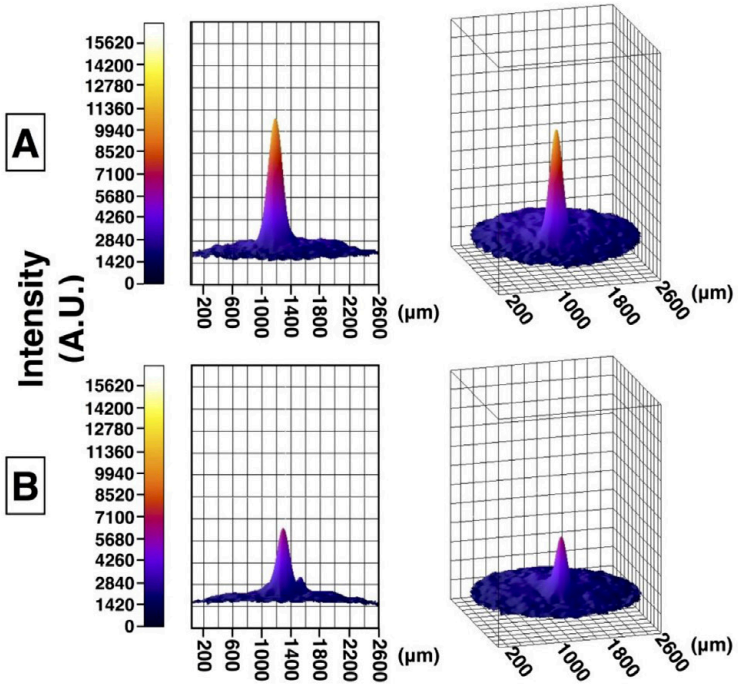

Figure S8. Effect of the focused NIR irradiation of the UC-labels captured at the bottom of the wells when using ∗cProbe (A) or cProbe (B). The high signals obtained when using ∗cProbe confirms the NIR photoligation.

S2.5. Target detection by focused NIR photoligation

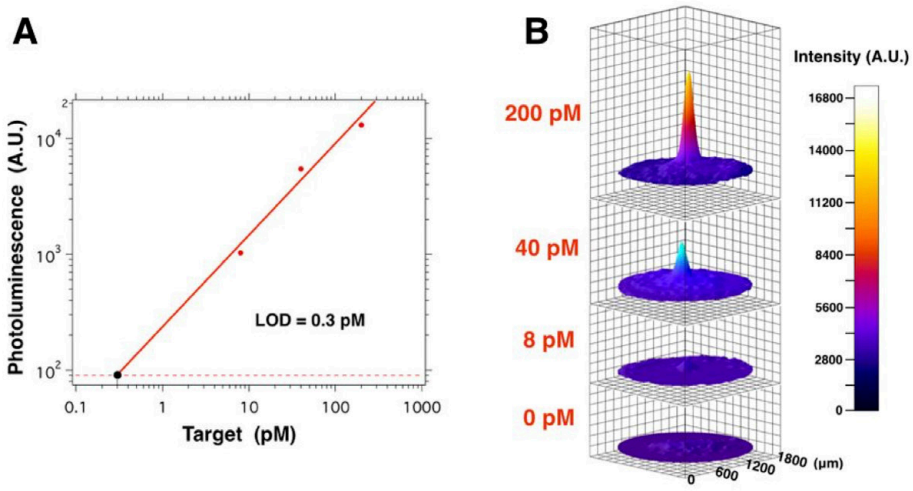

Figure S9. Target detection by focused NIR photoligation. A) Calibration curve at different target concentration (200 pM to 8 pM), the dotted red line represents the LOD defined as the Bg + 3xSD. B) Variation of spot intensity at the bottom of microwells as a function of target concentration. Target concentration, from top to bottom: 200 pM, 40 pM, 8 pM and 0 pM. The PL intensity scale bar is depicted in the right side.

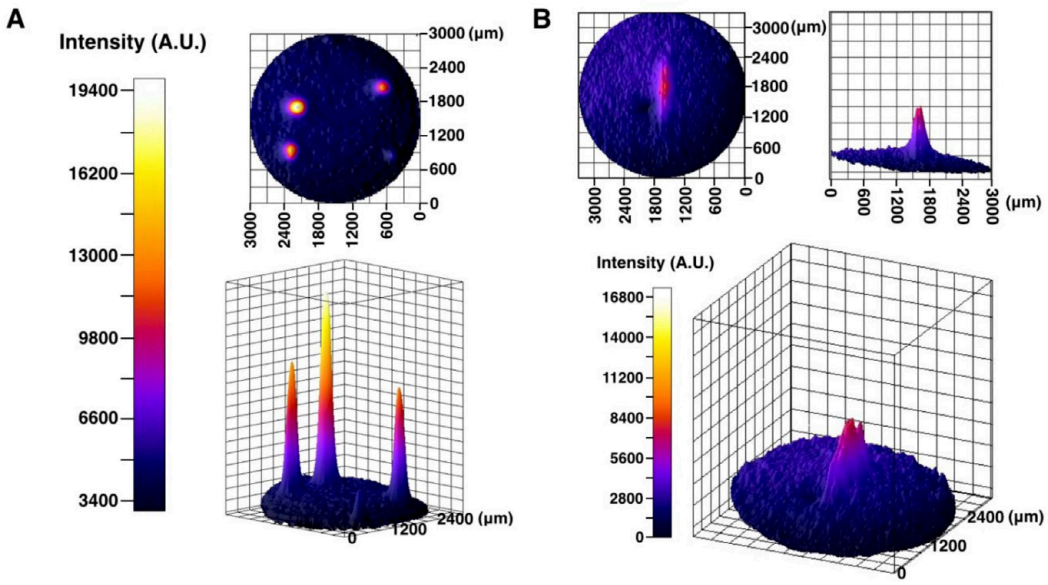

S2.6 Patterning, spot shape and intensity variation

Figure S10. Patterning, spot shape, and intensity variation. A) Intensity patterning. The NIR photoligation in the presence of target allows the selective creation of patterns, spatially and intensity controlled. This can be simply achieved choosing the spatial coordinates within the well to irradiate it, and modifying the irradiation time in order to vary the intensity of the spot. The NIR irradiation time of the different spots shown was 1.5 min, 5 min, 10 min and 20 min B) Shape control. The shape of the photochemically ligated spot can be modified by changing the shape of the NIR laser excitation beam. In this case a rectangular beam shape has been used, in contrast to the circular shape used in S8A. The PL intensity scale bar is depicted on the left side.

S3. References

(1) Soukka, T.; Kuningas, K.; Rantanen, T.; Haaslahti, V.; Lövgren, T. Photochemical Characterization of up-Converting Inorganic Lanthanide Phosphors as Potential Labels. *J. Fluoresc.* **2005**, *15*, 513.

(2) Ylihärsilä, M.; Valta, T.; Karp, M.; Hattara, L.; Harju, E.; Hölsä, J.; Saviranta, P.; Waris, M.; Soukka, T. Oligonucleotide Array-in-Well Platform for Detection and Genotyping Human Adenoviruses by Utilizing Upconverting Phosphor Label Technology. *Anal. Chem.* **2011**, *83*, 1456.

(3) Yin, A.; Zhang, Y.; Sun, L.; Yan, C. Colloidal Synthesis and Blue Based Multicolor Upconversion Emissions of Size and Composition Controlled Monodisperse Hexagonal NaYF4 : Yb,Tm Nanocrystals. *Nanoscale* **2010**, *2*, 953.

(4) Kale, V.; Lastusaari, M.; Holsa, J.; Soukka, T. Intense UV Upconversion through Highly Sensitized NaREF4:Tm(R:Y,Yb) Crystals. *RSC Adv.* **2015**, *5*, 35858.

III.2.5 Conclusions

- The successful target-induced ligation between the capture probes has been demonstrated by using both SPAAC, and the photochemical ligation mediated by ^{cv}U.

- Both strategies have shown specificity, as low background signals were obtained in the absence of the target sequence.

- These target-induced ligation strategies allowed the improvement of the Sg/Bg ratio upon harsh or repeated washes, leading to the development of highly sensitive heterogeneous assays.

- The SPAAC strategy has demonstrated potential for quick and sensitive assays (LOD ~ 100 fM), which could be ideally applied in POC detection platforms.

- Although not so straightforward as SPAAC, the use of the photochemical ligation strategy allowed the development of even more sensitive assays (21 fM), as well as controlling the moment at which the ligation reaction started and stopped.

- Local photochemical ligation at the surface of the UC-labels using 980 nm photons as external light source has been demonstrated.

- The possibility to control the place, as well as the amount of time the photochemical ligation takes place in a flat surface was demonstrated by creating patterns at the bottom of microwells. This offers new possibilities in order to construct arrays, sensors, and perform light-controlled surface modifications.

IV. Discussion

IV) Discussion

The synthesis of high-quality UCNPs has been an important aim in this thesis work. The fact that it conforms the first step in the nano-construction of the different UC-labels makes it essential to have a tight synthetic control over it, as this will further condition the performance of the resulting reporters. As evidenced in the different publications, monodisperse UCNPs were obtained using the Ostwald ripening method. This could be achieved independently of the dopant nature and concentration, in spite of their reported influence on crystal growth rate and nucleation,[1] whereas the use of the different activator Ln^{3+} ions (Er^{3+} and Tm^{3+}) allowed to control the UCNPs emission color (e.g. green or blue). The importance of monodispersity when designing UC-labels comes in part from the fact that these reporters experience a size-dependent emission intensity and ratio between emission peaks.[2–4] Thus, when detecting minute amounts of labeled analytes, and consequently of UC-labels, differences in size between the individual UCNPs should be avoided. Apart from monodispersity, the structural analyses showed that UCNPs were formed in β-phase, which is quite important in bioassays as it yields intense upconversion luminescence and permits to use relatively small particle sizes while keeping a good detectability.

It is obvious that depending on the detection strategy involved, there will be certain characteristics that may be required from UC-labels in order to achieve good detection performances. In this sense, different surface functionalization were successfully implemented in this thesis' work, each possessing some desired characteristics: controlled silica shell thicknesses that acted as spacer, thin silica coatings to yield stable shells in order to separate the UCNPs from the media and give a solid support where subsequent covalent surface modifications could be easily performed, further functionalization with APTES to yield positively charged surfaces and with succinic anhydride to give carboxylic groups, or the ligand exchange of oleic acid with PAA, which directly yielded carboxylic acid modified surfaces as well as moderately robust and thin coatings. Besides these specific features, all these surface modification strategies share that they turned UCNPs water-dispersible and made possible their further bioconjugation with ssDNA capture probes, when required.

As shown in the section III.1, the combination of proper UC-labels with specific FRET pairs has important implications on the mechanism of the potential sensor and its overall performance. For example, the use of Q-dots as acceptors permits to design sensors based on FRET, in which UCNPs' luminescence is quenched in close proximity to Q-dots while the emission of the latter is activated through this mechanism (publication 2). This would allow using the upconversion quenching and/or the Q-dot emission as transducer of the presence of the targeted oligonucleotide sequence. However, despite the complete overlap between UCNPs' emission and CdTe Q-dots absorption, a maximum FRET efficiency (*E*) of 10% was obtained for the thinnest silica shell tested (3 nm). After calculating a Förster radius of R_0 = 5.5 nm, the size of the UCNPs used in the work (33 nm) together with their multi-emitter nature (i.e. the distribution of Er^{3+} ions within the NP) arise as the main limiting parameters behind this relatively low *E*. In fact, the theoretical model permitted to quantify an *E* much higher than 10% for Er^{3+} ions very close to the UCNPs' surface (i.e. less than 5 nm). This clearly indicates that total FRET efficiencies higher than 10% are possible for systems based on UCNPs / CdTe Q-dots if some strategies, when if not a combination of them, are implemented: using small UCNPs as donors (e.g. 20 nm in diameter or lower), using UCNPs based on an inert core (i.e. with no Ln doping) and an active shell architecture to locate the majority of the Er^{3+} close to the surface, using a very thin surface functionalization (e.g. less than 1 nm if possible) when designing UCNPs detection labels.

On the other hand, AuNPs can not only be used as acceptors in RET systems, but as plasmonic nanostructures to increase upconversion emissions due to the Purcell effect, which may serve as a new alternative sensing mechanism based on target-induced luminescence enhancement. As demonstrated in publication 3, the size of the AuNP conditions the effect exerted over UCNPs' luminescence (i.e. quenching or enhancement), and to which extent the luminescence is influenced by this effect. For example, small AuNPs are better quenchers, finding an optimum size of ~14 nm in diameter. Contrary to what occurs with UCNPs/Q-dots pairs, the energy transferred to AuNPs that produce quenching of upconversion luminescence is dissipated by the acceptor in a non-radiative way, and not partially in the form of a new emission as it is the case in Q-dots. When the AuNPs size continue to increase,

the quenching exerted over UCNPs is compensated by the enhancement of their emission, which results in a decrease of effective quenching up to a total compensation of both effects (i.e. neither quenching or enhancement of emission is observed) for AuNPs ranging 40-50 nm in size. Higher diameters exert a predominant enhancement effect over UCNPs' emission by increasing the radiative decay. It is important to highlight that all these effects have been found using a constant separation between UCNPs/AuNPs of ~4 nm, which correspond to the UCNPs SiO_2 shell. The maximum luminescence quenching achieved in these conditions was around 40%, thanks to the use of AuNPs of ~14 nm. As pointed out in publication 2, the use of smaller UCNPs may allow more Er^{3+} ions to participate in the RET process resulting in a higher RET efficiency, which may be one of the reasons for the relatively high quenchings observed for 18 nm UCNPs in publication 3. As also suggested in publication 2, the use of thinner shells may further increase the efficiency of this process, which should be considered for the optimal design of RET sensors based on the quenching of UCNPs with AuNPs. In addition, a luminescence enhancement of around 30% was achieved with 66 nm AuNPs. Noteworthy, although not being the optimum size for the development of potential sensors based on luminescence enhancement, it establishes a lower size limit from which an effective enhancement can be obtained.

As explained in the work of this thesis, reducing background noise while conserving the same levels of specific signal formed by the presence of the target can be a way to improve the Sg/Bg ratio and sensitivity of heterogeneous assays using UC-labels. This approach has been proposed to be possible using a target-induced covalent ligation between the two capture probes used for its detection: one attached to the UCNPs (UC-label), and the other containing a biotin modification in order to subsequently capture the resulting hybridized complexes in SA-coated microwells.

In publication 4 we studied a target-induced SPAAC reaction between an N_3-modified capture probe, which was attached to UCNPs, and another capture probe containing a DBCO group and a biotin modification. The formation of this covalent bond in the presence of the target was demonstrated, by comparison with a non-ligated capture probe, using harsh washes (50 mM NaCl at 50ºC). Under these conditions, the signal from the target was conserved when using the modified

probes (i.e. the formation of the covalent bond avoided the loss of signal upon harsh washes), while the signal dropped in the case of the non-ligated probes. On the other hand, when no target was present, the background signal of the modified probes was comparable to the background signal of the non-ligated ones, proving the specificity of the SPAAC reaction. This strategy allowed a LOD of 100 fM, and it proceeded automatically by mixing the UC-labels, the DBCO containing biotinylated probes, the sample containing the target, and letting them to react for a fixed amount of time. Due to its simplicity, it could be easily implemented into automatized processes or other detection platforms (e.g. lateral-flow assays), different from the one used in this work (i.e. microwell plates). The fact that this reaction is also bioorthogonal implies that it avoids any interference from molecules and functional groups normally present in biological samples. This is very important, as it potentially permits to detect the target sequences in complex samples such as serum, bypassing miRNA isolation steps and other sources of bias from current well-established detection/quantification methods.[5]

Another strategy for the target-induced ligation of capture probes was studied in "publication 5". In this work, a special capture probe, containing a photoactivatable nucleotide (^{cv}U) at the 5' end and a biotin modification at the 3' end, and another probe, attached to UCNPs by its 5' end and containing a cytidine at its 3' end, were required. Upon hybridization with the target sequence, the ^{cv}U is hold, facing the cytidine of the other probe in a specific spatial configuration. In this situation, the irradiation with light at 365 nm produced the photochemical ligation of the probes via formation of a cyclobutane group. In this publication, the assessment of the photochemical ligation rate, and the optimization of the process were demonstrated by comparison with a traditional capture probe. The use of a 365 nm centered LED as UV source made it possible to carry out this photochemical ligation in a relatively short period of time (20 min), while also permitting to decide the moment at which this reaction could be started/stopped. This translated in a time-effective and a tightly controlled ligation of the probes, which provided a LOD of 21 fM after using repeated washings to reduce the background signal. In this work, UCNPs doped with Yb^{3+}/Tm^{3+} were used. As they exhibit an emission peak at 365 nm under 980 nm excitation, we tested the feasibility to locally carry out the photochemical ligation at the surface of the UC-labels using

this emission while externally illuminating at 980 nm. This strategy was proved to be possible, allowing a new photochemical ligation modality that could be employed to detect specific sequences when the more common external UV sources could exert a negative effect on the sample. Taking advantage of the use of a 980 nm laser in this modality, the beam was focused at the bottom of SA-coated microwells to photochemically ligate the hybridized complexes (previously captured) only at certain regions of the wells. In this way, the bottom of the microwells was used as a canvas, where intensity patterns could be written in the form of spots by this photochemical ligation strategy and later revealed by removing the non-ligated complexes using a denaturalizing solution (NaOH). Parameters such as photochemical ligation rate, irradiation time, intensity of the photochemically ligated spots, spatial localization of the intensity spots, spot shape and pattern formation could be controlled by these means.

IV. Discusión

IV) Discusión

La síntesis de nanopartículas de conversión ascendente (UCNPs) de alta calidad ha sido un objetivo importante en este trabajo de tesis. El hecho de que ésta conforma el primer paso en la nano-construcción de las diferentes etiquetas de conversión ascendente (UC-labels) hace esencial el tener un estrecho control sintético sobre la misma, ya que condicionará el funcionamiento de las etiquetas resultantes. Tal y como se ha demostrado en las diferentes publicaciones, se han logrado obtener UCNPs monodispersas mediante el método de maduración de Ostwald. Esto se ha logrado con independencia de la naturaleza y la concentración del dopante, a pesar de su influencia sobre la velocidad de crecimiento del cristal y su nucleación,[1] mientras que el uso de diferentes iones Ln^{3+} activadores (Er^{3+} y Tm^{3+}) permitió el control del color de la emisión de las UCNPs (e.g. verde o azul). La importancia de la monodispersidad durante el diseño de las UC-labels procede, en parte, de que estas etiquetas experimentan una intensidad de emisión y un ratio entre picos que depende del tamaño de partícula.[2–4] Así, al detectar cantidades minúsculas de analitos etiquetados, y por tanto de UC-labels, diferencias en tamaño entre las UCNPs deberían ser evitadas. Aparte de la monodispersidad, los análisis estructurales mostraron que las UCNPs estaban formadas por fase-β, lo cual es bastante importante para los bioensayos, ya que permite usar tamaños de partícula relativamente pequeños mientras se mantiene una buena detectabilidad. Es obvio que, dependiendo de la estrategia de detección involucrada, habrá ciertas características que serán requeridas por parte de las UC-labels para obtener un funcionamiento óptimo durante la detección. En este sentido, en este trabajo de tesis se implementaron satisfactoriamente diferentes funcionalizaciones superficiales, cada una poseyendo características deseadas: Recubrimientos de sílice de espesores controlados usados como espaciadores, espesores de sílice delgados para dar recubrimientos estables con el objetivo de separar las UCNPs del medio y dar lugar a un soporte sólido donde se pudieran llevar a cabo subsiguientes modificaciones superficiales covalentes, posterior funcionalización con APTES para dar lugar a superficies cargadas positivamente y con anhídrido succínico para dar grupos carboxílicos, o el intercambio de ligando de ácido oleico con PAA, el cual dio directamente superficies modificadas con ácidos carboxílicos

así como recubrimientos relativamente finos y robustos. Además de estas características específicas, todas estas estrategias de modificación superficial comparten que permitieron a las UCNPs ser dispersables en agua e hicieron posible su posterior bioconjugación con sondas de captura de ssDNA (DNA monocateario), cuando fue requerido.

Tal como se ha mostrado en la sección III.1, la combinación de UC-labels apropiadas con parejas FRET específicas tiene importantes implicaciones en el mecanismo del potencial sensor y su óptimo funcionamiento global. Por ejemplo, el uso de puntos quánticos (Q-dots) como aceptores permite diseñar sensores basados en FRET en los que la luminiscencia de las UCNPs es desactivada en cercana proximidad a los Q-dots, mientras que la emisión de estos últimos es activada a través de este mecanismo (publicación 2). Esto permitiría usar la desactivación de la conversión ascendente y/o la emisión del Q-dot como transductor de la presencia de la secuencia del oligonucleótido buscado. Sin embargo, a pesar del completo solapamiento entra la emisión de las UCNPs y la absorbancia de los Q-dots de CdTe, se obtuvo una eficiencia de FRET (E) máxima del 10% para el recubrimiento de sílice más delgado que fue testado (3 nm). Tras calcular un radio de Förster de R_0 = 5.5 nm, el tamaño de las UCNPs usadas en este trabajo (33 nm), junto con su naturaleza de multi-emisor (i.e. la distribución de iones de Er^{3+} dentro de la NP), destaca como el principal parámetro limitante detrás de esta E relativamente baja. De hecho, el modelo teórico permitió cuantificar una E mucha mayor al 10% para iones de Er^{3+} muy cercanos a la superficie de las UCNPs (i.e. menos de 5 nm). Esto indica claramente que son posibles eficiencias totales de FRET superiores al 10% para sistemas basados en UCNPs/Q-dots de CdTe si algunas estrategias, cuando no una combinación de ellas, son implementadas: usar UCNPs pequeñas como donadores (e.g. de 20 nm de diámetro o menos), usar UCNPs con una arquitectura basada en un núcleo inerte (i.e. sin dopado con Ln) y un recubrimiento activo para situar la mayoría de los iones de Er^{3+} cerca de la superficie, usar una funcionalización superficial muy delgada (e.g. menos de 1 nm si es posible) cuando se diseñen las UCNPs como etiquetas para detección.

Por otro lado, las AuNPs pueden no solamente usarse como aceptores en sistemas RET sino como nanoestructuras plasmónicas para incrementar las emisiones de

conversión ascendente debido al efecto Purcell, lo cual puede servir como un mecanismo nuevo y alternativo de detección basado en el aumento de luminiscencia inducido por la diana. Como se demostró en la publicación 3, el tamaño de la AuNP condiciona el efecto ejercido sobre la luminiscencia de las UCNPs (i.e. desactivación o incremento), y hasta que punto la luminiscencia se ve afectada por este efecto. Por ejemplo, AuNPs pequeñas son mejores desactivadores, encontrando un tamaño óptimo de ~14 nm de diámetro. Al contrario de lo que ocurre con pares UCNPs/Q-dots, la energía transferida a las AuNPs que produce la desactivación de la luminiscencia de conversión ascendente es disipada por el aceptor de manera no radiativa, y no parcialmente en forma de una nueva emisión como es el caso de los Q-dots. Cuando el tamaño de las AuNPs continúa incrementando, la desactivación ejercida sobre las UCNPs es compensada por el incremento de su emisión, lo que resulta en una reducción efectiva de la desactivación hasta una compensación total de ambos efectos (i.e. no se observa ni desactivación ni incremento de la emisión) para AuNPs de tamaños en el rango 40-50 nm. Tamaños mayores ejercen predominantemente un efecto de incremento sobre la emisión de las UCNPs debido al aumento del decaimiento radiativo. Es importante destacar que todos estos efectos se han encontrado usando una separación constante entre UCNPs/AuNPs de ~4 nm, que corresponde con el grosor del recubrimiento de SiO_2 de las UCNPs. La máxima desactivación de la luminiscencia obtenida en estas condiciones fue de alrededor del 40%, gracias al uso de AuNPs de ~14 nm. Tal y como se indicó en la publicación 2, el uso de UCNPs más pequeñas permitiría a un mayor número de iones de Er^{3+} participar en el proceso RET, resultando en una eficiencia de RET mayor, lo cual puede ser una de las razones por las que se observaron desactivaciones relativamente altas para UCNPs de 18 nm en la publicación 3. Como también se sugirió en la publicación 2, el uso de recubrimientos más delgados podría incrementar la eficiencia de este proceso, lo cual debería ser tenido en cuenta para un diseño óptimo de sensores RET basados en la desactivación de UCNPs con AuNPs. Adicionalmente, se obtuvo un incremento de la luminiscencia de en torno a un 30% con AuNPs de 66 nm. Es de destacar que, aunque éste no es el tamaño óptimo para el desarrollo de potenciales sensores basados en incremento de la luminiscencia, establece un

límite de tamaño inferior a partir del cual se puede conseguir un incremento efectivo.

Como se ha explicado en esta tesis, reducir el ruido de fondo a la vez que conservando los mismos niveles de señal específica formados por la presencia de la secuencia diana puede ser una forma de mejorar la relación señal/ruido (Sg/Bg ratio) y la sensibilidad de los ensayos heterogéneos que usan UC-labels. Se ha propuesto que este enfoque podría ser posible usando una ligación covalente, inducida por secuencia diana, entre las dos sondas de captura usadas para su detección: una enganchada a las UCNPs (UC-labels), y la otra conteniendo una biotina como modificación, para capturar de manera subsiguiente los resultantes complejos hibridados en micropocillos recubiertos con estreptavidina (SA). En la publicación 4 se estudió el uso de una reacción SPAAC, mediada por secuencia diana, entre una sonda de captura modificada con N_3 (la cuál fue unida a las UCNPs), y otra sonda de captura que contenía un grupo DBCO y una modificación de biotina. La formación de este enlace covalente en presencia de la secuencia diana se demostró, mediante su comparación con una sonda de captura no ligada, usando lavados fuertes (50 mM NaCl a 50ºC). En estas condiciones, la señal proveniente de la secuencia diana se conservó cuando se usaron las sondas modificadas (i.e. la formación del enlace covalente evitó la pérdida de señal durante los lavados fuertes), mientras que la señal cayó en el caso de las sondas no ligadas. Por otro lado, cuando la secuencia diana no estaba presente, la señal del ruido de fondo de las sondas modificadas fue comparable a la del ruido de fondo de las hebras no ligadas, probando la especificidad de la reacción SPAAC.

Esta estrategia permitió un LOD de 100 fM, y ocurre automáticamente mezclando las UC-labels, las hebras biotiniladas que contienen DBCO, la muestra conteniendo la secuencia diana y dejándolas reaccionar durante una cantidad de tiempo fija. Debido a su simplicidad, ésta podría implementarse fácilmente en procesos automatizados u otras plataformas de detección (e.g. Tiras de ensayo), diferentes de la usada en este trabajo (i.e. placas de multipocillos). El hecho de que esta reacción también es bioortogonal implica que evita cualquier interferencia de las moléculas y grupos funcionales que están normalmente presentes en las muestras biológicas. Esto es muy importante, ya que ello permite potencialmente la detección de secuencias diana en muestras como el suero, sorteando los pasos de

aislamiento de miRNA y otras fuentes de sesgo típicos de métodos de detección/cuantificación actuales y bien establecidos.[5]

Otra estrategia para la ligación inducida por secuencia diana de sondas de captura fue estudiada en la "publicación 5". En este trabajo, se requirieron una sonda de captura especial, que contenía un nucleótido fotoactivable (^{cv}U) en el extremo 5' y una biotina en el extremo 3', así como otra sonda, unida a las UCNPs por su extremo 5' y conteniendo una citidina en su extremo 3'. Al hibridar con la secuencia diana, el ^{cv}U se mantiene encarado a la citidina de la otra sonda con una configuración espacial específica. En esta situación, la irradiación con luz a 365 nm produjo la ligación fotoquímica de las sondas mediante la formación de un grupo ciclobutano. En esta publicación, la evaluación de la tasa de fotoligación, y la optimización del proceso fueron demostrados mediante la comparación con una sonda de captura tradicional. El uso de un LED centrado a 365 nm como fuente de excitación hizo posible la ligación fotoquímica en un tiempo relativamente corto (20 min), mientras permitió controlar el momento al cual esta reacción podría ser empezada/terminada. Esto se tradujo en una ligación rápida y altamente controlada de las sondas, lo cual finalmente permitió obtener un LOD de 21 fM tras usar lavados repetidos para reducir la señal de fondo. En este trabajo se usaron UCNPs dopadas con Yb^{3+}/Tm^{3+}. Debido a que éstas exhiben un pico de emisión a 365 nm cuando se excitan a 980 nm, se investigó también la viabilidad de llevar a cabo la ligación fotoquímica localmente en la superficie de las UC-labels usando esta emisión mientras se iluminaba externamente a 980 nm. Esta estrategia demostró ser posible, permitiendo una nueva modalidad de ligación fotoquímica que podría ser usada para detectar secuencias específicas cuando las fuentes externas de UV, más comunes, puedan ejercer un efecto negativo en la muestra. Aprovechando el uso de un láser a 980 nm en esta modalidad, se focalizó el haz en el fondo de micropocillos recubiertos con SA para ligar fotoquímicamente los complejos hibridados (capturados previamente) solamente en ciertas regiones de los pocillos. De esta forma, el fondo de los pocillos se usó como un "lienzo", donde se pudieron grabar patrones de intensidad en forma de puntos mediante esta estrategia de fotoligación fotoquímica, y revelarse posteriormente mediante la eliminación de los complejos no ligados usando una solución desnaturalizante (NaOH). Parámetros como la tasa de ligación fotoquímica, el tiempo de irradiación,

la intensidad de los puntos ligados fotoquímicamente, la localización espacial de los puntos de intensidad, la forma de los puntos y la formación de patrones pudieron ser controlados por estos medios.

References

(1) Kale, V.; Lastusaari, M.; Hölsä, J.; Soukka, T. Intense UV Upconversion through Highly Sensitized NaRF4:Tm (R:Y,Yb) Crystals. *RSC Adv.* **2015**, *5*, 35858.

(2) Wang, F.; Wang, J.; Liu, X. Direct Evidence of a Surface Quenching Effect on Size-Dependent Luminescence of Upconversion Nanoparticles. *Angew. Chemie Int. Ed.* **2010**, *49*, 7456.

(3) Schietinger, S.; Menezes, L. de S.; Lauritzen, B.; Benson, O. Observation of Size Dependence in Multicolor Upconversion in Single Yb 3+ , Er 3+ Codoped NaYF 4 Nanocrystals. *Nano Lett.* **2009**, *9*, 2477.

(4) Lim, S. F.; Ryu, W. S.; Austin, R. H. Particle Size Dependence of the Dynamic Photophysical Properties of NaYF_4:Yb, Er Nanocrystals. *Opt. Express* **2010**, *18*, 2309.

(5) Chugh, P.; Dittmer, D. P. Potential Pitfalls in microRNA Profiling. *Wiley Interdiscip. Rev. RNA* **2012**, *3*, 601.

V. Conclusions

V) Conclusions

- Monodisperse β-$NaYF_4$ nanoparticles doped with Yb^{3+}/Er^{3+} and $Yb^{3}+/Tm^{3+}$ pairs for red/green and blue/UV emissions, respectively, have been synthesized and characterized.

- Successful implementation of different surface functionalization of UCNPs was demonstrated: growth of robust silica shells with controlled thicknesses, successive surface modifications with APTES and succinic anhydride, ligand exchange of oleic acid with PAA to yield a relatively thin and robust coating. These strategies eventually yielded UCNPs ready for bioconjugation.

- Water-dispersible UCNPs, modified by either of the aforementioned methods, were successfully bioconjugated with traditional or modified ssDNA probes, yielding UC-labels with different functionalities depending on the detection strategy involved.

- Fundamental studies of UCNPs/CdTe Q-dots FRET pairs permitted to calculate the Förster radius (R_0 = 5.5 nm) and find general guidelines to develop effective sensors: small and efficient UCNPs, inert core/active shell UCNPs architectures, thin surface functionalization.

- Systematic studies on the effect of AuNP size on UCNPs' luminescence have revealed that an optimum quenching can be obtained for ~14 nm AuNPs, compensation between quenching and enhancement (i.e. almost no effect on luminescence) occurs in the 40-50 nm range, and luminescence enhancement is predominant for ~66 nm and higher diameters.

- The target-induced ligation of capture probes was successfully achieved using a SPAAC reaction. The assay developed using this strategy permitted to directly detect a small RNA sequence of the *Plasmodium falciparum* ribosomal subunit with a LOD = 100 fM.

- The use of a target-induced photochemical ligation was used to build a highly sensitive sensor for the direct detection of a DNA-analogue of the potential breast cancer biomarker miR-195. Its LOD was 21 fM, which is already within the concentration range of low to moderately abundant miRNAs in serum.

- The emission at 365 nm from Yb^{3+}/Tm^{3+} doped UCNPs under 980 nm external excitation was used to perform local photochemical ligations at the surface of the UC-labels. The potential of this strategy for detection and patterning purposes was demonstrated.

V. Conclusiones

V) Conclusiones

- Se han sintetizado y caracterizado nanopartículas monodispersas de β-$NaYF_4$ dopadas con parejas de Yb^{3+}/Er^{3+} e $Yb^{3}+/Tm^{3+}$ para emisiones en rojo/verde y azul/UV, respectivamente.

- Se ha demostrado la implementación exitosa de diferentes estrategias de funcionalización superficial de UCNPs: El crecimiento de revestimientos robustos de sílice de grosores controlados, modificaciones superficiales sucesivas con APTES y anhídrido succínico, intercambio de ligando de ácido oleico con PAA para producir un recubrimiento relativamente fino y robusto. Estas estrategias produjeron UCNPs preparadas finalmente para su bioconjugación.

- Las UCNPs dispersables en agua, modificadas por alguno de los métodos anteriores, fueron bioconjugadas satisfactoriamente con sondas de ssDNA tradicionales o modificadas, dando lugar a UC-labels con diferentes funcionalidades dependiendo de las estrategia de detección involucrada.

- Estudios fundamentales de los pares FRET UCNPs/Q-dots de CdTe permitieron calcular su radio de Förster (R_0 = 5.5 nm) y encontrar guías generales para desarrollar sensores efectivos: UCNPs pequeñas y eficientes, arquitecturas de UCNPs tipo núcleo inactivo/recubrimiento activo, funcionalización superficial delgada.

- Estudios sistemáticos sobre el efecto del tamaño de las AuNPs en la luminiscencia de las UCNPs han revelado que se puede obtener una desactivación máxima con AuNPs de ~14 nm, una compensación entre desactivación e incremento (i.e. casi ningún efecto en la luminiscencia) ocurre en el rango 40-50 nm, y un incremento de la luminiscencia predomina para diámetros de 66 nm y mayores.

- Se logró llevar a cabo satisfactoriamente la ligación inducida por secuencia diana de sondas de captura mediante reacción SPAAC. El ensayo desarrollado mediante

esta estrategia permitió detectar directamente una pequeña secuencia de RNA de la subunidad ribosomal de *Plasmodium Falciparum* con un LOD = 100 fM.

- El uso de una ligación fotoquímica inducida por secuencia diana se usó para construir un sensor de elevada sensibilidad para la detección directa de un análogo de DNA del potencial marcador de cáncer de mama miR-195. Su LOD fue 21 fM, el cual se encuentra ya dentro del rango de concentraciones de miRNAs de baja a moderada abundancia en suero.

- Se usó la emisión a 365 nm de UCNPs dopadas con Yb^{3+}/Tm^{3+} cuando son excitadas externamente a 980 nm para llevar a cabo ligaciones fotoquímicas locales en la superficie de las UC-labels. Se demostró el potencial de esta estrategia para propósitos de detección y formación de patrones.

VI. Publications and patents during the PhD period

Publications

1) Rafael Contreras-Caceres, Paulino Alonso-Cristobal, Diego Mendez-Gonzalez, Marco Laurenti, Ana Maldonado-Valdivia, Francisco Garcia-Blanco, Enrique López Cabarcos, Antonio Fernandez-Barbero, José Manuel Lopez-Romero, and Jorge Rubio-Retama. "*Temperature Controlled Fluorescence on Au@Ag@PNIPAM-PTEBS Microgels: Effect of the Metal Core Size on the MEF Extension*". Langmuir, 2014, 30 (51), 15560-15567.

2) Paulino Alonso-Cristobal, Olalla Oton-Fernandez, Diego Mendez-Gonzalez, J. Fernando Díaz, Enrique López-Cabarcos, Isabel Barasoain, and Jorge Rubio-Retama. "*Synthesis, Characterization and Application in HeLa cells of NIR Light Responsive Doxorubicin Delivery System based on NaYF4:Yb,Tm@SiO2-PEG Nanoparticles*" ACS Appl. Mater.Interfaces, 2015, 7, 14992-14999.

3) Diego Mendez-Gonzalez, Paulino Alonso-Cristobal, Enrique Lopez-Cabarcos, Jorge Rubio-Retama. "*Multi-responsive hybrid Janus nanoparticles: Surface functionalization through solvent physisorption*", European Polymer Journal, 2016, 75, 363–370.

4) Marco Laurenti, Miguel Paez-Perez, Manuel Algarra, Paulino Alonso-Cristobal, Enrique Lopez-Cabarcos, Diego Mendez-Gonzalez, and Jorge Rubio-Retama. "*Enhancement of the Upconversion Emission by Visible-to-Near-Infrared Fluorescent Graphene Quantum Dots for miRNA Detection*". ACS Appl. Mater. Interfaces, 2016, 8 (20), 12644–12651.

5) Diego Mendez-Gonzalez, Marco Laurenti, Alfonso Latorre, Alvaro Somoza, Ana Vazquez, Ana Isabel Negredo, Enrique López-Cabarcos, Oscar G. Calderón, Sonia Melle and Jorge Rubio-Retama. "*Oligonucleotide Sensor Based on Selective Capture of Upconversion Nanoparticles Triggered by Target-Induced DNA Interstrand Ligand Reaction*". ACS Appl. Mater. Interfaces, 2017, 9 (14), 12272-12281.

6) Diego Mendez-Gonzalez, Enrique Lopez-Cabarcos, Jorge Rubio-Retama, Marco Laurenti. "*Sensors and bioassays powered by upconverting materials*". Advances in Colloid and Interface Science, 2017, 249, 66–87.

7) Sonia Melle, Oscar G. Calderón, Marco Laurenti, Diego Mendez-Gonzalez, Ana Egatz-Gómez, Enrique López-Cabarcos, E. Cabrera-Granado, Elena Díaz, and Jorge Rubio-Retama. "*Förster Resonance Energy Transfer Distance Dependence from Upconverting Nanoparticles to Quantum Dots*". J. Phys. Chem. C, 2018, 122, 18751−18758.

This publication was ACS Editor's choice for immediate, free open access by ACS due to its potential for broad public interest. This honor is given each day of the year to only one article out of all the different ACS journals.

8) Diego Mendez-Gonzalez, Satu Lahtinen, Marco Laurenti, Enrique López-Cabarcos, Jorge Rubio-Retama, Tero Soukka. "*Photochemical Ligation to Ultrasensitive DNA Detection with Upconverting Nanoparticles*". Anal. Chem., **2018**, *90* (22), pp 13385−13392.

This work was awarded the 3rd poster prize at 2nd conference and spring school on properties, design and applications of upconverting nanomaterials organized by The European Upconversion Network (COST Action CM1403).

9) Diego Mendez-Gonzalez, Sonia Melle, Oscar G. Calderón, Marco Laurenti, E. Cabrera-Granado, Ana Egatz-Gómez, Enrique López-Cabarcos, Jorge Rubio-Retama and Elena Díaz. "*Control of upconversion luminescence by gold nanoparticle size: from quenching to enhancement*". Submitted

Patents

1) "*Biosensor for the detection of nucleic acids, method of manufacture and use thereof*" / "*Biosensor para la detección de ácidos nucleicos, método de elaboración y de uso*". Application (reference): ES2580138A1
Grant (reference): ES2580138B2 ; Oficina Española de Patentes.
Inventors: Enrique José López Cabarcos, Diego Méndez González, Marco Laurenti, Paulino Alonso Cristóbal, Jorge Rubio Retama.
Universidad Complutense de Madrid.

2)"*Super fluorescent Ag_2S nanoparticles in the near infrared region and method to obtain them/ Nanopartículas de Ag_2S súper fluorescentes en la región del infrarrojo cercano y método de obtención*".
Application number: P201900006
Inventors: Jorge Rubio Retama, Harrison David Assis Santos, Daniel Jaque García, Diego Méndez González, Marco Laurenti.

VII) Table of acronyms

VII. Table of acronyms

43S PIC	pre-initiation complex
Ago	Argonaute family proteins
APTES	(3-aminopropyl) triethoxysilane
Au	Gold
Au NPs	Gold nanoparticles
C153	Coumarin 153
CdTe	Cadmium telluride
CR	Cross relaxation
CSU	Cooperative sensitization upconversion
^{cv}U	5'carboxyvinyl-2'-deoxyuridine
CW	Continuous wave
Cy3	Cyanine 3 dye
DBCO	Dibenzocyclooctine
DCL-1	Dicer like-1
E	(FRET) Efficiency
EDC·HCl	1-ethyl-3-(3-dimethylaminopropyl)carbodiimide hydrochloride
Er^{3+}	Erbium (III) ion
ESA	Excited-state absorption
ETU	Energy transfer upconversion
EXP5	Exportin-5
Fl	Fluorescein
fM	FemtoMolar (10^{-15} M)
FRET	Förster resonance energy transfer
h	Planck's constant
HCl	Hydrochloric acid
HCV	Hepatitis C virus
HEPES	4-(2-hydroxyethyl)-1-piperazineethanesulfonic acid
HPLC	High performance liquid chromatography
HST	HASTY
K_{nr}	Non-radiative decay parameter

Ln^{3+}	Trivalent Lanthanide ions
LNA	Locked nucleic acid
M	Molar
miRNA	Micro RNA
MNP	Metallic nanoparticle
mRNA	Messenger RNA
N_3	Azide
NaF	Sodium fluoride
NaOH	Sodium hydroxide
NH_4F	Ammonium fluoride
NH_4OH	Ammonium hydroxide
NIR	Near infrared region
nm	Nanometer
NP	Nanoparticle
nt	Nucleotide
OX1	Oxazine 1
PA	Photon avalanche
PAA	Poly-acrylic acid
PABP	Poly(A) binding protein
POC	Point-of-care
Pol II	RNA polymerase II
pre-miRNA	Precursor miRNA
pri-miRNAs	Primary miRNAs
Q	Fluorescence quantum yield
Q-dots	Quantum dots
QS	Quinine sulfate dihydrate
q-PCR	Quantitative polymerase chain reaction
R101	Rhodamine 101
R6G	Rhodamine 6G
RE	Rare earths
RET	Long range resonance energy transfer
RISC	RNA-induced silencing complex

RT	Room temperature
S_0	Singlet ground state
S_1	First singlet excited electronic state
SA	Streptavidin
Sg/bg ratio	Signal-to-background ratio
Si-OH	Silanol group
SPAAC	Strain promoted alkyne-azide cycloaddition
ssDNA	Single stranded DNA
Sulfo-NHS	N-hydroxysulfosuccinimide
T_1	First triplet excited state
TEM	Transmission electron microscopy
TEOS	Tetraethyl orthosilicate
Tm^{3+}	Thulium (III) ion
UC-labels	Upconverting labels
UCNPs	Upconverting nanoparticles
UV-Vis	UV-Visible spectroscopy
XPS	X-ray photoelectron spectroscopy
Yb^{3+}	Ytterbium (III) ion
Γ	Emissive rate (of the fluorophore)
ν_{Exc}	Frequency of excitation light
τ	Fluorescence lifetimes